

Dissertation zur Erlangung des Doktorgrades der Fakultät für Chemie und Pharmazie der Ludwig-
Maximilians-Universität München

**Synthesis, Characterization and
Quantum-Chemical Analysis of $\{\text{Ru}(\text{NO})_n\}^m$ Compounds**

Anja Emmy Ruth Belz

aus

Weißenburg in Bayern, Deutschland

2017

Erklärung

Diese Dissertation wurde im Sinne von § 7 der Promotionsverordnung vom 28. November 2011 von Herrn Prof. Dr. Peter Klüfers betreut.

Eidesstattliche Versicherung

Diese Dissertation wurde eigenständig und ohne unerlaubte Hilfe erarbeitet.

München, den 02.Juni 2017

Anja Belz

Dissertation eingereicht am: 06.06.2017

1. Gutachter: Prof. Dr. Peter Klüfers

2. Gutachter: Prof. Dr. Hans-Christian Böttcher

Mündliche Prüfung am: 24.07.2017

Diese Arbeit wurde in der Zeit von Mai 2013 bis Juni 2017 am Department für Chemie der Ludwig-Maximilians-Universität München am Lehrstuhl für Bioanorganische Chemie und Koordinationschemie unter Anleitung von Herrn Prof. Dr. Peter Klüfers durchgeführt.

"When life gets you down, do you know what you've got to do?

Just keep swimming!"

(Dorie, Finding Nemo)

Table of Contents

1	Introduction	1
1.1	Biological relevance of nitrogen monoxide	1
1.2	Properties of nitrogen monoxide.....	4
1.3	Ruthenium-nitrosyl complexes	6
1.4	<i>N</i> -heterocyclic carbenes	13
1.5	Aim of this work.....	18
2	Results	19
2.1	Synthesis of the enetetramines	19
2.2	Synthesis of the precursor compounds	20
2.3	Synthesis of the {RuNO} ⁶⁻⁸ phosphane compounds.....	22
2.4	Synthesis of the tetra-coordinated {RuNO} ⁸ phosphane compounds.....	23
2.5	Synthesis of the tetra-coordinated {RuNO} ⁸ NHC compounds.....	25
2.6	Synthesis of the penta-coordinated {RuNO} ⁸ phosphane compounds	28
2.7	Synthesis of the penta-coordinated {RuNO} ⁸ NHC compounds	30
2.8	Synthesis of the {RuNO} ⁶ NHC compounds	34
2.9	Synthesis of the {Ru(NO) ₂ } ⁸ phosphane compounds.....	39
2.10	Synthesis of the {Ru(NO) ₂ } ⁸ NHC compounds.....	42
2.11	Synthesis of the {Ru(NO) ₂ } ¹⁰ compounds	45
2.12	Analytical study of the solution behavior of the [RuX(NO)(PPh ₃) ₃] compounds 9a and 9b	51
2.13	Quantum-chemical calculations	53
2.14	The structures of [Ru(NO) ₂ (PPh ₃) ₂ SO ₄] (16) and [RuX(NO)(PPh ₃) ₃] (9a, b).....	61
3	Discussion	66
3.1	The ligand properties of phosphanes and NHCs and their influence on the reactivity and the structure of the {Ru(NO) _n } ^m compounds.....	66
3.2	The RuNO moiety in the context of the MO theory	70
3.3	Populations analyses.....	85
4	Summary.....	87
5	Experimental Part.....	92

Table of Contents

5.1	Common working techniques	92
5.2	Analytic methods	93
5.3	Reagents and solvents	94
5.4	Preparation of the enetetramines	96
5.5	Preparation of the precursor compounds	100
5.6	Synthesis of the {RuNO} ⁶⁻⁸ phosphane compounds	106
5.7	Synthesis of the tetra-coordinated {RuNO} ⁸ phosphane compounds.....	109
5.8	Synthesis of the tetra-coordinated {RuNO} ⁸ NHC compounds.....	112
5.9	Synthesis of the penta-coordinated {RuNO} ⁸ phosphane compounds	114
5.10	Synthesis of the penta-coordinated {RuNO} ⁸ NHC compounds	116
5.11	Synthesis of the {RuNO} ⁶ NHC compounds	126
5.12	Synthesis of the {Ru(NO) ₂ } ⁸ phosphane compounds.....	131
5.13	Synthesis of the {Ru(NO) ₂ } ⁸ NHC compounds.....	133
5.14	Synthesis of the {Ru(NO) ₂ } ¹⁰ compounds	135
5.15	Computational methods	140
6	Appendix.....	141
6.1	Packing diagrams of the crystal structures	141
6.2	Crystallographic tables.....	164
7	Bibliography	172

List of Figures

Figure 1.1: The all heme-model for sGC activation. ^[23]	3
Figure 1.2: Qualitative molecular orbital diagram of the neutral NO radical.....	4
Figure 1.3: Schematic illustration of the GS, MS1 and MS2 bonding mode in square-pyramidal (<i>sqp</i>) nitrosyl complex.	5
Figure 1.4: Molecular orbital illustration for the metal-nitrosyl bond. Left: σ bond ($2\sigma+d_z^2$), right: π back bonding ($\pi^*_{xz}+d_{xz}$).....	6
Figure 1.5: The molecular orbital diagram for a six-coordinated $[ML_5(NO)]$ complex with C_{4v} symmetry.	7
Figure 1.6: Possible geometries for penta-coordinated nitrosyl complexes.	8
Figure 1.7: Correlation diagram of penta-coordinated nitrosyl complexes in fields of C_{2v} , C_4 and C_s symmetry.	9
Figure 1.8: The two structure types for halogenido-bis(phosphane)-type $\{Ru(NO)_2\}^8$ compounds.	10
Figure 1.9: The ligand-localized molecular orbitals in C_{2v} symmetry derived from the $\pi^*(NO)$ orbitals in dinitrosyl compounds.	11
Figure 1.10: Correlation diagram of penta-coordinated $\{Ru(NO)_2\}^8$ compounds with C_s and C_{2v} symmetry.	11
Figure 1.11: $\{Ru(NO)_2\}^8$ complexes known in literature.....	12
Figure 1.12: $\{Ru(NO)_2\}^{10}$ complexes known in literature.	12
Figure 1.13: Correlation diagram of tetrahedral $\{Ru(NO)_2\}^{10}$ compounds with C_s symmetry.	13
Figure 1.14: Some classes of N-heterocyclic carbenes	14
Figure 1.15: 1,3-Bis(adamantyl)imidazole-2-ylidene (IAd) the first isolated stable carbene.	14
Figure 1.16: The electronic situation of carbenes.....	14
Figure 1.17: Schematic representation of a carbene metal complex.	16
Figure 1.18: a) Metal-carbon bonding in Fischer-type complexes. b) Metal-carbon bonding in Schrock-type complexes.....	17
Figure 2.1: ORTEP plot of the nitrosonium salt $NO(HSO_4)$ (2) in crystals of 2	21
Figure 2.2: Projection of the structure of the nitrosonium salt 2	21
Figure 2.3: ORTEP plot of the complex $[RuBr(NO)(PPh_3)_2]$ in crystals of 7b	24
Figure 2.4: ORTEP plot of the complex $[Ru(NO)(PPh_3)_2]$ in crystals of 7c · C_7H_8	25
Figure 2.5: ORTEP plot of complex $[RuCl(NO)L^{Bn_2}]$ in crystals of 8a	27
Figure 2.6: ORTEP plot of the complex $[RuBr(NO)L^{Bn_2}]$ in crystals of 8b	27
Figure 2.7: ORTEP plot of the complex $[RuCl(NO)(PPh_3)_3]$ in crystals of 9a · $0.5 C_7H_8$	29
Figure 2.8: ORTEP plot of the complex $[Ru(NO)(PPh_3)_3]$ in crystals of 9b · $2 C_7H_8$	30
Figure 2.9: ORTEP plot of the cation $[Ru(NO)(L^{Me})_4]^+$ in crystals of 10b	32

List of Figures

Figure 2.10: ORTEP plot of the cation $[\text{Ru}(\text{NO})(\text{L}^{\text{Et}})_4]^+$ in crystals of 11a .	33
Figure 2.11: ORTEP plot of the cation $[\text{Ru}(\text{NO})(\text{L}^{\text{Bn}})_4]^+$ in crystals of 13a · C ₄ H ₁₀ O.	34
Figure 2.12: ORTEP plot of the cation $[\text{RuCl}(\text{NO})(\text{L}^{\text{Me}})_4]^{2+}$ in crystals of 14a .	36
Figure 2.13: ORTEP plot of the cation $[\text{RuCl}(\text{NO})(\text{L}^{\text{Et}})_4]^{2+}$ in crystals of 15a .	37
Figure 2.14: ORTEP plot of the cation $[\text{RuBr}(\text{NO})(\text{L}^{\text{Et}})_4]^{2+}$ in crystals of 15a .	38
Figure 2.15: ORTEP plot of the cation $[\text{RuI}(\text{NO})(\text{L}^{\text{Et}})_4]^{2+}$ in crystals of 15c · I ₂ .	39
Figure 2.16: ORTEP plot of the complex $[\text{Ru}(\text{NO})_2(\text{PPh}_3)_2\text{SO}_4]$ in crystals of 16 · CH ₂ Cl ₂ .	40
Figure 2.17: ORTEP plot of the cation $[\text{RuI}(\text{NO})_2(\text{PPh}_3)_2]^+$ in crystals of 17 · CH ₂ Cl ₂ .	42
Figure 2.18: ORTEP plot of the cation $[\text{RuCl}(\text{NO})_2(\text{L}^{\text{Bn}})_2]^+$ in crystals of 18a · CH ₂ Cl ₂ .	44
Figure 2.19: ORTEP plot of the cation $[\text{RuBr}(\text{NO})_2(\text{L}^{\text{Bn}})_2]^+$ in crystals of 18b · CH ₂ Cl ₂ .	45
Figure 2.20: ORTEP plot of the complex $[\text{Ru}(\text{NO})_2(\text{PPh}_3)_2]$ in crystals of 21 .	46
Figure 2.21: ORTEP plot of the complex $[\text{RuCl}(\text{NO})_2(\text{L}^{\text{Bn}})_2]^+$ in crystals of 20 .	48
Figure 2.22: ORTEP plot of the complex $[\text{RuCl}(\text{NO})_2(\text{L}^{\text{Et}})_2]^+$ in crystals of 21 .	49
Figure 2.23: ORTEP plot of the complex $[\text{Ru}(\text{NO})_2(\text{L}^{\text{Bn}})_2]$ in crystals of 22 .	49
Figure 2.24: ORTEP plot of the complex $[\text{Ru}(\text{NO})_2(\text{L}^{\text{nPr}})(\text{PPh}_3)]$ in crystals of 23 .	50
Figure 2.25: UV-vis spectra of $[\text{RuI}(\text{NO})(\text{PPh}_3)_2]$ (7c).	52
Figure 2.26: I–Ru–N bending potential of 9b .	62
Figure 2.27: The Ru–N–O angle as a function of the I–Ru–N angle.	62
Figure 2.28: Ru–N–O bending potential of 9b .	63
Figure 2.29: Possible structures for 16 .	63
Figure 2.30: The penta-coordinated isomer of D (F) .	64
Figure 2.31: Electrostatic potential surface map of 7c , 10 and the penta-coordinated isomer of 16 (F) .	65
Figure 3.1: Different reaction behaviors of the square-planar $\{\text{RuNO}\}^8$ species 7a , 8a and 8b .	69
Figure 3.2: Definition of the relevant angles in the tetrahedral $\{\text{Ru}(\text{NO})_2\}^{10}$ species.	69
Figure 3.3: Molecular orbital scheme of the frontier orbitals of $[\text{RuI}(\text{NO})(\text{PPh}_3)_2]$ (7c).	71
Figure 3.4: Interaction diagram for a linear nitrosyl in the apical position of a square pyramid.	73
Figure 3.5: Molecular orbital scheme of the frontier orbitals of the cation $[\text{Ru}(\text{NO})(\text{L}^{\text{Me}})_4]^+$ of 10b .	74
Figure 3.6: Schematic representation and energetic order of the molecular orbitals of a trigonal bipyramidal fragment with C _{3v} symmetry.	75
Figure 3.7: Molecular orbital scheme of the frontier orbitals of $[\text{RuI}(\text{NO})(\text{PPh}_3)_3]$ (9b).	76
Figure 3.8: Contours of the five limiting occupied orbitals of $[\text{RuH}(\text{NO})(\text{PPh}_3)_3]$.	76
Figure 3.9: Contours of the five limiting occupied orbitals of structures A , B and C .	77
Figure 3.10: Correlation diagram of the molecular orbitals of structure B with Ru–N–O = 180°, 164° and 130°.	78

List of Figures

Figure 3.11: Oxidation of the penta-coordinated $\{\text{RuNO}\}^8$ NHC derivatives to the corresponding $\{\text{RuNO}\}^6$ compounds.....	79
Figure 3.12: Molecular orbital scheme of the frontier orbitals of cation $[\text{RuCl}(\text{NO})(\text{L}^{\text{Et}})_4]^+$ of 15a	79
Figure 3.13: Schematic representation of the molecular interactions stabilizing the wide angle between the π acceptors in a tetrahedral X_2ML_2 system.....	80
Figure 3.14: Molecular orbital scheme of the occupied frontier orbitals of $[\text{Ru}(\text{NO})_2(\text{PPh}_3)_2]$ (19).	81
Figure 3.15: Molecular orbital scheme of the occupied frontier orbitals of $[\text{Ru}(\text{NO})_2(\text{L}^{\text{Et}})_2]$ (21).	82
Figure 3.16: The HOMO of 18a and the HOMO–1 of 17	82
Figure 3.17: Possible isomers for $[\text{Ru}(\text{NO})_2(\text{PPh}_3)_2\text{SO}_4]$ (16).	83
Figure 3.18: HOMOs of the isomers D and E of $[\text{Ru}(\text{NO})_2(\text{PPh}_3)_2\text{SO}_4]$ (16).	84
Figure 3.19: HOMO–1 of the penta-coordinated isomer F of $[\text{Ru}(\text{NO})_2(\text{PPh}_3)_2\text{SO}_4]$ (16).....	84
Figure 3.20: NPA (top) and QTAIM (bottom) NO-charges of the $\{\text{RuNO}\}^8$ mononitrosyl species (left) and the dinitrosyl species (right) in this work plotted against the Ru–N–O angle.	86
Figure 4.1: ORTEP plot of the complex $[\text{Ru}(\text{NO})(\text{PPh}_3)_2]$ in crystals of 7b	87
Figure 4.2: Ortep plots of the complex $[\text{Ru}(\text{NO})(\text{PPh}_3)_3]$ in crystals of 9b and of the cation $[\text{Ru}(\text{NO})(\text{L}^{\text{Bn}})_4]^+$ in crystals of 13a	88
Figure 4.3: ORTEP plot of the cation $[\text{RuCl}(\text{NO})(\text{L}^{\text{Et}})_4]^{2+}$ in crystals of 15a	89
Figure 4.4: Ortep plots of the cation $[\text{RuCl}(\text{NO})_2(\text{L}^{\text{Bn}})_2]^+$ in crystals of 18a and of the cation $[\text{Ru}(\text{NO})_2(\text{PPh}_3)_2]^+$ in crystals of 17	90
Figure 4.5: ORTEP plot of the molecule $[\text{Ru}(\text{NO})_2(\text{PPh}_3)_2\text{SO}_4]$ in crystals of 16	90
Figure 4.6: ORTEP plot of the molecule $[\text{RuCl}(\text{NO})_2(\text{L}^{\text{Bn}})_2]^+$ in crystals of 21	91
Figure 6.1: (tv283): Packing diagram of 2	141
Figure 6.2: (tv429): Packing diagram of 7b	142
Figure 6.3: (tv132): Packing diagram of 7c	143
Figure 6.4: (sv026): Packing diagram of 8a	144
Figure 6.5: (sq028): Packing diagram of 8b	145
Figure 6.6: (sv255) Packing diagram of 9a	146
Figure 6.7: (tv134) Packing diagram of 9b	147
Figure 6.8: (tv074): Packing diagram of 10b	148
Figure 6.9: (so030): Packing diagram of 11a	149
Figure 6.10: (sv283): Packing diagram of 13b	150
Figure 6.11: (to062)): Packing diagram of 14a	151
Figure 6.12: (to061)): Packing diagram of 15a	152
Figure 6.13: (to063)): Packing diagram of 15b	153
Figure 6.14: (tqo015): Packing diagram of 15c	154

List of Figures

Figure 6.15: (uv126): Packing diagram of 16	155
Figure 6.16: (sv250): Packing diagram of 17	156
Figure 6.17: (sv070) Packing diagram of 18a	157
Figure 6.18: (sv118): Packing diagram of 18b	158
Figure 6.19: (tv276): Packing diagram of 19	159
Figure 6.20: (uv027) Packing diagram of 20	160
Figure 6.21: (uv108): Packing diagram of 21	161
Figure 6.22: (uv118): Packing diagram of 22	162
Figure 6.23: (uv190): Packing diagram of 23	163

List of Tables

Table 1.1: Ru–N–O angles and nitrosyl-stretching frequencies $\nu(\text{NO})$ of selected hexa-coordinated $\{\text{RuNO}\}^6$ complexes.	7
Table 1.2: Ru–N–O angles and nitrosyl-stretching frequencies $\nu(\text{NO})$ of selected penta-coordinated $\{\text{RuNO}\}^8$ complexes.	10
Table 2.1: ^1H NMR data for the enetetramines (1a–d).....	19
Table 2.2: $^{13}\text{C}\{^1\text{H}\}$ NMR data for the enetetramines (1a–d).....	20
Table 2.3: $^{31}\text{P}\{^1\text{H}\}$ NMR and $^{31}\text{P}\{^1\text{H}\}$ NMR solid-state data for 7a–c	24
Table 2.4: ^1H NMR data for 8a and b in CD_2Cl_2	26
Table 2.5: ^{13}C -NMR data for 8a and b in CD_2Cl_2	26
Table 2.6: ^1H NMR data for the complexes 10a , 11a , 12a and 13a in $\text{dmsO-}d_6$	32
Table 2.7: $^{13}\text{C}\{^1\text{H}\}$ NMR data for the complex cations 10a , 11a , 12a and 13a in $\text{dmsO-}d_6$	32
Table 2.8: ^1H NMR data for the complexes 14a , 14b and 15a–c in $\text{dmsO-}d_6$	35
Table 2.9: $^{13}\text{C}\{^1\text{H}\}$ NMR data for the complex the complexes 14a , 14b and 15a–c in $\text{dmsO-}d_6$	36
Table 2.10: ^1H NMR data for the complexes 18a in $\text{dmsO-}d_6$ and for 18b in CD_2Cl_2	43
Table 2.11: $^{13}\text{C}\{^1\text{H}\}$ NMR data for the complexes 18a in $\text{dmsO-}d_6$ and for 18b in CD_2Cl_2	43
Table 2.12: ^1H NMR data for the complexes 20–23 in CD_2Cl_2	47
Table 2.13: $^{13}\text{C}\{^1\text{H}\}$ NMR data for the complexes 20–23 in CD_2Cl_2	47
Table 2.14: DFT results on $[\text{Ru}(\text{NO})(\text{PPh}_3)_2]$ (7c)..	54
Table 2.15: DFT results on $[\text{Ru}(\text{NO})(\text{PPh}_3)_2]$ (7c)..	54
Table 2.16: DFT results on $[\text{RuCl}(\text{NO})\text{L}^{\text{Bn}}_2]$ (8a).	54
Table 2.17: DFT results on $[\text{Ru}(\text{NO})(\text{PPh}_3)_3]$ (9b).....	55
Table 2.18: DFT results on the complex cation of $[\text{Ru}(\text{NO})\text{L}^{\text{Et}}_4]\text{Cl}$ (11a).....	55
Table 2.19: DFT results on the complex cation of $[\text{RuCl}(\text{NO})\text{L}^{\text{Et}}_4](\text{I}_3)_2$ (15a).	56
Table 2.20: DFT results on $[\text{Ru}(\text{NO})_2(\text{PPh}_3)_2\text{SO}_4]$ (16).....	57
Table 2.21: DFT results on the cation of $[\text{Ru}(\text{NO})_2(\text{PPh}_3)_2]\text{BF}_4$ (17).....	57
Table 2.22: DFT results on the cation of $[\text{RuCl}(\text{NO})_2(\text{L}^{\text{Bn}})_2]\text{BF}_4$ (18a).	58
Table 2.23: DFT results on $[\text{Ru}(\text{NO})_2(\text{L}^{\text{Me}})_2]$ (20).....	58
Table 2.24: QTAIM and NPA charges of the mononitrosyl complexes with NHC ligands.....	59
Table 2.25: QTAIM and NPA charges of the mononitrosyl complexes with phosphane ligands.	60
Table 2.26: QTAIM and NPA charges of the dinitrosyl complexes with NHC ligands.	60
Table 2.27: QTAIM and NPA charges of the dinitrosyl complexes with phosphane ligands.	61
Table 3.1: Selected structural parameters and nitrosyl-stretching frequencies of the $\{\text{Ru}(\text{NO})_2\}^{10}$ compounds 19–23	70
Table 5.1: Analytical methods and equipment.	93

List of Tables

Table 5.2: Manufacturer and percentage purity of the solvents and reagents.....	94
Table 6.1: Crystallographic data of NO(HSO ₄) (2), [RuBr(NO)(PPh ₃) ₂] (7b) and [RuI(NO)(PPh ₃) ₂] · C ₇ H ₈ (7c) · C ₇ H ₈	164
Table 6.2: Crystallographic data of [RuBr(NO)L ^{Bn} ₂] (8a), [RuBr(NO)L ^{Bn} ₂] (8b) and [RuCl(NO)(PPh ₃) ₃] · 0.5 C ₇ H ₈ (29a · C ₇ H ₈).	165
Table 6.3: Crystallographic data of [RuI(NO)(PPh ₃) ₃] · 2 C ₇ H ₈ (9b · 2C ₇ H ₈), [Ru(NO)(L ^{Me}) ₄]Br (10b) and [Ru(NO)(L ^{Et}) ₄]Cl (11a).....	166
Table 6.4: Crystallographic data of [Ru(NO)(L ^{Bn}) ₄]Br (13a), [RuCl(NO)(L ^{Me}) ₄](I ₅) ₂ (14a) and [RuCl(NO)(L ^{Et}) ₄](I ₃) ₂ (15a).....	167
Table 6.5: Crystallographic data of [RuBr(NO)(L ^{Et}) ₄](I ₃) ₂ (15b), [RuI(NO)(L ^{Et}) ₄](I ₅)(I ₃) (15c) and [Ru(NO) ₂ (PPh ₃) ₂ SO ₄] (16).....	168
Table 6.6: Crystallographic data of [RuI(NO) ₂ (PPh ₃) ₂]BF ₄ · CH ₂ Cl ₂ (17 · CH ₂ Cl ₂), [RuCl(NO) ₂ (L ^{Bn}) ₂]BF ₄ (18a) and [RuBr(NO) ₂ (L ^{Bn}) ₂]BF ₄	169
Table 6.7: Crystallographic data of [Ru(NO) ₂ (PPh ₃) ₂] (19), [Ru(NO) ₂ (L ^{Me}) ₂] (20) and [Ru(NO) ₂ (L ^{Et}) ₂] (21).	170
Table 6.8: Crystallographic data of [Ru(NO) ₂ (L ^{Bn}) ₂] (22) and [Ru(NO) ₂ (L ^{nPr})(PPh ₃)] (23).....	171

List of Schemes

Scheme 1.1: The nitric oxide synthetic pathway.	1
Scheme 1.2: The mayor reactions involved in the production and fates of peroxynitrite under physiological conditions.	2
Scheme 1.3: The overall multistep reaction of NO with O ₂	2
Scheme 1.4: The reaction of NO with HbFe(II) and HbFe(II)O ₂	3
Scheme 1.5: a) Crossover experiment carried out by Lemal <i>et al.</i> b) Explanation for the reaction of electrophiles with enetetramines.	15
Scheme 1.6: Proposed reaction pathway of the reaction of an enetetramine (L ^R ₂) to a carbene complex of the M(CO) ₅ L ^R type:	16
Scheme 2.1: General procedure for the synthesis of the enetetramines L ^R ₂ (1a–d).	19
Scheme 2.2: Synthesis of the nitrosonium salt NO(HSO ₄).	20
Scheme 2.3: Synthesis of the {RuNO} ⁶ precursor compounds. (1) Synthesis of K ₂ [Ru(OH)(NO ₂) ₄ (NO)] (3), (2) synthesis of K ₂ [Ru(NO)X ₅] (X = Br, I; 4b, 4c) and (3) synthesis of K ₂ [Ru(NO)Cl ₅] (4a).	22
Scheme 2.4: Synthesis of [RuH ₂ (PPh ₃) ₄] (5).	22
Scheme 2.5: Synthesis of [RuX ₁₋₃ (NO)(PPh ₃) ₂] (X = Cl, Br, I; 6a, 6b, 6c).	23
Scheme 2.6: Synthesis of [RuX(NO)(PPh ₃) ₂] (X = Cl, Br, I; 7a, 7b, 7c).	23
Scheme 2.7: Synthesis of [RuX(NO) L ^{Bn} ₂] (X = Cl, Br; 8a, 8b).	25
Scheme 2.8: Synthesis of [RuX(NO)(PPh ₃) ₃] (X = Cl, I; 9a, 9b).	28
Scheme 2.9: Synthesis of [Ru(NO)(L ^{Me}) ₄]X (X = Cl, Br, I; 10a–c), [Ru(NO)(L ^{Et}) ₄]X (X = Cl, Br, I; 11 a–c), [Ru(NO)(L ^{nPr}) ₄]X (X = Cl, Br, I; 12a–c) and [Ru(NO)(L ^{Bn}) ₄]X (X = Br, I; 13a, 13b).	31
Scheme 2.10: Synthesis of [RuX(NO)(L ^{Me}) ₄](I ₅) ₂ (X = Cl, Br; 14a, 14b) and [Ru(NO)(L ^{Et}) ₄](I ₃) ₂ (X = Cl, Br, I; 15a, 15b) and [RuI(NO)(L ^{Et}) ₄](I ₅)(I ₃) (15c).	35
Scheme 2.11: Synthesis of [Ru(NO) ₂ (PPh ₃) ₂ SO ₄] (16).	39
Scheme 2.12: Synthesis of [RuI(NO) ₂ (PPh ₃) ₂]BF ₄ (17).	41
Scheme 2.13: Synthesis of [RuX(NO) ₂ (L ^{Bn}) ₂]BF ₄ (X = Cl, Br; 18a, 18b).	42
Scheme 2.14: Synthesis of [Ru(NO) ₂ (PPh ₃) ₂] (19).	45
Scheme 2.15: Synthesis of [Ru(NO) ₂ (L ^R)(L)] (L = L ^R , R = Me, Et, Bn; 20, 21, 22 ; L = PPh ₃ , R = <i>n</i> Pr; 23). ..	47
Scheme 2.16: Equilibrium between [RuX(NO)(PPh ₃) ₃] (X = Cl, I; 9a, 9b) and [RuX(NO)(PPh ₃) ₂] (X = Cl, I; 7a, 7c).	51

Abbreviations

ATR	attenuated total reflection
Bn	benzyl
br	broad
calcd	calculated
cGMP	cyclic guanosine monophosphate
CShM	continous shape measurement
d	doublet
DCM	dichloromethane
DEI	desorption electron ionization
DFT	density functional theory
diazald	N-methyl-N-nitroso-p-toluenesulfonamide
EI	electron ionization
eNOS	endothelial nitric oxid synthase
eq	equivalent
Et	ethyl
FAB	fast atom bombardement
GTP	guanosine triphosphate
h	hour
Hb	desoxy-hemoglobin
HOMO	highest occupied molecular orbital
iNOS	inducible nitric oxide synthase
IR	infrared spectroscopy
L	ligand
L ^R	NHC ligand
L ^R ₂	enetetramine
LUMO	lowest occupied orbital
m	medium (IR spectroscopy), multiplet (NMR spectroscopy)
Me	methyl
MO	molecular orbital
MS	mass spectroscopy
NMR	nuclear magnetic resonance
nNOS	neuronal nitric oxide synthase
NOS	nitric oxide synthase
<i>n</i> Pr	<i>n</i> -propyl
OC-6	octahedron (IUPAC polyhedral symbol)

Abbreviations

of th	of theory
<i>p</i>	<i>para</i>
Ph	phenyl
PLI	photo-induced linkage isomerism
ppm	parts per million
q	quartet
R	rest
rt	room temperature
s	strong (IR spectroscopy), singulet (NMR spectroscopy)
sGC	soluble guanylate cyclase
<i>SP-4</i>	square-planar
<i>SPY-5</i>	square pyramid (IUPAC polyhedral symbol)
sqp	square pyramid
<i>T-4</i>	tetrahedron
tbp	trigonal bipyramide
TBPY-5	trigonal bipyramid (IUPAC polyhedral symbol)
THF	tetrahydrofurane
UV-vis	ultraviolet-visible
vOC-5	vacant octahedron (CShM-nomenclature)
vs	very strong
vw	very weak
w	weak

Overview of numbered compounds

Enetetramines

- 1a** Bis-1,3-dimethyl-imidazoline-2-ylidene
1b Bis-1,3-diethyl-imidazoline-2-ylidene
1c Bis-1,3-di-*n*-propyl -imidazoline-2-ylidene
1d Bis-1,3-dibenzyl-imidazoline-2-ylidene

Precursor compounds

- 2** NO(HSO₄)
3 K₂[Ru(OH)(NO₂)₄(NO)]
4a K₂[RuCl₅(NO)]
4b K₂[RuBr₅(NO)]
4c K₂[RuI₅(NO)]
5 [RuH₂(PPh₃)₄]

{RuNO}⁶⁻⁸ phosphane compounds

- 6a** [RuCl₁₋₃(NO)(PPh₃)₂]
6b [RuBr₁₋₃(NO)(PPh₃)₂]
6c [RuI₃(NO)(PPh₃)₂]

Tetra-coordinated {RuNO}⁸ phosphane compounds

- 7a** [RuCl(NO)(PPh₃)₂]
7b [RuBr(NO)(PPh₃)₂]
7c [RuI(NO)(PPh₃)₂]

Tetra-coordinated {RuNO}⁸ NHC compounds

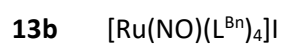
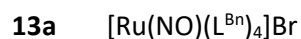
- 8a** [RuCl(NO)(L^{Bn})₂]
8b [RuBr(NO)(L^{Bn})₂]

Penta-coordinated {RuNO}⁸ phosphane compounds

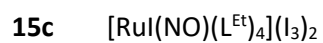
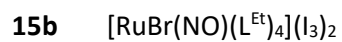
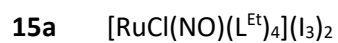
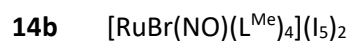
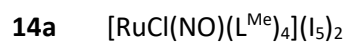
- 9a** [RuCl(NO)(PPh₃)₃]
9b [RuI(NO)(PPh₃)₃]

Penta-coordinated {RuNO}⁸ phosphane compounds

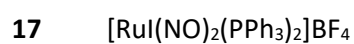
- 10a** [Ru(NO)(L^{Me})₄]Cl
10b [Ru(NO)(L^{Me})₄]Br
11a [Ru(NO)(L^{Et})₄]Cl
11b [Ru(NO)(L^{Et})₄]Br
11c [Ru(NO)(L^{Et})₄]I
12a [Ru(NO)(L^{nPr})₄]Cl
12b [Ru(NO)(L^{nPr})₄]Br
12c [Ru(NO)(L^{nPr})₄]I



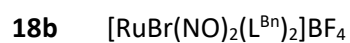
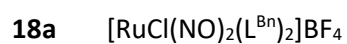
{RuNO}⁶ NHC compounds



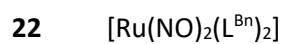
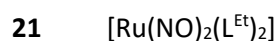
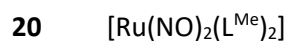
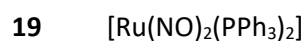
{Ru(NO)₂}⁸ phosphane compounds



{Ru(NO)₂}⁸ NHC compounds



{Ru(NO)₂}¹⁰ compounds

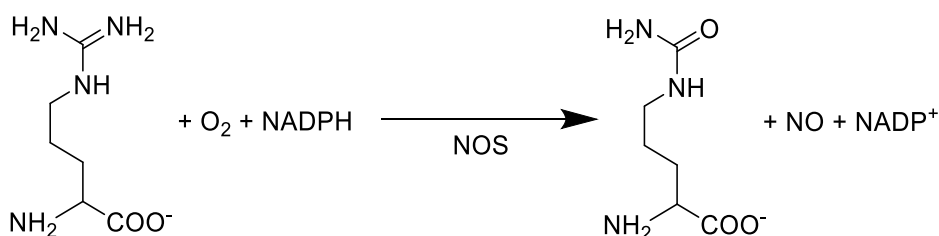


1 Introduction

1.1 Biological relevance of nitrogen monoxide

Nitric oxide was long known as a gas of bad repute—a toxic pollutant that was jointly responsible for the depletion of the ozone layer. But almost two hundred years after its discovery in the 17th century, this simple molecule received great media coverage due to its state as a messenger in biological systems. Research in several disciplines revealed that NO plays a major role in regulating blood vessel dilatation and immune functions. Furthermore, it serves as a neurotransmitter in the brain and the peripheral nervous system.^[1] As a free neutral radical, NO is about ten times more soluble in hydrophobic solvents than it is in water. Thus, it can cross the hydrophobic double layer of biological membranes by simple diffusion. In contrast to other second messengers, NO needs no channels and its biological activity is limited only by its half-life. It was merited that Furchgott, Ignarro and Murad received the Nobel Prize in Physiology or Medicine in 1998 not only for the discovery of NO as a messenger molecule but for the discovery of a whole new class of second-messenger molecules.^[2–6]

In mammals, NO is produced by the nitric-oxide synthase (NOS) that oxidizes L-arginine to citrulline and NO with molecular O₂ and NADPH as co-substrates (SCHEME 1.1).^[7]



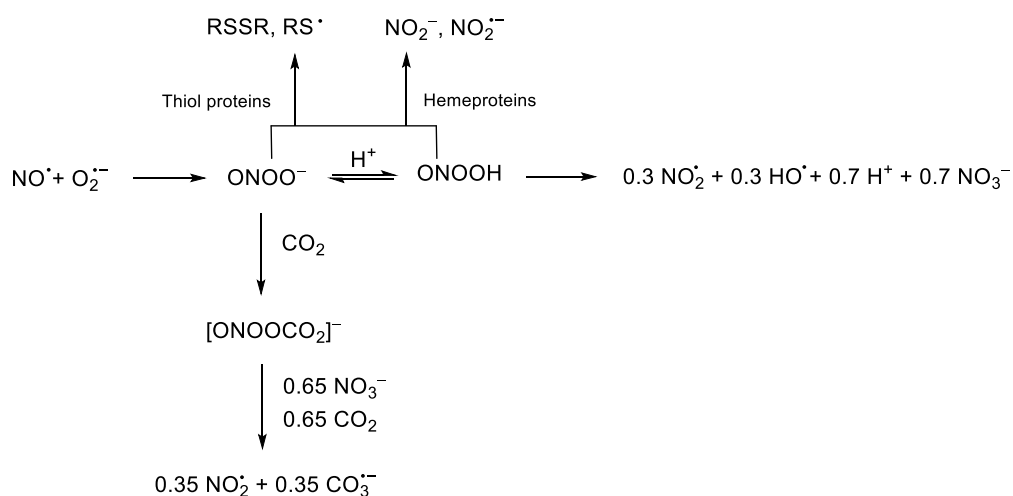
Scheme 1.1: The nitric oxide synthetic pathway. Adapted from Reference [7].

There are three known NOS isoforms (endothelial, neuronal and inducible NOS) which can be divided in two classes: constitutive and inducible enzymes. eNOS (endothelial NOS) and nNOS (neuronal NOS) which are constitutive enzymes are always present in the cell and produce only low amounts of NO. The inducible NOS (iNOS) is transcriptionally regulated, expressed in macrophages and can provide a much higher amount of NO than the former ones.^[2,6]

NO reacts, amongst others, with the superoxide anion, O₂⁻, and molecular oxygen, O₂. The fast diffusion-controlled reaction of NO with the superoxide anion may be the major route of NO depletion besides the destruction of NO to NO₃⁻ by oxyhemoglobin.^[8,9] Furthermore it leads to the formation of the powerful oxidant peroxynitrite (ONOO⁻) that decays in multiple toxic products such as the hydroxyl

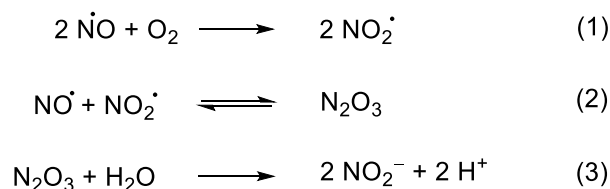
Introduction

radical (HO^\bullet) and reacts, amongst others, with the thiol group (RSH) of the peroxyredoxin protein family to disulfides (RSSR) or thiol radicals (RS^\bullet).^[10–12] A schematic representation of the main reactions of peroxynitrite is given in SCHEME 1.2.



Scheme 1.2: The major reactions involved in the production and fates of peroxynitrite under physiological conditions. Adapted from Reference [6].

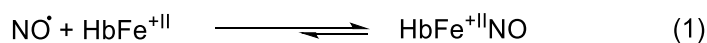
The reaction of NO with O_2 is much slower than the former. It yields two molecules of nitrogen dioxide (NO_2^\bullet) that combine with another molecule of NO to yield N_2O_3 that reacts with water to NO_2^- (SCHEME 1.3, equation 1–3). The intermediates NO_2^\bullet and N_2O_3 are strong nitrosating agents and are likely involved in the nitrosylation of different biomolecules.^[13–16]



Scheme 1.3: The overall multistep reaction of NO with O_2 . Adapted from Reference [6].

In bioinorganic coordination chemistry the role of NO as a ligand for protein-metal centers is a challenging subject. As a messenger molecule, NO interacts mainly with protein-iron centers.^[17] Among the ferrous heme proteins hemoglobin (Hb) and cytochrome *c* oxidase are the best-understood targets of NO.^[6] Deoxyhemoglobin (HbFe^{II}) and oxyhemoglobin ($\text{HbFe}^{II}\text{O}_2$) both react very quickly with NO but in different ways.^[18] Hereby deoxyhemoglobin is nitrosylated to $\text{HbFe}^{II}\text{NO}$ complexes that dissociate so slowly that the reaction can be considered irreversible (SCHEME 4, equation 1).^[6] The irreversible reaction with NO and $\text{HbFe}^{II}\text{O}_2$ is called deoxygenation since both atoms of O_2 are incorporated into the building of nitrate (NO_3^-) with concurrent oxidation of the heme group (SCHEME 1.4, equation 2).^[19,20]

Introduction



Scheme 1.4: The reaction of NO with HbFe(II) and HbFe(II)O₂.

Most NO-regulated physiological processes are initiated by the activation of another heme protein—the soluble guanylate cyclase (sGC). This protein converts GTP to cGMP that in turn regulates the relaxation of the smooth vascular muscles in blood vessels.^[21] For the activation of sGC Russwurm and Koesling proposed the all heme site model (FIGURE 1.1). The first step of the activation is the formation of the His-Fe-NO complex **2** by binding NO to the iron center of the heme group. In the second step another NO ligand binds to the iron center *trans* to the first one and replaces the histidine ligand to build the NO-Fe-NO complex **3**. This intermediate can convert into an inactive species **4a** that is obtained in the absence of cGMP and pyrophosphate and at low NO concentrations or in the fully active species **4b**.^[22]

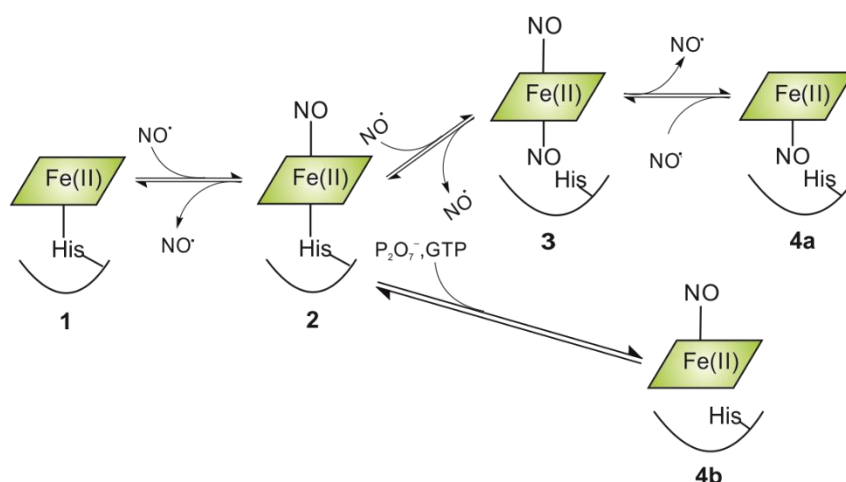


Figure 1.1: The all-heme model for sGC activation.^[23]

Another possible non-heme-site model has been proposed by Cary *et al.* Here the second NO binds at a non heme site of the enzyme to give fully active sGC.^[24] But this model has been challenged by *in vivo* studies that reveal the all-heme model as the better fit for the sGC activation mechanism.^[25]

The reactions of NO with heme proteins in the Fe^{+III} state, such as met-hemoglobin and ferric cytochrome c, are much slower than its interactions with ferrous heme proteins. Furthermore Fe^{+III}NO adducts are prone to reduction due to the great stability of Fe^{+II}NO adducts.

Even though the biological activity of NO is indisputable today the question remains why an unstable and highly reactive molecule serves such critically important signaling functions. A possible answer may be the properties of NO as a ligand in transition-metal complexes.

1.2 Properties of nitrogen monoxide

In this work the term nitrosyl refers to nitric oxide as a ligand.

Nitric oxide is a stable free radical. It has fifteen electrons whereby the unpaired electron is located in the π^* -orbital that is polarized toward nitrogen (FIGURE 1.2).^[26] This electron configuration explains the high reactivity of NO: it can easily be oxidized to the nitrosonium ion (NO^+) or be reduced to the nitroxyl ion NO^- . Also it reacts readily with O_2 to yield NO_2 and it, furthermore, forms XNO adducts with halogens (X_2).^[27] NO^+ is isoelectronic with CO and CN^- , NO^\cdot with the dioxygen cation (O_2^+) and NO^- with O_2 .^[28] NO^- and the isoelectronic O_2 both have a triplet ground state and therefore share electronic and structural properties.

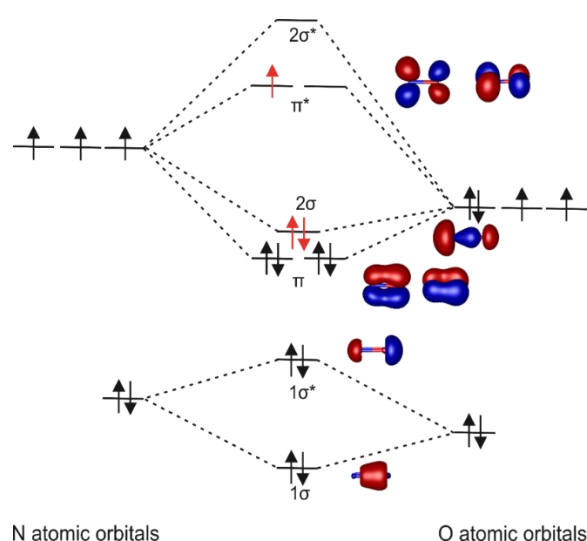


Figure 1.2: Qualitative molecular orbital diagram of the neutral NO radical. Adopted from Reference [26].

The NO ligand features two possible binding sites. Thus, it is a so-called ambident ligand and three binding states can be discussed: the κN (nitrosyl) binding state that is the structural and electronic ground state, the κO (isonitrosyl)- and the $\kappa^2\text{N,O}$ (side-on) binding state.^[27] Some metal-nitrosyl systems can switch between these binding states upon irradiation with light of characteristic wavelength. The ability to form photoinduced long-lived metastable states is called photoinduced linkage isomerism (PLI). Upon irradiation with light the metal-nitrosyl bond of the ground state (κN -bonded) may be cleaved and the NO ligand either dissociates or it switches in one of the two metastable states (MS1, MS2) (FIGURE 1.3).^[29,30]

Introduction

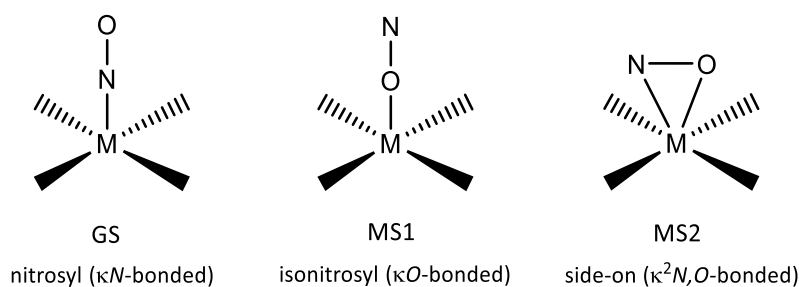


Figure 1.3: Schematic illustration of the GS, MS1 and MS2 bonding mode in a square-pyramidal (*sqp*) nitrosyl complex.

Metal-nitrosyls showing controlled release of NO are of considerable interest for photodynamic therapy since they may deliver NO to the target tissue and release it in a controlled manner. Due to the fact that the three linkage isomers have different refractive indices, nitrosyl complexes that are PLI active have potential technical importance as very high-capacity storage devices.^[31] Sodium nitroprusside, $\text{Na}_2[\text{Fe}(\text{CN})_5\text{NO}]$ is capable of both, NO release in solution and PLI in the solid state.^[30,32] The NO ligand is not only an ambident but also a so-called non-innocent ligand – that is a ligand which does not allow the definition of the spectroscopic oxidation state of the central atom.^[33] Due to its redox activity, nitrosyl can bind to a metal center in four binding modes exhibiting different M–N–O angles: bent (ca. 120°) as $^1\text{NO}^-$ in a low-spin complex, weakly bent (ca 140°) as a neutral $^2\text{NO}^\cdot$ radical in a low-spin complex, almost linear as either $^3\text{NO}^-$ diradical in a high-spin complex or as $^1\text{NO}^+$ (that hardly is a cation due to extensive back-bonding).^[34] The analysis of the electronic state of the M–N–O unit is usually based on the spectroscopic and X-ray-crystallographic data of the compound in question. In consideration of the confusing determination of the oxidation states of NO and the metal center the Enemark and Feltham notation was established. The metal-nitrosyl entity is considered separated $\{\text{M}(\text{NO})_n\}^m$, where m is the sum of the electrons in the d orbitals of the metal and the electrons in the π^* orbital(s) of the NO ligand and n is the number of nitrosyl ligands coordinating to the metal center M. Enemark and Feltham also used Walsh-type diagrams to answer the question why the M–N–O unit bends, when it does. When the other ligands on the metal exhibit a strong C_{4v} perturbation the M–N–O angle is predicted to be linear for $n \leq 6$ but bent for $n \geq 6$.^[35] This topic will be further discussed in Chapter 1.3.

The NO ligand is both σ base and π acid, thus, the metal-nitrosyl bond is thought to have two components. First, the donation of electron density from the 2σ orbital on the N atom to the d_z^2 orbital of the metal and second, the back donation from symmetry-permitted metal d orbitals (d_{xz} , d_{yz}) to the π^* orbitals of the NO (FIGURE 1.4).^[27]

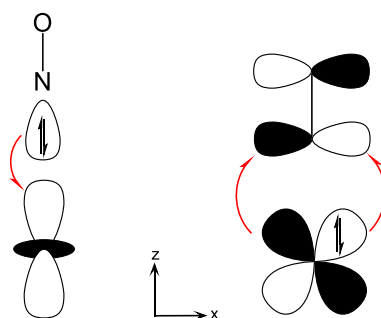


Figure 1.4: Molecular orbital illustration for the metal-nitrosyl bond. Left: σ bond ($2\sigma+d_z^2$), right: π back bonding ($\pi^*_{xz}+d_{xz}$).

1.3 Ruthenium-nitrosyl complexes

Transition-metal-NO complexes are known for Cr, Mo, Mg, Te, Re, Fe, Ru, Co, Rh, Ni, Pd, Pt, Cu and Ag and nearly 3000 X-ray structures have been reported.^[36,37] While iron is certainly the most relevant metal to interact with nitrosyl under biological aspects, the nitrosyl coordination chemistry of its higher homologue ruthenium is on the rise. The advantage of nitrosyl complexes with Ru as central atom is their greater thermal stability. Ruthenium-nitrosyl complexes are applied in medicine as NO scavenging- or releasing complexes,^[38–41] are suitable for catalytic purposes and are promising candidates for information processing due to their photochemical and photophysical properties.^[42–47] In literature there are reports on mononitrosyl ruthenium complexes having $\{\text{RuNO}\}^5$,^[48,49] $\{\text{RuNO}\}^6$,^[46,50–55] $\{\text{RuNO}\}^7$,^[56,57] $\{\text{RuNO}\}^8$ moieties.^[58–60] For dinitrosyls some $\{\text{Ru}(\text{NO})_2\}^8$ compounds and two $\{\text{Ru}(\text{NO})_2\}^{10}$ derivatives have been structurally identified.^[34,61,62] This work contains complexes with $\{\text{RuNO}\}^{6/8}$ and $\{\text{Ru}(\text{NO})_2\}^{8/10}$ moieties. Therefore these types of compounds will be discussed in the following.

1.3.1 $\{\text{RuNO}\}^6$ complexes

The $\{\text{RuNO}\}^6$ configuration is generally the most stable configuration with nearly 600 known X-ray structures.^[63] Most of these compounds are hexa-coordinated with an electron-rich low-spin d^6 ruthenium center (Ru^{II}) and a π -accepting NO^+ ligand. The RuNO moiety is usually linear with a Ru–N–O angle between 170° and 180° and short Ru–N bonds (approx. 1.74 \AA). Furthermore, they exhibit $\tilde{\nu}(\text{NO})$ vibrational bands up to 1960 cm^{-1} . An exception are cases like $[\text{Ru}(\text{OEP})(\text{NO})(\text{aryl})]$ (OEP = octaethylporphinato(2–)) where a strong σ donor *trans* to NO causes a Ru–N–O angle less than 155° and a lowering of the $\tilde{\nu}(\text{NO})$ band below 1800 cm^{-1} .^{[64][57]} Characteristic ranges of $\tilde{\nu}(\text{NO})$ and typical Ru–N–O angles are given in TABLE 1.1.

Introduction

Table 1.1: Ru–N–O angles and nitrosyl-stretching frequencies $\tilde{\nu}(\text{NO})$ of selected hexa-coordinated $\{\text{RuNO}\}^6$ complexes.

Complex	Ru–N–O ($^\circ$)	$\tilde{\nu}(\text{NO})$ ($/\text{cm}^{-1}$)	Reference
$\text{K}_2[\text{RuCl}_5(\text{NO})]$	176.8(9)	1900	[65,66]
$[\text{RuCl}_3(\text{NO})(\text{PPh}_3)_2]$	180.0	1881	[67]
$[\text{RuNO}(\text{NH}_3)_4]\text{Cl}_3$	172.8(9)	1913	[57,68]
$[\text{Ru}(\text{NO})\text{Cl}_2(\text{L-his})]$	177.7(2)	1891	[46]
$[\textit{trans}\text{-RuCl}_4(\text{dmsO-O})(\text{NO})]$	178.0(5)	1864	[69]

Enemark and Feltham discussed the high stability of $\{\text{RuNO}\}^6$ species with a linear RuNO moiety with a molecular orbital approach. For the following discussions, the z axis is defined along the M–N vector of the RuNO group. FIGURE 1.5 shows molecular orbitals of a $[\text{ML}_5(\text{NO})]$ complex with C_{4v} symmetry. It must be pointed out that the energetic order of the $4a_2$ and the $3e$ orbital can be inverted. For a $\{\text{RuNO}\}^6$ species with a linear RuNO moiety, the energetically, favorable orbitals are occupied and the antibonding orbitals are empty. Since bending the MNO fragment would lead to a destabilization of the binding $d_{xz}+\pi^*(\text{NO})$ interaction and stabilization of the empty $d_{z^2}-\sigma(\text{NO})$ orbital, a linear RuNO moiety is favored for an octahedral d^6 -nitrosyl complex.

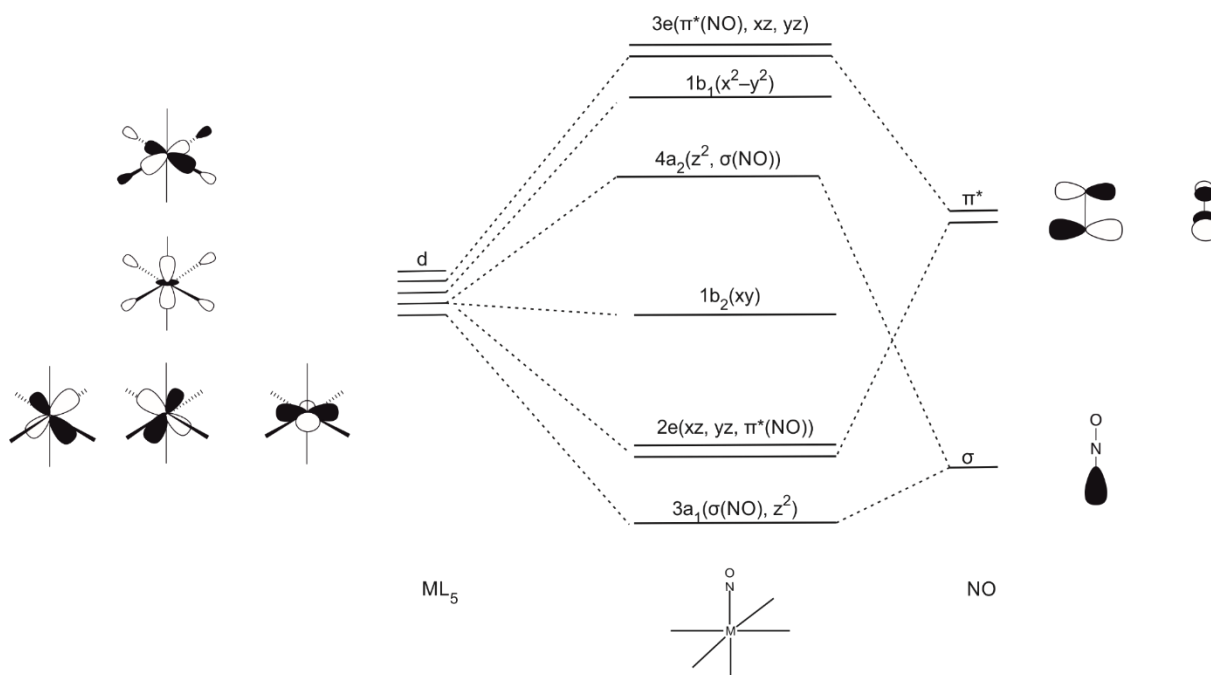


Figure 1.5: The molecular orbital diagram for a hexa-coordinated $[\text{ML}_5(\text{NO})]$ complex with C_{4v} symmetry. Note that the energetic order of the $4a_2$ and the $3e$ orbital can be converted depending on the complex under discussion. Adapted from References [35] and [67].

1.3.2 {RuNO}⁸ complexes

According to FIGURE 1.5, the two electrons added to a {RuNO}⁶ to form a {RuNO}⁸ complex will occupy an antibonding orbital. If the {RuNO}⁸ complex is hexa-coordinated, bending would be strongly favored due to the stabilization of the $d_{z^2}-\sigma(\text{NO})$ orbital.^[35,71,72] However no hexa-coordinated {RuNO}⁸ species has been isolated yet. In fact penta or tetracoordination is much more likely for {RuNO}⁸ complexes since the electron density on the z axis is diminished by the loss of the sixth ligand. In a penta-coordinated complex the structure of the RuNO moiety will depend on the structure of the complex and the properties of the other ligands.^[35,72,73] The better part of the structurally known penta-coordinated {MNO}⁸ complexes can be divided roughly in two types: The trigonal bipyramid (*tbp*) with a linear equatorial nitrosyl and the square pyramid (*sqp*) with a strongly bent apical nitrosyl (FIGURE 1.6).

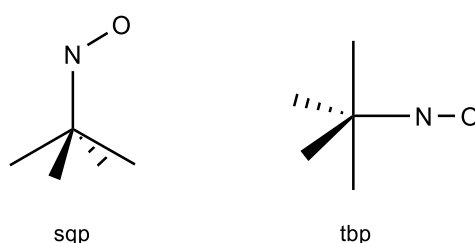


Figure 1.6: Possible geometries for penta-coordinated nitrosyl complexes. The structures are defined by Addison's τ_5 parameter.^[72,74]

There are structures in between such as a trigonal bipyramid with a bent nitrosyl in the plane in $[\text{Ru}(\text{FBF}_3)(\text{CO})(\text{NO})(\text{P}^t\text{Bu}_2\text{Me})_2]^+$ or one with a linear NO in an axial position in $[\text{RuH}(\text{NO})(\text{PPh}_3)_3]$.^[59,75] These exceptions will be discussed in Chapter 4.2.1. For now, the focus will be on the two extremes. Which structure is adopted depends on the energy levels of the d_{z^2} and d_{xz} orbitals. Enemark and Feltham constructed a correlation diagram that relates the molecular orbitals of the two possible geometries for penta-coordinated MNO complexes (FIGURE 1.7).

Introduction

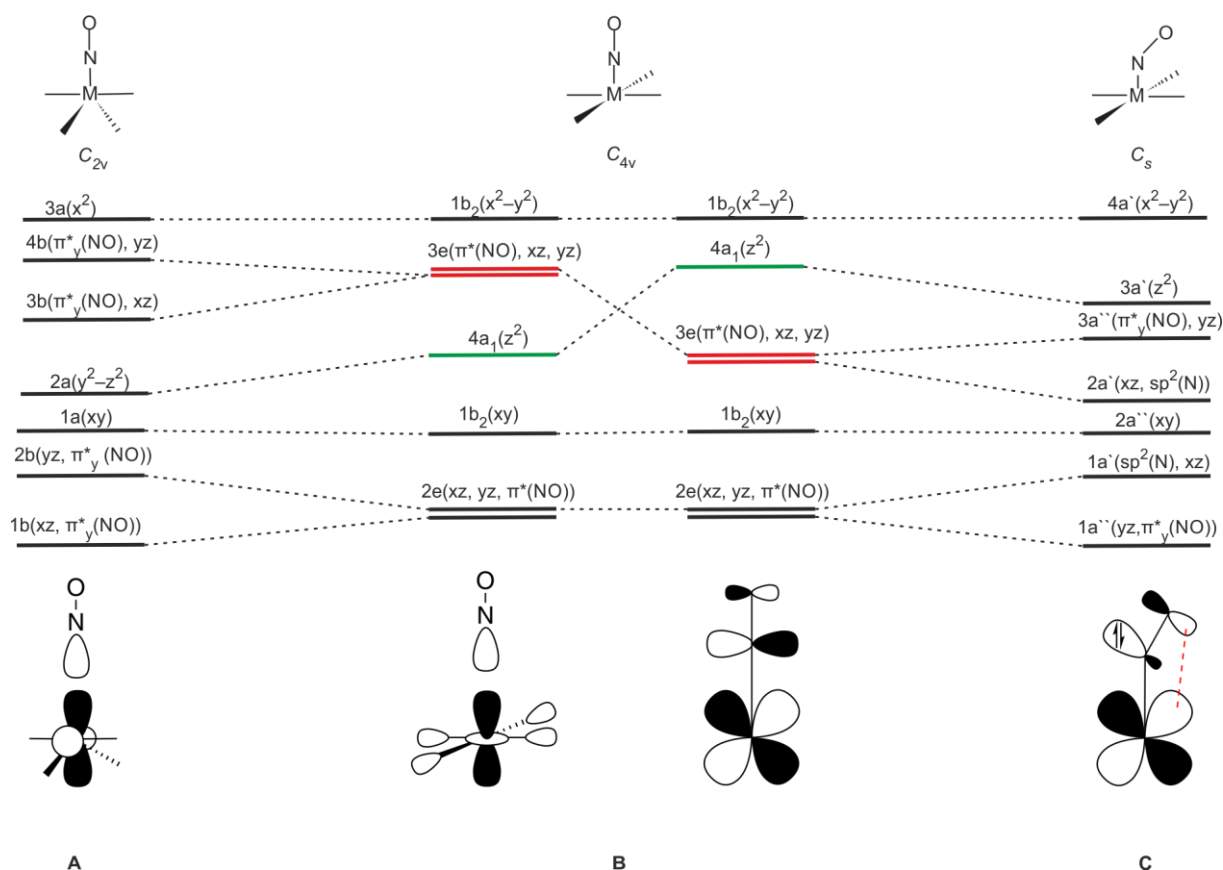


Figure 1.7: Correlation diagram of penta-coordinated nitrosyl complexes in fields of C_{2v} , C_{4v} and C_s symmetry. Note that the z axis is the principal symmetry axis of the *tbp* complex in C_{2v} geometry. Adapted from References [35] and [73].

In the middle (FIGURE 1.7B), the two possible orbital schemes for a C_{4v} -nitrosyl complex are depicted. If the $d_{xz}-\pi^*(NO)$ orbitals are lower in energy than the $d_{z^2}-\sigma(NO)$ (FIGURE 1.7B, right) then an $\{MNO\}^8$ complex would have the electron configuration $(2e)^4 (1b_2)^2 (3e)^2$. Bending of the MNO group will have several effects: (1) the symmetry will be reduced from C_{4v} to C_s . Thus, the 3e orbitals are no longer degenerated. (2) The energies of the occupied 3e orbital will be lowered as a new interaction between the oxygen atom and the metal is formed and the resulting new HOMO $2a'$ is energetically similar to the nitrogen atom. Thus, the electrons remain as a lone pair on the N atom (FIGURE 1.7C). When the $d_{z^2}-\sigma(NO)$ orbital is lower in energy than the $d_{xz}-\pi^*(NO)$ orbitals (FIGURE 1.7B, left), distortion of the molecule toward *tbp* structure is favored to lower the strongly antibonding $d_{z^2}-\sigma(NO)$ orbital.^[35] The *tbp* structure has C_{2v} symmetry and the d_{z^2} orbital and the $d_{x^2-y^2}$ orbital are of a_1 symmetry. Due to the linear combination of these orbitals, some electron density is transferred from the nitrosyl axis in the region along the y axis (FIGURE 1.7A).^[72]

The energy differences between the *tbp* and *sqp* structure are small and subtle differences may decide the geometry of both the complex and the MNO moiety. Most of the known penta-coordinated $\{RuNO\}^8$ species adopt *sqp* structure with a bent RuNO fragment, and characteristic ranges of $\tilde{\nu}(NO)$ and typical Ru-N-O angles are given in TABLE 1.2.

Table 1.2: Ru–N–O angles and nitrosyl-stretching frequencies $\tilde{\nu}(\text{NO})$ of selected penta-coordinated $\{\text{RuNO}\}^8$ complexes.

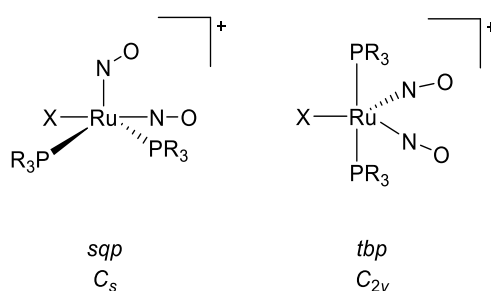
Complex	Ru–N–O (/°)	$\tilde{\nu}(\text{NO})$ (/cm ⁻¹)	structure	Reference
[Ru(diphos) ₂ NO](BPh ₄)	174(1)	1673	<i>tbp</i>	[76]
[RuCl(PNN)(NO)]	130.2(4)	1679	<i>sqp</i>	[77]
[RuCl(NO)(PPh ₃) ₂ { = C = CH(C ₆ H ₄ Me)}]	144.3(8)	1600	<i>sqp</i>	[78]
[Ru(NO)(^s S ₂) ₂](NBu ₄)	177.48(6)	1728	<i>sqp</i>	[79]

PNN = 2-(^tBu₂PCH₂)-6-(Et₂NCH₂)pyridine, ^sS = 3-triphenylsilyl-1,2-enzenedithiol

Besides the penta-coordinated $\{\text{RuNO}\}^8$ complexes there are also tetra-coordinated $\{\text{RuNO}\}^8$ species known in literature. A typical representative of this class is the ruthenium analog to Vaska's compound $[\text{IrCl}(\text{CO})(\text{PPh}_3)_2]$. $[\text{RuCl}(\text{NO})(\text{PPh}_3)_2]$ adopts a square-planar structure with a linear NO ligand (176°) *trans* to the chlorine atom and a formal d⁸-Ru(0) center. [58,80]

1.3.3 $\{\text{Ru}(\text{NO})_2\}^8$ complexes

The first structurally characterized $\{\text{Ru}(\text{NO})_2\}^8$ dinitrosyl compound, $[\text{RuCl}(\text{NO})_2[\text{PPh}_3)_2]\text{PF}_6$, was reported by Eisenberg and co-workers. $[\text{RuCl}(\text{NO})_2[\text{PPh}_3)_2]\text{PF}_6$ has a *sqp* structure and exhibits both types of nitrosyl coordination, bent and linear. In terms of structural and spectroscopic parameters, the electronic state of the $\text{Ru}(\text{NO})_2$ moiety is characterized by one NO^+ and one ${}^1\text{NO}^-$ ligand. [81] The class of halogenido-bis(phosphane) type $\{\text{Ru}(\text{NO})_2\}^8$ compounds was further extended by Klüfers *et al.* X-ray studies of these dinitrosyls reveal that they adopt two different structure types: First, the already known square pyramid with one linear, equatorial NO^+ ligand and one bent NO^- ligand in the apical position and second, a trigonal bipyramid with two equal, more or less linear, NO ligands in the plane (FIGURE 1.8). [34]

**Figure 1.8:** The two structure types for halogenido-bis(phosphane)-type $\{\text{Ru}(\text{NO})_2\}^8$ compounds.

To understand the structure of dinitrosyl complexes the nitrosyl ligand group orbitals are essential. For dinitrosyl complexes in C_{2v} symmetry there are four of these orbitals to be considered (FIGURE 1.9). The $\pi^*a_1(\text{NO})$ and the $\pi^*b_2(\text{NO})$ orbitals are bonding with respect to the two N atoms and with respect to the two O atoms. In contrast, $\pi^*b_1(\text{NO})$ and $\pi^*a_2(\text{NO})$ are antibonding. Therefore, decreasing the distance of the two oxygen atoms will stabilize a_1 and b_2 and destabilize b_1 and a_2 .

Introduction

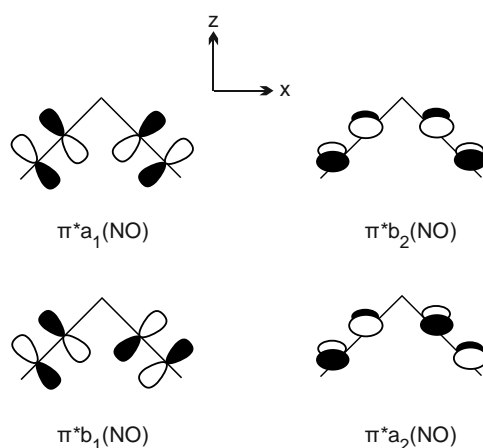


Figure 1.9: The ligand-localized molecular orbitals in C_{2v} symmetry derived from the $\pi^*(\text{NO})$ orbitals in dinitrosyl compounds. Adapted from Reference [35].

As in the $\{\text{RuNO}\}^8$ complexes, the energetic order of two orbitals decides which structure type will be adopted in $\{\text{Ru}(\text{NO})_2\}^8$ systems. FIGURE 1.10 shows the correlation diagram that relates the relevant molecular orbitals of the two possible geometries. The two orbitals to discuss are the ligand $\pi^*b_1(\text{NO})$ orbital and the metal d_{xz} orbital. As a starting point an idealized conformation was considered with 90° N–M–N angle and linear MNO fragments (FIGURE 1.10B). In this conformation the two orbitals are orthogonal to each other. If the $\pi^*b_1(\text{NO})$ orbital is lower in energy than the d_{xz} orbital (FIGURE 1.10B, left), the system relaxes by bending of one of the nitrosyl ligands, thus, the symmetry is lowered to C_s and a σ overlap of the respective orbital of the formal ${}^1\text{NO}^-$ ligand and the d_{xz} orbital occurs. If the d_{xz} orbital is lower in energy, the structure converges to the *tbp* by increasing the N–M–N angle to achieve some degree of bonding overlap.^[34,35]

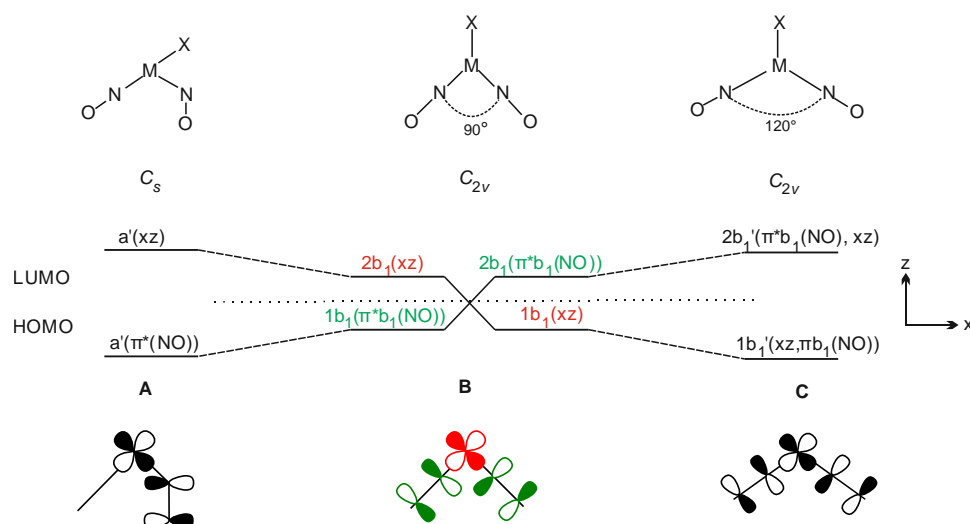


Figure 1.10: Correlation diagram of penta-coordinated $\{\text{Ru}(\text{NO})_2\}^8$ compounds with C_s and C_{2v} symmetry. Adapted from References [34] and [35].

Besides the $[\text{RuX}(\text{NO})_2\text{L}]^+$ ($X = \text{Cl}, \text{Br}, \text{I}$; $\text{L} =$ monodentate phosphane) derivatives, only three structurally characterized $\{\text{Ru}(\text{NO})_2\}^8$ complexes (**A**, **B**, **C**) are known (FIGURE 1.11).

Introduction

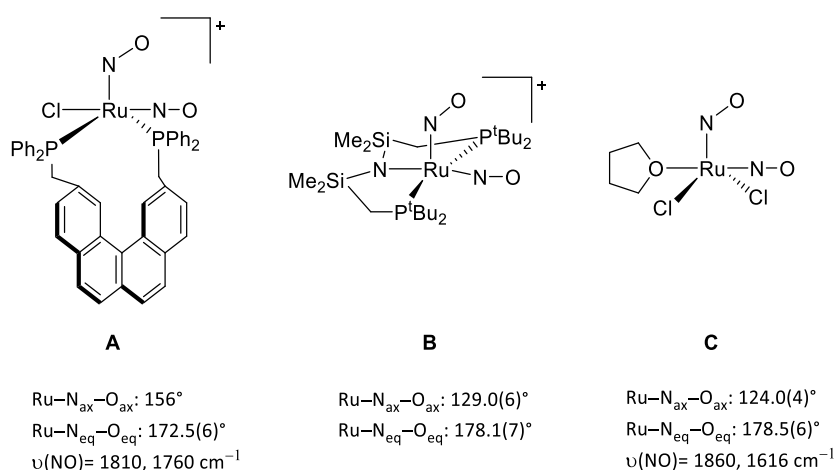


Figure 1.11: $\{\text{Ru}(\text{NO})_2\}^8$ complexes known in literature. $\tilde{\nu}(\text{NO})$ vibrational bands are given where specified.^[82–84]

1.3.4 $\{\text{Ru}(\text{NO})_2\}^{10}$ complexes

$[\text{Ru}(\text{NO})_2(\text{PPh}_3)_2]$ (**D**) and $[\text{Ru}(\text{dppf})(\text{NO})_2]$ (dppf = 1,1'-bis(diphenylphosphino)ferrocene) (**E**) are the only structurally characterized $\{\text{Ru}(\text{NO})_2\}^{10}$ representatives (FIGURE 1.12). Both compounds have a distorted tetrahedral structure with a Ru(–II) center. The low oxidation state is stabilized by the two strongly π accepting NO^+ ligands that coordinate linearly to the ruthenium center. The two O atoms of the nitrosyl groups point in opposite directions and the N–Ru–N angles are exceptionally large for a tetrahedral structure.^[61,62]

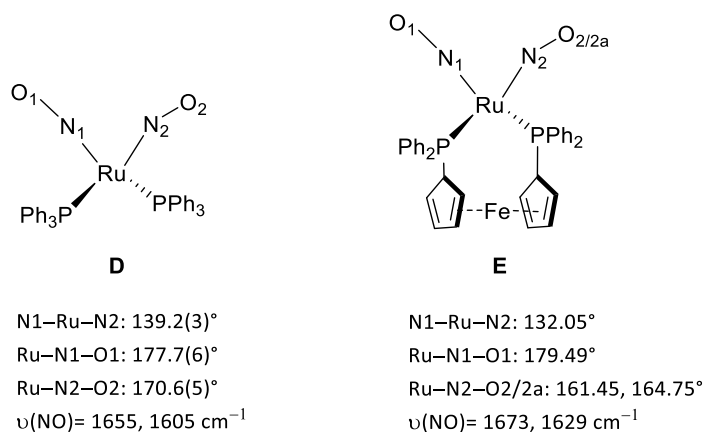


Figure 1.12: $\{\text{Ru}(\text{NO})_2\}^{10}$ complexes known in literature. O2 in $[\text{Ru}(\text{dppf})(\text{NO})_2]$ (**E**) is disordered.

This structural behavior agrees with the qualitative molecular orbital considerations of Enemark and Feltham. Analog to the $\{\text{Ru}(\text{NO})_2\}^8$ compounds, the coordination mode of the nitrosyls in $\{\text{Ru}(\text{NO})_2\}^{10}$ species depends on the composition of the HOMO. In a pseudo-tetrahedral structure a dinitrosyl complex has two molecular orbitals of b_1 symmetry which can be very similar in energy ($1b_1$, $2b_1$; $\pi^*b_1(\text{NO})$, d_{xz}). The energetic order of these two orbitals depends upon the σ -donating and π -accepting character of the other ligands. For an N–M–N angle of 90° , these two orbitals are orthogonal and, thus, are non-bonding to the metal (FIGURE 1.13B). If the $\pi b_1(\text{NO})$ orbital is much lower in energy than the

d_{xz} orbital, the HOMO has mostly a $\pi^*b_1(\text{NO})$ character. Consecutively, the N–M–N angle and the distance between the two oxygen atoms increase in order to alleviate non-bonded repulsion between the two nitrosyls (FIGURE 1.13A). If the HOMO has mainly a d_{xz} contribution (FIGURE 1.13C), then a nearly tetrahedral structure will be expected with some slight bending of the M–N–O groups in such a way that the two O atoms point to each other due to the respective contribution of $\pi^*a_1(\text{NO})$ and $\pi^*b_2(\text{NO})$ (FIGURE 1.10) to the HOMO–1 and the HOMO–2.

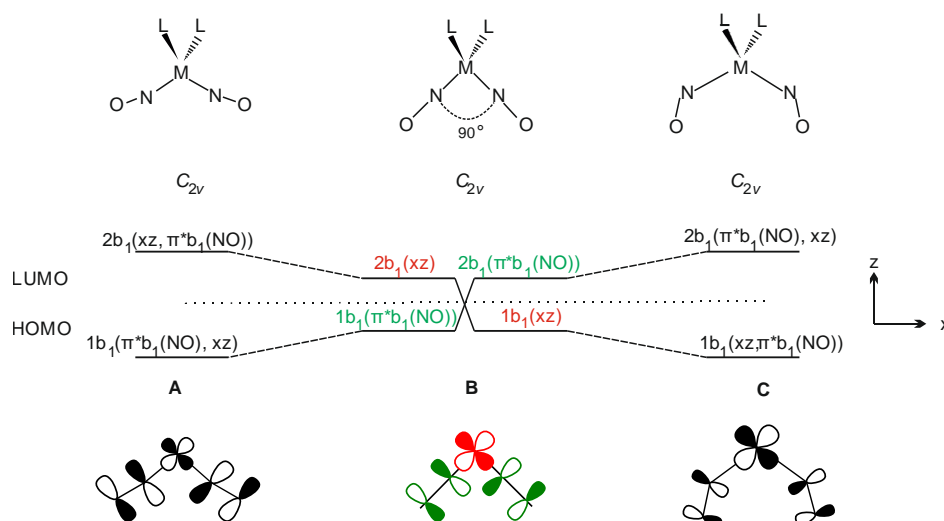


Figure 1.13: Correlation diagram of tetrahedral $\{\text{Ru}(\text{NO})_2\}^{10}$ compounds with C_s symmetry. Adapted from Reference [35].

The prediction of Enemark *et al.* that the distorted tetrahedral structure (FIGURE 1.14A) will be favored for $[\text{Ru}(\text{NO})_2\text{L}_2]$ complexes, with L being bad π acceptors is true for the two known complexes D and E (FIGURE 1.13) since organyl phosphanes are considered poor π acceptors.^[35]

1.4 N-heterocyclic carbenes

1.4.1 General properties of N-heterocyclic carbenes

For a long time, N-heterocyclic carbenes (NHCs) had the status only as alternatives to ubiquitous phosphane ligands, but in the last two decades, NHCs have risen to multifunctional and widely-employed compounds in a variety of applications and can be considered a well-established class of ligands themselves.^[85] As phosphanes, NHCs are neutral, two-electron spectator ligands the electronic and steric properties of which can be tuned.^[86] By definition carbenes are neutral compounds with a divalent carbon atom with only six electrons. In NHCs, this divalent carbon atom is part of a ring with at least one heteroatom as neighbor. The class of NHCs therefore encompasses a high diversity of compounds such as imidazolylidenes, imidazolidinylidenes, oxazolylidenes, thiazolylidines, triazolylidene or tetrahydropyrimidinylidene (FIGURE 1.14).^[87]

Introduction

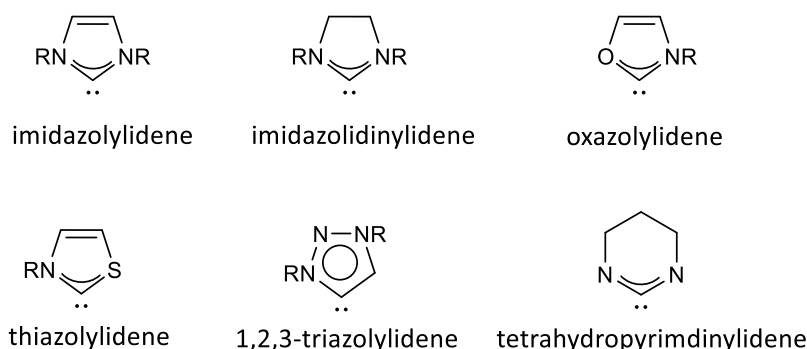


Figure 1.14: Some classes of N-heterocyclic carbenes.

In 1991 Arduengo *et al.* isolated the first stable carbene IAd (1,3-bis(adamantyl)imidazole-2-ylidene) by the deprotonation of the corresponding imidazolium chloride.^[88] The steric hindrance of the adamantyl groups certainly plays a key role in the stabilization of Arduengos' carbene, but the isolation of NHCs with far less bulky N-substituents indicates that adequate electronic stabilization is enough to isolate free NHCs (FIGURE 1.15).^[89]

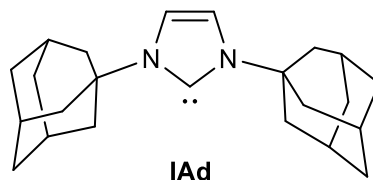


Figure 1.15: 1,3-Bis(adamantyl)imidazole-2-ylidene (IAd), the first isolated stable carbene.^[88]

Generally, the two electrons at the carbon center of carbenes can be either paired (singlet) or unpaired (triplet). Linear carbenes exhibit an sp -hybridized carbene center with two non-bonding degenerate orbitals (p_x and p_y).

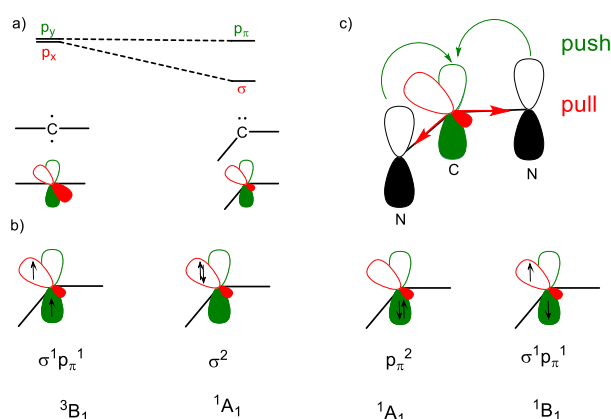


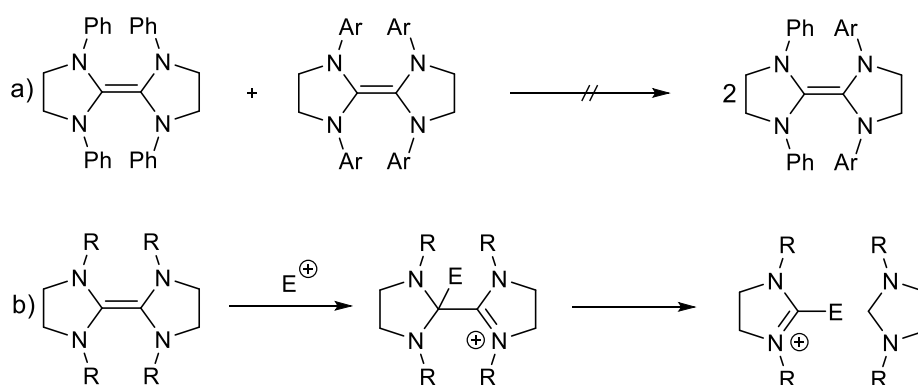
Figure 1.16: The electronic situation of carbenes. a) Relationship between the carbene bond angle and the nature of the frontier orbitals. b) Electronic configurations of carbenes. c) Stabilization of the σ^2 configuration due to the push-pull effect of the nitrogen atoms. Adapted from Reference ^[90].

In NHCs the molecule is bent and the carbon atom adopts an sp^2 -type hybridization, thus, the former p_y orbital (p_π) remains almost unchanged and the former p_x (σ) orbital is stabilized since it acquires some s character (FIGURE 1.6a). Therefore the electronic situation for NHCs can be differentiated into

four electronic configurations: two singlet states, an excited singlet state and one triplet state (FIGURE 1.16b). In the triplet state, the two non-bonding electrons occupy the two orbitals with parallel spin ($\sigma^1 p_\pi^1, ^3B_1$). In the excited singlet state, the electrons are still located in both orbitals but with antiparallel spin ($\sigma^1 p_\pi^1, ^1B_1$). In contrast, for singlet carbenes, both electrons occupy either the σ or the p_π orbital resulting in two different $^1A^1$ states in which the σ^2 is the more stable one. In NHCs the σ^2 configuration is further stabilized by the electron-withdrawing and electron-donating character of the N atoms (push-pull effect) (FIGURE 1.16c). That is because the σ orbital is further lowered in energy by the inductive effect and the p_π orbital is destabilized by the mesomeric effect. Thus, the energy gap between both increases. [85,87,90]

1.4.2 Dimerization of *N*-heterocyclic carbenes: enetetramines as carbenoids

One fundamental aspect of the behavior of NHCs is their dimerization to derivatives of electron rich tetraaminoethylenes (enetetramines). Especially non-aromatic five-membered-ring diaminocarbenes are thermodynamically unstable with regard to dimerization.^[91] Wanzlick *et al.* proposed, in 1961, that the diaminocarbene 1,3-diphenylimidazolidin-2-ylidene dimerizes reversibly to form the corresponding enetetramine.^[92–95] This conclusion was rebutted by Lemal *et al.* who showed that typical tetraaminoethylenes did not dissociate, even under much more drastic conditions than used by Wanzlick *et al.* (SCHEME 1.5a). Furthermore, he proposed that the dimer dissociates rather by an attack of an electrophile (H^+ or metal center) into one equivalent of product and one of carbene, subsequently also attacked by E^+ (SCHEME 1.5b).^[96] Computational studies by Alder *et al.* proved a proton-catalyzed dimerization to be the most common mechanism for dimer formation. This mechanism for proton catalysis is simply the reverse of Lemal's mechanism.^[91]

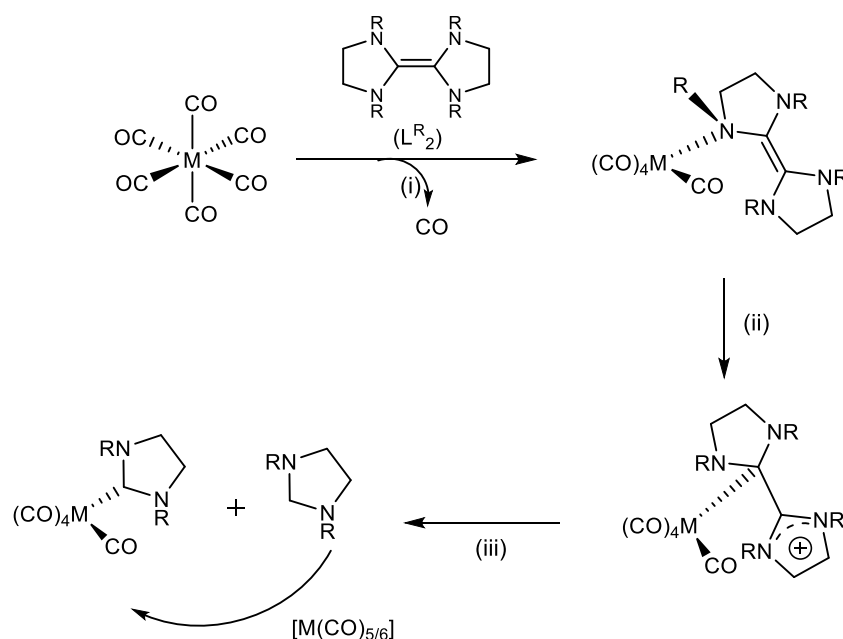


Scheme 1.5: a) Crossover experiment carried out by Lemal *et al.* b) Explanation for the reaction of electrophiles with enetetramines. Adopted from References [91] and [98].

Even though dimerization may be a handicap for the isolation of stable NHCs, electron rich tetraaminoethylenes can be used as so-called carbenoids (carbene precursors) to generate NHC-transition-metal complexes. Lappert *et al.* have synthesized a multitude of enetetramine-derived complexes, having between one and four carbene ligands, of $Cr^{0/I}$, $Mo^{0/II}$, $W^{0/II}$, Mn^I , $Fe^{-II/0/I/II}$, $Ru^{-II/0/II}$,

Introduction

Os^{II}, Co^{-I/II/III}, Rh^{I/III}, Ir^{I/III}, Ni^{0/I/II}, Pd^{II}, Pt^{II}, Au^I and Hg^{II}. Lappert further proposed a reaction pathway, in accordance with Lemal's mechanism, from an enetetramine to a carbene metal complex (SCHEME 1.6).



Scheme 1.6: Proposed reaction pathway of the reaction of an enetetramine (L^R₂) to a carbene complex of the M(CO)₅L^R type: (i) initial olefin-N-metal complex formation, then (ii) subsequent rearrangement to a C-bonded species which may then (iii) dissociate to form the carbene metal complex under release of a resonance-stabilized carbene fragment, :L^R. The latter may be free and dimerize or be captured by another metal center by [M(CO)_n] (n = 5 or 6). Adapted from Reference [97].

Enetetramines are synthesized from diamines and *N,N*-dimethylformamide under formation of methanol and dimethylamine. It must be noted that this synthesis is restricted to primary alkyl- and unhindered aryldiamines. Due to their weak C=C bond, they react with electrophiles or protic reagents to yield the corresponding amins. Another advantage of these compounds is their strong reducing ability which enables them, for example, to abstract a chlorine atom from a chloroalkane.^[97-99]

1.4.3 *N*-heterocyclic carbenes as ligands

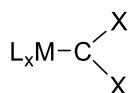


Figure 1.17: Schematic representation of a carbene metal complex, where M represents a transition-metal and L_x the sum of all the other ligands, except the carbene moiety CXY (X and Y being a dialkyl-substituted heteroatom).

Since the first metal complexes containing NHC ligands were reported independently by Öfele and Wanzlick *et al.*, the numbers of NHC complexes are on the rise, especially in the field of catalysis. A surprising advantage of NHC-based catalysts is their high stability under many catalytic conditions. In many cases these catalysts even have better activity than the corresponding phosphane-based

catalysts the Ru-based Grubbs catalyst of the second generation, for example.^[100–104] To understand the stability of the carbene-metal bond, geometric and electronic effects have to be considered. For the formation of the C–M bond by overlapping orbitals, the valence angle (X–C–X) at the carbene center has to be narrowed. NHCs (X = N) adopt a small valence angle due to their cyclic structure and can easily bind a metal fragment. Considering the electronic character of the M–C bond, carbene complexes can be divided into either Fischer-type complexes or Schrock-type complexes. In general, electron-rich carbene complexes featuring carbenes stabilized by heteroatoms or phenyl substituents are defined as Fischer-type complexes. In contrast, Schrock-type carbene complexes are usually electron deficient and have only hydrogen or simple alkyl substituents at the carbene.^[105–108] The M–C bond in Fischer-type complexes reveals a mutual donor-acceptor interaction of two closed-shell (singlet) fragments. The bonding arises from carbene-metal σ donation and simultaneously from metal-carbene π back donation.^[109] Therefore, the carbon-metal bond exhibits partial double-bond character which decreases with the stabilization of the carbene by its alpha groups. Since the π electrons are polarized to the metal center, Fischer-type complexes are electrophilic at the carbon double bond to the metal (FIGURE 1.18a). In NHC-based complexes the metal carbon bond is considered a simple bond since the carbon atom is already stabilized by the π back donation of the nitrogen atoms.^[110] But it must be noted that the role of π back donation increases with an increasing d-electron count at the metal center.^[89] The M–C bond in Schrock-type complexes is created by the coupling of two triplet fragments whereby the electrons are nearly equally distributed between the carbon and the metal center giving the M–C bond a covalent, double-bond character.^[108] Therefore, Schrock-type carbene complexes are nucleophilic at the carbon-metal bond (FIGURE 1.18b).^[109,111]

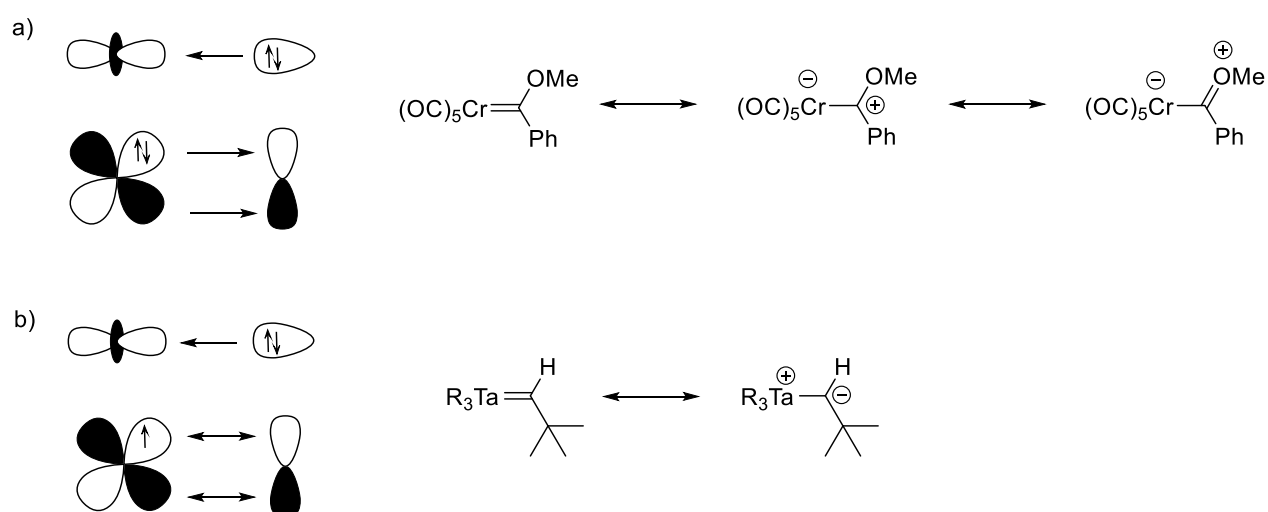


Figure 1.18: a) Metal-carbon bonding in Fischer-type complexes. b) Metal-carbon bonding in Schrock-type complexes. Adapted from Reference ^[112].

There are carbene complexes that do not, or only partially, fit the definition of either category. For example Lappert's enetetramine-derived complexes differ from both categories since the coordinated NHC ligands are resistant to electrophilic and nucleophilic attack at the carbon atom.^[98]

1.5 Aim of this work

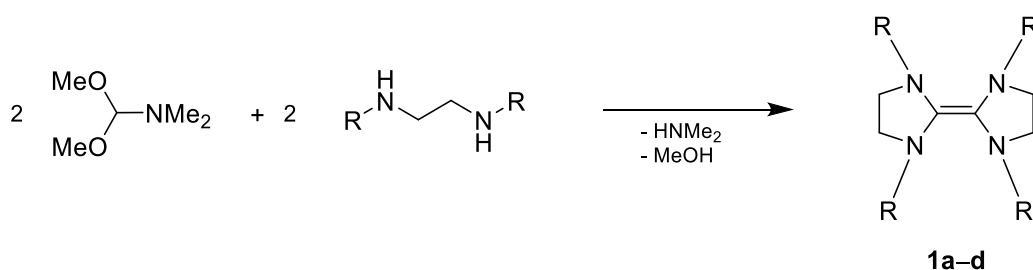
To sum it up the better part of mononuclear ruthenium nitrosyl complexes belongs to the stable hexa-coordinated $\{\text{RuNO}\}^6$ species with over 600 X-ray structures listed in the Cambridge Structural Database (July 2016). Adding more electrons to the RuNO moiety leads to ligand loss. Thus, no hexa-coordinated $\{\text{RuNO}\}^8$ compound and only nineteen tetra- or penta-coordinated $\{\text{RuNO}\}^8$ compounds are structurally characterized by now. The RuNO moiety of the tetra-coordinated $\{\text{RuNO}\}^8$ compounds is linear, but the RuNO moiety of the penta-coordinated $\{\text{RuNO}\}^8$ compounds is either bent or linear.^[63] In $\{\text{Ru}(\text{NO})_2\}^8$ systems the nitrosyl ligands can either bind equally or unequally. Our group already extended the class of the $\{\text{Ru}(\text{NO})_2\}^8$ species by several dinitrosyls of the halogenido-bis(phosphane) type. Experimental and theoretical studies showed that the adopted structure of these compounds is primarily influenced by the halogenido ligand and secondarily by the electronic character of the phosphane ligand.^[34] For $\{\text{Ru}(\text{NO})_2\}^{10}$ compounds $[\text{Ru}(\text{NO})_2(\text{PPh}_3)_2]$ and $[\text{Ru}(\text{dppf})(\text{NO})_2]$ are the only structurally characterized representatives and both compounds have a distorted tetrahedral structure with the oxygen atoms of the nitrosyl ligands pointing away from each other.^[61,62] The better part of the $\{\text{Ru}(\text{NO})_n\}^m$ ($m > 6$) compounds have co-ligands, but neither a mono- nor a dinitrosyl carbene ruthenium complex with $m > 6$ has been structurally characterized by now.

The aim of this work was the analysis of the electronic states of the RuNO moiety and its influence on the structure of different $\{\text{Ru}(\text{NO})_n\}^m$ species. Furthermore, the effect of diverse co-ligands on the structure were investigated as well. To that end, first mono- and dinitrosyls, differing in the electronic state of their RuNO moiety, were synthesized, whereby a combination of either a halogenido ligand with triphenylphosphane or halogenido ligand with different NHC ligands of the 1,3-di-*R*-imidazoline-2-ylidene-type was used to examine the co-ligand influence. Since most of the structurally characterized $\{\text{Ru}(\text{NO})_m\}^n$ compounds have phosphane ligands the focus here was on the structural characterization of the NHC derivatives. In that matter the classes of the $\{\text{RuNO}\}^8$, $\{\text{Ru}(\text{NO})_2\}^8$ and $\{\text{Ru}(\text{NO})_2\}^{10}$ species were successfully extended by several new NHC nitrosyl complexes. In addition the first hexa-coordinated mononuclear $\{\text{Ru}(\text{NO})_2\}^8$ compound was structural characterized. In the second part of this work the structural properties of the ruthenium nitrosyl complexes were analyzed by consideration of the relevant molecular orbital interactions with quantum-chemical calculations. Furthermore the electronic character of the different RuNO moieties was analyzed by charge and population analysis.

2 Results

2.1 Synthesis of the enetetramines

In this work the bis-1,3-di-*R*-imidazoline-2-ylidene-type enetetramines will be abbreviated with L^R_2 and the corresponding carbenes with L^R . The enetetramines L^{Me_2} (**1a**), L^{Et_2} (**1b**), L^{nPr_2} (**1c**) and L^{Bn_2} (**1d**) were used as reducing agents for the reduction of the trihalogenido Ru(II) precursors to the monohalogenido Ru(I) products, and as carbenoids for the synthesis of the carbene $\{RuNO\}^{6-8}$ and $\{Ru(NO)_2\}^{8-10}$ derivatives. The synthesis of L^{Me_2} (**1a**), L^{Et_2} (**1b**), L^{nPr_2} (**1c**) and L^{Bn_2} (**1d**), followed similar procedures according to a simple route by Lappert *et al.*^[113] The corresponding diamine and *N,N*-dimethylformamide were dissolved in toluene or methylcyclohexane and the solution was slowly heated to 110 – 130 °C. The reaction was a succession of equilibria which were driven toward the enetetramines by the removal of the developing methanol and the dimethylamine by distillation (SCHEME 2.1).



Scheme 2.1: General procedure for the synthesis of the enetetramines L^R_2 (**1a-d**).

The compounds were characterized by 1H NMR, $^{13}C\{^1H\}$ NMR spectroscopy and mass spectrometry. L^{Me_2} (**1a**), L^{Et_2} (**1b**), L^{nPr_2} (**1c**) and L^{Bn_2} (**1d**) were obtained in 96 %, 84 %, 85 % and 76 % yield. The 1H NMR and $^{13}C\{^1H\}$ NMR data are summarized in TABLE 2.1 and 2.2. **1a-1d** are oxygen- and moisture-sensitive solids, whereby **1a-1c** have a very low melting point, thus, they were further handled in toluene solutions.

Table 2.1: 1H NMR data for the enetetramines (**1a-d**). Chemical shifts δ in ppm and coupling constant J in Hz.

	N- $\underline{CH_2CH_2}$ -N	N- $\underline{CH_2}$ -	N- $\underline{CH_2CH_2CH_3}$	- $\underline{CH_3}$	-Ph
L^{Me_2} (1a)	2.49 (s)			2.31 (s)	7.36–7.17 (m)
L^{Et_2} (1b)	2.79 (s)	3.00 (q) $^3J = 7.1$		1.04 (t) $^3J = 7.1$	
L^{nPr_2} (1c)	2.85–2.79 (m)	2.85–2.79 (m)	1.52–1.42 (m)	0.87 (t) $^3J = 7.5$	
L^{Bn_2} (1d)	2.88 (s)	4.26 (s)			

Results

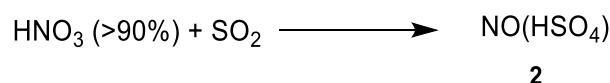
Table 2.2: $^{13}\text{C}\{^1\text{H}\}$ NMR data for the enetetramines (**1a–d**). Chemical shifts δ in ppm.

	N $\underline{\text{C}}\text{N}$	N– $\underline{\text{C}}\text{H}_2\text{C}\underline{\text{H}}_2\text{–N}$	N– $\underline{\text{C}}\text{H}_2\text{–}$	N–	– $\underline{\text{C}}\text{H}_3$	–Ph
L ^{Me} ₂ (1a)	128.27	51.36			38.82	
L ^{Et} ₂ (1b)	125.70	45.60	49.05		12.88	
L ^{nPr} ₂ (1c)	127.19	50.00	54.54	22.12	12.49	
L ^{Bn} ₂ (1d)		56.07	49.33			140.45, 129.29, 128.58, 127.09

2.2 Synthesis of the precursor compounds

2.2.1 Synthesis of NO(HSO₄) (**2**)

NO(HSO₄) (**2**) was synthesized by passing gaseous SO₂ through a mixture of anhydrous nitric acid and acetic acid between –5 °C and 5 °C according to a route known in literature (SCHEME 2.2).^[114]



Scheme 2.2: Synthesis of the nitrosonium salt NO(HSO₄).

2 was obtained in form of colorless crystals in 38 % yield. The compound was characterized by Raman spectroscopy and single-crystal X-ray diffraction. Due to the extreme moisture sensitivity of the compound, no further characterization by elemental analysis was possible. The Raman spectrum shows one strong peak for the NO stretching frequency at 2275 cm⁻¹.

*Crystal structure of NO(HSO₄) (**2**)*

Crystals of **2** were obtained directly from the reaction mixture. The structure of **2** is illustrated in FIGURE 2.1 and FIGURE 2.2.

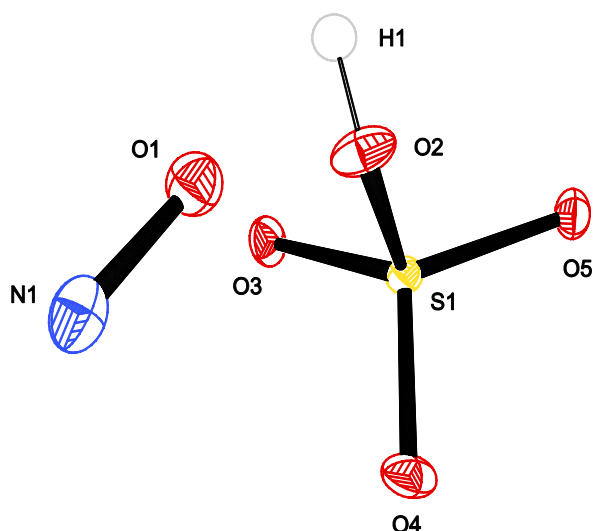


Figure 2.1: ORTEP plot of the nitronium salt $\text{NO}(\text{HSO}_4)$ (**2**) in crystals of **2**. Sp.Gr. $Pna2_1$. The thermal ellipsoids are drawn at 50 % probability level at 173 Interatomic distances (Å) and angles (°), the standard deviation of the last decimal digit is given in parentheses: N1–O1 1.057(4), S1–O2 1.562(3), S1–O3 1.447(3), S1–O4 1.459(3), S1–O5 1.4455(2), O2–H1 0.818(11); O2–S1–O3 108.46(15), O2–S1–O4 103.12(15), O2–S1–O5 106.97(16), O3–S1–O4 112.9(2), O3–S1–O5 112.35(15), O4–S1–O5 112.32(17), S1–O2–H1 108(4).

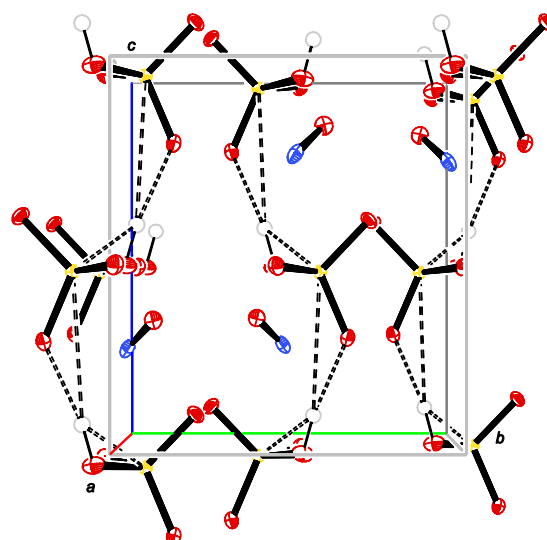


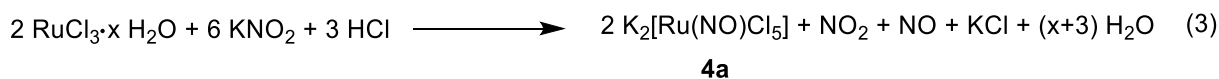
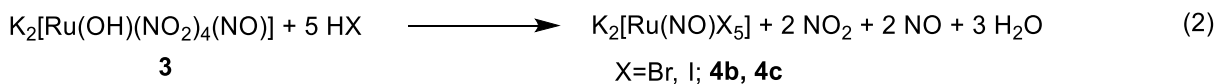
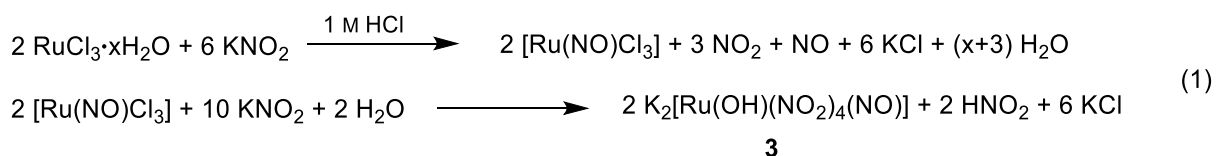
Figure 2.2: Projection of the structure of the nitronium salt **2** with view along [100].

The structure solution succeeded in the orthorhombic space group $Pna2_1$. The primitive cell contains four ion pairs, the asymmetric unit contains one ion pair. The $[\text{HSO}_4]^-$ ion has a distorted tetrahedral structure with S–O distances at about 1.5 Å and the O–S–O angles between 103 and 113°. The hydrogen sulfate ions are arranged in chains by the formation of the hydrogen along the c axis. The N–O bond length of 1.06 Å is in the range typical for nitronium salts.^[115]

2.2.2 Synthesis of the $\{\text{RuNO}\}^6$ precursors

$\text{K}_2[\text{Ru}(\text{OH})(\text{NO}_2)_4(\text{NO})]$ (**3**) was synthesized by a procedure known in literature in 45 % yield and was characterized by elemental analysis, IR spectroscopy and mass spectrometry (SCHEME 2.3, equation 1).^[116] Following the route by Griffith *et al.*, **3** reacted with the corresponding hydrogen halides (HX) to give $\text{K}_2[\text{Ru}(\text{NO})\text{X}_5]$ (X = Br, I; **4b,4c**) (SCHEME 2.3, equation 2) in 44 % yield and 90 % yield.^[117] $\text{K}_2[\text{Ru}(\text{NO})\text{Cl}_5]$ (**4a**) was obtained directly by the reaction of the commercially available $\text{RuCl}_3 \cdot x\text{H}_2\text{O}$ with KNO_2 and HCl in 90 % yield (SCHEME 2.3, equation 3). **4a–4c** were characterized by elemental analysis, mass spectrometry and IR spectroscopy. Characteristic for **4a–4c**, is a strong nitrosyl-stretching frequency between 1840 and 1900 cm^{-1} in the IR spectrum.

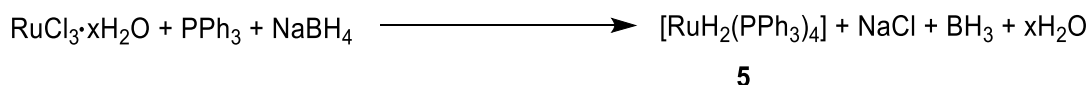
Results



Scheme 2.3: Synthesis of the {RuNO}⁶ precursor compounds. (1) Synthesis of K₂[Ru(OH)(NO₂)₄(NO)] (**3**), (2) synthesis of K₂[Ru(NO)X₅] (X = Br, I; **4b, 4c**) and (3) synthesis of K₂[Ru(NO)Cl₅] (**4a**).

2.2.3 Synthesis of [RuH₂(PPh₃)₄] (**5**)

[RuH₂(PPh₃)₄] (**5**) was synthesized by reaction of RuCl₃·xH₂O with triphenylphosphane and sodium hydrido borate in 93 % yield following the route by Levison *et al* (SCHEME 2.4).^[118] **5** was characterized by elemental analysis, IR spectroscopy and mass spectrometry.

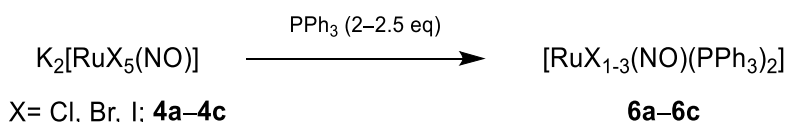


Scheme 2.4: Synthesis of [RuH₂(PPh₃)₄] (**5**).

2.3 Synthesis of the {RuNO}⁶⁻⁸ phosphane compounds

The synthesis of [RuX₁₋₃(NO)(PPh₃)₂] (X = Cl, Br, I; **6a, 6b, 6c**) followed the route by Chatt *et al.* (SCHEME 2.5).^[119] The iodido derivative **6c** was obtained as pure {RuNO}⁶ species in 95 % yield and was characterized by elemental analysis, ³¹P{¹H} NMR and IR spectroscopy. In the case of the chlorido and bromido species (**6a, 6b**) a redox reaction with simultaneous triphenylphosphane addition occurred due to the weak reductive character of the phosphane. Thus, **6a** and **6b** were obtained as partially reduced {RuNO}⁶⁻⁸ mixtures. Since **6a** and **6b** were uniformly reduced to the corresponding {RuNO}⁸ species in the consecutive reaction no further purification of the {RuNO}⁶⁻⁸ mixtures was needed. For **6a** and **6b** no yields and no data for elemental analysis are given. Characteristic for **6a-6c** is a strong nitrosyl-stretching frequency between 1855 and 1875 cm⁻¹ in the IR spectrum (**6a** and **6b** reveal several peaks in the region assignable to coordinated nitrosyl due to their mixed character).

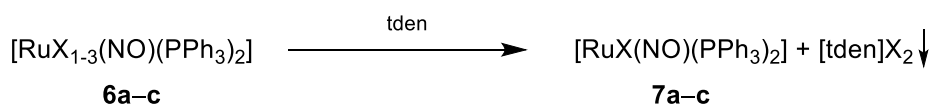
Results



Scheme 2.5: Synthesis of $[\text{RuX}_{1-3}(\text{NO})(\text{PPh}_3)_2]$ (X = Cl, Br, I; **6a**, **6b**, **6c**).

2.4 Synthesis of the tetra-coordinated $\{\text{RuNO}\}^8$ phosphane compounds

$[\text{RuX}(\text{NO})(\text{PPh}_3)_2]$ (X = Cl, Br, I; **7a**, **7b**, **7c**) were synthesized by the reduction of **6a-6c** with tetrakis(dimethylamino)ethylene (tden) according to a route by Lappert *et al.* in 19 %, 22 % and 82 % yield respectively (SCHEME 2.6).^[120] Tetrakis(dimethylamino)ethylene is known as strong electron donor with a reduction power close to zinc.^[121] The reduction of a $\{\text{RuNO}\}^6$ species of the $[[\text{RuX}_{1-3}(\text{NO})(\text{PPh}_3)_2]$ type with zinc-copper couple is a sluggish reaction that requires high temperatures and long reaction times.^[34,60] In contrast, the reduction with tetrakis(dimethylamino)ethylene proceeds rapidly even at room temperature and the only by-product of the reaction, the dicarbocation salt ($[\text{tden}]_2\text{X}$), can easily be removed by filtration. Furthermore, the synthesis of **7c** that was not successful via the reduction with zinc copper couple, succeeded with tden as the reducing agent.



Scheme 2.6: Synthesis of $[\text{RuX}(\text{NO})(\text{PPh}_3)_2]$ (X = Cl, Br, I; **7a**, **7b**, **7c**).

7a-7c were obtained as oxygen- and moisture-sensitive dark green crystals by cooling the reaction solutions to room temperature and concentrating the solutions, if necessary. In the presence of excess triphenylphosphane, the dark green solutions of **7a-7c** turned reddish brown in the cold due to the addition of a third phosphane to the ruthenium center. This reaction is reversible, thus, **7a-7c** can be retrieved upon warming the solutions. The compounds were characterized by elemental analysis, IR, $^{31}\text{P}\{^1\text{H}\}$ NMR and $^{31}\text{P}\{^1\text{H}\}$ NMR solid-state spectroscopy and mass spectrometry. In comparison to the trishalogenido species **6a-6c**, the nitrosyl-stretching frequencies for **7a-7c** are shifted over 100 cm^{-1} to lower wave numbers to 1727 cm^{-1} for **7a** and **7b** and to 1739 cm^{-1} for **7c**. The reason for this is the – due to the reduction– higher electron density that is primarily located in the π^* orbitals of the NO ligand. The $^{31}\text{P}\{^1\text{H}\}$ NMR and $^{31}\text{P}\{^1\text{H}\}$ NMR solid-state spectra of the three complexes are comparable and a summary of NMR data is given in TABLE 2.3. Crystals of **7b** and **c** were suitable for single-crystal X-ray diffraction.

Results

Table 2.3: $^{31}\text{P}\{^1\text{H}\}$ NMR and $^{31}\text{P}\{^1\text{H}\}$ NMR solid-state data for **7a–c**. Chemical shifts δ in ppm coupling constant J in Hz.

	$^{31}\text{P}\{^1\text{H}\}$ NMR in toluene at 80 °C	$^{31}\text{P}\{^1\text{H}\}$ NMR solid-state
$[\text{RuCl}(\text{NO})(\text{PPh}_3)_2]$ (7a)	33.55 (s,br)	34.22 (d, $^2J = 274$) 31.65 (d, $^2J = 272$)
$[\text{RuBr}(\text{NO})(\text{PPh}_3)_2]$ (7b)	32.17 (s, br)	36.15 (d, $^2J = 303$) 32.05 (d, $^2J = 303$)
$[\text{RuI}(\text{NO})(\text{PPh}_3)_2]$ (7c)	28.95 (s,br)	30.08 (d, $^2J = 304$) 24.20 (d, $^2J = 300$)

Crystal structure of $[\text{RuBr}(\text{NO})(\text{PPh}_3)_2]$ (**7b**)

Dark green crystals of **7b** were obtained directly from the reaction solution by storing it over night at room temperature. The structure of **7b** is illustrated in FIGURE 2.3.

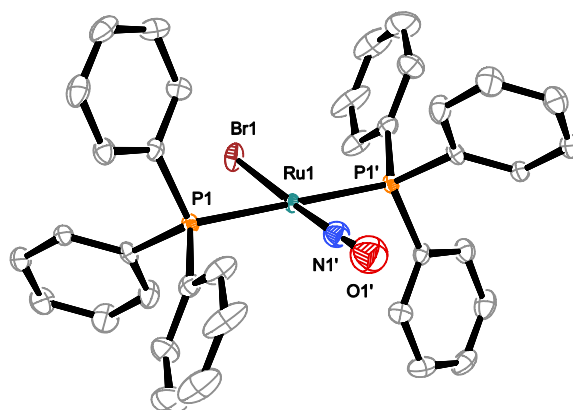


Figure 2.3: ORTEP plot of the complex $[\text{RuBr}(\text{NO})(\text{PPh}_3)_2]$ in crystals of **7b** (disorder not depicted). Sp.Gr. $P\bar{1}$. The thermal ellipsoids are drawn at 50 % probability level at 173 K. Due to clarity, hydrogen atoms are not depicted. Interatomic distances (Å) and angles (°), the standard deviation of the last decimal digit is given in parentheses: Ru–N1 1.707(9), Ru–P1 2.833(8), Ru1–Br1 2.4420(11), N1–O 1.188(11); O1–N1–Ru1 177.7(8), N1–Ru1–P1 87.9(2), N1–Ru1–P1' 92.1(2), N1–Ru1–Br1 177.9(2), P1–Ru1–Br1 89.14(3), P1'–Ru1–Br1 90.86(3).

The structure solution succeeded in the triclinic space group $P\bar{1}$. The primitive cell contains one complex molecule, the asymmetric unit contains half a complex molecule that is completed via an inversion center. As the chlorido analog (**7a**) known from literature the molecule has a square-planar structure ($\text{CShM}_{\text{SP-4}}$ value 0.478). Due to the inversion center, the bromine atom and the *trans* nitrosyl group are disordered in such a way as to superimpose themselves onto each other and the two *trans* phosphane ligands are equal. The Ru–N–O angle (178°) displays almost linear geometry and the short Ru–N distance (1.707(9) Å) is due to the strong π back donation.

Results

Crystal structure of $[\text{Ru}(\text{NO})(\text{PPh}_3)_2]$ (**7c**)

Analog to **7b**, dark green crystals of **7c** were obtained directly from the reaction solution by storing it over night at room temperature. The structure of **7c** · C₇H₈ is illustrated in FIGURE 2.4.

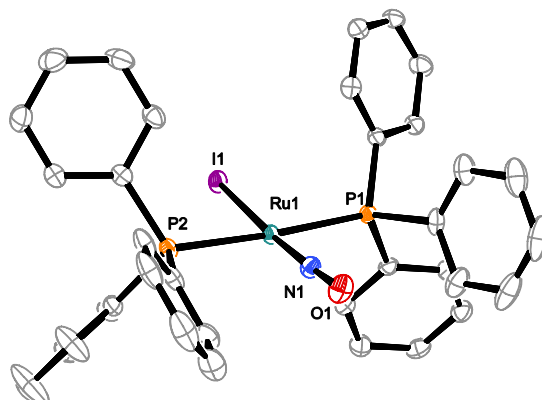
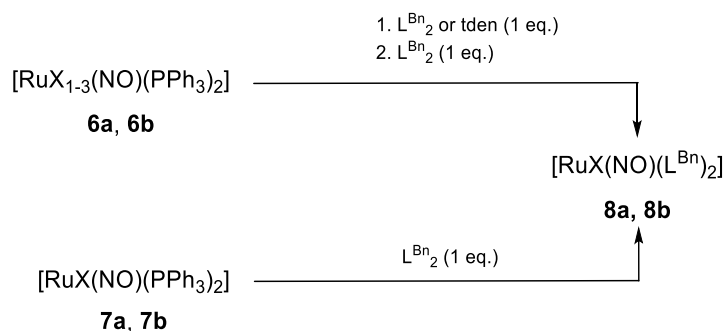


Figure 2.4: ORTEP plot of the complex $[\text{Ru}(\text{NO})(\text{PPh}_3)_2]$ in crystals of **7c** · C₇H₈. Sp.Gr. $P2_1/c$. The thermal ellipsoids are drawn at 50 % probability level at 173 K. Due to clarity, hydrogen atoms and solvent molecules are not depicted. Interatomic distances (Å) and angles (°), the standard deviation of the last decimal digit is given in parentheses: Ru1–N1 1.7201(17), Ru1–P1 2.3748(5), Ru1–P2 2.3930(5), Ru1–I1 2.6750(2), N1–O1 1.173(2); O1–N1–Ru1 177.22(16), N1–Ru1–P1 89.24(6), N1–Ru1–P2 92.59(6), P1–Ru1–P2 176.449(19), N1–Ru1–I1 176.70(6), P1–Ru1–I1 87.976(13), P2–Ru1–I1 0.097(13).

7c crystallizes in the monoclinic space group $P2_1/c$ with four complex molecules in the primitive cell. As in **7b** the structure is best described as square-planar ((CShM $Sp-4$ value 1.303) and the angles and bond lengths are comparable to those of the structure of **7b**. The Ru–I bond length (2.68 Å) is longer than the ruthenium halogenido bond in **7a** and **7b** due to the larger ion radius of the iodido ligand. One phenyl group as well as the co-crystallized toluene are disordered.

2.5 Synthesis of the tetra-coordinated $\{\text{RuNO}\}^8$ NHC compounds

The synthesis of $[\text{RuX}(\text{NO})(\text{L}^{\text{Bn}})_2]$ (X = Cl, Br; **8a**, **8b**) succeeded in two ways: In a one-pot reaction by *in situ* generation of the $\{\text{RuNO}\}^8$ compounds $[\text{RuX}(\text{NO})(\text{PPh}_3)_2]$ (X = Cl, Br; **7a**, **7b**) via reduction of the $\{\text{RuNO}\}^{6-8}$ compounds $[\text{RuX}_{1-3}(\text{NO})(\text{PPh}_3)_2]$ (X = Cl, Br; **6a**, **6b**) with tden or the enetetramine L^{Bn}_2 and subsequent ligand substitution or by isolating the corresponding $\{\text{RuNO}\}^8$ phosphane analog before the ligand substitution (SCHEME 2.7).^[120]



Scheme 2.7: Synthesis of $[\text{RuX}(\text{NO}) \text{L}^{\text{Bn}}_2]$ (X = Cl, Br; **8a**, **8b**).

Results

8a, **8b** were obtained as oxygen- and moisture-sensitive dark blue crystals in 52 % yield and 69 % yield by storing the reaction solutions at 7 °C over night. Similar to the {RuNO}⁸ phosphane analogs the blue solution of the bromido compound **8b** turns red in the presence of excess enetetramine L^{Bn}₂ upon cooling due to the formation of a penta-coordinated species by substitution of the bromido ligand by two NHC ligands. Since this reaction is an equilibrium **8b** can be retrieved by heating the solution. Attempts to isolate [RuI(NO)(L^{Bn})₂] were not successful since the mentioned equilibrium is strongly shifted on the side of the penta-coordinated species. **8a** is already known in literature even though the crystal structure was unidentified.^[120] The compounds were characterized by elemental analysis, IR, ¹³C{¹H} NMR and ¹H NMR spectroscopy and mass spectrometry. In comparison to the phosphane species the nitrosyl-stretching frequencies for **8a** and **b** are shifted over 50 cm⁻¹ to lower frequencies to 1686 cm⁻¹. The NMR spectra of both complexes are comparable and a summary of NMR data is given in TABLE 2.4 and 2.5. Worth mentioning is the downshifted signal for the carbene C-atom at 216 ppm in the ¹³C{¹H} NMR spectra of **8a** and **b**.

Table 2.4: ¹H NMR data for **8a** and **b** in CD₂Cl₂. Chemical shifts δ in ppm.

	N-CH ₂ CH ₂ -N	N-CH ₂ -	-Ph
[RuCl(NO)L ^{Bn} ₂] (8a)	3.70 (s)	5.41 (s)	7.36–7.23 (m)
[RuBr(NO)L ^{Bn} ₂] (8b)	3.72 (s)	5.42 (s)	7.47–7.23 (m)

Table 2.5: ¹³C-NMR data for **8a** and **b** in CD₂Cl₂. Chemical shifts δ in ppm.

	N _C N	N-CH ₂ CH ₂ -N	N-CH ₂ -	-Ph
[RuCl(NO)L ^{Bn} ₂] (8a)	216.67	56.37	48.92	137.92, 129.05, 128.97, 127.99,
[RuBr(NO)L ^{Bn} ₂] (8b)	216.28	56.49	48.98	129.06, 128.97, 127.99

*Crystal structure of [RuCl(NO)L^{Bn}₂] (**8a**)*

Dark blue crystals of compound **8a** were obtained by storing the reaction solution at 7 °C over night. The structure of **8a** is depicted in FIGURE 2.5.

Results

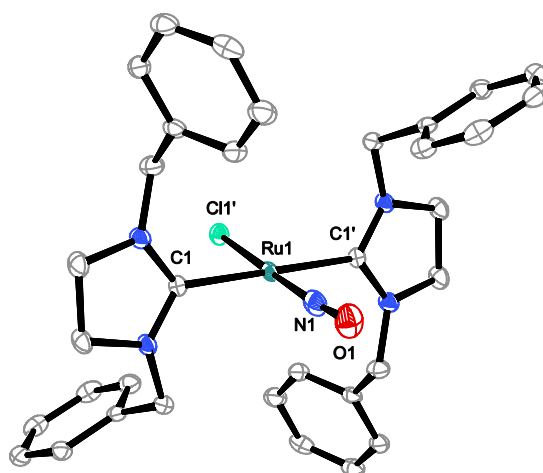


Figure 2.5: ORTEP plot of the complex $[\text{RuCl}(\text{NO})\text{L}^{\text{Bn}_2}]$ in crystals of **8a** (disorder not depicted). Sp.Gr. $P2_1/n$. The thermal ellipsoids are drawn at 50 % probability level at 173 K. Due to clarity, hydrogen atoms and solvent molecules are not depicted. Interatomic distances (Å) and angles ($^\circ$), the standard deviation of the last decimal digit is given in parentheses: Ru1–N1 1.800(6), Ru1–C1 2.1139(15), Ru1–Cl1' 2.2806(17), N1–O1 1.177(5); O1–N1–Ru1 177.22(16), N1–Ru1–C1 90.9(2), N1–Ru1–C1' 89.1(2), N1–Ru1–Cl1 178.4(3), C1–Ru1–Cl1' 90.77(6), C1'–Ru1–Cl1' 89.23(6).

The structure solution succeeded in the monoclinic space group $P2_1/n$. The primitive cell contains two complex molecules and the asymmetric unit contains half a complex molecule that is completed via an inversion center. As the phosphane analogs (**7b** and **c**) the molecule has a square-planar structure ($\text{CShM}_{\text{SP-4}}$ value 0.489). Due to the inversion center, the chlorine atom and the *trans* nitrosyl group are disordered in such a way as to superimpose themselves onto each other and the two *trans* NHC ligands are equal. The Ru–N–O angle (175.6°) displays almost linear geometry.

Crystal structure of $[\text{RuBr}(\text{NO})\text{L}^{\text{Bn}_2}]$ (**8b**)

Dark blue crystal of compound **8b** were obtained by storing the reaction solution at 7°C over night. The structure of **8b** is depicted in FIGURE 2.6.

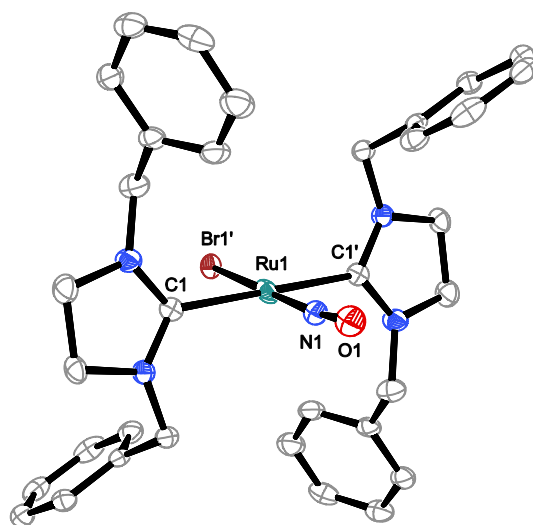


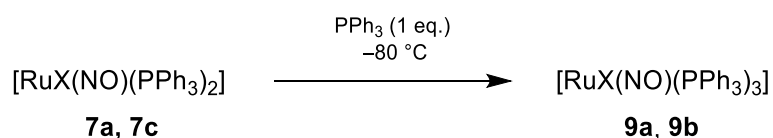
Figure 2.6: ORTEP plot of the complex $[\text{RuBr}(\text{NO})\text{L}^{\text{Bn}_2}]$ in crystals of **8b** (disorder not depicted). Sp.Gr. $P2_1/n$. The thermal ellipsoids are drawn at 50 % probability level at 173 K. Due to clarity, hydrogen atoms and solvent molecules are not depicted. Interatomic distances (Å) and angles ($^\circ$), the standard deviation of the last decimal digit is given in parentheses: Ru1–N1 1.829(8), Ru1–C1 2.116(3), Ru1–Br1' 2.3587(11), N1–O1 1.148(8); O1–N1–Ru1 174.0(7), N1–Ru1–C1 90.2(2), N1–Ru1–C1' 89.8(2), N1–Ru1–Br1' 179.1(2), C1–Ru1–Br1' 90.61(7), C1'–Ru1–Br1' 89.39(7).

Results

The structure of **8b** is isomorphous to the structure of **8a**. As in the chlorine analog the halogenido ligand and the nitrosyl ligand are disordered in such a way as to superimpose themselves onto each other due to an inversion center. Mentionable is the elongated Ru–N distance of **8b** in comparison to **8a** due to the stronger *trans*-influence of the bromido ligand.

2.6 Synthesis of the penta-coordinated {RuNO}⁸ phosphane compounds

[RuX(NO)(PPh₃)₃] (X = Cl, I; **9a**, **9b**) were synthesized by the addition of one equivalent triphenylphosphane to [RuX(NO)(PPh₃)₂] (X = Cl, I; **7a**, **7c**) in the cold (–80 °C) (SCHEME 2.8).



Scheme 2.8: Synthesis of [RuX(NO)(PPh₃)₃] (X = Cl, I; **9a**, **9b**).

Since this reaction is an equilibrium, it is essential to keep the reaction mixture below –50 °C to isolate **9a** and **9b**. Compound **9b** was obtained as red crystals in 80 % yield and characterized by elemental analysis, IR, ³¹P{¹H} NMR, ³¹P{¹H} NMR solid-state spectroscopy and mass spectrometry. The isolation of **9a** has proved to be more problematic due to its minor stability even at low temperatures. Thus, **9a** was characterized by IR- and mass-spectroscopy and no yield is given since either a mixture of **7a** and **9a** was isolated or the product was contaminated with triphenylphosphane. The addition of the triphenylphosphane ligand increases the electron density of the complexes and the nitrosyl-stretching frequency of **9a** and **b** is lowered about 100 cm⁻¹ (1630 and 1625 cm⁻¹) in comparison to their tetra-coordinated analogs **7a** and **c**. The mass spectrum of **9b** shows one peak for the fragment [M–I]⁺ at *m/z* = 919.8 and one peak for the fragment [M–PPh₃]⁺ at *m/z* = 782.6. Due to the instability of **9a**, its mass spectrum only shows the peak for the fragment [M–PPh₃]⁺ at *m/z* = 691.7. The ³¹P{¹H} NMR spectrum of **9c** in solution was measured at –80 °C and reveals one broad singlet at 48.71 ppm for the apical phosphane ligand and one broad singlet at 20.33 ppm for the basal phosphane ligands. Furthermore, two signals at 27.52 and –6.78 ppm can be detected which can be assigned to the oxidized species and free triphenylphosphane. The solid-state ³¹P{¹H} NMR spectrum reveals two duplets at 15.9 and 18.3 ppm for the basal phosphane ligands (P_{A/B}) and one singlet at 52.2 ppm for the apical phosphane (P_X). The ²J_{AB} scalar coupling is 267 Hz for the *trans* phosphanes. The expected *cis* P–Ru–P couplings ²J_{AX} and ²J_{BX} cannot be detected in the spectrum because their magnitudes are much smaller than the typical line widths encountered in solid-state NMR spectra (ω_{1/2} ~ 50-100 Hz).^[122]

Crystal structure of [RuCl(NO)(PPh₃)₃] (**9a**)

Deep red crystals of **9a** were obtained directly from the reaction solution by storing it over night at –60 °C. The structure of the **9a** is illustrated in FIGURE 2.7.

Results

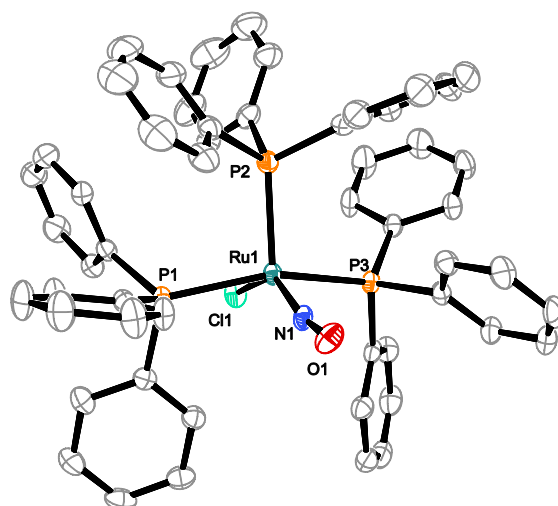


Figure 2.7: ORTEP plot of the complex $[\text{RuCl}(\text{NO})(\text{PPh}_3)_3]$ in crystals of $\mathbf{9a} \cdot 0.5 \text{ C}_7\text{H}_8$. Sp.Gr. $P\bar{1}$. The thermal ellipsoids are drawn at 50 % probability level at 173 K. Due to clarity, hydrogen atoms and solvent molecules are not depicted. Interatomic distances (\AA) and angles ($^\circ$), the standard deviation of the last decimal digit is given in parentheses: Ru–N 1.759(3), Ru–P1 2.4162(8), Ru–P2 2.3659(10), Ru–P3 2.3910(9), Ru1–Cl 2.4850(9), N1–O 1.181(4); O1–N1–Ru1 168.1(3), N1–Ru1–P1 94.84(10), N1–Ru1–P2 119.46(10), N1–Ru1–P3 89.57(9), P2–Ru1–P1 99.05(3), P2–Ru1–P3 97.83(3), P3–Ru1–P1 157.59(3) N1–Ru1–Cl 138.79(10), P1–Ru1–Cl 79.60(3), P2–Ru1–Cl 101.71(3), P3–Ru1–Cl 82.62(3).

The structure solution succeeded in the triclinic space group $P\bar{1}$. The primitive cell contains two complex molecules and one disordered toluene molecule, the asymmetric unit contains one complex molecule and half a toluene molecule. The structure is best described as a square pyramid ($\text{CShM}_{\text{SPV-5}}$ value 1.407) composed of a chloride, a nitrosyl and two *trans*-configured phosphane ligands in the plane and of a third phosphane ligand in the apical position. The apical Ru–P distance (2.37 \AA) is shorter than the basal Ru–P distances (2.42 and 2.39 \AA). The Ru–Cl bond (2.49 \AA) and the Ru–N distance (1.76 \AA) are elongated in comparison to the corresponding bonds (Ru–Cl 2.34 and Ru–N 1.71 \AA) in the square-planar $[\text{RuCl}(\text{NO})(\text{PPh}_3)_2]$ $\mathbf{7a}$.^[80] The Ru–N–O angle is decreased by 12° from linearity.

Crystal structure of $[\text{Ru}(\text{NO})(\text{PPh}_3)_3]$ ($\mathbf{9b}$)

Deep red crystals of $\mathbf{9b}$ were obtained directly from the reaction solution by storing it over night at -60°C . The structure of $\mathbf{9b}$ is illustrated in FIGURE 2.8.

Results

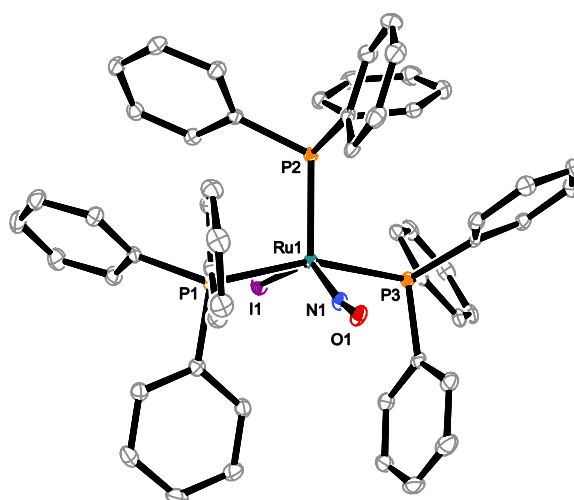


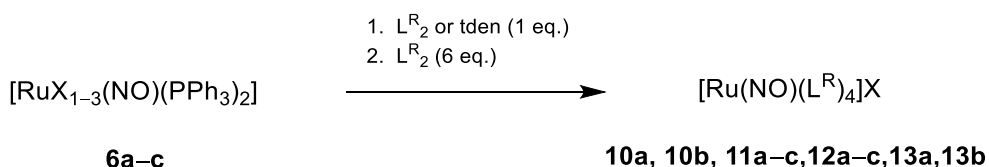
Figure 2.8: ORTEP plot of the complex $[\text{Ru}(\text{NO})(\text{PPh}_3)_3]$ in crystals of $\mathbf{9b} \cdot 2 \text{C}_7\text{H}_8$. Sp.Gr. $P\bar{1}$. The thermal ellipsoids are drawn at 50 % probability level at 173 K. Due to clarity, hydrogen atoms and solvent molecules are not depicted. Interatomic distances (\AA) and angles ($^\circ$), the standard deviation of the last decimal digit is given in parentheses: Ru1–N1 1.7898(19), Ru1–P1 2.4106(6), Ru1–P2 2.3152(6), Ru1–P3 2.4036(6), Ru1–I1 2.8119(2), N1–O1 1.145(2); O1–N1–Ru1 165.71(17), N1–Ru1–P1 83.12(6), N1–Ru1–P2 118.61(6), N1–Ru1–P3 86.86(6), P2–Ru1–P1 101.48(2), P2–Ru1–P3 97.83(3), P3–Ru1–P1 158.85(2), N1–Ru1–I1 139.99(6), P1–Ru1–I1 88.195(14), P2–Ru1–I1 101.388(15), P3–Ru1–I1 87.581(14).

The structure solution succeeded in the triclinic space group $P\bar{1}$. The primitive cell contains two complex molecules and four toluene molecules, the asymmetric unit contains one complex molecule and two toluene molecules. The structure of $\mathbf{9b}$ is isostructural to the structure of $\mathbf{9a}$, thus, the structure is a square pyramid ((CShM_{SPY-5} value 1.839) with the iodide, the nitrosyl and two *trans*-configured phosphane ligands in the plane and the third phosphane ligand in the apical position. The apical Ru–P distance (2.31 \AA) is even shorter than the apical Ru–P distance in $\mathbf{9a}$ (2.37 \AA). The basal Ru–P distances (2.41 and 2.40 \AA) can be considered equal to the corresponding bonds in $\mathbf{9a}$. The Ru–N distance (1.79 \AA) is even longer than the Ru–N distance in $\mathbf{9a}$ (1.76 \AA) and the Ru–N–O angle (165.71 $^\circ$) is smaller than the one in $\mathbf{9a}$.

2.7 Synthesis of the penta-coordinated $\{\text{RuNO}\}^8$ NHC compounds

$[\text{Ru}(\text{NO})(\text{L}^{\text{Me}})_4]\text{X}$ (X = Cl, Br; $\mathbf{10a}$, $\mathbf{10b}$), $[\text{Ru}(\text{NO})(\text{L}^{\text{Et}})_4]\text{X}$ (X = Cl, Br, I; $\mathbf{11a-c}$), $[\text{Ru}(\text{NO})(\text{L}^{\text{nPr}})_4]\text{X}$ (X = Cl, Br, I; $\mathbf{12a-c}$) and $[\text{Ru}(\text{NO})(\text{L}^{\text{Bn}})_4]\text{X}$ (X = Br, I; $\mathbf{13a}$, $\mathbf{13b}$) were synthesized according to a route by Lappert *et al.* by the reduction of the $\{\text{RuNO}\}^{6-8}$ compounds $[\text{RuX}_{1-3}(\text{NO})(\text{PPh}_3)_2]$ (X = Cl, Br, I; $\mathbf{6a-c}$) with tden or the corresponding enetetramine (L^{Me}_2 , L^{Et}_2 , L^{nPr}_2 , L^{Bn}_2 ($\mathbf{1a-d}$)) and subsequent ligand substitution by the addition of six equivalents of the corresponding enetetramine (SCHEME 2.9). $\mathbf{10a}$ is already known in literature but the crystal structure has not been identified yet.^[6]

Results



Scheme 2.9: Synthesis of $[\text{Ru}(\text{NO})(\text{L}^{\text{Me}})_4]\text{X}$ (X = Cl, Br, I; **10a-c**), $[\text{Ru}(\text{NO})(\text{L}^{\text{Et}})_4]\text{X}$ (X = Cl, Br, I; **11 a-c**), $[\text{Ru}(\text{NO})(\text{L}^{\text{nPr}})_4]\text{X}$ (X = Cl, Br, I; **12a-c**) and $[\text{Ru}(\text{NO})(\text{L}^{\text{Bn}})_4]\text{X}$ (X = Br, I; **13a, 13b**).

10a and **10b** were obtained as red crystals in 27 % and 35 % yield respectively. Attempts to synthesize $[\text{Ru}(\text{NO})(\text{L}^{\text{Me}})_4]\text{I}$ resulted in a brown oily product which could not be identified. In the case of the enetetramines **1b** and **c** (R = Et, *n*Pr) the six halogenido salts **11a-c** and **12a-c** were obtained in 15–50 % yield as deep red crystals. The reaction of L^{Bn}_2 **1d** with the $\{\text{RuNO}\}^{6-8}$ compounds **5b-c** resulted in an equilibrium between the penta-coordinated compounds **13a** and **13b** and the corresponding tetra-coordinated species of the $[\text{RuX}(\text{NO})(\text{L}^{\text{Bn}})_2]$ -type. **13a** and **13b** were isolated in 45 % and 71 % yield by cooling the reaction mixture to room temperature. The isolation of **13a** often resulted in a mixture of **7a** and **13a** since the equilibrium is far on the side of the tetra-coordinated complex **7a**. The compounds are moisture and oxygen-sensitive and were characterized by elemental analysis, IR, $^{13}\text{C}\{^1\text{H}\}$ NMR and ^1H NMR spectroscopy and mass spectrometry. The nitrosyl-stretching frequencies are shifted to exceptionally low values (1480–1490 cm^{-1}) due to the four strongly σ -donating NHC ligands, but an unambiguous assignment of the $\tilde{\nu}(\text{NO})$ is difficult because of the proximity to $\tilde{\nu}(\text{CN}_2)$ and $\delta(\text{C-H})$. The mass spectra of **10a** and **b** show one peak for the fragment $[\text{M}+\text{O}]^+$ at $m/z = 540.23$. due to moisture and oxygen sensitivity. The compounds **11a-c**, **12a-c**, **13a** and **13b** show one peak for the complex cation at $m/z = 636.9$, 764.8 and 1131.6 respectively. Since the anions do not have any influence on the NMR spectra of the complex cations the ^1H NMR and $^{13}\text{C}\{^1\text{H}\}$ NMR of **10a**, **11a**, **12a** and **13a** will be discussed as example. The ^1H NMR and the $^{13}\text{C}\{^1\text{H}\}$ NMR spectra of **10a** consist of two sharp singlets for the CH_3 group and the CH_2 groups of the ring. The NMR spectra get more complicated with increasing steric hindrance of the alkyl rest. Thus, the ^1H NMR spectra of **11a-13a** show only multiplets, whereby the signals for the CH_2 groups of the ring and the N-CH_2 are overlapping. The $^{13}\text{C}\{^1\text{H}\}$ NMR spectra for **11a** and **13a** show the expected singlets for the alkyl substituent of the NHCs, even though the CH_2 groups of the ring of **13a** give a doublet of signals. At room temperature, the signals of the $^{13}\text{C}\{^1\text{H}\}$ NMR spectrum of **12a** are broadened and no signal for the CH_2 groups of the ring or the N-CH_2 can be detected due to the rigid steric environment of the *n*-propyl substituent. In order to obtain a better resolution, the $^{13}\text{C}\{^1\text{H}\}$ NMR of **12a** was measured at 80 °C to ensure free rotation around the Ru-C bonds. The ^1H NMR and the $^{13}\text{C}\{^1\text{H}\}$ NMR data are summarized in TABLE 2.6 and 2.7.

Results

Table 2.6: ^1H NMR data for the complexes **10a**, **11a**, **12a** and **13a** in $\text{dms}\text{-}d_6$. Chemical shifts δ in ppm ^a Measured at 80 °C.

	$\text{N}-\underline{\text{CH}_2\text{CH}_2}-$	$\text{N}-\underline{\text{CH}_2}-$	$\text{N}-\underline{\text{CH}_2\text{CH}_2\text{CH}_3}$	$-\underline{\text{CH}_3}$	$-\text{Ph}$
$[\text{Ru}(\text{NO})(\text{L}^{\text{Me}})_4]^+$ (10a)	3.51 (s)			2.70 (s)	
$[\text{Ru}(\text{NO})(\text{L}^{\text{Et}})_4]^+$ (11a)	3.87–2.90 (m)	3.87–2.90 (m)		1.18–0.93(m)	
$[\text{Ru}(\text{NO})(\text{L}^{\text{nPr}})_4]^+$ (12a) ^a	3.90–2.88 (m)	3.90–2.88 (m)	1.74–1.34 (m)	0.89–0.80 (m)	
$[\text{Ru}(\text{NO})(\text{L}^{\text{Bn}})_4]^+$ (13a)	3.85–2.66 (m)	5.28–3.88 (m)			7.44–7.05 (m)

Table 2.7: $^{13}\text{C}\{^1\text{H}\}$ NMR data for the complex cations **10a**, **11a**, **12a** and **13a** in $\text{dms}\text{-}d_6$. Chemical shifts δ in ppm. ^a Measured at 80 °C.

	$\text{N}\underline{\text{C}}\text{N}$	$\text{N}-\underline{\text{CH}_2\text{CH}_2}-$	$\text{N}-\underline{\text{CH}_2}-$	$\text{N}-$	$-\underline{\text{CH}_3}$	$-\text{Ph}$
$[\text{Ru}(\text{NO})(\text{L}^{\text{Me}})_4]^+$ (10a)		51.22			37.54	
$[\text{Ru}(\text{NO})(\text{L}^{\text{Et}})_4]^+$ (11a)	218.30	47.06	43.50		13.05	
$[\text{Ru}(\text{NO})(\text{L}^{\text{nPr}})_4]^+$ (12a) ^a	219.26	51.61	47.53	20.38	10.76	
$[\text{Ru}(\text{NO})(\text{L}^{\text{Bn}})_4]^+$ (13a)	221.24	57.54, 55.01	50.39, 47.87			137.02, 129.23, 127.91, 126.70

Crystal structure of $[\text{Ru}(\text{NO})(\text{L}^{\text{Me}})_4]\text{Br}$ (**10b**)

Dark red crystals of compound **10b** were obtained directly from the reaction solution. The structure of **10b** is depicted in FIGURE 2.9.

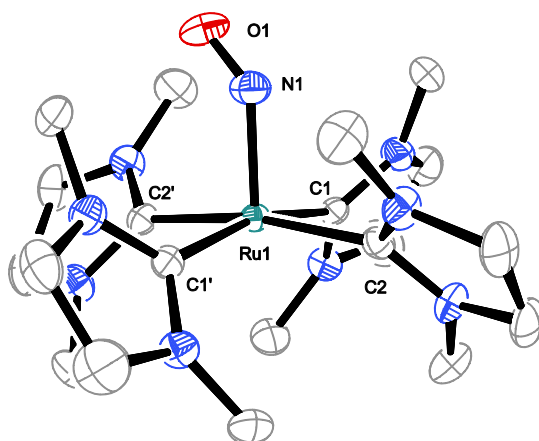


Figure 2.9: ORTEP plot of the cation $[\text{Ru}(\text{NO})(\text{L}^{\text{Me}})_4]^+$ in crystals of **10b** (disorder not depicted). Sp.Gr. $C2/c$. The thermal ellipsoids are drawn at 30 % probability level at 298 K. Due to clarity, hydrogen atoms are not depicted. Interatomic distances (\AA) and angles ($^\circ$), the standard deviation of the last decimal digit is given in parentheses: Ru1–N1 1.861(4), Ru1–C1 2.107(3), Ru1–C2 2.108(3), N1–O1 1.106(5); O1–N1–Ru1 137.1(3), N1–Ru1–C1 95.11(8), N1–Ru1–C2 96.91(8), C1–Ru1–C1' 169.77(16), C2'–Ru1–C2 166.18(16), C1–Ru1–C2 87.29(11), C1'–Ru1–C2 91.48(11).

The structure solution succeeded in the monoclinic space group $C2/c$. The primitive cell contains four complex molecules and the asymmetric unit contains half a complex molecule that is completed via a twofold rotation axis passing through the ruthenium center and the nitrogen atom of the nitrosyl

Results

group. The oxygen atom of the nitrosyl ligand is disordered over the same twofold rotation axis. The coordination sphere is best described as a vacant octahedron ($vOC-5$) ($CShM_{vOC-5}$ value 0.245) with the four NHC ligands in the plane and the nitrosyl ligand in the apical position. The Ru–N–O moiety is bent in such a manner that the oxygen points toward one of the NHC ligands (torsion angle C1'–Ru–N–O 2.6°). The Ru–N–O angle is small (137°) and the Ru–N distance (1.86 Å) is elongated in consequence of poor π back bonds from the ruthenium to the nitrosyl. The planar NHC ligands are coordinated in a propeller-like arrangement with torsion angles N1–Ru–C_{carb}–N_{carb} of 33° and 44°.

Crystal structure of $[Ru(NO)(L^{Et})_4]Cl$ (**11a**)

Dark red crystals of compound **11a** were obtained directly from the reaction solution. The structure of **11a** is depicted in FIGURE 2.10.

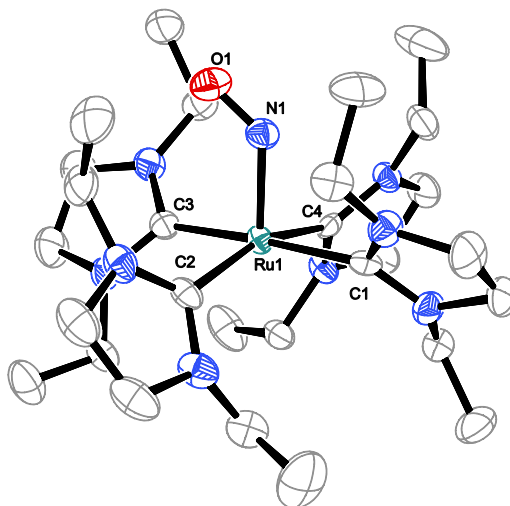


Figure 2.10: ORTEP plot of the cation $[Ru(NO)(L^{Et})_4]^+$ in crystals of **11a**. Sp.Gr.*Pbca*. The thermal ellipsoids are drawn at 50 % probability level at 173 K. Due to clarity, hydrogen atoms are not depicted. Interatomic distances (Å) and angles (°), the standard deviation of the last decimal digit is given in parentheses: Ru1–N1 1.881(3), Ru1–C1 2.164(4), Ru1–C2 2.096(4), Ru1–C3 2.080(4), Ru1–C4 2.100(4), N1–O1 1.207(4); O1–N1–Ru1 128.4(2), N1–Ru1–C1 88.12(13), N1–Ru1–C2 100.63(15), N1–Ru1–C3 95.32(13), N1–Ru1–C4 97.99(15) C1–Ru1–C3 176.43(14), C2–Ru1–C4 161.34(14), C1–Ru1–C2 90.11(15), C2–Ru1–C3 90.16(16), C3–Ru1–C4 89.17(15), C4–Ru1–C1 89.44(15).

The structure solution succeeded in the orthorhombic space group *Pbca*. The primitive cell contains eight complex molecules and the asymmetric unit contains one complex molecule. **10b** and **11a** are isostructural, thus, the coordination sphere of **11a** is a vacant octahedron ($vOC-5$) ($CShM_{vOC-5}$ value 0.581) with the four NHC ligands in the plane and the nitrosyl ligand in the apical position. In contrast to **10b** the Ru–N–O moiety of **11a** is bent in such a manner that the oxygen points between two of the NHC ligands (torsion angle C3–Ru–N–O 15.9°). The Ru–N–O angle is even smaller than in **10b** (128°) and the Ru–N distance (1.88 Å) is elongated as well. The planar NHC ligands are coordinated in a propeller-like arrangement with torsion angles N1–Ru–C_{carb}–N_{carb} between 30° and 39°.

Results

Crystal structure of $[Ru(NO)(L^{Bn})_4]Br$ (**13a**)

Dark red crystals of compound **13a** were obtained directly from the reaction solution. The structure of **13a** is depicted in FIGURE 2.11.

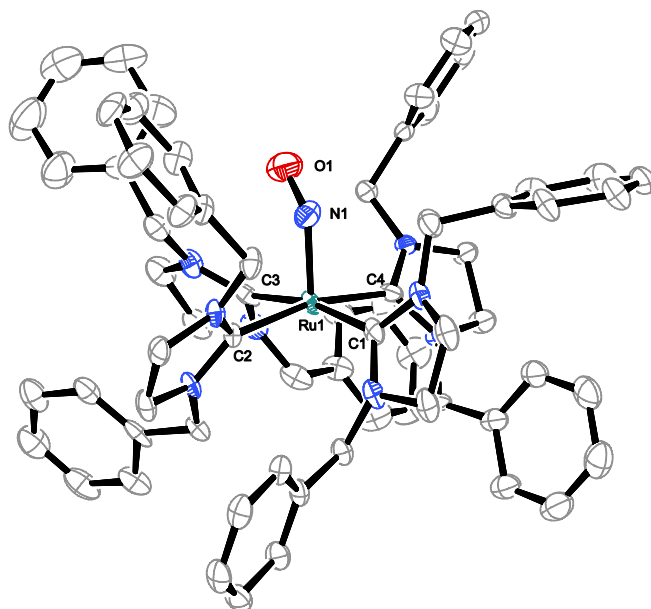


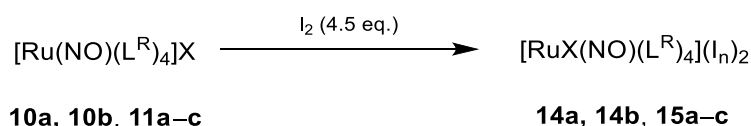
Figure 2.11: ORTEP plot of the cation $[Ru(NO)(L^{Bn})_4]^+$ in crystals of **13a** · $C_4H_{10}O$. Sp.Gr. $P2_1/c$. The thermal ellipsoids are drawn at 50 % probability level at 173 K. Due to clarity, hydrogen atoms and solvent molecules are not depicted. Interatomic distances (Å) and angles ($^\circ$), the standard deviation of the last decimal digit is given in parentheses: Ru1–N1 1.871(4), Ru1–C1 2.146(4), Ru1–C2 2.114(4), Ru1–C3 2.103(4), N1–O1 1.243(5); O1–N1–Ru1 130.8(3), N1–Ru1–C1 93.95(15), N1–Ru1–C2 96.12(16), N1–Ru1–C3 96.67(16), N1–Ru1–C4 96.29(15), C1–Ru1–C3 168.48(15), C2–Ru1–C4 167.34(14), C1–Ru1–C2 84.85(14), C2–Ru1–C3 89.59(14), C3–Ru1–C4 91.42(15), C4–Ru1–C1 91.84(15).

The structure solution succeeded in the monoclinic space group $P2_1/c$. The primitive cell contains four complex molecules and four diethyl ether molecules. The asymmetric unit contains one complex molecule and one diethyl ether molecule. The coordination sphere of **13a** is a vacant octahedron ($\nu OC-5$) ($CShM_{\nu OC-5}$ -value 0.260) with the four NHC ligands in the plane and the nitrosyl ligand in the apical position. The Ru–N–O moiety of **13a** is bent in such a manner that the oxygen points between two of the NHC ligands (torsion angle C3–Ru–N–O 12.6°). The value of the Ru–N–O angle (131°) is between the angle of **10b** and **11b** and the Ru–N distance (1.87 Å) is comparable. The planar NHC ligands are coordinated in a propeller-like arrangement with torsion angles N1–Ru– C_{carb} – N_{carb} between 27° and 43° .

2.8 Synthesis of the $\{RuNO\}^6$ NHC compounds

To study the reaction behavior of the $\{RuNO\}^8$ species (**10a**, **10b**, **11a–c**) toward oxidants they were oxidized with I_2 to obtain the $\{RuNO\}^6$ species $[RuX(NO)(L^{Me})_4](I_5)_2$ ($X = Cl, Br$; **14a**, **14b**), $[Ru(NO)(L^{Et})_4](I_3)_2$ ($X = Cl, Br$; **15a**, **15b**) and $[Ru(NO)(L^{Et})_4](I_5)(I_3)$ (**15c**) (SCHEME 2.10).

Results



Scheme 2.10: Synthesis of $[\text{RuX}(\text{NO})(\text{L}^{\text{Me}})_4](\text{I}_5)_2$ ($\text{X} = \text{Cl, Br}$; **14a, 14b**) and $[\text{Ru}(\text{NO})(\text{L}^{\text{Et}})_4](\text{I}_3)_2$ ($\text{X} = \text{Cl, Br, I}$; **15a, 15b**) and $[\text{RuI}(\text{NO})(\text{L}^{\text{Et}})_4](\text{I}_5)(\text{I}_3)$ (**15c**).

14a, 14b and **15a–c** were obtained as black crystals in 29–45 % yield. The compounds are thermally and air-stable and were characterized by elemental analysis, IR, $^{13}\text{C}\{^1\text{H}\}$ NMR and ^1H NMR spectroscopy and mass spectrometry. The nitrosyl-stretching frequencies $\tilde{\nu}(\text{NO})$ of **14a, 14b** and **15a–c** are decreasing with increasing *trans*-effect of the halogenido ligand, thus $\tilde{\nu}(\text{NO})$ of **14a** and **14b** is at 1840 and 1834 cm^{-1} and those for **15a–c** are at 1836, 1829 and 1828 cm^{-1} . The mass spectra of **14a, 14b** and **15b** show one peak for the fragment $[\text{M}]^+$ at $m/z = 559.4, 603.7$ and 715.8 respectively and the mass spectra of compounds **15a** and **15c** show one peak for the fragment $[\text{M}]^{2+}$ at $m/z = 336.0$ and 381.8 respectively. The ^1H NMR of **14a** and **14b** consist of one multiplet for the ring CH_2 groups and a doublet of singlets for the CH_3 groups. In accordance with the ^1H NMR spectra, complex **14a** and **14b** show a single C_{carb} signal but a doublet of signals for the ring CH_2 and the inequivalent CH_3 groups in the $^{13}\text{C}\{^1\text{H}\}$ NMR spectra. The ^1H NMR spectra get more complicated with increasing steric hindrance of the alkyl rest and increasing size of the halogenido ligand. Thus, the ^1H NMR spectra of **15a** and **15b** show a doublet of signals for the CH_2 groups of the ring and the protons of the ethyl groups. The ^1H NMR spectrum of **15c** shows a doublet of signals for the ring CH_2 groups and the two methyl groups and four duplet of quartets for the four inequivalent protons of the ethyl CH_2 groups. The ^1H NMR and the $^{13}\text{C}\{^1\text{H}\}$ NMR data are summarized in TABLE 2.8 and 2.9.

Table 2.8: ^1H NMR data for the complexes **14a, 14b** and **15a–c** in $\text{dms-}d_6$. Chemical shifts δ in ppm and coupling constant J in Hz.

	N- <u>CH₂CH₂</u> -N	N- <u>CH₂</u> -	- <u>CH₃</u>
$[\text{RuCl}(\text{NO})(\text{L}^{\text{Me}})_4](\text{I}_5)_2$ (14a)	3.87–3.68 (m)		3.08 (s), 2.96 (s)
$[\text{RuBr}(\text{NO})(\text{L}^{\text{Me}})_4](\text{I}_5)_2$ (14b)	3.90–3.68 (m)		3.09 (s), 2.96 (s)
$[\text{RuCl}(\text{NO})(\text{L}^{\text{Et}})_4](\text{I}_3)_2$ (15a)	4.01–3.82 (m),	3.26 (dq, $J = 14.3, 7.2$),	1.22 (t, $J = 7.0$)
	3.70–3.53 (m)	3.07 (dq, $J = 13.3, 6.52$)	1.10 (t, $J = 7.0$)
$[\text{RuBr}(\text{NO})(\text{L}^{\text{Et}})_4](\text{I}_3)_2$ (15b)	4.05–3.84 (m),	3.17–3.34 (m),	1.22 (t, $J = 7.1$)
	3.67–3.54 (m)	3.05 (dq, $J = 13.5, 6.7$)	1.13 (t, $J = 6.7$)
$[\text{RuI}(\text{NO})(\text{L}^{\text{Et}})_4](\text{I}_5)(\text{I}_3)$ (15c)	4.03–3.79 (m),	4.16 (dq, $J = 13.9, 7.0$),	1.22 (t, $J = 7.1$)
	3.74–3.49 (m)	3.29 (dq, $J = 15.0, 7.0$),	1.13 (t, $J = 6.7$)
		3.19 (dq, $J = 14.2, 7.1$),	
		3.01 (dq, $J = 13.4, 6.7$)	

Results

Table 2.9: $^{13}\text{C}\{^1\text{H}\}$ NMR data for the complexes **14a**, **14b** and **15a–c** in $\text{dms}\text{-}d_6$. Chemical shifts δ in ppm.

	$\text{N}\underline{\text{C}}\text{N}$	$\text{N}\text{--}\underline{\text{C}}\text{H}_2\text{--}\underline{\text{C}}\text{H}_2\text{--}\text{N}$	$\text{N}\text{--}\underline{\text{C}}\text{H}_2\text{--}$	$\text{--}\underline{\text{C}}\text{H}_3$
$[\text{RuCl}(\text{NO})(\text{L}^{\text{Me}})_4](\text{I}_5)_2$ (14a)	190.41	52.17, 51.53		37.95, 37.22
$[\text{RuBr}(\text{NO})(\text{L}^{\text{Me}})_4](\text{I}_5)_2$ (14b)	188.94	52.14, 51.38		37.95, 37.38
$[\text{RuCl}(\text{NO})(\text{L}^{\text{Et}})_4](\text{I}_3)_2$ (15a)	190.80	48.22, 47.38	44.93, 44.46	13.42, 13.18
$[\text{RuBr}(\text{NO})(\text{L}^{\text{Et}})_4](\text{I}_3)_2$ (15b)	189.46	48.24, 47.40	45.94, 44.48	13.50, 13.33
$[\text{RuI}(\text{NO})(\text{L}^{\text{Et}})_4](\text{I}_5)(\text{I}_3)$ (15c)	187.74	48.18, 47.80	47.41, 44.46	13.54, 13.33

Crystal structure of $[\text{RuCl}(\text{NO})(\text{L}^{\text{Me}})_4](\text{I}_5)_2$ (**14a**)

Black crystals of compound **14a** were obtained by covering dimethyl sulfoxide solutions of the raw product with a layer of ethanol. The structure of **14a** is depicted in FIGURE 2.12.

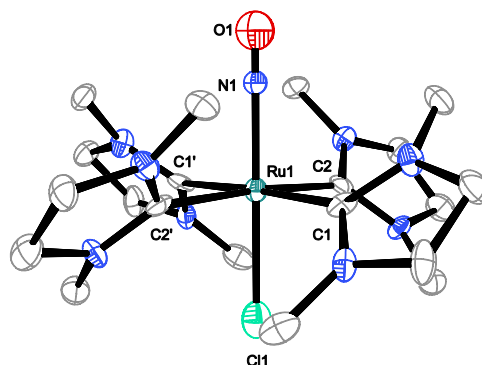


Figure 2.12: ORTEP plot of the cation $[\text{RuCl}(\text{NO})(\text{L}^{\text{Me}})_4]^{2+}$ in crystals of **14a**. Sp.Gr. $C2/c$. The thermal ellipsoids are drawn at 50 % probability level at 121 K. Due to clarity, hydrogen atoms are not depicted. Interatomic distances (\AA) and angles ($^\circ$), the standard deviation of the last decimal digit is given in parentheses: Ru1–N1 1.890(10), Ru1–Cl1 2.136(9), Ru1–C1 2.136(9), Ru1–C2 2.134(9), N1–O1 0.902(11); O1–N1–Ru1 180.0, N1–Ru1–Cl1 180.0, N1–Ru1–C1 91.3(2), N1–Ru1–C2 92.1(2), C1–Ru1–C1' 177.5(4), C1–Ru1–C2 89.6(3), C1–Ru1–C2' 90.3(3), C2–Ru1–C2' 175.7(4), Cl1–Ru1–C1 88.7(2), Cl1–Ru1–C2 89.6(3).

The structure solution succeeded in the monoclinic space group $C2/c$. The primitive cell contains four complex molecules. The asymmetric unit contains half a complex molecule that is completed via a twofold rotation axis passing through the chlorido ligand and the nitrosyl group. The coordination sphere of **14a** is an octahedron ($OC\text{-}6$) ($\text{CShM}_{OC\text{-}6}$ value 0.167) with the four NHC ligands in the plane and the nitrosyl ligand and the chlorido ligand *trans* to each other in the axial position. The nitrosyl ligand coordinates linearly to the ruthenium ($\text{Ru}\text{--}\text{N}\text{--}\text{O}$ angle 180°). The nitrosyl group and the chlorido ligand are disordered in such a manner as to superimpose themselves onto each other. The disorder cannot be resolved by refinement and decreases the N–O bond (0.9 \AA), thus, the distance is not significant. The planar NHC ligands are coordinated in a propeller-like arrangement with torsion angles $\text{N1}\text{--}\text{Ru}\text{--}\text{C}_{\text{carb}}\text{--}\text{N}_{\text{carb}}$ of 42° and 45° .

Results

Crystal structure of $[RuCl(NO)(L^{Et})_4](I_3)_2$ (**15a**)

Black crystals of compound **15a** were obtained by covering dimethylsulfoxide solutions of the raw product with a layer of ethanol. The structure of **15a** is depicted in FIGURE 2.13.

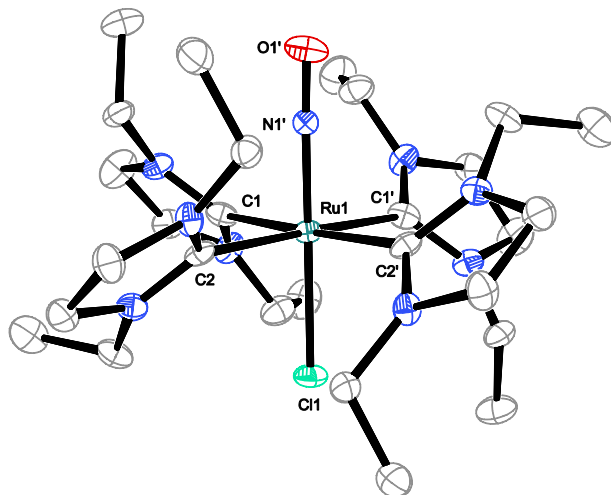


Figure 2.13: ORTEP plot of the cation $[RuCl(NO)(L^{Et})_4]^{2+}$ in crystals of **15a** (disorder not depicted). Sp.Gr. $C2/c$; complex symmetry C_2 . The thermal ellipsoids are drawn at 50 % probability level at 121 K. Due to clarity, hydrogen atoms are not depicted. Interatomic distances (Å) and angles ($^\circ$), the standard deviation of the last decimal digit is given in parentheses: Ru1–N1 1.735(8), Ru1–Cl1 2.330 (3), Ru1–C1 2.164(4), Ru1–C2 2.166(4), N1–O1 1.174(9); O1–N1–Ru1 175.7(15), N1–Ru1–Cl1 176.5(4), N1–Ru1–C1 91.7(5), N1–Ru1–C1' 91.00(5), N1–Ru1–C2 87.0(5), N1–Ru1–C2' 90.3(5), C1–Ru1–C1' 88.5(2), C1–Ru1–C2 90.13(16), C1–Ru1–C2' 177.61(15), C2–Ru1–C2' 91.3(2), Cl1–Ru1–C1 91.74(14), Cl1–Ru1–C1' 90.48(14), Cl1–Ru1–C2 87.58(14), Cl1–Ru1–C2' 90.25(13).

The structure solution succeeded in the monoclinic space group $C2/c$. The primitive cell contains four complex molecules. The asymmetric unit contains half a cation molecule and $2\frac{2}{3} I_3^-$ molecules, hereby the first anion is completed by a twofold rotation axis and the second one by an inversion center. The cation is completed via a twofold rotation axis that is the bisecting line of the C1–Ru1–C1' angle. The cation is isostructural to the cation of **14a** and is therefore adopting octahedral symmetry ($OC-6$) ($CShM_{OC-6}$ value 0.611) with a propeller-like arrangement the four NHC ligands in the plane (N1–Ru– C_{carb} – N_{carb} 40° and 45°) and the nitrosyl ligand and the chlorido ligand *trans* to each other in the axial position. The Ru–N–O angle (176°) almost displays linearity and the nitrosyl group and the chlorido ligand are rotational disordered in such a manner as to superimpose themselves onto each other.

Crystal structure of $[RuBr(NO)(L^{Et})_4](I_3)_2$ (**15b**)

Black crystals of compound **15b** were obtained by covering dimethyl sulfoxide solutions of the raw product with a layer of ethanol. The structure of **15b** is depicted in FIGURE 2.14.

Results

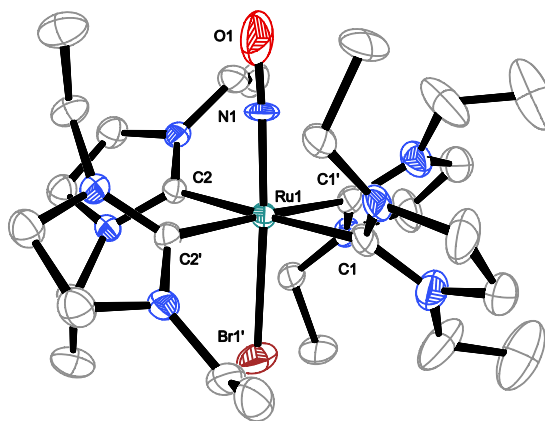


Figure 2.14: ORTEP plot of the cation $[\text{RuBr}(\text{NO})(\text{L}^{\text{Et}})_4]^{2+}$ in crystals of **15a** (disorder not depicted). Sp.Gr. $C2/c$. The thermal ellipsoids are drawn at 50 % probability level at 293 K. Due to clarity, hydrogen atoms are not depicted. Interatomic distances (Å) and angles ($^\circ$), the standard deviation of the last decimal digit is given in parentheses: Ru1–N1 1.725(13), Ru1–Br1 2.465(3), Ru1–C1 2.167(6), Ru1–C2 2.174, N1–O1 1.20(2); O1–N1–Ru1 176.7(18), N1–Ru1–Br1 176.1(4), N1–Ru1–C1 91.7(5), N1–Ru1–C1' 93.1(4), N1–Ru1–C2 89.7(5), N1–Ru1–C2' 85.6(4), C1–Ru1–C1' 89.4(3), C1–Ru1–C2 178.4(2), C1–Ru1–C2' 89.7(2), C2–Ru1–C2' 91.2(3), Br1–Ru1–C1 89.75(19), Br1–Ru1–C1' 90.51(18), Br1–Ru1–C2 88.94(18), Br1–Ru1–C2' 90.79(16).

The structure of **15b** is isomorph to **15a**. Thus, structure solution succeeded in the monoclinic space group $C2/c$ and the primitive cell contains four complex molecules. The asymmetric unit contains half a cation molecule and $2 \frac{2}{3} \text{I}_3^-$ molecules. The structure of **15b** is completed via the same symmetry operations as the structure of **15a**. The coordination sphere is of octahedral symmetry ($OC-6$) (CShM_{OC-6} value 0.786) with a propeller-like arrangement of the four NHC ligands in the plane (N1–Ru– C_{carb} – N_{carb} 40° and 45°) and the nitrosyl ligand and the bromido ligand *trans* to each other in the axial position. The Ru–N–O angle (177°) almost displays linearity and the nitrosyl group and the bromido ligand are rotational disordered in such a manner as to superimpose themselves onto each other.

*Crystal structure of $[\text{Ru}(\text{NO})(\text{L}^{\text{Et}})_4](\text{I}_5)(\text{I}_3)$ (**15c**)*

Black crystals of compound **15c** were obtained by covering dimethyl sulfoxide solutions of the raw product with a layer of ethanol. The structure of **15c** is depicted in FIGURE 2.15.

Results

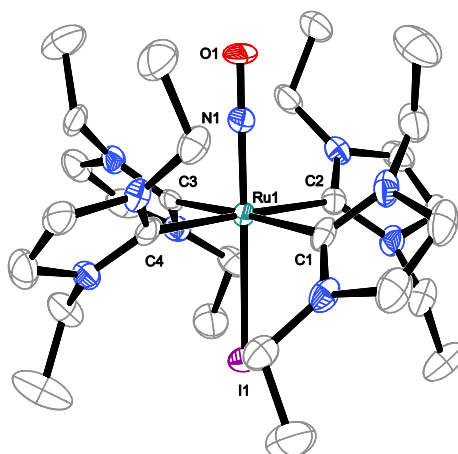


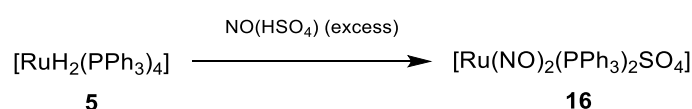
Figure 2.15: ORTEP plot of the cation $[\text{Ru}(\text{NO})(\text{L}^{\text{Et}})_4]^{2+}$ in crystals of **15c**· I_2 . Sp.Gr. $P2_1/c$. The thermal ellipsoids are drawn at 50 % probability level at 121 K. Due to clarity, hydrogen atoms and the I_2 molecule are not depicted. Interatomic distances (Å) and angles ($^\circ$), the standard deviation of the last decimal digit is given in parentheses: Ru1–N1 1.727(7), Ru1–I1 2.740(10), Ru1–C1 2.167(4), Ru1–C2 2.171(4), Ru1–C3 2.180(4), Ru1–C4 2.177(4), N1–O1 1.19(3); O1–N1–Ru1 179.6(12), N1–Ru1–I1 177.99(16), N1–Ru1–C1 91.8(2), N1–Ru1–C2 90.87(19), N1–Ru1–C3 90.24(19), N1–Ru1–C4 89.95(19), N1–Ru1–C2', C1–Ru1–C2 89.04(16), C1–Ru1–C4 89.20(16), C2–Ru1–C3 91.34(15), C3–Ru1–C4 90.39(15), C1–Ru1–C3 177.95(16), C2–Ru1–C4 178.08(15), I1–Ru1–C1 90.22(12), I1–Ru1–C2 88.90(11), I1–Ru1–C3 87.77(11), I1–Ru1–C4 90.35(11).

The structure solution succeeded in the monoclinic space group $P2_1/c$. The primitive cell contains four complex molecules. The asymmetric unit contains one complex molecule and a half I_2 molecule that is completed by an inversion center. The cation is isostructural to the cations of **14a** and **15b** thus, it adopts octahedral symmetry ($OC-6$) (CSHM $_{OC-6}$ value 1.193) with a propeller-like arrangement of the four NHC ligands in the plane (N1–Ru–C $_{carb}$ –N $_{carb}$ about 42°) and the nitrosyl ligand and the iodido ligand *trans* to each other in the axial position. The Ru–N–O angle (180°) displays linearity, and the nitrosyl group and the iodido ligand are disordered in such a manner as to superimpose themselves onto each other.

2.9 Synthesis of the $\{\text{Ru}(\text{NO})_2\}^8$ phosphane compounds

2.9.1 Synthesis of $[\text{Ru}(\text{NO})_2(\text{PPh}_3)_2\text{SO}_4]$ (**16**)

$[\text{Ru}(\text{NO})_2(\text{PPh}_3)_2\text{SO}_4]$ (**16**) was synthesized by adding $\text{NO}(\text{HSO}_4)$ (**2**) to a solution of **5** in hot ethanol until a color change from yellow to black occurred. Thereby two NO ligands and a bidentate sulfate ligand bind to the metal center and two phosphane ligands and the two hydrido ligands leave the complex (SCHEME 2.11).



Scheme 2.11: Synthesis of $[\text{Ru}(\text{NO})_2(\text{PPh}_3)_2\text{SO}_4]$ (**16**).

16 precipitated from the reaction solution as black crystalline powder in 77 % yield. The compound was characterized by elemental analysis, IR and $^{31}\text{P}\{^1\text{H}\}$ NMR spectroscopy and mass spectrometry. The infrared spectrum of **16** shows two bands in the region for coordinated nitrogen monoxide at 1814

Results

and 1614 cm^{-1} . Since both NO ligands are coordinated to the same metal center the $\tilde{\nu}(\text{NO})$ vibrations are coupled in a symmetrical ($\tilde{\nu}(\text{NO})_{\text{sym}}$) and an asymmetrical mode ($\tilde{\nu}(\text{NO})_{\text{asym}}$). Thus, the infrared bands at 1814 and 1614 cm^{-1} are assignable to $\tilde{\nu}(\text{NO})_{\text{sym}}$ and $\tilde{\nu}(\text{NO})_{\text{asym}}$, respectively. The mass spectrum of **16** shows one peak for the complex fragment $[M]^+$ at $m/z = 783.0$ and one peak for the fragment $[M - 2\text{NO}]^+$ at $m/z = 721.2$. The $^{31}\text{P}\{^1\text{H}\}$ NMR spectrum of **16** shows four signals at 31.0, 30.5, 23.0 and 19.8 ppm. The additional signals can be assigned to the penta-coordinated isomer of **16** that results from the dissociation of one oxygen atom of the sulfate ligand from the Ru center in polar solvents. The solution behavior of **16** and its corresponding penta-coordinated isomer will be further discussed in Chapter 2.14 and Chapter 3.2.2.

Crystal structure of $[\text{Ru}(\text{NO})_2(\text{PPh}_3)_2\text{SO}_4]$ (**16**)

Black crystals of **16** were obtained directly from the reaction mixture. The structure of the complex is illustrated in FIGURE 2.16.

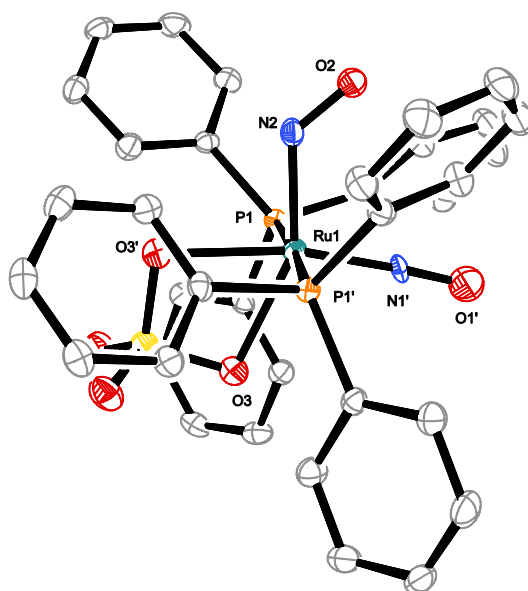


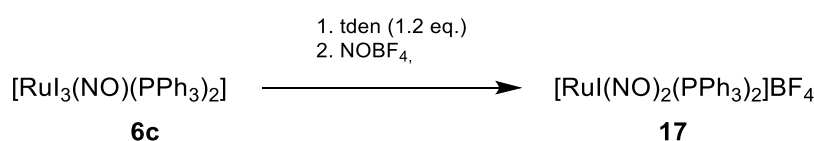
Figure 2.16: ORTEP plot of the complex $[\text{Ru}(\text{NO})_2(\text{PPh}_3)_2\text{SO}_4]$ in crystals of **16** (disorder not depicted). Sp.Gr $Pbcn$. The thermal ellipsoids are drawn at 50 % probability level at 173 K. Due to clarity, hydrogen atoms are not depicted. Interatomic distances (\AA) and angles ($^\circ$), the standard deviation of the last decimal digit is given in parentheses: Ru1–N1' 1.743(7), Ru–N2 1.918(8), Ru–O3 2.2126(16), Ru1–P1 2.4725(6), N1'–O1' 1.138(10), N2–O2 1.233(10); O1'–N1'–Ru1 176.8(6), O2–N2–Ru1 128.5(5), N1'–Ru1–N2 102.7(3), N1'–Ru1–O3 104.94(19), N1'–Ru1–O3' 168.37(19), N2–Ru1–O3 152.35(18), N2–Ru1–O3' 88.91(18), O3–Ru1–O3' 63.44(9), N1'–Ru1–P1 90.7(2), N1'–Ru1–P1' 91.8(2), N2–Ru1–P1 91.2(2), N2–Ru1–P1' 90.6(2), O3–Ru1–P1 88.35(5), O3–Ru1–P1' 88.72(5), P1–Ru1–P1' 176.56(3).

The structure solution succeeded in the orthorhombic space group $Pbcn$. The primitive cell contains four complex molecules, the asymmetric unit contains half a complex molecule that is completed by a twofold rotation axis that passes through the ruthenium center and the sulfur atom. The complex molecule adopts distorted octahedral symmetry ($OC-6$) (CShM_{OC-6} value 2.52) with the bidentate sulfate ligand and the two NO groups in the plane and the *trans*-arranged phosphane ligands in the axial positions. The two nitrosyl ligands are rotationally disordered and are unequal in their binding

situations: The Ru–N bond length differ by 0.175 Å and the Ru–N1–O1 moiety is almost linear while the Ru–N2–O2 fragment is bent (O–N–Ru 140°), thus, O2 points toward O1.

2.9.2 Synthesis of $[\text{Ru}(\text{NO})_2(\text{PPh}_3)_2]\text{BF}_4$ (**17**)

$[\text{Ru}(\text{NO})_2(\text{PPh}_3)_2]\text{BF}_4$ (**17**) was synthesized by an oxidative addition reaction of the nitrosonium cation of $\text{NO}(\text{BF}_4)$ to the *in-situ*-generated $[\text{Ru}(\text{NO})(\text{PPh}_3)_2]$ (**6c**) following a modified route by Klüfers *et al.* (SCHEME 2.12).^[34] Therefore, $[\text{Ru}(\text{NO})(\text{PPh}_3)_2]$ (**6c**) was generated by reduction of **5c** with tden in toluene and after the removal of the precipitated carbocation salt ($[\text{tden}]\text{2I}$), solid $\text{NO}(\text{BF}_4)$ was added until a color change from green to brown occurred.



Scheme 2.12: Synthesis of $[\text{Ru}(\text{NO})_2(\text{PPh}_3)_2]\text{BF}_4$ (**17**).

17 was obtained as brown crystalline powder in 34 % yield. The compound is air-resistant and was characterized by elemental analysis, IR and $^{31}\text{P}\{^1\text{H}\}$ NMR and mass spectrometry. The infrared bands in the spectrum of **17** at 1817 and 1771 cm^{-1} are assignable to $\tilde{\nu}(\text{NO})_{\text{sym}}$ and $\tilde{\nu}(\text{NO})_{\text{asym}}$ respectively. The mass spectrum of **17** shows one peak for the complex cation $[\text{M}]^+$ at $m/z = 813.3$ and one peak for the fragment $[\text{M} - \text{NO}]^+$ at $m/z = 783.2$. The $^{31}\text{P}\{^1\text{H}\}$ NMR spectrum of **17** shows one signal for the chemically equivalent phosphor atoms at 17.13 ppm.

*Crystal structure of $[\text{Ru}(\text{NO})_2(\text{PPh}_3)_2]\text{BF}_4$ (**17**)*

Dark brown crystals of **17** were obtained by covering a dichloromethane solution with a layer of diethyl ether overnight. The structure of the cation is illustrated in FIGURE 2.17.

Results

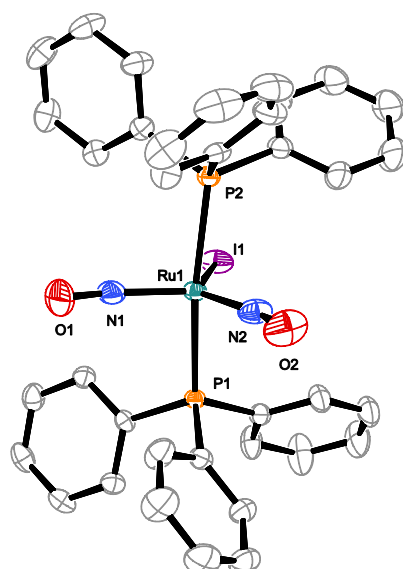
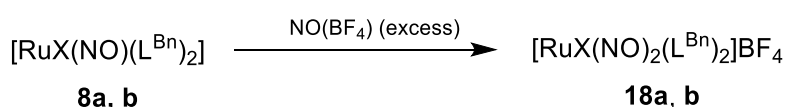


Figure 2.17: ORTEP plot of the cation $[\text{Ru}(\text{NO})_2(\text{PPh}_3)_2]^+$ in crystals of **17** · CH_2Cl_2 . Sp.Gr $Pbca$. The thermal ellipsoids are drawn at 50 % probability level at 173 K. Due to clarity, hydrogen atoms, solvent molecules and the anion are not depicted. Interatomic distances (Å) and angles ($^\circ$), the standard deviation of the last decimal digit is given in parentheses: Ru1–N1 1.782(4), Ru–N2 1.789(4), Ru1–P1 2.4289(9), Ru1–P2 2.4343(10), Ru1–I1 2.7326(4), N1–O1 1.147(5), N2–O2 1.145(5); O1–N1–Ru1 168.9(4), O2–N2–Ru1 167.2(4), N1Ru1–N2 119.72(19), N1–Ru1–P1 93.73(12), N2–Ru1–P1 90.35(12), N1–Ru1–P2 95.10(12), N2–Ru1–P2 91.51(12), P1–Ru1–P2 168.61(3), N1–Ru1–I1 114.01(13), N2–Ru1–I1 126.26(13), P1–Ru1–I1 84.80(2), P2–Ru1–I1 85.04(2).

The structure solution succeeded in the orthorhombic space group $Pbca$. The primitive cell contains eight complex molecules and eight dichloromethane molecules, the asymmetric unit contains one complex molecule and one dichloromethane molecule. The structure is best described as a trigonal bipyramid ($\text{CShM}_{\text{TBPY-5}}$ value 2.197). The two *trans*-coordinating phosphane ligands represent the apices of the bipyramid and the iodido ligand and the two nitrosyl ligands form the trigonal plane. The P–Ru–P angle deviates from 180° since the two phosphane ligands point away from the nitrosyl ligands. The binding situation of the two nitrosyl ligands can be assumed as equal: the Ru–N bonds only differ by 0.007 \AA and both NO groups are slightly bent (O–N–Ru $167\text{--}168^\circ$) whereupon the two oxygen atoms point toward each other. The coordination sphere and the bonding mode of the two nitrosyl ligands are in conformity with one of the two structure types of halogenido-bis(phosphane) $\{\text{Ru}(\text{NO})_2\}^8$ compounds mentioned by Klüfers *et al.*^[34]

2.10 Synthesis of the $\{\text{Ru}(\text{NO})_2\}^8$ NHC compounds

$[\text{RuX}(\text{NO})_2(\text{L}^{\text{Bn}})_2]\text{BF}_4$ (X = Cl, Br; **18a**, **18b**) were synthesized by an oxidative addition reaction of the nitrosonium cation of $\text{NO}(\text{BF}_4)$ to $[\text{RuX}(\text{NO})(\text{L}^{\text{Bn}})_2]$ (**7a**, **7b**) (SCHEME 2.13). Therefore, solid $\text{NO}(\text{BF}_4)$ was added to a solution of **7a** or **b** in dichloromethane until a color change from blue to orange occurred.



Scheme 2.13: Synthesis of $[\text{RuX}(\text{NO})_2(\text{L}^{\text{Bn}})_2]\text{BF}_4$ (X = Cl, Br; **18a**, **18b**).

Results

18a and **b** were obtained as orange powders in 60 % and 56 % yield. The compounds were characterized by elemental analysis, IR, $^{13}\text{C}\{^1\text{H}\}$ NMR and ^1H NMR spectroscopy and mass spectrometry. The infrared spectra show two bands at 1847 and 1672 and at 1836 and 1684 cm^{-1} respectively. The $\tilde{\nu}(\text{NO})$ with higher wavenumbers are assignable to $\tilde{\nu}(\text{NO})_{\text{sym}}$ and the ones with lower wavenumbers to $\tilde{\nu}(\text{NO})_{\text{asym}}$. The mass spectra of **18a** and **b** show one peak for the complex cation $[M]^+$ at $m/z = 697.6$ and 743.4 and one peak for the molecule fragment $[M - \text{NO}]^+$ at $m/z = 667.6$ and 713.4 . ^1H NMR spectra of **18a** and **b** show three multiplets, one for the aromatic H atoms of the phenyl group and two for the CH_2 groups, since the signals for the CH_2 groups of the ring and the $\text{N}-\text{CH}_2$ are overlapping. The $^{13}\text{C}\{^1\text{H}\}$ NMR spectra show one strong singlet for the NCN carbon atom at 190 ppm and a multiplet for the phenyl groups in the aromatic range. The CH_2 groups give two signals for **18a** and four signals for **18b**. The ^1H NMR and the $^{13}\text{C}\{^1\text{H}\}$ NMR data are summarized in TABLE 2.10 and 2.11.

Table 2.10: ^1H NMR data for the complexes **18a** in $\text{dms}\text{-}d_6$ and for **18b** in CD_2Cl_2 . Chemical shifts δ in ppm.

	$\text{N}-\underline{\text{CH}_2}\underline{\text{CH}_2}-\text{N}$	$\text{N}-\underline{\text{CH}_2}-$	$-\text{Ph}$
$[\text{RuCl}(\text{NO})_2(\text{L}^{\text{Bn}})_4]^+$ (18a)	5.75–3.14 (m)	5.75–3.14 (m)	7.71–7.13 (m)
$[\text{RuBr}(\text{NO})_2(\text{L}^{\text{Bn}})_4]^+$ (18b)	5.36–3.71(m)	5.36–3.71(m)	7.70–7.01 (m)

Table 2.11: $^{13}\text{C}\{^1\text{H}\}$ NMR data for the complexes **18a** in $\text{dms}\text{-}d_6$ and for **18b** in CD_2Cl_2 . Chemical shifts δ in ppm.

	$\text{N}\underline{\text{C}}\text{N}$	$\text{N}-\underline{\text{C}}\underline{\text{H}_2}\underline{\text{C}}\underline{\text{H}_2}-\text{N}$	$\text{N}-\underline{\text{C}}\underline{\text{H}_2}-$	$-\text{Ph}$
$[\text{RuCl}(\text{NO})_2(\text{L}^{\text{Bn}})_4]^+$ (18a)	190.34	53.46	49.50	134.78–126.76
$[\text{RuBr}(\text{NO})_2(\text{L}^{\text{Bn}})_4]^+$ (18b)	190.78	55.46, 52.91	50.27, 48.49	128.88–127.05

Crystal structure of $[\text{RuCl}(\text{NO})_2(\text{L}^{\text{Bn}})_2]\text{BF}_4$ (**18a**)

Orange crystals of **18a** were obtained by covering a dichloromethane solution with a layer of diethyl ether overnight. The structure of the cation is illustrated in FIGURE 2.18.

Results

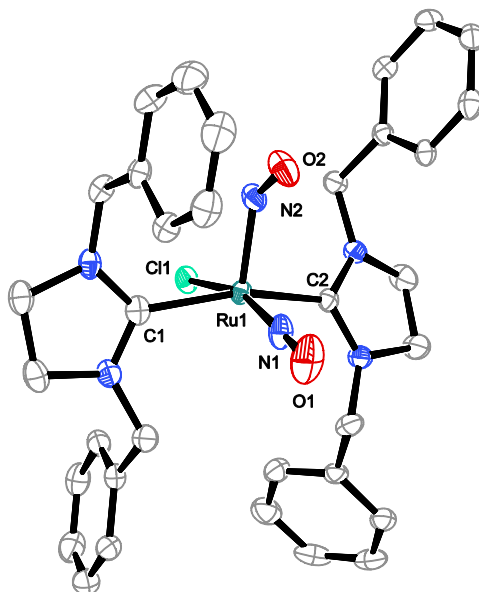


Figure 2.18: ORTEP plot of the cation $[\text{RuCl}(\text{NO})_2(\text{L}^{\text{Bn}})_2]^+$ in crystals of **18a** · CH_2Cl_2 . Sp.Gr. $P\bar{1}$. The thermal ellipsoids are drawn at 50 % probability level at 173 K. Due to clarity, hydrogen atoms, solvent molecules and the anion are not depicted. Interatomic distances (Å) and angles (°), the standard deviation of the last decimal digit is given in parentheses: Ru1–N1 1.750(3), Ru–N2 1.887(3), Ru1–C1 2.134(3), Ru1–C2 2.121(3), Ru1–Cl1 2.3700(8), N1–O1 1.143(4), N2–O2 1.157(4); O1–N1–Ru1 179.3(3), O2–N2–Ru1 132.2(3), N1Ru1–Cl1 161.09(10), N2Ru1–Cl1 99.48(10), N1Ru1–N2 99.42(14), N1–Ru1–C1 92.27(12), N1–Ru1–C2 94.67(12), N2–Ru1–C1 101.16(12), N2–Ru1–C2 95.53(11), C1–Ru1–Cl1 84.66(8), C2–Ru1–Cl1 82.91(8), C1–Ru1–C2 160.62(11).

The structure solution succeeded in the triclinic space group $P\bar{1}$. The primitive cell contains two complex molecules and two dichloromethane molecules, the asymmetric unit contains one complex molecule. The structure is best described as a vacant octahedron (vOC-5) ($\text{CShM}_{\text{vOC-5}}$ –value 0.951) with the chlorido ligand, one nitrosyl group and the *trans*-arranged NHC ligands in the plane and the second nitrosyl ligand in the apical position. The two nitrosyl ligands differ remarkably in their binding situation: The Ru–N–O angle of the NO ligand in the plane is linear while the apical NO group is bent in such a manner that the oxygen atom points toward the other nitrosyl ligand. The Ru–N bond of the linear Ru–N–O moiety is 0.137 Å shorter than the one of the apical nitrosyl ligand. The coordination sphere and the bonding mode of the two nitrosyl ligands are in conformity with the second structure type of halogenido-bis(phosphane) $\{\text{Ru}(\text{NO})_2\}^8$ compounds mentioned by Klüfers *et al.*^[34]

Crystal structure of $[\text{RuBr}(\text{NO})_2(\text{L}^{\text{Bn}})_2]\text{BF}_4$ (**18b**)

Orange crystals of **18b** were obtained by covering a dichloromethane solution with a layer of diethyl ether overnight. The structure of the cation is illustrated in FIGURE 2.19.

Results

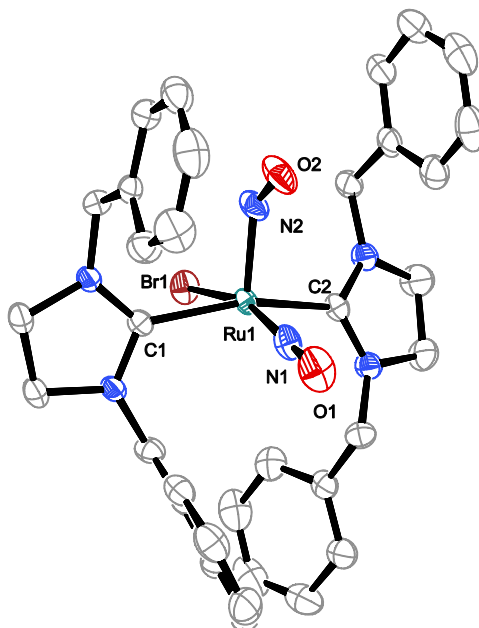


Figure 2.19: ORTEP plot of the cation $[\text{RuBr}(\text{NO})_2(\text{L}^{\text{Bn}})_2]^+$ in crystals of **18b** · CH_2Cl_2 . Sp.Gr $C2/c$. The thermal ellipsoids are drawn at 50 % probability level at 173 K. Due to clarity, hydrogen atoms and the anion are not depicted. Interatomic distances (Å) and angles ($^\circ$), the standard deviation of the last decimal digit is given in parentheses: Ru1–N1 1.7519(19), Ru–N2 1.869(2), Ru1–C1 2.131(2), Ru1–C2 2.147(2), Ru1–Br1 2.5178(3), N1–O1 1.154(3), N2–O2 1.166(3); O1–N1–Ru1 178.6(2), O2–N2–Ru1 133.1(2), N1Ru1–Br1 160.92(7), N2Ru1–Br1 99.60(7), N1Ru1–N2 99.45(10), N1–Ru1–C1 93.50(8), N1–Ru1–C2 93.87(8), N2–Ru1–C1 99.42(8), N2–Ru1–C2 97.97(8), C1–Ru1–Br1 82.36(6), C2–Ru1–Br1 84.52(6), C1–Ru1–C2 159.71(8).

The structure solution succeeded in the monoclinic space group $C2/c$. The primitive cell contains eight complex molecules and the asymmetric unit contains one complex molecule. **18b** is isostructural to **18a**. Thus, the structure is best described as a vacant octahedron (vOC-5) ($\text{CShM}_{\text{vOC-5}}$ -value 1.125) with the bromido ligand, one nitrosyl group and the *trans*-arranged NHC ligands in the plane and the second nitrosyl ligand in the apical position. As in **18a** the Ru–N–O angle of the NO ligand in the plane is linear while the apical NO group is bent and the Ru–N bond of the linear Ru–N–O moiety is shorter than the one of the apical nitrosyl ligand.

2.11 Synthesis of the $\{\text{Ru}(\text{NO})_2\}^{10}$ compounds

2.11.1 Synthesis of $[\text{Ru}(\text{NO})_2(\text{PPh}_3)_2]$ (**19**)

$[\text{Ru}(\text{NO})_2(\text{PPh}_3)_2]$ (**19**) was synthesized by the addition of diazald (*N*-methyl-*N*-nitroso-*p*-toluenesulfonamide) to a solution of **5** in ethanol according to Gaughan *et al.*^[123]



Scheme 2.14: Synthesis of $[\text{Ru}(\text{NO})_2(\text{PPh}_3)_2]$ (**19**).

19 was obtained as red crystalline powder in 46 % yield. The compound is thermally and air-stable and was characterized by elemental analysis, IR and $^{31}\text{P}\{^1\text{H}\}$ NMR spectroscopy. The infrared bands in the

Results

spectrum of **19** at 1652 and 1605 cm^{-1} are assignable to $\tilde{\nu}(\text{NO})_{\text{sym}}$ and $\tilde{\nu}(\text{NO})_{\text{asym}}$ respectively. The $^{31}\text{P}\{^1\text{H}\}$ NMR spectrum of **19** shows one signal for the chemically equivalent phosphorus atoms at 55.81 ppm.

Crystal structure of $[\text{Ru}(\text{NO})_2(\text{PPh}_3)_2]$ (**19**)

Orange crystals of **19** were obtained by covering a dichloromethane solution with a layer of diethyl ether overnight. The structure of the complex is illustrated in FIGURE 2.20.

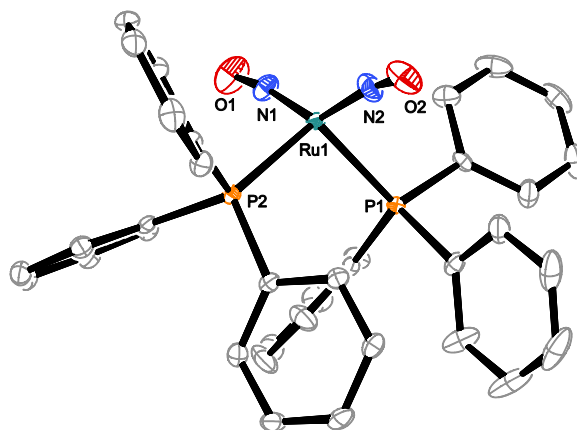


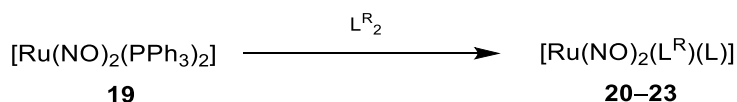
Figure 2.20: ORTEP plot of the complex $[\text{Ru}(\text{NO})_2(\text{PPh}_3)_2]$ in crystals of **19**. Sp.Gr. $P2_1/n$. The thermal ellipsoids are drawn at 50 % probability level at 173 K. Due to clarity, hydrogen atoms are not depicted. Interatomic distances (\AA) and angles ($^\circ$), the standard deviation of the last decimal digit is given in parentheses: Ru1–N1 1.7911(19), Ru–N2 1.824(2), Ru1–P1 2.3439(5), Ru1–P2 2.3389(5), N1–O1 1.182(2), N2–O2 1.160(3); O1–N1–Ru1 171.87(19), O2–N2–Ru1 169.10(18), N1–Ru1–N2 141.33(9), N1–Ru1–P1 102.71(6), N1–Ru1–P2 106.46(6), N2–Ru1–P1 102.35(6), N2–Ru1–P2 94.80(6), P1–Ru1–P2 105.083(19).

The structure solution succeeded in the monoclinic space group $P2_1/n$. The primitive cell contains four complex molecules and the asymmetric unit contains one complex molecule. The ruthenium center is coordinated by two nitrosyl ligands and two triphenylphosphane ligands. The coordination of the ruthenium center is irregular and is best described as distorted tetrahedral (CShM $_{T-4}$ value 2.073). The N–Ru–P angles range from 95° to 102° , the N–Ru–N angle is 141° and the P–Ru–P angle is 105° . The two nitrosyl ligands bind almost linearly to the ruthenium center (Ru–N–O angles: 171° and 169°) and the Ru–N bonds differ by 0.02 \AA . The two nitrosyls slightly point away from each other. The short Ru–N bond lengths indicate a high degree of back donation from the metal center to the π^* orbitals of the nitrosyls.

2.11.2 Synthesis of the $\{\text{Ru}(\text{NO})_2\}^{10}$ NHC compounds

$[\text{Ru}(\text{NO})_2(\text{L}^R)_2]$ (R = Me, Et, Bn; **20**, **21**, **22**) and $[\text{Ru}(\text{NO})_2(\text{L}^{n\text{Pr}})(\text{PPh}_3)]$ (**23**) were synthesized by the addition of the corresponding enetetramine (L^{Me_2} , L^{Et_2} , L^{nPr_2} , L^{Bn_2} (**1a–d**)) to a solution of $[\text{Ru}(\text{NO})_2(\text{PPh}_3)_2]$ (**19**) in toluene (SCHEME 2.15). Thereby the two phosphane ligands were substituted for the corresponding NHC ligands. The addition of L^{nPr_2} to $[\text{Ru}(\text{NO})_2(\text{PPh}_3)_2]$ (**19**) afforded only the mono carbene complex **23** due to the steric hindrance of the $n\text{Pr}$ group.

Results



Scheme 2.15: Synthesis of $[\text{Ru}(\text{NO})_2(\text{L}^{\text{R}})(\text{L})]$ ($\text{L} = \text{L}^{\text{R}}$, $\text{R} = \text{Me, Et, Bn}$; **20, 21, 22**; $\text{L} = \text{PPh}_3$, $\text{R} = n\text{Pr}$; **23**).

20–23 were obtained as orange crystals in 70–96 % yield. The compounds are moisture and oxygen-sensitive and were characterized by elemental analysis, IR, $^{13}\text{C}\{^1\text{H}\}$ NMR and ^1H NMR spectroscopy. Compound **23** was also characterized by $^{31}\text{P}\{^1\text{H}\}$ NMR spectroscopy. The IR spectra for **20–22** show two bands for the nitrosyl-stretching frequencies with almost equal wavenumbers at around 1600 and 1550 cm^{-1} . For compound **23** the two bands for $\tilde{\nu}(\text{NO})$ are shifted to higher wavenumbers (1625 and 1590 cm^{-1}) due to weaker σ -donating phosphane ligand. The ^1H NMR and the $^{13}\text{C}\{^1\text{H}\}$ NMR spectra of **20–22** show the expected signals for the NHC ligands. For compound **23** the spectra show additional signals for the phenyl groups in the aromatic range. Furthermore, the $^{31}\text{P}\{^1\text{H}\}$ NMR of compound **23** shows one sharp singlet at 53.8 ppm. The ^1H NMR and the $^{13}\text{C}\{^1\text{H}\}$ NMR data are summarized in TABLE 2.12 and 2.13.

Table 2.12: ^1H NMR data for the complexes **20–23** in CD_2Cl_2 . Chemical shifts δ in ppm and coupling constant J in Hz. ^a Signals for the phosphane ligand are not depicted.

	N–	N– <u>CH</u> ₂ –	N–CH ₂ <u>CH</u> ₂ CH ₃	– <u>CH</u> ₃	–Ph
$[\text{Ru}(\text{NO})_2(\text{L}^{\text{Me}})_2]$ (20)	3.60			3.07	
$[\text{Ru}(\text{NO})_2(\text{L}^{\text{Et}})_2]$ (21)	2.81 (s)	3.48 (q) $J = 7.16$		0.97 (t) $J = 7.16$	
$[\text{Ru}(\text{NO})_2(\text{L}^{\text{Bn}})_2]$ (22)	4.64 (s)	3.23 (s)			7.21–7.16 (m)
$[\text{Ru}(\text{NO})_2(\text{L}^{n\text{Pr}})(\text{PPh}_3)]$ (23) ^a	3.43 (s)	2.81 (t) $J = 8.1$	1.34 (dt) $J = 7.6, 7.8$		

Table 2.13: $^{13}\text{C}\{^1\text{H}\}$ NMR data for the complexes **20–23** in CD_2Cl_2 . Chemical shifts δ in ppm. ^a Signals for the phosphane ligand are not depicted.

	N <u>C</u> N	N– <u>CH</u> ₂ <u>CH</u> ₂ –N	N– <u>CH</u> ₂ –	N–CH ₂ <u>CH</u> ₂ CH ₃	– <u>CH</u> ₃	–Ph
$[\text{Ru}(\text{NO})_2(\text{L}^{\text{Me}})_2]$ (20)	219.59	52.32			38.56, 38.49	
$[\text{Ru}(\text{NO})_2(\text{L}^{\text{Et}})_2]$ (21)	220.53	47.87	45.88		13.42	
$[\text{Ru}(\text{NO})_2(\text{L}^{\text{Bn}})_2]$ (22)	219.90	55.66	49.15			137.62, 129.11, 128.20, 128.06
$[\text{Ru}(\text{NO})_2(\text{L}^{n\text{Pr}})(\text{PPh}_3)]$ (23) ^a		53.08	49.55	21.73	11.31	

Crystal structure of [Ru(NO)₂(L^{Me})₂] (20)

Orange crystals of **20** were obtained by covering a dichloromethane solution with a layer of diethyl ether overnight. The structure of the complex is illustrated in FIGURE 2.21.

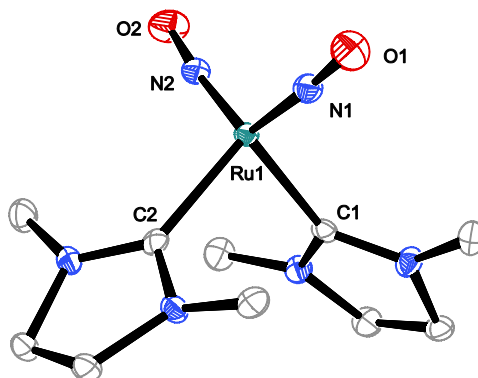


Figure 2.21: ORTEP plot of the complex [RuCl(NO)₂(L^{Bn})₂]⁺ in crystals of **20**. Sp.Gr. $P\bar{1}$. The thermal ellipsoids are drawn at 50 % probability level at 173 K. Due to clarity, hydrogen atoms are not depicted. Interatomic distances (Å) and angles (°), the standard deviation of the last decimal digit is given in parentheses: Ru1–N1 1.7787(19), Ru–N2 1.7740(19), Ru1–C1 2.097(2), Ru1–C2 2.100(2), N1–O1 1.209(2), N2–O2 1.203(2); O1–N1–Ru1 176.88(17), O2–N2–Ru1 175.00(17), N1–Ru1–N2 127.33(8), N1–Ru1–C1 112.15(8), N1–Ru1–C2 106.25(8), N2–Ru1–C1 103.06(8), N2–Ru1–C2 111.45(8), C1–Ru1–C2 90.50(8).

The structure solution succeeded in the triclinic space group $P\bar{1}$. The primitive cell contains two complex molecules and the asymmetric unit contains one complex molecule. The ruthenium center is coordinated by two nitrosyl ligands and two NHC ligands. The coordination of the ruthenium center is irregular and is best described as distorted tetrahedral (CShM_{T-4} value 0.901). The N–Ru–C angles range from 103° to 112°. The N–Ru–N angle (127°) and C–Ru–C angle (91°) are smaller than the corresponding angles in **19**. The two nitrosyl ligands bind to the ruthenium uniformly: the Ru–N bonds only differ by 0.0047 Å and the Ru–N–O angles are 175° and 176°. The two nitrosyls slightly point to each other. The short Ru–N bond lengths indicate a high degree of back donation from the metal center to the π* orbitals of the nitrosyls.

Crystal structure of [Ru(NO)₂(L^{Et})₂] (21)

Orange crystals of **21** were obtained directly from the reaction solution by storing it at –70 °C overnight. The structure of the complex is illustrated in FIGURE 2.22.

Results

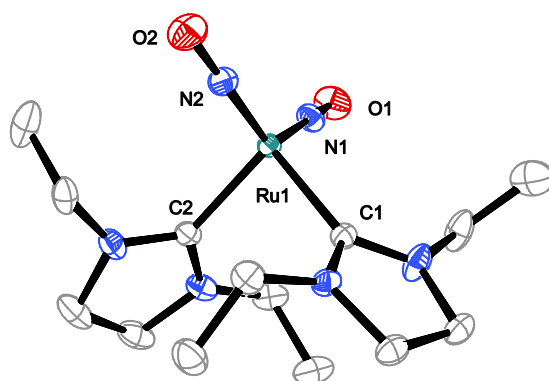


Figure 2.22: ORTEP plot of the complex $[\text{RuCl}(\text{NO})_2(\text{L}^{\text{Et}})_2]^+$ in crystals of **21**. Sp.Gr. $P2_1/c$. The thermal ellipsoids are drawn at 50 % probability level at 173 K. Due to clarity, hydrogen atoms are not depicted. Interatomic distances (Å) and angles (°), the standard deviation of the last decimal digit is given in parentheses: Ru1–N1 1.775(4), Ru–N2 1.774(2), Ru1–C1 2.093(2), Ru1–C2 2.114(3), N1–O1 1.207(3), N2–O2 1.204(3); O1–N1–Ru1 175.2(2), O2–N2–Ru1 176.0(2), N1Ru1–N2 128.77(11), N1–Ru1–C1 104.13(10), N1–Ru1–C2 110.69(10), N2–Ru1–C1 107.99(10), N2–Ru1–C2 108.49(10), C1–Ru1–C2 89.40(9).

The structure solution succeeded in the monoclinic space group $P2_1/c$. The primitive cell contains eight complex molecules and the asymmetric unit contains two complex molecules. The ruthenium center is coordinated by two nitrosyl ligands and two NHC ligands. The coordination of the ruthenium center is irregular and is best described as distorted tetrahedral (CShM₇₋₄ value 0.920). **21** is isostructural to **20**. Thus, it also has a large N–Ru–N angle (128°) and a small C–Ru–C angle (89°).

Crystal structure of $[\text{Ru}(\text{NO})_2(\text{L}^{\text{Bn}})_2]$ (**22**)

Orange crystals of **22** were obtained directly from the reaction solution. The structure of the complex is illustrated in FIGURE 2.23.

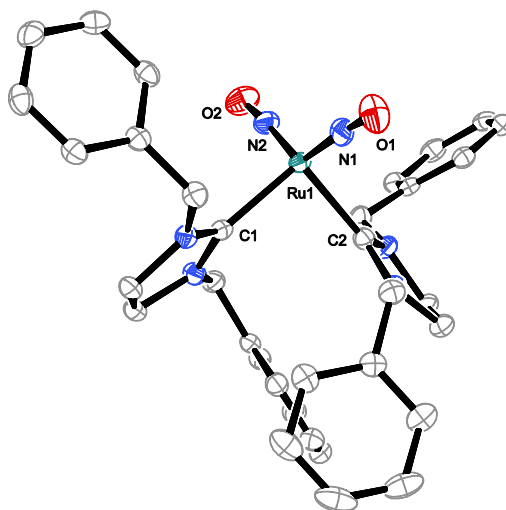


Figure 2.23: ORTEP plot of the complex $[\text{Ru}(\text{NO})_2(\text{L}^{\text{Bn}})_2]$ in crystals of **22**. Sp.Gr. $P2_1/c$. The thermal ellipsoids are drawn at 50 % probability level at 173 K. Due to clarity, hydrogen atoms are not depicted. Interatomic distances (Å) and angles (°), the standard deviation of the last decimal digit is given in parentheses: Ru1–N1 1.781(3), Ru–N2 1.772(3), Ru1–C1 2.097(3), Ru1–C2 2.089(3), N1–O1 1.201(4), N2–O2 1.204(4); O1–N1–Ru1 176.0(3), O2–N2–Ru1 175.3(3), N1–Ru1–N2 133.40(14), N1–Ru1–C1 111.47(13), N1–Ru1–C2 101.07(13), N2–Ru1–C1 100.61(13), N2–Ru1–C2 110.37(13), C1–Ru1–C2 92.88(12).

The structure solution succeeded in the monoclinic space group $P2_1/c$. The primitive cell contains four complex molecules and the asymmetric unit contains one complex molecule. The two NHC ligands and the two nitrosyl ligands coordinate to the ruthenium center in a distorted tetrahedral manner (CShM₇₋₄

Results

value 1.141). **22** is isostructural to **20** and **21**. The N–Ru–N angle (134°) of **22** is even larger than the corresponding angles in **20** and **21** and is close to the N–Ru–N angle (137°) of the phosphane analog $[\text{Ru}(\text{NO})_2(\text{PPh}_3)_2]$ (**19**).

Crystal structure of $[\text{Ru}(\text{NO})_2(\text{L}^{\text{nPr}})(\text{PPh}_3)]$ (**23**)

Orange crystals of **23** were obtained directly from the reaction solution by storing it over night at -20°C . The structure of the complex is illustrated in FIGURE 2.24.

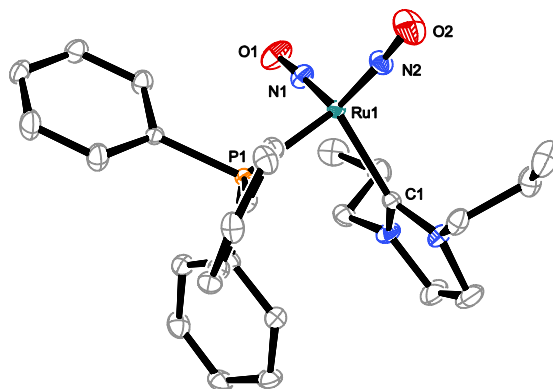
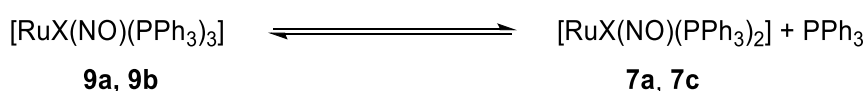


Figure 2.24: ORTEP plot of the complex $[\text{Ru}(\text{NO})_2(\text{L}^{\text{nPr}})(\text{PPh}_3)]$ in crystals of **23**. Sp.Gr. $P2_1/c$. The thermal ellipsoids are drawn at 50 % probability level at 173 K. Due to clarity, hydrogen atoms are not depicted. Interatomic distances (\AA) and angles ($^\circ$), the standard deviation of the last decimal digit is given in parentheses: Ru1–N1 1.780(2), Ru–N2 1.782(2), Ru1–C1 2.102(2), Ru1–P1 2.3417(6), N1–O1 1.192(3), N2–O2 1.197(3); O1–N1–Ru1 176.15(19), O2–N2–Ru1 176.3(2), N1Ru1–N2 129.32(9), N1–Ru1–C1 107.19(9), N1–Ru1–P1 105.21(7), N2–Ru1–C1 109.55(9), N2–Ru1–P1 107.93(7), C1–Ru1–P1 90.75(6).

The structure solution succeeded in the monoclinic space group $P2_1/c$. The primitive cell contains four complex molecules and the asymmetric unit contains one complex molecule. The NHC ligand, the phosphane and the two nitrosyl ligands coordinate to the ruthenium center in a distorted tetrahedral manner (CShM $_{T-4}$ value 0.953). **23** is isostructural to **20–22**. The N–Ru–N angle (129°) and the P–Ru–C angle of **23** are comparable to the corresponding angles in **20** and **21**.

2.12 Analytical study of the solution behavior of the [RuX(NO)(PPh₃)₃] compounds **9a** and **9b**

When the orange penta-coordinated species [RuX(NO)(PPh₃)₃] (X = Cl, I; **9a**, **9b**) are solved in toluene at room temperature, green solutions are obtained indicating an extensive dissociation to the green square-planar species [RuX(NO)(PPh₃)₂] (X = Cl, I; **7a**, **7c**). This dissociation can be reversed by cooling the solution to low temperatures, accompanied by a color change from green to orange. A color change from green to orange also occurs by adding excess of triphenylphosphane to the solutions. Thus, an equilibrium between the penta-coordinated species **9a/9b** and the square-planar species **7a/7c** as depicted in SCHEME 2.16 can be postulated.



Scheme 2.16: Equilibrium between [RuX(NO)(PPh₃)₃] (X = Cl, I; **9a**, **9b**) and [RuX(NO)(PPh₃)₂] (X = Cl, I; **7a**, **7c**).

Since the isolation of **9a** has proved to be more problematic, only the solution behavior of complex **9b** was further investigated by UV-vis spectroscopy. Cooling the solutions of **9b** resulted in a distinct change in the visible spectrum (FIGURE 2.25 top). Spectra recorded at different temperatures show isosbestic points at 425, 490 and 575 nm. At room temperature the spectrum shows two absorption bands at 445 and 645 nm which decrease upon cooling. At -30 °C the solution turns orange-red and the absorption band at 645 nm vanishes while the band at 445 nm is red shifted. In order to investigate the phosphane concentration dependence, **7c** was solved in toluene and phosphane was added. The spectra recorded at intermediate concentrations of added phosphane are shown in FIGURE 2.25 at the bottom. Analog to the temperature-depending spectra the spectra give three isosbestic points. The spectrum of **7c** without any phosphane addition shows the same absorption bands as the spectrum of **9b** at room temperature. This absorptions bands are decreasing upon phosphane addition, but the absorption band at 645 nm does not vanish completely even at high phosphane concentrations (15 eq.).

Results

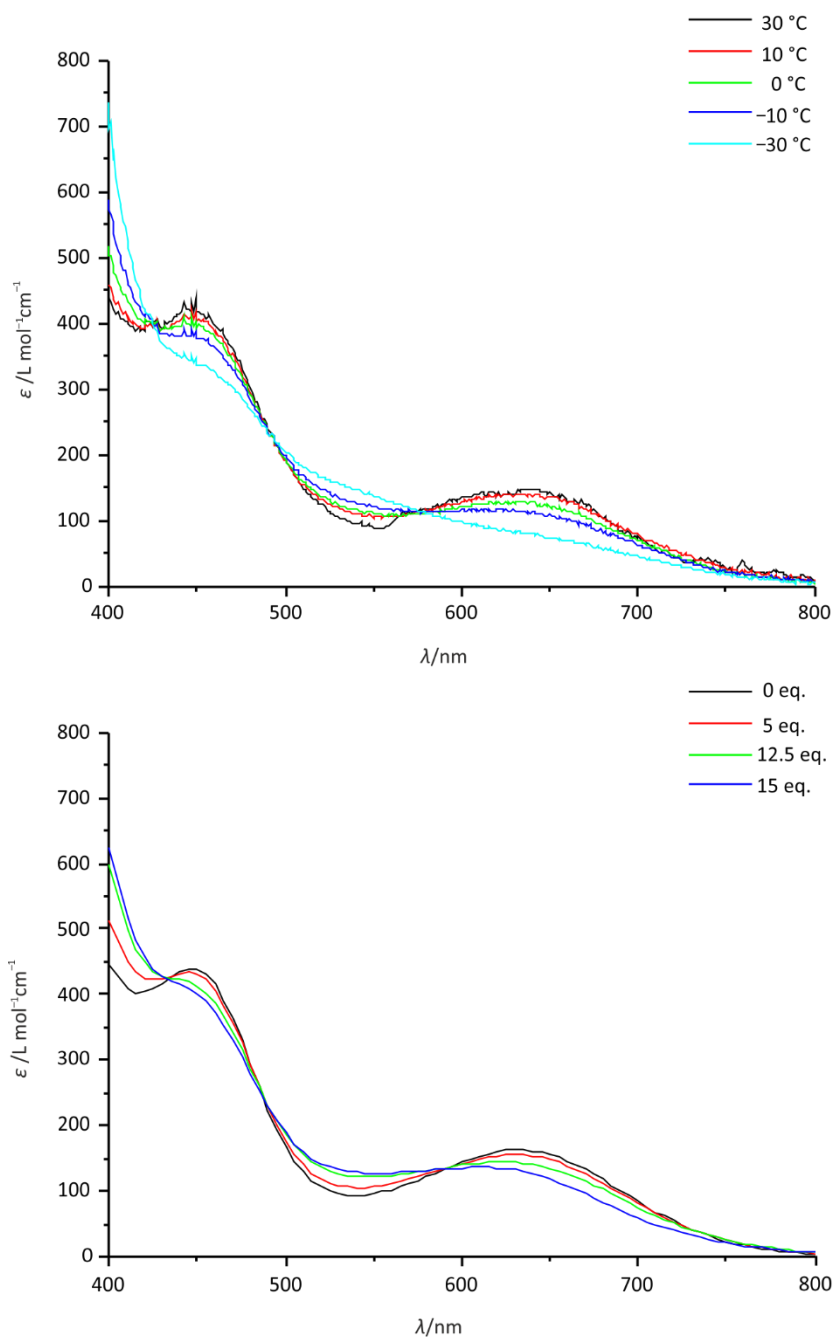


Figure.2.25: UV-vis spectra of $[\text{RuI}(\text{NO})(\text{PPh}_3)_3]$ (**9b**) recorded at varying temperatures (top) and UV-vis spectra of $[\text{RuI}(\text{NO})(\text{PPh}_3)_2]$ (**7c**) recorded at intermediate triphenylphosphane concentrations at 297 K (bottom).

2.13 Quantum-chemical calculations

To attain a better perception of the electronic structure of the $\{\text{Ru}(\text{NO})_n\}^m$ moieties and for the characterization of the oxidation states of the ruthenium center quantum-chemical calculations were performed.

2.13.1 Structural optimization

The calculations were expected to reproduce the Ru–N–O angle, the Ru–N and the N–O distances and the $\tilde{\nu}(\text{NO})$ stretching vibration energies as accurately as possible. In the case of the penta-coordinated species the calculated CSHM-values are of interest as well, since the binding mode of the nitrosyl ligand, bent or linear, corresponds to the two isomeric forms (*sqp* or *tbp*). Geometry optimizations using the BP86 functional^[124,125] and the TZVP basis set^[126] already proved to be suitable for predictions of the structure in ruthenium dinitrosyl compounds.^[34] Since the ruthenium-nitrosyl compounds featured in this work show a wide variety of electronic states, the influence of more polarization functions was analyzed by using the def2-TZVP basis set^[127]. Furthermore, the influence of dispersion correction^[128,129] and the COSMO solvation model was investigated^[130]. The geometry of **7b** was also optimized by the hybrid functional TPSSH^[131–133] in combination with the TZVP and def2-TZVP basis set. All calculations were performed using spin-restricted closed-shell systems.

Tetra-coordinated $\{\text{RuNO}\}^8$ compounds

In combination with the BP86 functional the structures of the square-planar $\{\text{RuNO}\}^8$ compounds **7b** and **8a** are well described by both the TZVP and the def2-TZVP basis sets. Regarding bond distances only, adding more polarization functions does not result in any noticeable improvement, but the Ru–N–O angle is increased by the def2-TZVP basis set. Adding dispersion correction and the COSMO solvation model leads to more precise $\tilde{\nu}(\text{NO})$ stretching vibration energies. The geometry of **7b** was also optimized by the TPSSH functional which gives comparable values for bond lengths and angles, but calculates the $\tilde{\nu}(\text{NO})$ stretching vibration energies far too high. Since the BP86 functional gives reasonable values for both the structure parameters and the frequencies, this functional was used for the calculations of the rest of the compounds. An exemplary comparison of results on the tetra-coordinated $\{\text{RuNO}\}^8$ compounds with different computational methods is given in TABLE 2.14 and TABLE 2.15 for $[\text{Ru}(\text{NO})(\text{PPh}_3)_2]$ (**7c**) and in TABLE 2.16 for $[\text{RuCl}(\text{NO})\text{L}^{\text{Bn}_2}]$ (**8a**).

Results

Table 2.14: DFT results on [Ru(NO)(PPh₃)₂] (**7c**) using the functional BP86, TZVP and def2-TZVP basis sets with dispersion correction (D) and the COSMO solvation model (C). Distances in Å, angles in ° and $\tilde{\nu}(\text{NO})$ energies in cm⁻¹.

	exp.	TZVP	TZVP D	TZVP D, C	def2-TZVP D	def2-TZVP D, C
Ru–N–O	177.22	172.47	173.66	174.21	173.60	176.00
N–O	1.17	1.18	1.18	1.18	1.18	1.18
Ru–N	1.72	1.76	1.77	1.77	1.77	1.77
Ru–I	2.68	2.73	2.72	2.72	2.72	2.73
Ru–P1	2.38	2.43	2.38	2.39	2.38	2.39
Ru–P2	2.39	2.43	2.39	2.39	2.39	2.39
CShM _{Sp-4}	1.303	1.420	1.037	0.846	0.978	0.866
$\tilde{\nu}(\text{NO})$	1739	1760	1769	1760	1770	1760

Table 2.15: DFT results on [Ru(NO)(PPh₃)₂] (**7c**) using the functional TPSSH, TZVP and def2-TZVP basis sets with dispersion correction (D) and the COSMO solvation model (C). Distances in Å, angles in ° and $\tilde{\nu}(\text{NO})$ energies in cm⁻¹.

	TZVP	TZVP D	TZVP D, C	def2-TZVP D	def2-TZVP D, C
Ru–N–O	173.59	173.80	174.52	173.79	174.51
N–O	1.17	1.17	1.17	1.17	1.17
Ru–N	1.76	1.76	1.76	1.77	1.76
Ru–I	2.73	2.72	2.72	2.72	2.72
Ru–P1	2.43	2.39	2.39	2.39	2.39
Ru–P2	2.43	2.39	2.39	2.39	2.39
CShM _{Sp-4}	1.443	1.299	1.221	1.299	1.222
$\tilde{\nu}(\text{NO})$	1819	1833	1808	1823	1808

Table 2.16: DFT results on [RuCl(NO)L^{Bn}]₂ (**8a**) using the functional BP86, TZVP and def2-TZVP basis sets with dispersion correction (D) and the COSMO solvation model (C). Distances in Å, angles in ° and $\tilde{\nu}(\text{NO})$ energies in cm⁻¹. ^aSymmetry generated.

	exp.	TZVP	TZVP D	TZVP D, C	def2-TZVP D	def2-TZVP D, C
Ru–N–O	174.0	179.02	177.35	178.99	177.32	178.23
N–O	1.19	1.18	1.19	1.86	1.19	1.19
Ru–N	1.78	1.76	1.76	1.76	1.76	1.76
Ru–Cl	2.29	2.42	2.41	2.42	2.41	2.43
Ru–C1	2.11	2.13	2.11	2.11	2.12	2.12
Ru–C2	2.11 ^a	2.13	2.12	2.12	2.11	2.11
CShM _{Sp-4}	0.489	0.483	0.428	0.473	0.481	0.496
$\tilde{\nu}(\text{NO})$	1668	1742	1743	1727	1743	1727

Penta-coordinated {RuNO}⁸ phosphane compounds

The RuNO moiety and the square-pyramidal coordination of the two penta-coordinated {RuNO}⁸ phosphane compounds **8a** and **8b** is best described on the BP86/TZVP level of theory. But the $\tilde{\nu}(\text{NO})$ stretching vibration energies are calculated better on the BP86/def2-TZVP level with dispersion correction and the COSMO solvation model (TABLE 2.17).

Results

Table 2.17: DFT results on [Ru(NO)(PPh₃)₃] (**9b**) using the functional BP86, TZVP and def2-TZVP basis sets with dispersion correction (D) and the COSMO solvation model (C). Distances in Å, angles in ° and $\tilde{\nu}(\text{NO})$ energies in cm⁻¹.

	exp.	TZVP	TZVP D	TZVP D, C	def2-TZVP D	def2-TZVP D, C
Ru–N–O	165.70	163.70	158.41	157.96	158.50	157.96
N–O	1.15	1.19	1.19	1.20	1.19	1.20
Ru–N	1.79	1.82	1.83	1.83	1.83	1.83
Ru–I	2.81	2.88	2.84	2.85	2.84	2.85
Ru–P1	2.41	2.49	2.42	2.42	2.42	2.42
Ru–P2	2.32	2.38	2.30	2.31	2.30	2.31
Ru–P3	2.40	2.49	2.40	2.41	2.40	2.41
CShM _{spy-5}	1.839	1.725	1.935	2.003	1.942	2.003
$\tilde{\nu}(\text{NO})$	1625	1656	1644	1629	1644	1629

Penta-coordinated {RuNO}⁸ NHC compounds

A combination of def2-TZVP, dispersion correction and the COSMO solvation model gives the best overall agreement with the experimental results for the complex cation structures of the penta-coordinated {RuNO}⁸ NHC compounds **10b**, **11a** and **13a**. The differences between the TZVP and def2-TZVP basis sets become obvious regarding the Ru–C bond distances, even though the CShM value is better described by the smaller basis set in combination with dispersion correction and the COSMO solvation model (TABLE 2.18).

Table 2.18: DFT results on the complex cation of [Ru(NO)(L^{Et})₄]Cl (**11a**) using the functional BP86, TZVP and def2-TZVP basis sets with dispersion correction (D) and the COSMO solvation model (C). Distances in Å, angles in ° and $\tilde{\nu}(\text{NO})$ energies in cm⁻¹.

	exp.	TZVP	TZVP D	TZVP D, C	def2-TZVP D	def2-TZVP D, C
Ru–N–O	128.40	127.10	126.52	127.03	126.56	126.49
N–O	1.21	1.21	1.21	1.21	1.21	1.21
Ru–N	1.89	1.91	1.91	1.90	1.91	1.90
Ru–C1	2.16	2.20	2.16	2.20	2.16	2.16
Ru–C2	2.10	2.17	2.14	2.17	2.14	2.14
Ru–C3	2.10	2.14	2.11	2.15	2.11	2.11
Ru–C4	2.10	2.16	2.12	2.16	2.12	2.12
CShM _{voc-5}	0.581	0.328	0.295	0.342	0.298	0.316
$\tilde{\nu}(\text{NO})$	1480	1525	1529	1501	1528	1508

Hexa-coordinated {RuNO}⁶ NHC compounds

The structures of the hexa-coordinated {RuNO}⁶ species of the complex cations of [RuCl(NO)(L^{Me})₄](I₅)₂ (**14a**), [Ru(NO)(L^{Et})₄](I₃)₂ (X = Cl, Br; **15a**, **15b**) and [RuI(NO)(L^{Et})₄](I₅)(I₃) (**15c**) are well described by both the TZVP and the def2-TZVP basis set. Def2-TZVP in combination with dispersion correction and the COSMO solvation model gives better results regarding the Ru–C bond distances and the Ru–N–O angle (TABLE 2.19).

Results

Table 2.19: DFT results on the complex cation of $[\text{RuCl}(\text{NO})\text{L}^{\text{Et}_4}] (\text{I}_3)_2$ (**15a**) using the functional BP86, TZVP and def2-TZVP basis sets with dispersion correction (D) and the COSMO solvation model (C). Distances in Å, angles in ° and $\tilde{\nu}(\text{NO})$ energies in cm^{-1} .

	exp.	TZVP	TZVP D	TZVP D, C	def2-TZVP D	def2-TZVP D, C
Ru–N–O	176.68	178.11	175.81	177.28	175.85	175.75
N–O	1.20	1.16	1.16	1.16	1.16	1.16
Ru–N	1.73	1.78	1.78	1.78	1.78	1.78
Ru–Cl	2.47	2.55	2.54	2.57	2.54	2.56
Ru–C1	2.17	2.24	2.20	2.22	2.20	2.19
Ru–C2	2.17	2.24	2.19	2.24	2.19	2.19
Ru–C3	2.17	2.23	2.19	2.23	2.19	2.18
Ru–C4	2.17	2.24	2.20	2.23	2.20	2.18
CShM _{OC-6}	0.786	0.559	0.596	0.625	0.594	0.619
$\tilde{\nu}(\text{NO})$	1829	1831	1837	1826	1837	1832

$\{\text{Ru}(\text{NO})_2\}^8$ phosphane compounds

The unequal bonding situation of the two nitrosyl ligands in $[\text{Ru}(\text{NO})_2(\text{PPh}_3)_2\text{SO}_4]$ (**16**) gets obvious in the calculated $\tilde{\nu}(\text{NO})$ stretching vibration energies. The difference in the wavenumbers of the symmetrical and the asymmetrical vibration derived from measurements and calculations is $\geq 180 \text{ cm}^{-1}$ and is therefore in the range of the $\Delta\tilde{\nu}(\text{NO})$ values for dinitrosyl compounds with two distinct NO ligands.^[34] Both basis sets, TZVP and def2-TZVP, calculate too acute angles for the linear RuNO moiety. The def2-TZVP basis set leads to better results regarding the Ru–P bond distances (TABLE 2.20).

The binding situation of the two nitrosyl ligands in the complex cation of $[\text{Ru}(\text{NO})_2(\text{PPh}_3)_2]\text{BF}_4$ (**17**) can be considered equal. The equality of the NO ligands is resembled in the calculated and measured $\Delta\tilde{\nu}(\text{NO})$ values of $\leq 40 \text{ cm}^{-1}$ which match the values of the known penta-coordinated dinitrosyls with two equal NO^+ ligands in a trigonal bipyramidal structure.^[34] Furthermore, the bond distances of Ru–N deviate only about 0.01 ppm in the measured structure and about 0.03 ppm in the calculated one. Both basis sets calculate the $\Delta\text{Ru–N–O}$ angle values too high which results in one almost linearly coordinated NO ligand and one slightly bent NO ligand. The best fit for the CShM_{TBPY-5} value is achieved by the TZVP basis set, the addition of dispersion correction and the COSMO solvation model leads to more accurate $\Delta\tilde{\nu}(\text{NO})$ values (TABLE 2.21).

Results

Table 2.20: DFT results on $[\text{Ru}(\text{NO})_2(\text{PPh}_3)_2\text{SO}_4]$ (**16**) using the functional BP86, TZVP and def2-TZVP basis sets with dispersion correction (D) and the COSMO solvation model (C). Distances in Å, angles in ° and $\tilde{\nu}(\text{NO})$ energies in cm^{-1} . ^aSymmetry generated.

	exp.	TZVP	TZVP D	TZVP D, C	def2-TZVP D	def2-TZVP D, C
Ru–N1–O1	176.80	171.44	171.96	172.70	171.96	172.70
Ru–N2–O2	128.50	129.93	129.99	130.67	129.99	130.67
$\Delta\text{Ru–N–O}$	48.30	41.51	41.97	42.03	41.97	42.03
N1–O1	1.14	1.17	1.17	1.17	1.17	1.17
N2–O2	1.23	1.19	1.19	1.19	1.19	1.19
Ru–N1	1.74	1.80	1.80	1.80	1.80	1.80
Ru–N2	1.92	1.93	1.92	1.92	1.92	1.92
Ru–O3	2.21	2.42	2.42	2.44	2.42	2.44
Ru–O4	2.21 ^a	2.04	2.04	2.06	2.04	2.06
Ru–P1	2.47	2.56	2.48	2.48	2.48	2.48
Ru–P2	2.47 ^a	2.56	2.49	2.49	2.49	2.49
CShM _{OC-6}	2.520	2.571	2.189	2.266	2.189	2.266
$\tilde{\nu}(\text{NO})$	1814, 1614	1800, 1617	1806, 1620	1803, 1618	1806, 1620	1803, 1618
$\Delta\tilde{\nu}(\text{NO})$	200	183	186	185	186	185

Table 2.21: DFT results on the cation of $[\text{Ru}(\text{NO})_2(\text{PPh}_3)_2]\text{BF}_4$ (**17**) using the functional BP86, TZVP and def2-TZVP basis sets with dispersion correction (D) and the COSMO solvation model (C). Distances in Å, angles in ° and $\tilde{\nu}(\text{NO})$ energies in cm^{-1} .

	exp.	TZVP	TZVP D	TZVP D, C	def2-TZVP D	def2-TZVP D, C
Ru–N1–O1	168.94	179.70	176.74	179.54	177.82	179.22
Ru–N2–O2	167.08	158.09	155.33	158.89	156.84	158.28
$\Delta\text{Ru–N–O}$	1.86	21.61	21.41	20.65	20.98	20.94
N1–O1	1.15	1.17	1.17	1.16	1.17	1.16
N2–O2	1.14	1.17	1.17	1.16	1.17	1.16
Ru–N1	1.78	1.82	1.81	1.81	1.81	1.81
Ru–N2	1.79	1.84	1.85	1.84	1.84	1.84
Ru–I	2.73	2.77	2.75	2.77	2.75	2.77
Ru–P1	2.43	2.52	2.45	2.46	2.46	2.46
Ru–P2	2.43	2.52	2.46	2.45	2.46	2.46
CShM _{TBPY-5}	2.197	1.994	1.797	1.783	1.773	1.797
$\tilde{\nu}(\text{NO})$	1853, 1817	1806, 1785	1809, 1780	1802, 1768	1812, 1782	1802, 1767
$\Delta\tilde{\nu}(\text{NO})$	36	21	29	34	30	35

$\{\text{Ru}(\text{NO})_2\}^8$ NHC compounds

The electronic nature of two nitrosyl groups of compounds $[\text{RuX}(\text{NO})_2(\text{L}^{\text{Bn}})_2]\text{BF}_4$ (X = Cl, Br; **18a**, **18b**) can be considered unequal which is proved by their measured and calculated $\Delta\text{Ru–N–O}$ and $\Delta\tilde{\nu}(\text{NO})$ values with $\geq 40^\circ$ and $\geq 120 \text{ cm}^{-1}$ respectively.^[34] The TZVP basis set with dispersion correction gives a slightly better result for the CShM_{VOc-5} value and the def2-TZVP basis set calculates the $\Delta\tilde{\nu}(\text{NO})$ value more precisely (TABLE 2.22).

Results

Table 2.22: DFT results on the cation of $[\text{RuCl}(\text{NO})_2(\text{L}^{\text{Bn}})_2]\text{BF}_4$ (**18a**) using the functional BP86, TZVP and def2-TZVP basis sets with dispersion correction (D) and the COSMO solvation model (C). Distances in Å, angles in ° and $\tilde{\nu}(\text{NO})$ energies in cm^{-1} .

	exp.	TZVP	TZVP D	TZVP D, C	def2-TZVP D	def2-TZVP D, C
Ru–N1–O1	179.29	177.97	175.23	175.64	175.27	176.20
Ru–N2–O2	132.18	132.16	131.36	131.71	131.38	132.07
$\Delta\text{Ru–N–O}$	47.11	45.81	43.87	43.93	43.89	44.13
N1–O1	1.14	1.16	1.16	1.16	1.16	1.16
N2–O2	1.16	1.18	1.17	1.17	1.17	1.90
Ru–N1	1.75	1.80	1.80	1.80	1.80	1.80
Ru–N2	1.89	1.91	1.91	1.91	1.91	1.17
Ru–Cl	2.37	2.40	2.40	2.41	2.40	2.42
Ru–C1	2.13	2.18	2.15	2.15	2.15	2.15
Ru–C2	2.14	2.18	2.16	2.16	2.16	2.16
CShM _{voc-5}	0.951	1.192	0.915	0.912	0.913	0.903
$\tilde{\nu}(\text{NO})$	1847, 1672	1831, 1696	1832, 1712	1827, 1699	1832, 1712	1824, 1684
$\Delta\tilde{\nu}(\text{NO})$	175	135	120	128	120	140

$\{\text{Ru}(\text{NO})_2\}^{10}$ NHC compounds

Both nitrosyl ligands in the $\{\text{Ru}(\text{NO})_2\}^{10}$ NHC compounds $[\text{Ru}(\text{NO})_2(\text{L}^{\text{R}})_2]$ (R = Me, Et, Bn; **20**, **21**, **22**) and $[\text{Ru}(\text{NO})_2(\text{L}^{\text{nPr}})(\text{PPh}_3)]$ (**23**) bind equally to the ruthenium center. The equality becomes quite evident in their small measured and calculated $\Delta\tilde{\nu}(\text{NO})$ - and $\Delta\text{Ru–N–O}$ values. The Ru–N–O angles are calculated 5° to 6° too acute with both basis sets. The best CShM_{T-4} value is achieved by applying the TZVP basis set and the def2-TZVP basis set calculates the $\Delta\tilde{\nu}(\text{NO})$ value more precisely (TABLE 2.23).

Table 2.23: DFT results on $[\text{Ru}(\text{NO})_2(\text{L}^{\text{Me}})_2]$ (**20**) using the functional BP86, TZVP and def2-TZVP basis sets with dispersion correction (D) and the COSMO solvation model (C). Distances in Å, angles in ° and $\tilde{\nu}(\text{NO})$ energies in cm^{-1} .

	exp.	TZVP	TZVP D	TZVP D, C	def2-TZVP D	def2-TZVP D, C
Ru–N1–O1	176.90	174.34	170.54	171.52	170.57	171.59
Ru–N2–O2	175.01	174.19	170.48	171.33	170.52	171.35
$\Delta\text{Ru–N–O}$	1.89	0.15	0.06	0.19	0.05	0.24
N1–O1	1.21	1.20	1.20	1.21	1.20	1.21
N2–O2	1.20	1.20	1.20	1.21	1.20	1.21
Ru–N1	1.78	1.83	1.84	1.83	1.84	1.83
Ru–N2	1.77	1.83	1.84	1.83	1.84	1.83
Ru–C1	2.10	2.10	2.07	2.07	2.06	2.07
Ru–C2	2.10	2.10	2.06	2.07	2.07	2.07
CShM _{T-4}	0.901	1.269	1.891	1.878	1.888	1.873
$\tilde{\nu}(\text{NO})$	1592, 1548	1657, 1626	1654, 1619	1625, 1579	1655, 1620	1625, 1580
$\Delta\tilde{\nu}(\text{NO})$	44	31	35	46	35	45

2.13.2 Charge and population analysis

To gain a better insight into the electronic situation of the RuNO moiety charge and population analysis of the metal center and the nitrosyl ligands were performed. Quantum theory of atoms (QTAIM)^[134] and natural population analysis (NPA)^[135] were used to compute the charges on the ruthenium and the nitrosyl ligands. In general, NPA leads to lower charges than QTAIM, but both approaches unfold clear trends for the different electronic states of the ruthenium-nitrosyl compounds. Except for compound **11a** all mononitrosyl with NHC ligands have positive charges on the ruthenium center and the nitrogen atom and negative charges on the oxygen. The lowest charges on the NO ligands are calculated for the penta-coordinated $\{\text{RuNO}\}^8$ species with a bent RuNO moiety. Slightly higher charges are found on the linearly coordinated NO group in the square-planar $\{\text{RuNO}\}^8$ compounds. The highest values are calculated for the $\{\text{RuNO}\}^6$ species, where NPA gives positive charges on the NO ligand. The charges on the ruthenium center follow the same trend, even though the differences between the two $\{\text{RuNO}\}^8$ species are insignificant (TABLE 2.24).

In the case of the mononitrosyl compounds with phosphane ligands the charges on the ruthenium and the nitrosyl ligand are lower for the penta-coordinated species **9a** and **9b** than the charges for the square-planar species **7b** and **7c**. In general, the charges for the phosphane compounds are estimated lower than the ones for the NHC derivatives (TABLE 2.25).

Table 2.24: QTAIM and NPA charges of the mononitrosyl complexes with NHC ligands. All values are elementary charges. All calculations were performed by using the def2-TZVP basis set and the BP86 functional with the COSMO solvation model and dispersion correction.

		$[\text{RuX}(\text{NO})\text{L}^{\text{Bn}}_2]$									
		Ru	N	O	NO			Ru	N	O	NO
8a	QTAIM	0.662	0.014	-0.428	-0.414	8b	QTAIM	0.584	0.037	-0.436	-0.399
	NPA	0.027	0.162	-0.244	-0.082		NPA	0.008	0.175	-0.245	-0.070
		$[\text{Ru}(\text{NO})(\text{L}^{\text{R}})_4]^+$									
		Ru	N	O	NO			Ru	N	O	NO
10b	QTAIM	0.655	0.034	-0.501	-0.467	13a	QTAIM	0.658	0.011	-0.507	-0.496
	NPA	0.047	0.062	-0.306	-0.244		NPA	0.136	0.050	-0.325	-0.275
11a	QTAIM	0.705	0.030	-0.504	-0.474						
	NPA	0.114	-0.420	0.142	-0.278						
		$[\text{RuX}(\text{NO})(\text{L}^{\text{R}})_4]^{2+}$									
		Ru	N	O	NO			Ru	N	O	NO
14a	QTAIM	1.043	0.143	-0.318	-0.175	15b	QTAIM	1.001	0.140	-0.328	-0.188
	NPA	0.279	0.289	-0.104	0.185		NPA	0.271	0.279	-0.115	0.164
15a	QTAIM	1.044	0.136	-0.328	-0.192	15c	QTAIM	0.885	0.141	-0.318	-0.177
	NPA	0.283	0.283	-0.115	0.168		NPA	0.256	0.275	-0.115	0.160

Results

Table 2.25: QTAIM and NPA charges of the mononitrosyl complexes with phosphane ligands. All values are elementary charges. All calculations were performed by using the def2-TZVP basis set and the BP86 functional with the COSMO solvation model and dispersion correction.

		[RuX(NO)(PPh ₃) ₂]									
		Ru	N	O	NO			Ru	N	O	NO
7b	QTAIM	0.374	0.044	-0.390	-0.346	7c	QTAIM	0.319	0.077	-0.412	-0.335
	NPA	-0.174	0.198	-0.203	-0.005		NPA	-0.201	0.196	-0.197	-0.001

		[RuX(NO)(PPh ₃) ₃]									
		Ru	N	O	NO			Ru	N	O	NO
9a	QTAIM	0.469	-0.021	-0.440	-0.461	9b	QTAIM	0.385	0.013	-0.444	-0.431
	NPA	-0.065	0.056	-0.251	-0.195		NPA	-0.135	0.069	-0.235	-0.166

The charges on the two nitrosyl ligands of the {Ru(NO)₂}⁸ NHC compounds **18a** and **18b** differ by 0.016 to 0.046 (QTAIM) and by 0.100 to 0.102 (NPA), whereupon the nitrosyl ligand which binds with a more acute angle to the ruthenium, has the lower charges. In contrast, the equality of the two nitrosyl ligands of the {Ru(NO)₂}¹⁰ species **20–23** is reflected by their charges which differ only by 0.01 to 0.02. In comparison to the other linearly bonded nitrosyl ligands the charges on the nitrosyl ligands in **20–23** are significant low (TABLE 2.26).

Table 2.26: QTAIM and NPA charges of the dinitrosyl complexes with NHC ligands. All values are elementary charges. All calculations were performed by using the def2-TZVP basis set and the BP86 functional with the COSMO solvation model and dispersion correction. The charges of the nitrosyl groups that bind linearly to the ruthenium are depicted in the upper row.

		[RuX(NO) ₂ (L ^{Bn}) ₂] ⁺									
		Ru	N	O	NO			Ru	N	O	NO
18a	QTAIM	1.017	0.173	-0.339	-0.166	18b	QTAIM	0.917	0.181	-0.348	-0.167
			0.108	-0.320	-0.212		QTAIM		0.156	-0.339	-0.183
	NPA	0.427	0.199	-0.110	0.089		NPA	0.410	0.199	-0.108	0.091
			0.140	-0.153	-0.013			0.139	-0.148	-0.009	

		[Ru(NO) ₂ L ₂]									
		Ru	N	O	NO			Ru	N	O	NO
20	QTAIM	0.777	-0.087	-0.459	-0.546	21	QTAIM	0.773	-0.077	-0.448	-0.525
			-0.085	-0.459	-0.544		QTAIM		-0.078	-0.447	-0.525
	NPA	0.318	-0.066	-0.287	-0.353		NPA	0.341	-0.062	-0.271	-0.333
			-0.063	-0.288	-0.351			-0.061	-0.271	-0.332	
22	QTAIM	0.786	-0.081	-0.458	-0.539	23	QTAIM	0.673	-0.053	-0.442	-0.495
			-0.085	-0.455	-0.540		QTAIM		-0.053	-0.441	-0.494
	NPA	0.348	-0.063	-0.284	-0.347		NPA	0.248	-0.038	-0.262	-0.300
			-0.069	-0.280	-0.349			-0.040	-0.259	-0.299	

A similar tendency is observed for the two dinitrosyl compounds with phosphane ligands **16** and **17**. The difference between the nitrosyl charges is more significant for the two nitrosyl groups of **16** than for the equally coordinated nitrosyl ligands of **17** (TABLE 2.27).

Table 2.27: QTAIM and NPA charges of the dinitrosyl complexes with phosphane ligands. All values are elementary charges. All calculations were performed by using the def2-TZVP basis set and the BP86 functional with the COSMO solvation model and dispersion correction. The charges of the nitrosyl groups which bind linear to the ruthenium are depicted in the upper row.

		Ru	N	O	NO			Ru	N	O	NO
16	QTAIM	0.968	0.161	-0.383	-0.222	17	QTAIM	0.705	0.1150	-0.314	-0.199
			0.143	-0.437	-0.294				0.123	-0.332	-0.209
	NPA	0.371	0.109	-0.232	-0.123		NPA	0.181	0.148	-0.122	0.026
			0.203	-0.142	0.061				0.134	-0.115	0.019

2.14 The structures of $[\text{Ru}(\text{NO})_2(\text{PPh}_3)_2\text{SO}_4]$ (**16**) and $[\text{RuX}(\text{NO})(\text{PPh}_3)_3]$ (**9a,b**)

2.14.1 The structure of $[\text{RuX}(\text{NO})(\text{PPh}_3)_3]$ (**9a,b**)

$[\text{RuCl}(\text{NO})(\text{PPh}_3)_3]$ (**9a**) and $[\text{RuI}(\text{NO})(\text{PPh}_3)_3]$ (**9b**) adopt a square-pyramidal structure with a slightly bent RuNO moiety in the plane. In order to understand the origin of this unusual coordination motif of these two compounds a relaxed surface scan of the I–Ru–N angle of **9b** was performed. Compound **9b** adopts a *tbp* structure for I–Ru–N = 180° with the iodido and the NO ligand in the axial position (structure **A**, FIGURE 2.26). Structure **A** shows a significant potential of 30 kJ mol⁻¹. Upon decreasing the I–Ru–N angle the Ru–N–O- and the P1–Ru–P3 angle decrease as well. The minimum structure is a square pyramid with an I–Ru–N angle of 139° and a slightly bent nitrosyl ligand (163°) in the plane (structure **B**). For an I–Ru–N angle of 110° a trigonal bipyramidal structure is adopted with P1 and P3 in axial positions and a bent NO ligand (Ru–N–O = 139°) in the plane (structure **C**).

Results

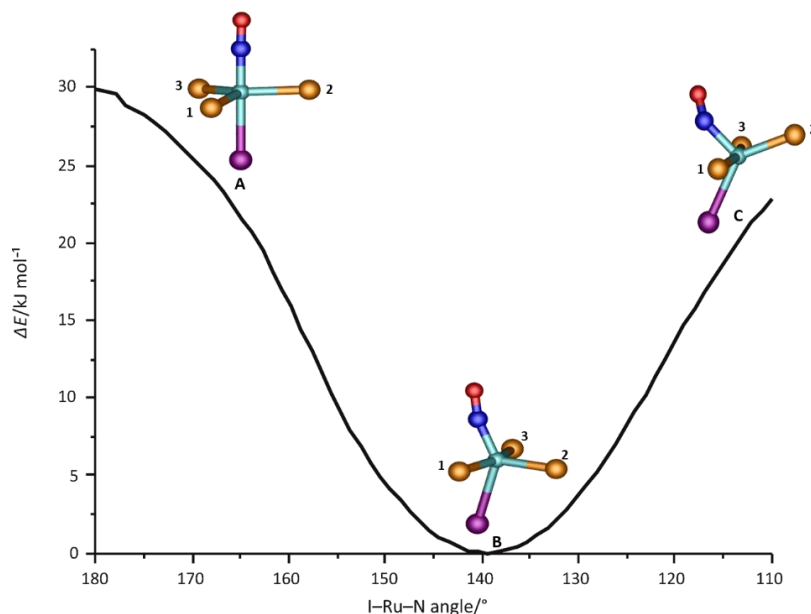


Figure 2.26: I–Ru–N bending potential of **9b**. Calculated using the def2-TZVP basis set and the BP86 functional with the COSMO solvation model and dispersion correction.

The correlation of the Ru–N–O and the I–Ru–N angle becomes even more obvious when the two angles are plotted against each other (FIGURE 2.27). In the case of an I–Ru–N angle of 180° the RuNO moiety is almost linear aligned as well and deviates with a decreasing I–Ru–N angle until it reaches 164°. The Ru–N–O angle remains constant until the I–Ru–N angle reaches 125°. Further decrease of the I–Ru–N angle leads to further deviation of the Ru–N–O angle.

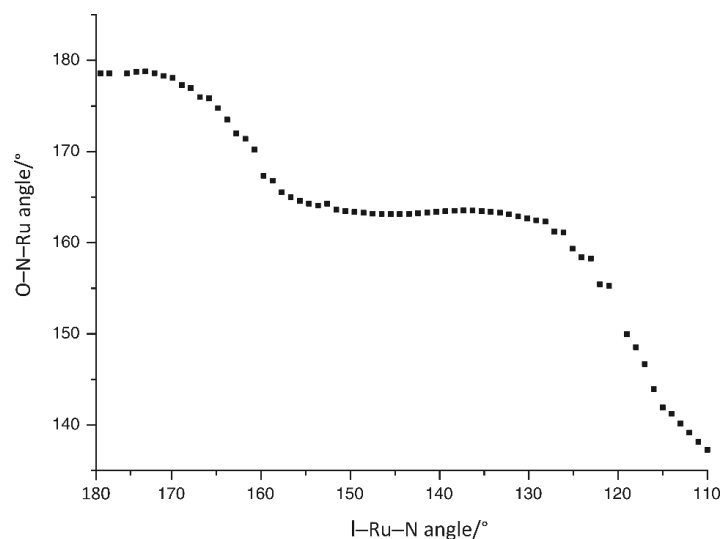


Figure 2.27: The Ru–N–O angle as a function of the I–Ru–N angle.

To explain the preference of a Ru–N–O angle of 164°, a relaxed surface scan of the Ru–N–O angle of structure **B** was performed (FIGURE 2.28). For a linear NO group a square pyramid is adopted and the structure has a low potential of 3 kJ mol⁻¹. Upon decreasing the Ru–N–O angle the I–Ru–N angle decreases as well, while the P1–Ru–P3 angle remains the same. Again the minimum structure proves

Results

to be a square pyramid with a slightly bent NO group (163°) in the plane, whereby the oxygen points toward P3 (torsion angle O–N–Ru–P3 = 19°). This torsion angle decreases with decreasing Ru–N–O angle. For a Ru–N–O angle of 130° the potential is over 20 kJ mol^{-1} and the NO ligand bisects the P2–Ru–P3 plane.

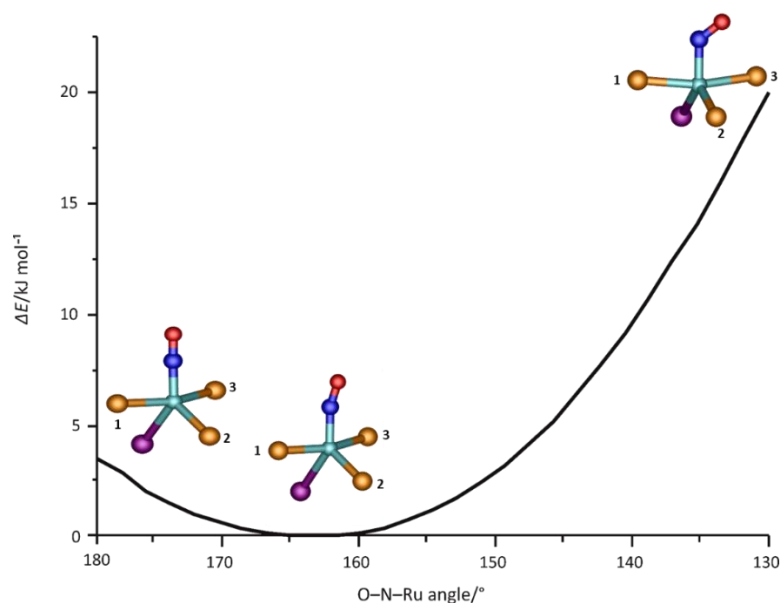


Figure 2.28: Ru–N–O bending potential of **9b**. Calculated using the TZVP basis set and the BP86 functional.

2.14.2 The structure of $[\text{Ru}(\text{NO})_2(\text{PPh}_3)_2\text{SO}_4]$ (**16**)

In the crystal structure **16** is octahedral with two rotationally disordered nitrosyl ligands (see FIGURE 2.16). Thus structure solution can either result in a conformer with two unequally coordinated nitrosyls (Ru–N1–O1 angle 130° and Ru–N2–O2 angle 172° , **D**) or a conformer with two equally coordinated nitrosyl ligands (Ru–N–O angle 154° , **E**). On attempts to model both conformers using the TZVP basis set, only **D** is found as minimum structure, whereas **E** converges into **D** on refinement. Upon application of the def2-TZVP basis set both conformers are minima on the conformational hypersurface with **D** being the global minimum, and **E** being at some 19 kJ mol^{-1} less stable. FIGURE 2.29 displays the two calculated structures.

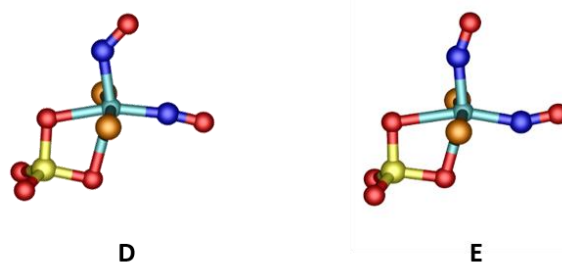


Figure 2.29: Possible structures for **16**. Calculated using the def2-TZVP basis set and the BP86 functional with the COSMO solvation model and dispersion correction.

Results

Octahedral symmetry is unusual for $\{\text{Ru}(\text{NO})_2\}^8$ species and the only hexa-coordinated compound known in literature is the dimer $[\{\text{RuCl}_2(\text{NO})_2(\text{THF})\}_2]$ with two unequal nitrosyls.^[83] Normally $\{\text{MNO}\}^8$ species prefer tetra- or penta-coordination to reduce the electron density along the z axis (definition of the z axis along the Ru–N bond). The penta-coordinated isomer of **D** (isomer **F**) was calculated with DFT by cleaving one Ru–O bond in **D**. Upon refinement the oxygen folds out of the yz plane to minimize the antibonding interaction on the z axis (FIGURE 2.30).

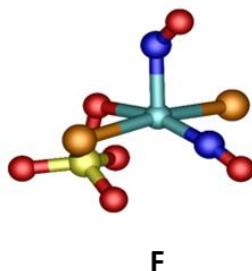


Figure 2.30: The penta-coordinated isomer of **D** (**F**). Calculated using the def2-TZVP basis set and the BP86 functional with the COSMO solvation model and dispersion correction.

To analyze the electron density along the z axis of **F**, its electronic potential surface (EPS) was mapped and compared to the EPS of $[\text{Ru}(\text{NO})(\text{PPh}_3)_2]$ (**7c**) and $[\text{Ru}(\text{NO})(\text{L}^{\text{Me}})_4]^+$ (**10**) (FIGURE 2.31). The tetra-coordinated $\{\text{RuNO}\}^8$ compound **7c** readily reacts with a fifth ligand. This reaction behavior is consistent with the low electron density along the z axis in **7c** (colored in green shades). In both penta-coordinated compounds **10** and **F** a high electron density is found along the z axis (colored in shades of red), avoiding the addition of a sixth ligand. With that in mind the hexa-coordination of **16** is even more surprising.

To verify if the hexa-coordinated species found in the crystalline structure represents also the energetic minimum in solution, the influence of solvation in polar and nonpolar solvents (water, ethanol and toluene) on **D** and **F** was investigated. Global minima for both structures can only be located by application of the COSMO solvation model with the parameters of toluene, **F** being only 5 kJ mol^{-1} less stable than **D**. When the COSMO solvation model with the parameters of ethanol and water is applied the refinement of **D** converges into **F** which is 69 kJ mol^{-1} more stable in water than in toluene.

Results

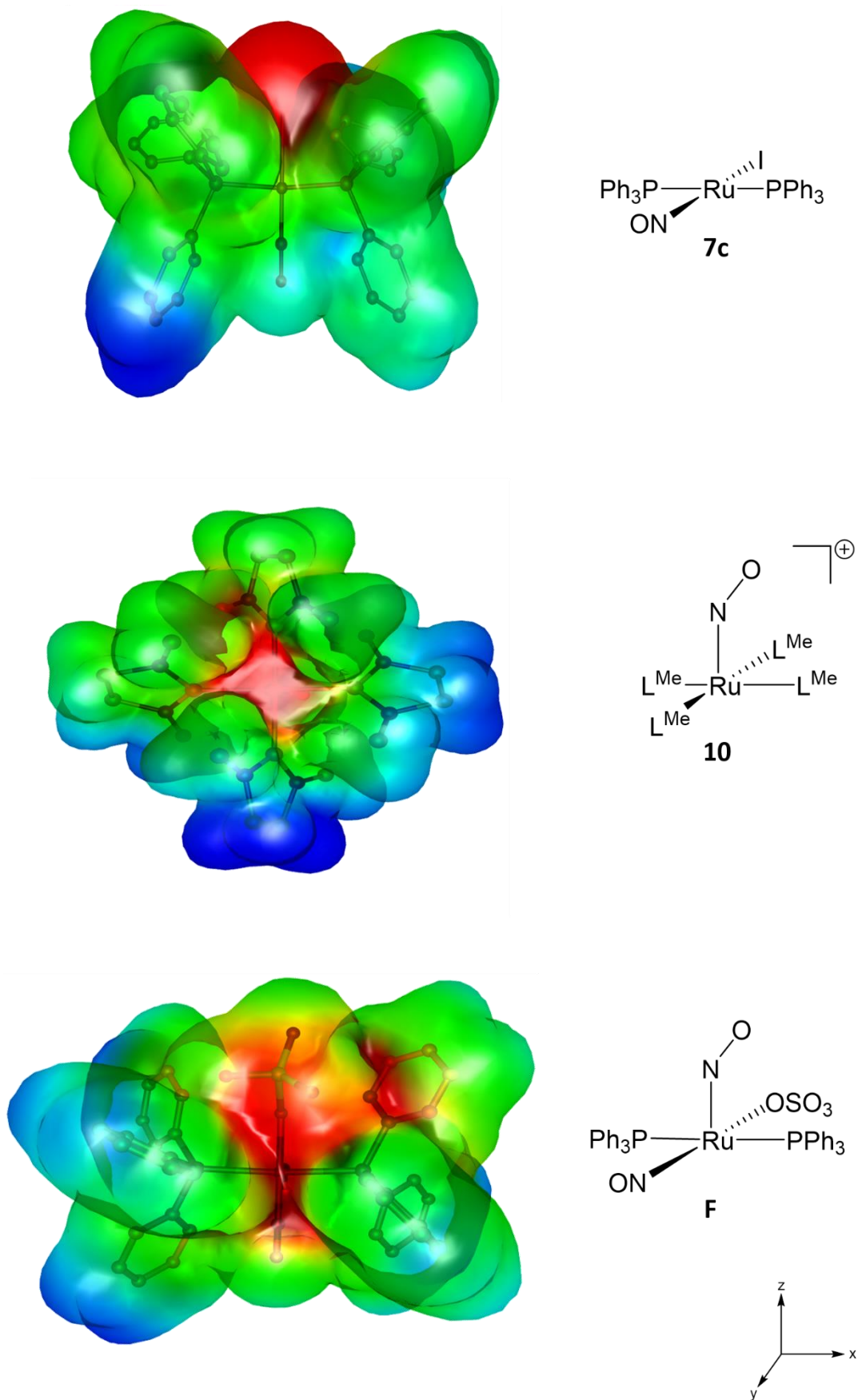


Figure 2.31: Electrostatic potential surface map of **7c**, **10** and the penta-coordinated isomer of **16** (**F**) with view along the z axis. Calculated using the def2-TZVP basis set and the BP86 functional.

3 Discussion

3.1 Comparison of the ligand properties of phosphanes and NHCs and their influence on the reactivity and the structure of the $\{\text{Ru}(\text{NO})_n\}^m$ compounds

Both reactivity and structural properties of the $\{\text{Ru}(\text{NO})_n\}^m$ compounds in this work are influenced mainly by the co-ligands. Thus, the ligand properties of the triphenylphosphane and the NHC derivatives will be compared and their effects on the structure and the reaction behavior of the $\{\text{Ru}(\text{NO})_n\}^m$ compounds will be discussed. Furthermore, the impact of the halogenido ligand is analyzed.

3.1.1 Comparison of the ligand properties of phosphanes and NHCs

Phosphanes and NHCs are neutral two-electron spectator ligands and their electronic and steric properties can be tuned by varying the substituent R and, in the case of the NHC, the properties of the ring (size, aromaticity). In phosphanes, a change of the substituent causes a change, not only in the steric, but also in the electronic effect of the ligand, since the R group that is varied is directly attached to the donor atom. Phosphanes are both σ donor and weak π acceptor ligands, whereby the π acidity of the phosphanes is the result of their unoccupied σ^* orbitals. The electronic and steric effects of different substituents in phosphanes have been estimated by Tolman *et al.* According to Tolman, triphenylphosphane is a rather moderate σ donor that disables other ligands from coordinating and thus, stabilizes low-coordinated species due to its steric demand.^[136–138]

In NHCs, the substituents are attached to atoms two bonds away from the donor atom, thus, a change of the substituent causes a steric, rather than an electronic change. For a significant change in the electronic effect, one has to change the nature of the ring. NHCs are σ donor and π acceptor ligands as well. The electronic effects of NHCs have been estimated by a Tolman-type method.^[139] Since the NHC carbene is much more readily protonated than PR_3 , the σ -donor power of the NHC lone pair is obviously much stronger than for PR_3 . The potential π acceptor orbitals in NHCs are the two C-N σ^* orbitals and the carbon p_π orbital. Calculations argue for stronger and for weaker π -acceptor power for NHCs than for PR_3 , but, in general, NHCs are well accepted as being much stronger net donors than phosphanes.^[86,140–142] In contrast to phosphanes, most NHCs can dimerize to derivatives of electron rich tetraaminoethylenes (enetetramines) (see INTRODUCTION, Chapter 1.4.2). In fact the NHC complexes in this work were obtained by the dimer fragmentation of the enetetramines L^{Me}_2 , L^{Et}_2 , L^{nPr}_2 and L^{Bn}_2 (**1a–d**). The dissociation of these enetetramines to free carbenes displays a possible pathway for these reactions, but experimental and theoretical studies revealed that no dissociation occurs in the absence of an electrophile.^[91,143] These results were confirmed by the NMR spectra of **1a–d** that

show no evidence of dissociation. Thus, it is most likely that the formation of the NHC complexes in this work follows the mechanism postulated by Lappert *et al.* (see INTRODUCTION, Chapter 1.4.2).

3.1.2 Co-ligand influence in the $\{\text{Ru}(\text{NO})_n\}^m$ compounds

Several ruthenium complexes with phosphane ligands, of the general composition $[\text{RuX}(\text{NO})\text{L}_2]$, are known in literature.^[80,144] In contrast, $[\text{RuCl}(\text{NO})\text{L}^{\text{Bn}}_2]$ which has not been structurally characterized as yet, is the only known NHC representative of this species.^[120] Both, the triphenylphosphane compounds **7a–c** and the 1,3-dibenzyl-imidazoline-2-ylidene derivatives **8a, b** in this work, were synthesized by the reduction of **6a–6c** with tetrakis(dimethylamino)ethylene (tden) similar by a route similar to that of Lappert *et al.* All attempts to obtain $[\text{RuX}(\text{NO})\text{L}^{\text{R}}_2]$ compounds with smaller substituents ($\text{R} = \text{Me}, \text{Et}$ or $n\text{Pr}$) resulted in the penta-coordinated $[\text{Ru}(\text{NO})\text{L}^{\text{R}}_4]\text{X}$ species (**10a, 10b, 11a–c, 12a–c**). Thus, only the steric demand of the L^{Bn} ligand is sufficient enough to stabilize an electronically and coordinatively unsaturated complex of the $[\text{RuX}(\text{NO})\text{L}_2]$ type.

7a–c and **8a, b** are isostructural and adopt square-planar structures with *trans*-phosphanes/NHCs and the halogen *trans* to the linearly coordinated NO. The NHC compounds **8a** and **8b** are disordered, thus, no meaningful comparison of bond length and angles to the phosphane adducts is possible. In general, the nitrosyl-stretching frequencies of the NHC compounds are shifted about 100 cm^{-1} to lower frequencies in comparison to the phosphane analogs. This shift is due to the increased electron density in the π^* orbitals of the nitrosyl ligand caused by the higher σ basicity of the NHC ligands.

All tetra-coordinated $\{\text{RuNO}\}^8$ compounds in this work are extremely sensitive toward oxygen and moisture. $[\text{RuX}(\text{NO})(\text{PR}_3)_2]$ compounds are known to react with oxygen to yield the O_2 adducts, in which the oxygen is side-on coordinated. Those compounds are stable as solids, but while the PPh_3 derivatives are also stable in solution, $[\text{RuCl}(\text{NO})(\eta^2\text{-O}_2)(\text{P}i\text{Pr}_3)_2]$ slowly decomposes in solution to give the corresponding phosphanoxides $\text{OP}i\text{Pr}_2\text{R}$.^[60,144] When the NHC compounds **8a** and **8b** were exposed to air or dry oxygen no defined species could be isolated. A reason for that might be the extreme oxygen sensitivity of the NHC ligand that accelerates decomposition.

Upon the addition of triphenylphosphane, a third phosphane ligand is added to **7a** and **7c** to form the trisphosphane compounds $[\text{RuX}(\text{NO})(\text{PPh}_3)_3]$ ($\text{X} = \text{Cl}, \text{I}$; **9a, 9b**). Compounds **9a** and **9b** adopt a square-pyramidal structure and the coordination mode of the nitrosyl stays almost linear. When the linear coordination of the nitrosyl ligand to the ruthenium is assigned as NO^+ , the additional PPh_3 ligand raises the number of electrons from 16 to 18 and the oxidation state of the ruthenium stays 0. When the square-planar NHC compounds **8a** and **8b** are reacted with an excess of L^{Bn}_2 (**1d**), the halogen is displaced and the tetracarbene compounds $[\text{Ru}(\text{NO})(\text{L}^{\text{Bn}})_4]\text{X}$ ($\text{X} = \text{Br}, \text{I}$; **13a, 13b**) are formed. In contrast to the phosphane derivatives, the Ru–N–O angle decreases heavily from linearity to 130° , when the coordination number is raised (**8a, b** \rightarrow **13a, b**). Thus, assigning the bent coordinated NO as NO^- , the

reaction **8a, b** \rightarrow **13a, b** can be treated as an intramolecular redox process, in which the nitrosyl gets reduced from NO^+ to NO^- , the ruthenium oxidizes from 0 to +II and the number of electrons stays 16. Correlations of electron counts of complexes and the coordination modes of NO were reported earlier, and were termed as “stereochemical control of valence” by Enemark and Feltham *et al.*^[35] The formation of the tetraphosphane species $[\text{Ru}(\text{NO})(\text{PPh}_3)_4]^+$ was never detected which can probably be assigned to steric requirements. Indeed the UV-vis spectra recorded in dependence of phosphane concentration show three isosbestic points confirming the existence of exactly two species in solution even in the presence of an excess of triphenylphosphane (see RESULTS, Chapter 2.11).

The square-planar species **7c**, **8a** and **8b** also react with $\text{NO}(\text{BF}_4)$ to form penta-coordinated $\{\text{Ru}(\text{NO})_2\}^8$ compounds of the $[\text{RuX}(\text{NO})_2\text{L}_2]^+$ type. Klüfers *et al.* synthesized several phosphane compounds of this type and discussed two possible structure types: a square pyramid with two unequally coordinating nitrosyls and a trigonal bipyramid with two almost linearly coordinating nitrosyls. Experimental and theoretical studies showed that the adopted structure is primarily influenced by the halogenido ligand X (X = Cl, Br, I) and secondarily by the electronic character of the phosphane ligand. If X is a strong π base, the electron density on the metal is increased and therefore the π back donation to the two nitrosyls is strengthened. Thus, the strong π back donation of I stabilizes two nearly linearly coordinated NO groups in the plane of a trigonal bipyramid. Formally, compounds of this type are regarded as derivations of Ru d^8 coordinating to two NO^+ ligands. For Cl and Br the π basicity is not sufficient enough to stabilize two NO^+ ligands and the coordination mode of one nitrosyl is changed to a bent coordination and the system adopts square-pyramidal coordination. In the ideal case those compounds can be regarded as Ru d^6 coordinating to one NO^+ - and one NO^- ligand.^[34,80] The results of this work confirm this thesis as well. The phosphane complex **17** adopts the trigonal bipyramid, due to the high π basicity of the iodido ligand. In contrast, the $\{\text{Ru}(\text{NO})_2\}^8$ NHC compounds **18a** and **18b** are square-pyramidal for X = Cl and Br.

The different reaction behaviors of the square-planar $\{\text{RuNO}\}^8$ NHC and the phosphane species are depicted in FIGURE 3.1.

Discussion

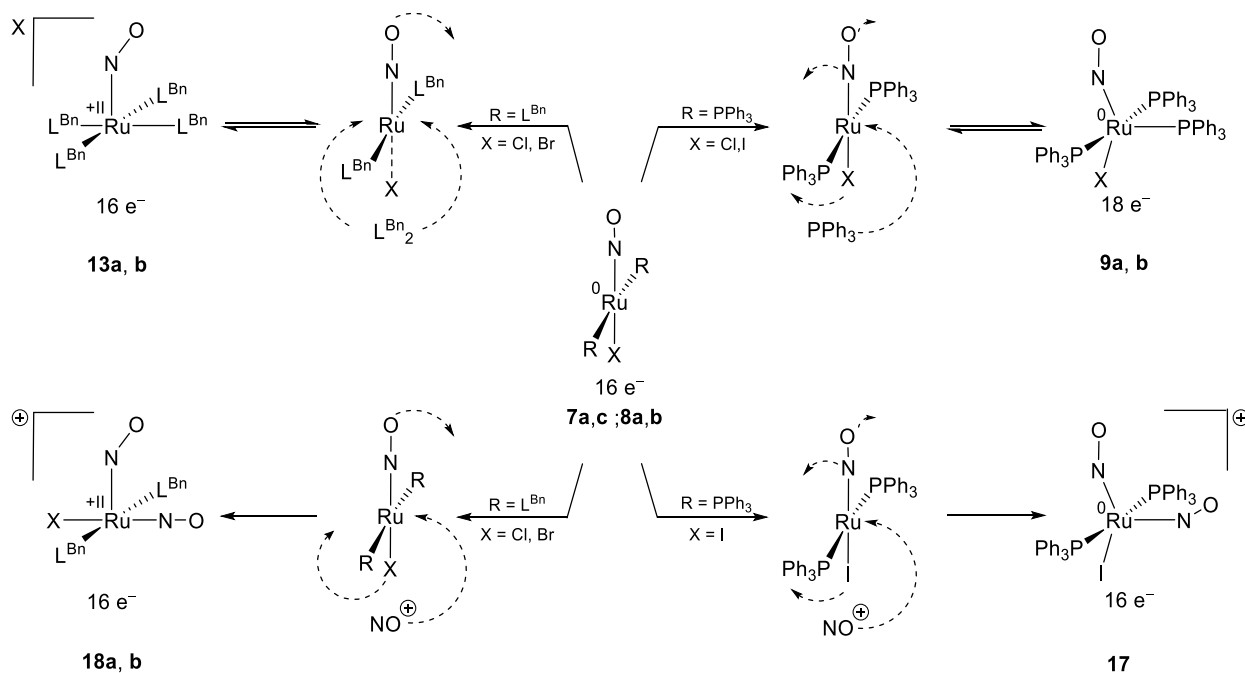


Figure 3.1: Different reaction behaviors of the square-planar $\{\text{RuNO}\}^8$ species **7a**, **8a** and **8b**.

The penta-coordinated $\{\text{Ru}(\text{NO})_2\}^{10}$ compounds of the type $[\text{Ru}(\text{NO})_2\text{L}_2]$ are particularly suitable for a comparison of the ligand properties of triphenylphosphane and the carbene ligands of this work, since they are the only co-ligands in these systems. $[\text{Ru}(\text{NO})_2(\text{PPh}_3)_2]$ (**19**) has been known a long time in the literature and was synthesized by a route by Gaughan *et al.* The NHC derivatives were obtained from **19** by ligand substitution. In the case of L^{nPr_2} , only the monocarbene complex **23** was obtained due to the steric hindrance of the *n*Pr group. All $\{\text{Ru}(\text{NO})_2\}^{10}$ compounds in this work are distorted tetrahedral with two almost linearly coordinating nitrosyl ligands. TABLE 3.1 summarizes the structural parameters and the nitrosyl-stretching frequencies. The angles are defined as depicted in FIGURE 3.2.

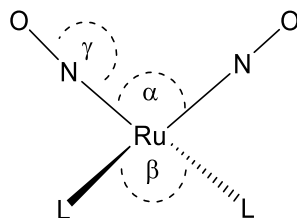


Figure 3.2: Definition of the relevant angles in the tetrahedral $\{\text{Ru}(\text{NO})_2\}^{10}$ species.

Discussion

Table 3.1: Selected structural parameters and nitrosyl-stretching frequencies of the {Ru(NO)₂}¹⁰ compounds **19–23**.

	α	β (L–Ru–L)/°	γ (Ru–N–O)/°	Ru–N/Å	N–O/Å	$\tilde{\nu}(\text{NO})/\text{cm}^{-1}$
[Ru(NO)(PPh ₃) ₂] (19)	141.33	105.08	188.13 190.90	1.79 1.82	1.18 1.16	1652 1605
[Ru(NO) ₂ (L ^{nPr})(PPh ₃)] (23)	129.32	90.75	176.15 176.3	1.78 1.78	1.19 1.20	1625 1592
[Ru(NO) ₂ (L ^{Bn}) ₂] (22)	133.40	92.88	176.0 175.3	1.78 1.77	1.20 1.20	1599 1549
[Ru(NO) ₂ (L ^{Et}) ₂] (21)	128.77	89.40	175.2 176.0	1.78 1.77	1.21 1.20	1600 1550
[Ru(NO) ₂ (L ^{Me}) ₂] (20)	127.33	90.50	176.88 175.0	1.78	1.21	1590

In general, the N–Ru–N angles are wider than the L–Ru–L angles in all compounds. It is striking that all angles in the NHC derivatives are smaller than in **19**. This effect is due to the stronger σ basicity of the NHC ligands and will be discussed by means of the molecular orbitals in Chapter 2.2.2. Due to the higher σ basicity of the NHC ligands, the electron density on the metal increases and the π back donation in the $\pi^*(\text{NO})$ orbitals becomes stronger, this leads to shorter Ru–N distances, longer N–O distances and lower nitrosyl-stretching frequencies of the NHC derivatives.

3.2 The RuNO moiety in the context of the MO theory

Due to its redox activity, the nitrosyl ligand can bind to a metal center in three binding modes: bent as ¹NO[−] in a low-spin complex, weakly bent as ³NO[−] diradical in a high-spin complex or linear as ¹NO⁺. In ruthenium-nitrosyl complexes, the ¹NO⁺ - and the ¹NO[−]-binding modes are possible. For a better understanding of the different electronic states of the RuNO moiety the relevant MO interactions of NO and Ru were considered in the context of the MO-theory. In general, the Ru–NO bond is based on the donation of electron density from the σ orbital on the N atom to the ruthenium ($d+\sigma(\text{NO})$) and on the back donation from the ruthenium to the π^* orbitals of the NO ($d+\pi^*(\text{NO})$). Especially the nature of the $d+\pi^*(\text{NO})$ interactions depends on the angle of the RuNO moiety. In a linear RuNO moiety both $d+\pi^*(\text{NO})$ interactions have π character, but bending replaces one π interaction by a σ interaction ($d_{z^2}+\pi^*(\text{NO})$).

3.2.1 Mononitrosyl compounds

Tetra-coordinated mononitrosyl compounds

For the following discussions the z axis is defined along the M–N vector of the RuNO group. In the case of the tetra-coordinated species the coordinate system is inconsistent with the conventional axis choice for $SP-4$ symmetry leading to the orbital transformations $d_{z^2} \rightarrow d_{x^2}$ and $d_{x^2-y^2} \rightarrow d_{z^2-y^2}$.

The tetra-coordinated $\{\text{RuNO}\}^8$ species in this work are educts for both the penta-coordinated mononitrosyl- and the penta-coordinated dinitrosyl compounds. A square-planar structure with a linear nitrosyl is characteristic for tetra-coordinated $\{\text{RuNO}\}^8$ species, since only the energetically favorable orbitals are filled and the antibonding orbitals are empty. The molecular orbital scheme of $[\text{Ru}(\text{NO})(\text{PPh}_3)_2]$ (**7c**) is depicted in FIGURE 3.3. The two occupied frontier orbitals HOMO and HOMO–1 are non-bonding and have a d_{x^2} and d_{xy} character, the subjacent orbitals represent the two back-donating interactions of the d_{xz} and d_{yz} orbitals with the corresponding π^* orbitals of the NO ligand. Since there are clearly two strong π back donations from the metal to the NO ligand, the nitrosyl can be equated with a formal NO^+ ligand. The two unoccupied frontier orbitals have antibonding $d_{yz}-\pi^*(\text{NO})$ and $d_{xz}-\pi^*(\text{NO})$ character and are degenerated. The energetically most unstable interaction is the antibonding $d_{z^2}-\sigma^*(\text{NO})$ orbital. The energetic order of the MOs of the tetra-coordinated NHC compounds is analog to the one depicted.

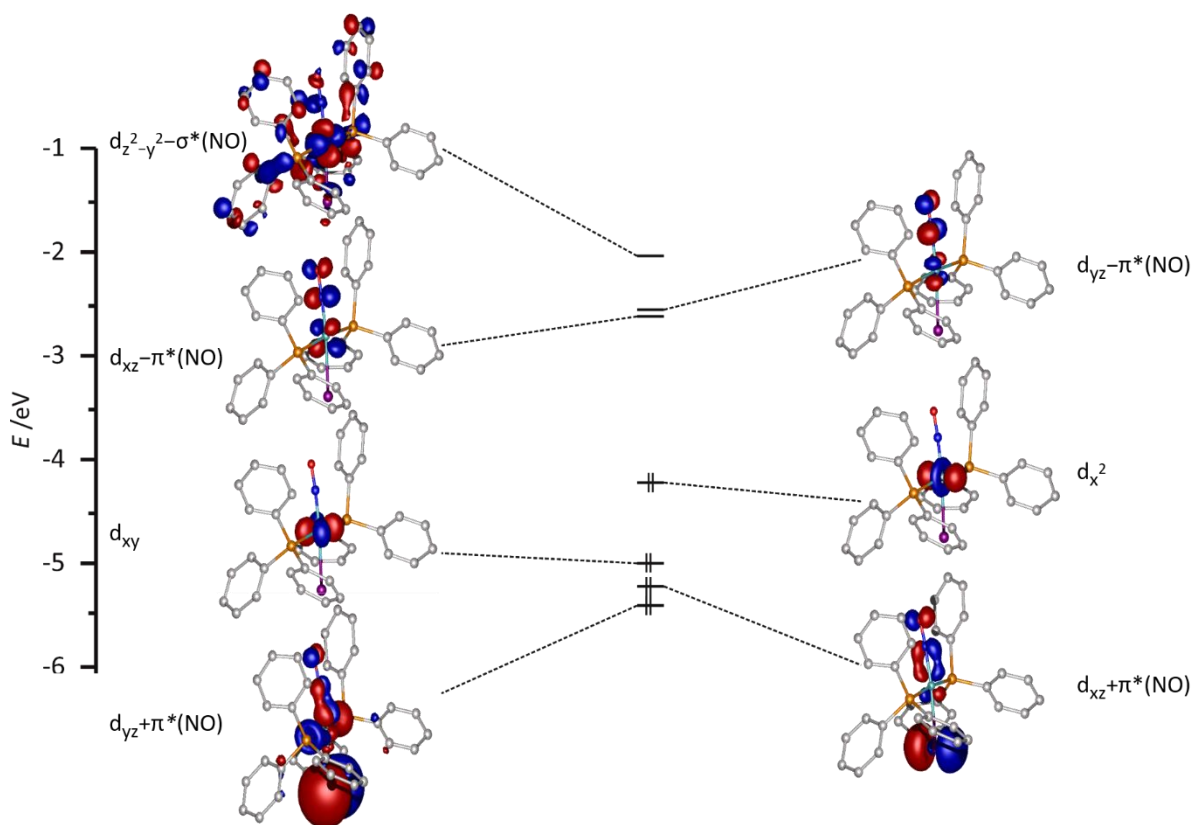


Figure 3.3: Molecular orbital scheme of the frontier orbitals of $[\text{Ru}(\text{NO})(\text{PPh}_3)_2]$ (**7c**). Calculated using the def2-TZVP basis set and the BP86 functional with the COSMO solvation model and dispersion correction.

Penta-coordinated mononitrosyl compounds

For penta-coordinated mononitrosyls four structural conformations are possible: A square pyramid with the NO in apical or equatorial position and the trigonally bipyramidal conformation with the NO ligand in the apical or equatorial position. The square pyramid with a bent RuNO moiety in the apical position and the trigonal bipyramid with a linear nitrosyl in the equatorial position are the characteristic coordination types for $\{MNO\}^8$ compounds (see INTRODUCTION, Chapter 1.3.2, FIGURE 1.6). The penta-coordinated phosphane compounds $[RuCl(NO)(PPh_3)_3]$ (**9a**) and $[RuI(NO)(PPh_3)_3]$ (**9b**) are square-pyramidal with a slightly bent RuNO moiety in the plane, while the NHC derivatives are square-pyramidal with a strongly bent RuNO moiety in the apical position. The coordination motif adopted by **9a** and **9b** is unknown for $\{RuNO\}^8$ species in literature as yet. For a better understanding of this unusual structure type the molecular orbital schemes of $[Ru(NO)(L^{Me})_4]^+$ (**10**) and $[RuI(NO)(PPh_3)_3]$ (**9b**) will be compared. Furthermore, the molecular orbitals of the structures **A–D** which were calculated by scanning the I–Ru–N and the Ru–N–O angle, will be discussed (see RESULTS, Chapter 2.14.1).

Several theoretical studies dealt with the question: Why do the nitrosyls bend, when they do?^[35,72,73,145]

In general, the bending of the nitrosyl depends mainly on the bonding and antibonding interactions of the metal d_{z^2} and d_{xz} orbitals with the σ and π^* orbitals of the nitrosyl. Enemark and Feltham postulated that the structure of penta-coordinated $\{MNO\}^8$ compounds will depend on the character of the highest occupied orbital (see INTRODUCTION, Chapter 1.3.2). The square pyramid with a bent RuNO moiety is predicted for a HOMO with $d_{xz}-\pi^*(NO)$ character and the trigonal bipyramid for one with $d_{z^2}-\sigma(NO)$ character.^[35] Hoffmann *et al.* constructed a molecular orbital model of penta-coordinated nitrosyl compounds, wherein the bending of the nitrosyl depends on the energy of the metal orbitals d_{z^2} and d_{xz} relative to those of the σ and π^* orbitals of the nitrosyl ligand. FIGURE 3.4 illustrates the interaction diagram for a linear nitrosyl in the apical position of a square pyramid postulated by Hoffmann *et al.* For an $\{MNO\}^8$ species the antibonding $d_{z^2}-\sigma(NO)$ is occupied and bending the M–N–O angle by moving the nitrosyl in the xz plane has several effects on the metal-nitrosyl orbital interactions (FIGURE 3.4, right):

- (a) The antibonding $d_{z^2}-\sigma(NO)$ and the bonding $d_{xz}+\pi^*(NO)$ interaction will be weakened.
- (b) The d_{z^2} orbital of the metal will form a new stabilizing interaction with the $\pi^*(NO)$ orbital which was symmetry forbidden in the linear coordination; and the d_{xz} orbital will begin a destabilizing interaction with the $\sigma(NO)$ orbital.^[72]

Discussion

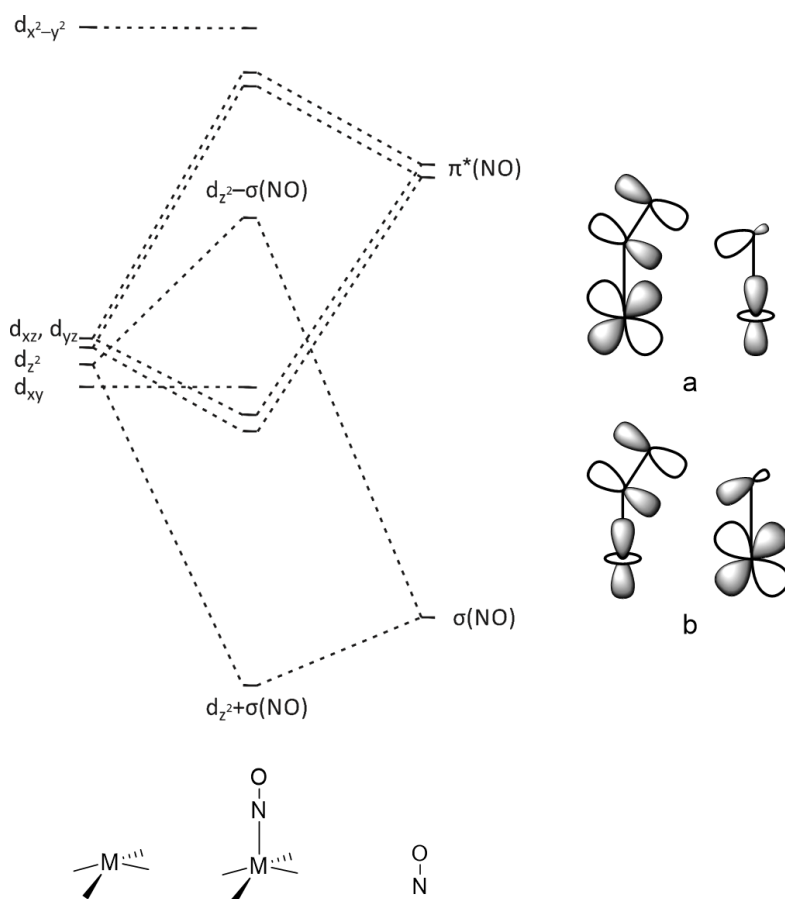


Figure 3.4: Left: Interaction diagram for a linear nitrosyl in the apical position of a square pyramid. Right: Effects of the metal-nitrosyl orbital interactions upon bending: a) Weakening of the antibonding $d_{z^2}-\sigma(\text{NO})$ and the bonding $d_{xz}+\pi^*(\text{NO})$ interaction and (b) enforcement of the former symmetry forbidden bonding $d_{z^2}+\pi^*(\text{NO})$ and antibonding $d_{xz}-\sigma(\text{NO})$ interaction. Depicted from Reference [72].

The higher the d_{z^2} and the d_{xz} lie, the stronger their stabilizing interaction with $\pi^*(\text{NO})$ and the less their destabilizing interaction with $\sigma(\text{NO})$. Thus, raising the energy of d_{z^2} and d_{xz} by strong donors favors the bending of the MNO-moiety in an apical square pyramid. The bending of the MNO-moiety also has consequences for the electronic structure of the nitrosyl itself: The binding interaction of the d_{z^2} orbital increases the electron density in the $\pi^*(\text{NO})$ orbital and, at the same time, the decreasing $d_{xz}+\pi^*(\text{NO})$ interaction reduces the electron density in the $\pi^*(\text{NO})$ orbital. Even though these two trends are directly opposing, the effect set by the d_{z^2} orbital dominates and the nitrosyl group, as a whole, gains electron density from the ML_4 fragment.^[72] This conclusion is in accordance with the low nitrosyl-stretching frequencies of the penta-coordinated $\{\text{RuNO}\}^8$ NHC species in this work.

When the z axis is chosen along the nitrosyl ligand in a trigonal bipyramid with an equatorial nitrosyl, the symmetry is reduced from D_{3h} to C_{2v} and the energetic order of the orbitals is analog to the one depicted in FIGURE 3.4, except that the d_{xz} and d_{yz} levels are split. Thus, the $d_{z^2}-\sigma(\text{NO})$ interaction is the controlling factor for the nitrosyl bending as well. In contrast to the square pyramid, the energy of the $d_{z^2}-\sigma(\text{NO})$ is lowered significantly in the trigonal bipyramid, since the d_{z^2} and the $d_{x^2-y^2}$ orbital are of a_1 symmetry and the mixing of these orbitals is enabled. This linear combination takes electron density

from the z axis and puts it in the region along the y axis. Thus, the bending of the nitrosyl is far less likely in the equatorial position of a trigonal bipyramid than in the apical site of a square pyramid.^[72] The molecular orbital scheme of the cation $[\text{Ru}(\text{NO})(\text{L}^{\text{Me}})_4]^+$ of **10b** is depicted in FIGURE 3.5. Upon the addition of the two NHC-ligands, a square pyramid is formed and the former HOMO ($d_{x^2-y^2}$) of the square-planar species is raised in energy while the energy of the $d_{z^2}-\sigma(\text{NO})$ is lowered. The bending of the RuNO moiety leads to a new HOMO with $d_{z^2}+\pi^*(\text{NO})$ character as discussed above. The HOMO-1 resembles the bonding interaction of the π^* orbital and the d_{xz} orbital. This interaction is clearly diminished by the bending of the RuNO moiety and has rather σ than π character. Thus, in contrast to the square-planar species only one π back donation from the metal to the nitrosyl remains upon bending the NO ligand ($d_{yz}+\pi^*(\text{NO})$). The molecular orbital scheme of **10b** confirms the predictions of Hoffmann *et al.* for a penta-coordinated $\{\text{RuNO}\}^8$ species with strong donor ligands.

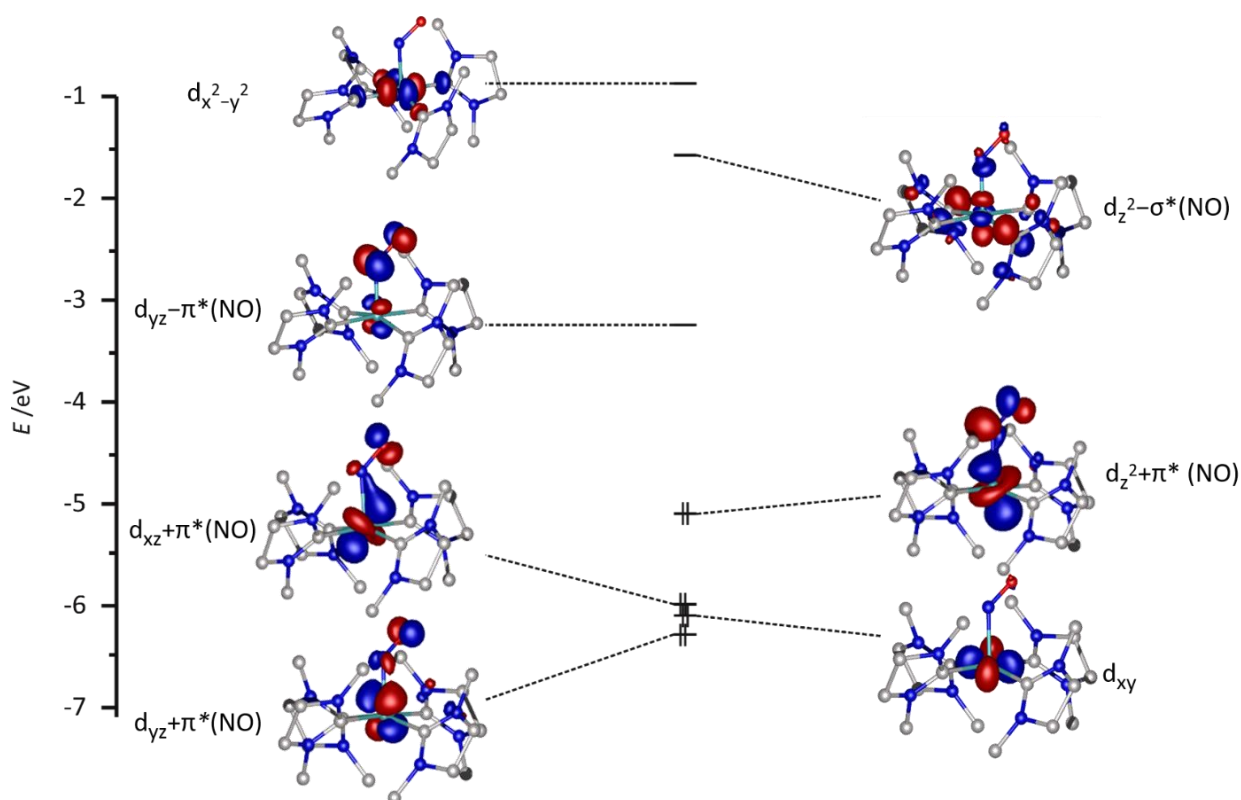


Figure 3.5: Molecular orbital scheme of the frontier orbitals of the cation $[\text{Ru}(\text{NO})(\text{L}^{\text{Me}})_4]^+$ of **10b**. Calculated using the def2-TZVP basis set and the BP86 functional with the COSMO solvation model and dispersion correction.

For an axial NO in a trigonal bipyramid and a basal NO in a square pyramid Hoffmann *et al.* predicted a strong preference for a linear geometry of the MNO moiety. Since the equatorial site of a square pyramid is essentially a perturbation of the apical trigonal bipyramid the following can be applied to both conformational structures. The energetic order for a trigonal pyramidal fragment with C_{3v} symmetry is given in FIGURE 3.6. When the nitrosyl coordinates along the z axis, it strongly bonds to the d_{xz} and d_{yz} orbitals. For a penta-coordinated $\{\text{MNO}\}^8$, system the d_{z^2} orbital in an apical trigonal

Discussion

bipyramid is unfilled. Thus, there is no antibonding interaction analog to the $d_{z^2}-\sigma(\text{NO})$ orbital in the apical square pyramid and the equatorial trigonal bipyramid, that favors bending. Moreover the bending of the MNO-moiety will lead to the loss of the π bonding.^[72]

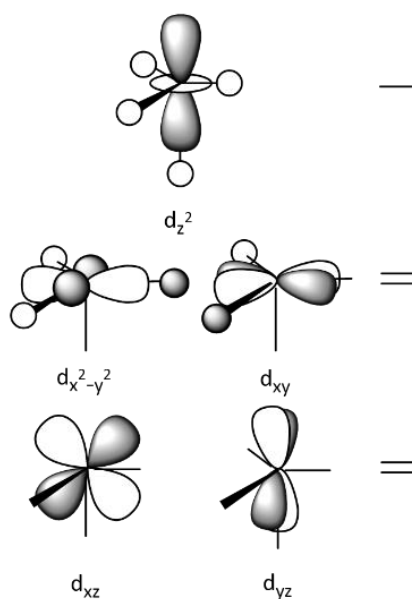


Figure 3.6: Schematic representation and energetic order of the molecular orbitals of a trigonally bipyramidal fragment with C_{3v} symmetry depicted from Reference [72].

The structure of **9b** is a structural intermediate between the equatorial square pyramid and the apical trigonal bipyramid, whereby the Ru–N–O angle deviates from linearity by 15° . FIGURE 3.7 shows the molecular orbital scheme of **9b**. In contrast to the postulations of Hoffmann *et al.*, the HOMO of **9b** has a $d_{z^2}-\sigma(\text{NO})$ character with an antibonding contribution of the p orbital of the iodido ligand.

Discussion

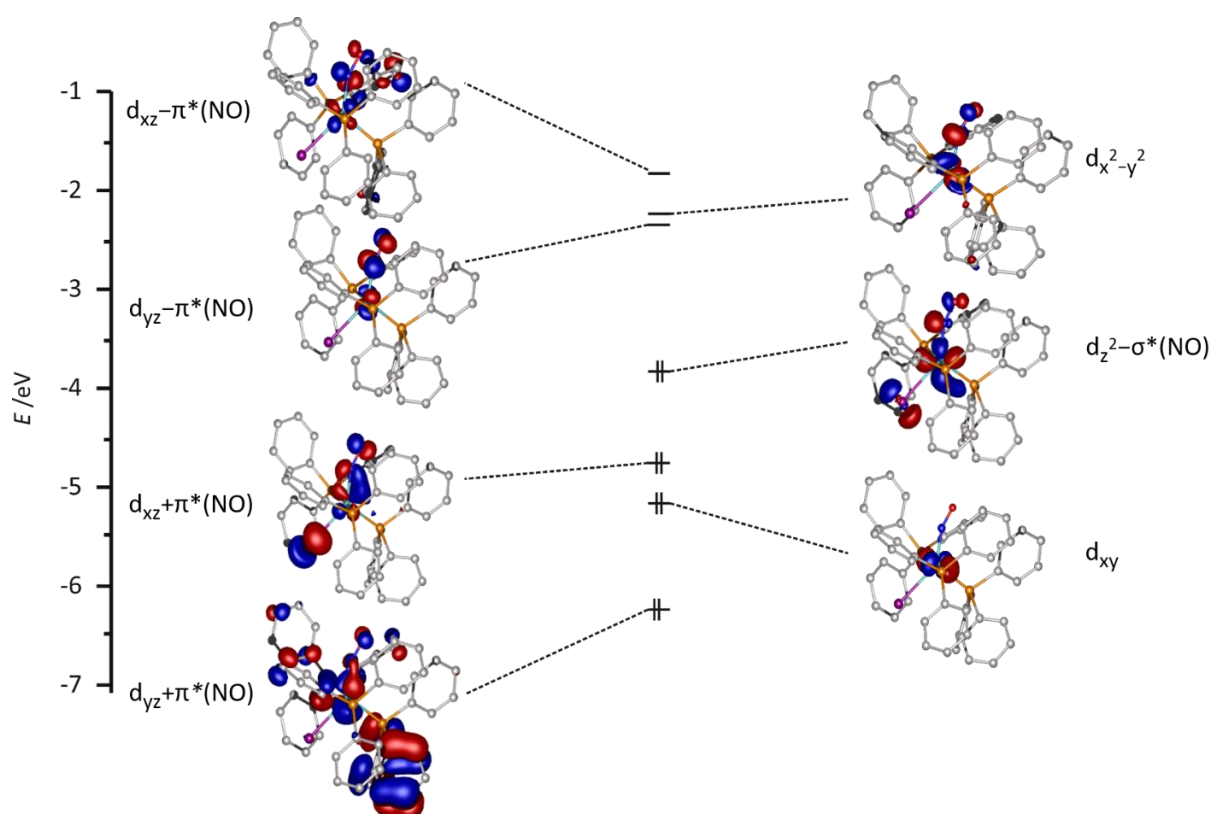


Figure 3.7: Molecular orbital scheme of the frontier orbitals of $[\text{RuI}(\text{NO})(\text{PPh}_3)_3]$ (**9b**). Calculated using the def2-TZVP basis set and the BP86 functional with the COSMO solvation model and dispersion correction.

As mentioned in Chapter 1.3, the complex $[\text{RuH}(\text{NO})(\text{PPh}_3)_3]$ known in literature adopts indeed a trigonal bipyramidal structure with the hydrido and a linear NO ligand in the axial position and three phosphane ligands in the plane. The five occupied frontier orbitals of $[\text{RuH}(\text{NO})(\text{PPh}_3)_3]$ in FIGURE 3.8 match the energetic order of an apical trigonal bipyramid in FIGURE 3.6.

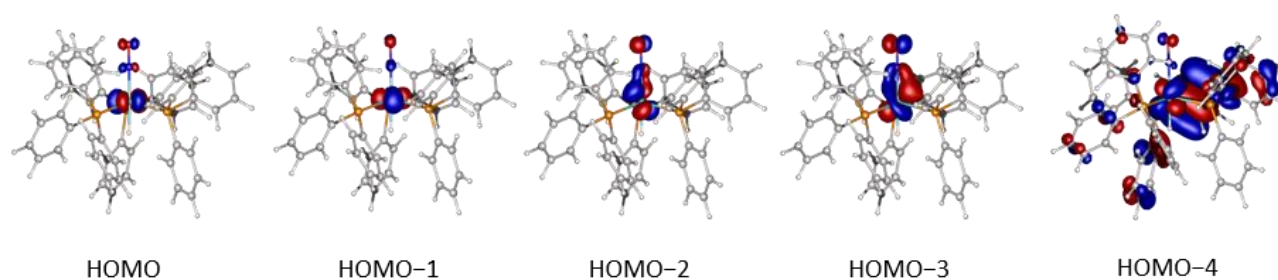


Figure 3.8: Contours of the five occupied frontier orbitals of $[\text{RuH}(\text{NO})(\text{PPh}_3)_3]$. Calculated using the TZVP basis set and the BP86 functional.

Obviously, the only difference between this complex and compounds **9a/b** is the hydrido ligand coordinating *trans* to the nitrosyl ligand. Nevertheless the coordination geometries differ greatly among each other. Considerations on the molecular orbitals of structures **A**, **B**, and **C** of the I-Ru-N angle scan in Chapter 2.13.1 explain the origin of the two different coordination geometries of **9b** and the corresponding hydrido complex (FIGURE 3.9).

As in $[\text{RuH}(\text{NO})(\text{PPh}_3)_3]$, the limiting occupied orbitals of structure **A** show contributions of the $d_{x^2-y^2}/d_{xy}$ orbitals and the π^* orbitals of the nitrosyl, but also of the p orbitals of the iodido ligand. All five interactions have a non-bonding character in regard to the nitrosyl and a rather anti-bonding character in regard to the p orbital of the iodido ligand. The first weak binding interaction can be detected in HOMO-4 between the π^* orbital of the nitrosyl and the $d_{x^2-y^2}$ orbital of the metal. For the minimum structure **B**, the orbitals have contributions of the nitrosyl and the iodido ligand as well, but, in contrast to structure **A**, the energetic order of the d orbitals has changed and only the HOMO has a non-bonding character in regard to the nitrosyl and an anti-bonding character in regard to the iodido ligand. The two subjacent orbitals show positive overlap between the nitrosyl ligand and the d-orbitals and HOMO-3 and HOMO-4 show strong positive π interactions between the iodido ligand and the ruthenium. The orbital composition of structure **C** is similar to that of **B**, even though the π overlap between the nitrosyl and the ruthenium in HOMO-2 and the π overlap between the iodido ligand and the ruthenium in HOMO-3 are smaller. Thus, the five limiting occupied orbitals are energetically most convenient for the minimum structure with an I-Ru-N angle of 140° . The crucial factor for the energetic stabilization of structure **B** is the positive π overlap between the iodido ligand and the ruthenium.

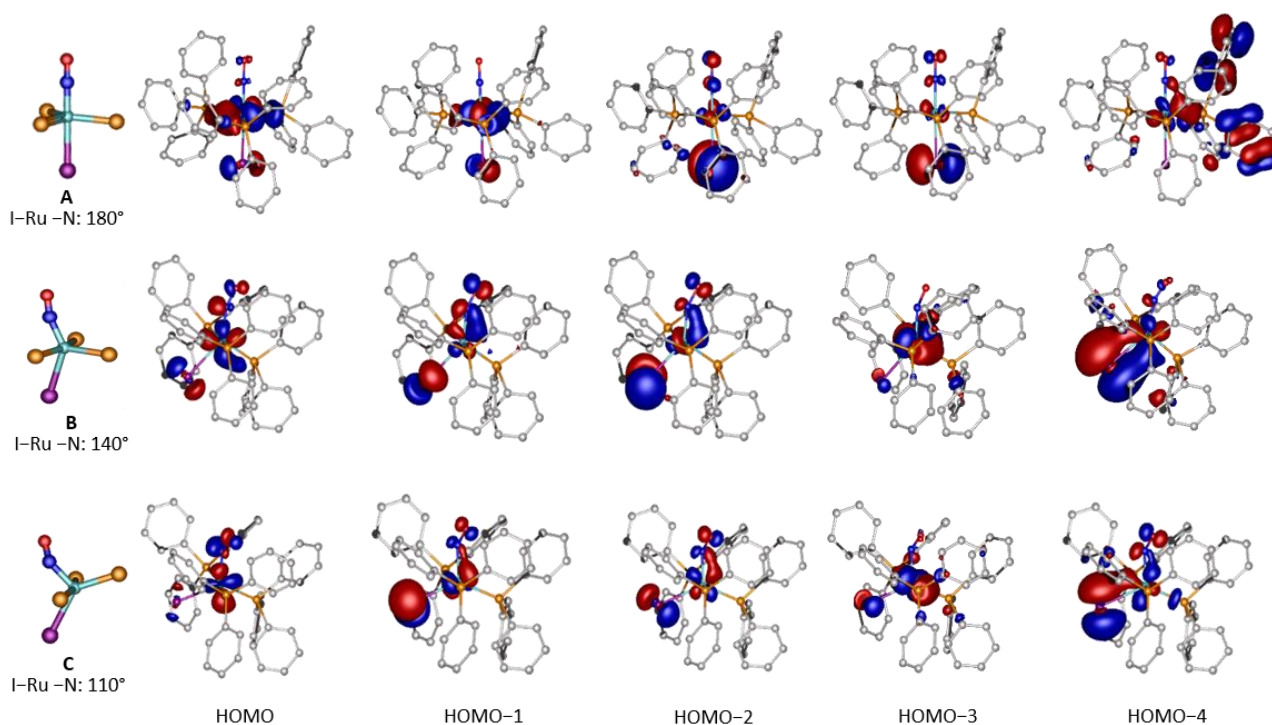


Figure 3.9: Contours of the five limiting occupied orbitals of structures **A**, **B** and **C**. Calculated using the TZVP basis set and the BP86 functional.

FIGURE 2.27 in Chapter 2.13.1 displays the correlation of the Ru-N-O angle on the I-Ru-N angle. A Ru-N-O angle of 164° is preferred for an I-Ru-N angle range of 125° – 160° . The preference for this

particular angle can be clarified by further consideration of the molecular orbitals of structure **B** for the Ru–N–O angles 180°, 160° and 130°. The correlation diagram in FIGURE 3.10 relates the relevant molecular orbitals to each other. The HOMO of all three geometries has an antibonding $d_z^2-\sigma(\text{NO})$ character. The energy of this orbital is lowered upon decreasing the Ru–N–O angle. The interaction between the d_{xy} orbital with the π^* orbitals of the NO ligand drops in energy upon bending, while the $d_{xz}+\pi^*(\text{NO})$ interaction rises in energy. For a Ru–N–O angle of 160° these two orbitals can be regarded as degenerate. The $d_{yz}+\pi^*(\text{NO})$ interaction remains unchanged in energy until the Ru–N–O angle reaches 160° and then strongly increases in energy upon further bending.

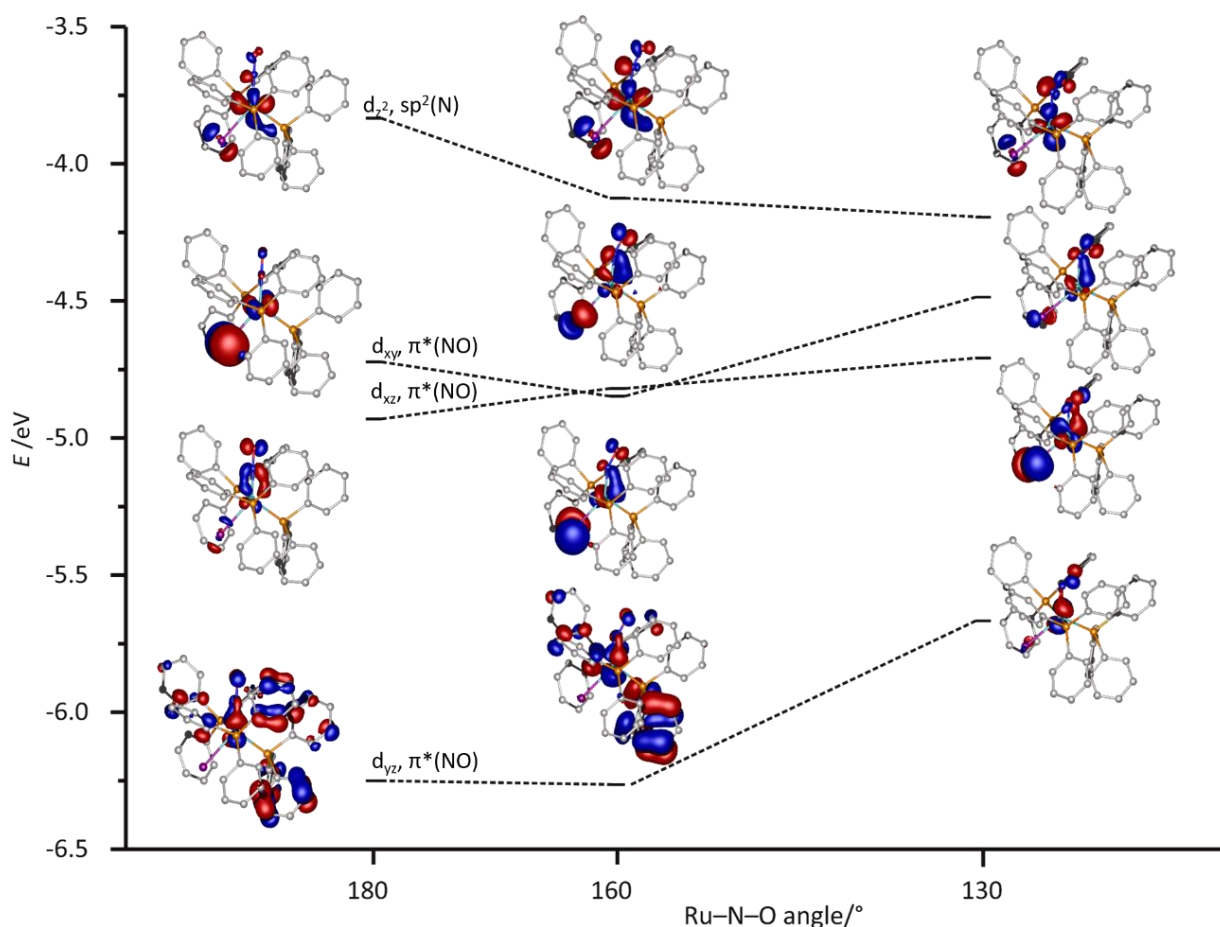


Figure 3.10: Correlation diagram of the molecular orbitals of structure **B** with Ru–N–O = 180°, 164° and 130°. Calculated using the TZVP basis set and the BP86 functional.

In the I–Ru–N angle range of 125°–165°, the HOMO has $d_z^2-\sigma^*(\text{NO})$ character analog to the HOMOs displayed in FIGURE 3.10. For an orbital of this nature a non-linear Ru–N–O angle is energetically more stable since the antibonding character is diminished. But to obtain both π back donations, the Ru–N–O angle must not be smaller than 160°.

In summary the square-pyramidal structure with a slightly bent RuNO moiety in the plane is the most stable structure for $[\text{RuX}(\text{NO})(\text{PPh}_3)_3]$ ($X = \text{Cl}, \text{I}$; **9a**, **9b**), since the π interactions between ruthenium

and both the nitrosyl and the halogenido ligand are ideal, while the antibonding character of the HOMO is minimized.

Hexa-coordinated mononitrosyl compounds

The penta-coordinated NHC compounds in this work can be oxidized with iodine to their corresponding $\{\text{RuNO}\}^6$ species. Upon oxidation the RuNO moiety becomes linear and the counter ion coordinates *trans* to the nitrosyl ligand forming an octahedral complex (FIGURE 3.11).

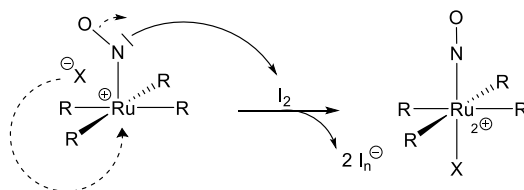


Figure 3.11: Oxidation of the penta-coordinated $\{\text{RuNO}\}^8$ NHC derivatives to the corresponding $\{\text{RuNO}\}^6$ compounds.

The antibonding $d_{z^2}-\sigma(\text{NO})$ interaction is determining for the small Ru–N–O angle in the $\{\text{RuNO}\}^8$ species (FIGURE 3.5). Upon oxidation the electron density on the z axis is diminished and the system relaxes by increasing the Ru–NO angle to linearity and thereby improving the binding $d_{xz}+\pi^*(\text{NO})$ interaction. Furthermore, the reduced electron density on the z axis enables the coordination of a sixth ligand. The molecular orbital scheme of $[\text{RuCl}(\text{NO})(\text{L}^{\text{Et}})_4]^+$ (**15a**) is depicted in FIGURE 3.12 and is consistent with the MO-scheme of a hexa-coordinated $\{\text{RuNO}\}^6$ species postulated by Enemark and Feltham (see INTRODUCTION, Chapter 1.3.1).^[35]

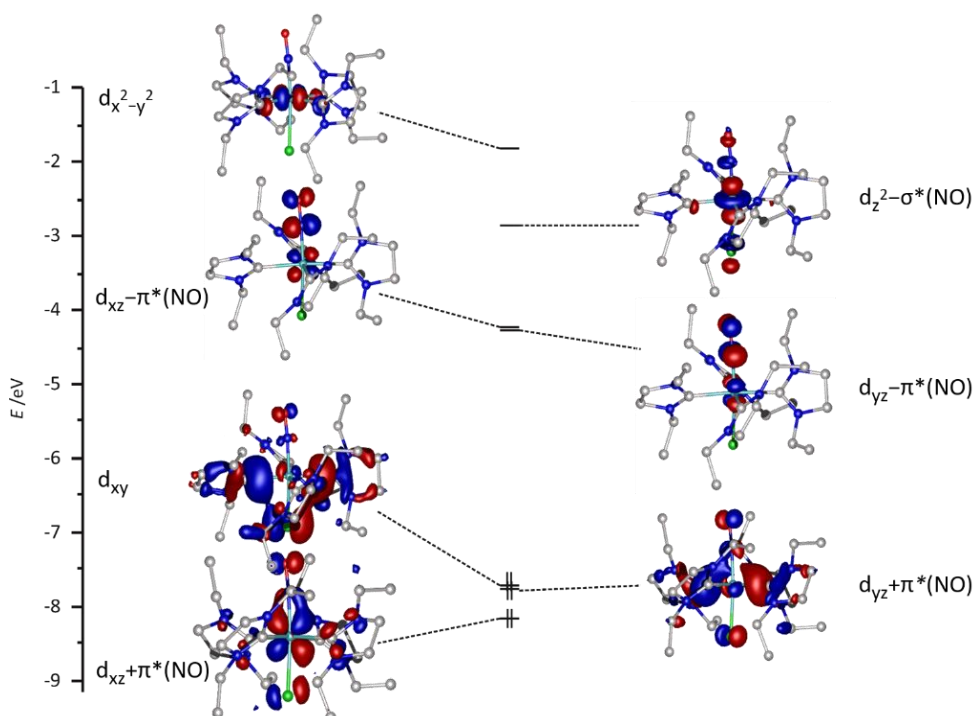


Figure 3.12: Molecular orbital scheme of the frontier orbitals of cation $[\text{RuCl}(\text{NO})(\text{L}^{\text{Et}})_4]^+$ of **15a**. Calculated using the def2-TZVP basis set and the BP86 functional with the COSMO solvation model and dispersion correction.

3.2.2 Dinitrosyls

Tetra-coordinated dinitrosyls

All tetra-coordinated $\{\text{Ru}(\text{NO})_2\}^{10}$ compounds adopt distorted tetrahedral structure with two equally coordinating nitrosyl ligands. This coordination motif is in accordance with the structures of the two literature-known compounds $[\text{Ru}(\text{NO})_2(\text{PPh}_3)_2]$ and $[\text{Ru}(\text{dppf})(\text{NO})_2]$ (see INTRODUCTION, Chapter 1.3.4).^[62,123] For the following discussion the z axis of the molecules is defined as the bisector of the N–Ru–N angle.

Hoffmann *et al.* discussed distortions of tetrahedral geometries in L_2MY_2 systems with $\text{X} = \pi$ acceptor and $\text{L} = \sigma$ donor. For this systems the X–M–X angle is predicted to be larger than the L–M–L angle, due to two effects. First the wider the X–M–X angle the better the stabilizing π interaction between the d_{xz} orbital and the X ligands. The second effect is the mixing of the ruthenium p orbital with the d_{yz} orbital, leading to a better π overlap with the X ligands. This hybridization increases with decreasing L–M–L angle. Both effects reinforce each other and Hoffmann *et al.* came to the conclusion that the angle between the π acceptors in a L_2ML_2 system will be wider than the angle between the σ donors (FIGURE 3.13).^[146]

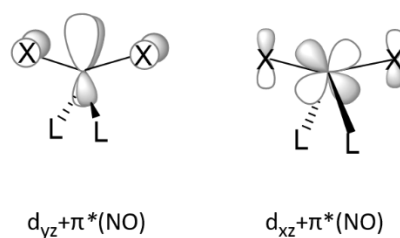


Figure 3.13: Schematic representation of the molecular interactions stabilizing the wide angle between the π acceptors in a tetrahedral X_2ML_2 system with $\text{X} = \pi$ acceptors and $\text{L} = \sigma$ donor. Depicted from Reference [72].

This conclusion is in agreement with the structures of the $\{\text{Ru}(\text{NO})_2\}^{10}$ compounds in this work, the N–Ru–N angles being larger than the C–Ru–C angles. FIGURES 3.14 and 3.15 display the molecular orbital schemes of the occupied frontier orbitals of $[\text{Ru}(\text{NO})_2(\text{PPh}_3)_2]$ (**19**) and $[\text{Ru}(\text{NO})_2(\text{L}^{\text{Et}})_2]$ (**21**). Except the inverted energetic order of the HOMO and the HOMO–1, the order of the orbitals is the same in both complexes. Furthermore, the energy gap between the HOMO–3 and HOMO–4 is greater in **21** than in **19**. As mentioned before the N–Ru–N angle in the NHC derivatives is, in general, up to 10° smaller than the angle in **19** and the two oxygen atoms in **19** point away from each other while the oxygen atoms in the NHC analogs point slightly toward each other. Enemark and Feltham postulated that the N–Ru–N angle and the direction of the nitrosyl bending in $\{\text{Ru}(\text{NO})_2\}^{10}$ species only depend on the composition of the $d_{xz} + \pi b_1^*(\text{NO})$ orbital which they claimed to be the HOMO: If the contribution of the $\pi b_1^*(\text{NO})$ is stronger the oxygens point away from each other and for a HOMO of d_{xz} character the oxygens point toward each other (see INTRODUCTION, Chapter 1.3.4).^[35] But the $d_{xz} + \pi b_1^*(\text{NO})$ orbital

is neither the HOMO in **19** nor in **21** but the HOMO–3. Furthermore, the contributions of $\pi b_1^*(\text{NO})$ and d_{xz} in the $d_{xz}+\pi b_1^*(\text{NO})$ orbital are equal in both complexes. Thus, the postulations of Enemark and Feltham do not clarify the structural differences between **19** and **21**.

The N–Ru–N angle and the bending direction of the nitrosyl ligands depends mostly on the $d_{xz}+\pi b_1^*(\text{NO})$ and the $d_{z^2}+\pi a_1^*(\text{NO})$ orbital. As discussed before, the $d_{xz}+\pi b_1^*(\text{NO})$ favors a larger N–Ru–N angle but also the oxygens to point away from each other to alleviate non-bonded repulsion between the two nitrosyl ligands. In contrast, the $d_{z^2}+\pi a_1^*(\text{NO})$ clearly favors a smaller N–Ru–N angle and the oxygen atoms to point toward each other. Thus the two molecular orbitals have directly opposing effects on the distortion of the N–Ru–N and the Ru–N–O angle. In the NHC derivatives the contribution of the $d_{z^2}+a_1\pi^*(\text{NO})$ orbital is stronger than in **19** since the strong σ -donating NHC ligands increase the electron density in the d_{z^2} orbital, and, thus, strengthen the π back donation from the d_{z^2} orbital to the nitrosyl ligands. The result is a smaller N–Ru–N angle in the NHC derivatives and the oxygen atoms pointing toward each other. Due to the smaller N–Ru–N angle, the interaction between the d_{xz} orbital and the $\pi^*(\text{NO})$ orbital is destabilized and raised in energy which also explains the greater energy gap between the HOMO–4 and the HOMO–3 in **21**. The C–Ru–C angle is also more acute than the P–Ru–P angle in **19**. Responsible for that is the antibonding interaction in the HOMO of **21** between the d_{xy} orbital with the strong σ donating NHC ligands that decreases with decreasing C–Ru–C angle.

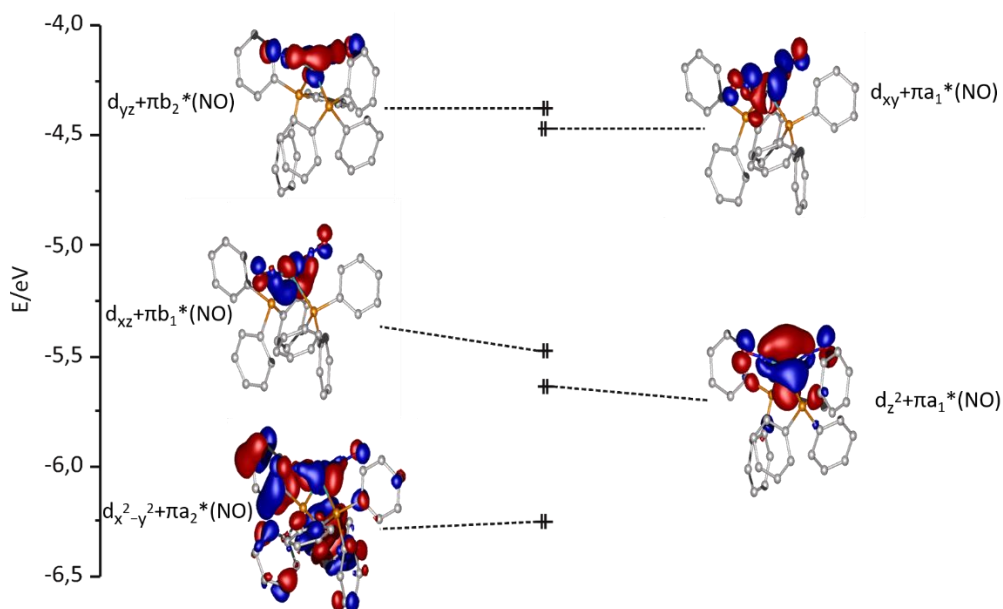


Figure 3.14: Molecular orbital scheme of the occupied frontier orbitals of $[\text{Ru}(\text{NO})_2(\text{PPh}_3)_2]$ (**19**). Calculated using the TZVP basis set and the BP86 functional.

Discussion

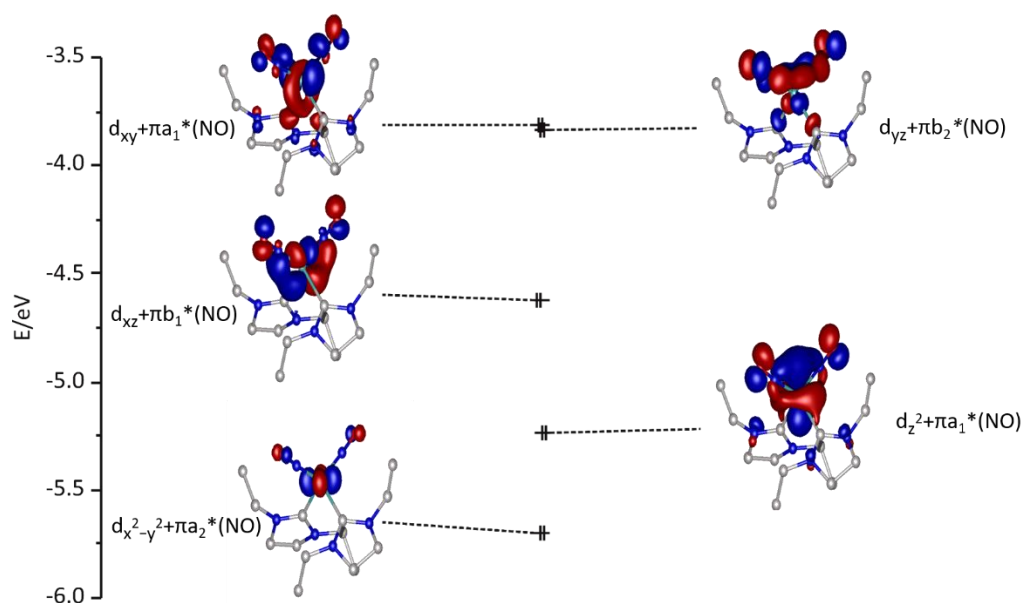


Figure 3.15: Molecular orbital scheme of the occupied frontier orbitals of $[\text{Ru}(\text{NO})_2(\text{L}^{\text{Et}})_2]$ (**21**). Calculated using the TZVP basis set and the BP86 functional.

Penta-coordinated dinitrosyls

Two different structures were found for the penta-coordinated dinitrosyl in this work: Firstly, a square pyramid with a bent RuNO moiety in the apical position and a linear NO group in the basal plane for **18a** and **18b**, and, secondly, a trigonal bipyramid with two almost linearly coordinated nitrosyl ligands in the basal plane for $[\text{Ru}(\text{NO})_2(\text{PPh}_3)_2]\text{BF}_4$ (**17**).

As in **10b** the HOMO of **18a** is a positive interaction of the d_{z^2} orbital with the π^* orbital of the bent nitrosyl in the apical position (FIGURE 3.16, left). In **17** the HOMO has d_{xy} - and $p(\text{I})$ character, thus, the HOMO-1 is the first occupied frontier orbital with contributions of the nitrosyl ligands (FIGURE 3.16, right). As stated before, the d_{z^2} and $d_{x^2-y^2}$ orbitals in a trigonal bipyramid with C_{2v} symmetry can mix and the electron density on the z axis is reduced. The HOMO-1 of **17** is in accordance with this conclusion and has a $d_{z^2-x^2}$ character interacting with both nitrosyl ligands.

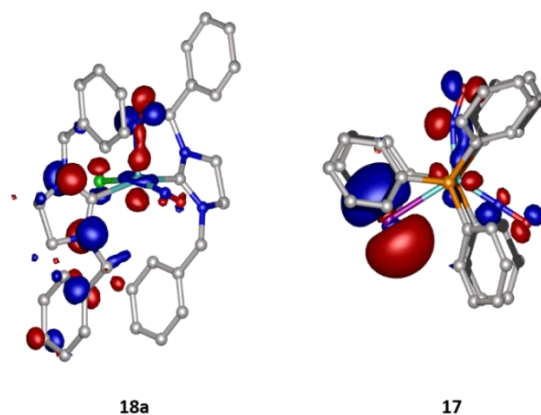


Figure 3.16: The HOMO of **18a** and the HOMO-1 of **17**. Calculated using the def2-TZVP basis set and the BP86 functional with the COSMO solvation model and dispersion correction.

By defining the z axis of the molecules as the bisector of the N–M–N angle the bonding of the dinitrosyls can be analyzed by the correlation diagram in FIGURE 1.11 of Chapter 1.3.3. The correlation diagram shows the dependence of the structure type of $\{\text{Ru}(\text{NO})_2\}^8$ systems from the energetic order of the ligand $\pi^*b_1(\text{NO})$ orbital and the metal d_{xz} orbital according to Enemark and Feltham. When the d_{xz} orbital is lower in energy, all eight electrons are metal-centered and the trigonal bipyramid with two equally coordinated nitrosyl ligands is adopted. In more metal-electron-poor complexes, the $\pi^*b_1(\text{NO})$ orbital is energetically more stable and the square pyramid with two unequally coordinated nitrosyl ligands is adopted.^[35] Klüfers *et al.* discussed both structure types for halogenido-bis(phosphane)-type $\{\text{Ru}(\text{NO})_2\}^8$ compounds; their theoretical studies supported the postulations of Enemark and Feltham.^[34] In **18a** the relevant orbital is the HOMO and in **17** the HOMO–1, both orbitals confirm the calculations of Klüfers *et al.* and thus, the postulations of Enemark and Feltham. In the square-pyramidal NHC complex **18a** the HOMO has strong contributions from the $\pi^*b_1(\text{NO})$ orbital and in the trigonal bipyramidal phosphane complex **17** the HOMO–1 has rather a d_{xz} character.

Hexa-coordinated dinitrosyl

When penta-coordinated $\{\text{MNO}\}^8$ species are coordinated by a sixth ligand normally oxidation to the corresponding $\{\text{MNO}\}^6$ -species occurs to reduce the electron density along the z axis. Thus, the octahedral structure of $[\text{Ru}(\text{NO})_2(\text{PPh}_3)_2\text{SO}_4]$ (**16**) is surprising. Furthermore, in the crystalline structure the two nitrosyl ligands are rotational disordered (see RESULTS, FIGURE 2.16) and therefore three isomers will be discussed in the following: Firstly two hexa-coordinated conformers with either two unequally or with two equally coordinating nitrosyl ligands (**D**, **E**) and secondly the penta-coordinated isomer **F** (FIGURE 3.17).

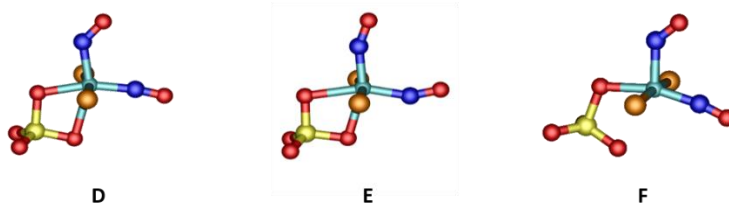


Figure 3.17: Possible isomers of $[\text{Ru}(\text{NO})_2(\text{PPh}_3)_2\text{SO}_4]$ (**16**). Calculated using the def2-TZVP basis set and the BP86 functional with the COSMO solvation model and dispersion correction.

FIGURE 3.18 displays the HOMOs of **D** and **E**. The HOMO of **D** is comparable with the HOMO of **18a** with additional antibonding contribution of the oxygen atom on the z axis. In **E** both nitrosyl ligands coordinate equally as in **17**, and their contributions to the HOMO are equivalent as well. Both conformers **D** and **E** are local minima. The energetic difference between these two conformers is 19 kJ mol^{-1} and explains the rotational disorder of the nitrosyls in the crystal structure of **16**. The experimental vibrational frequencies of **16** indicate unequal bonding of the nitrosyl ligands and since

conformer **D** is the global minimum on the conformational hypersurface, unequal coordination of the nitrosyls to the ruthenium in **16** is more likely than equal bonding.

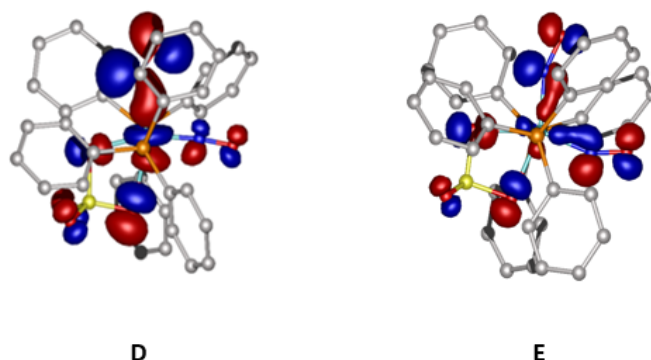


Figure 3.18: HOMOs of the isomers **D** and **E** of [Ru(NO)₂(PPh₃)₂SO₄] (**16**). Calculated using the def2-TZVP basis set and the BP86 functional with the COSMO solvation model and dispersion correction.

As expected for a penta-coordinated {RuNO}⁸ species, the electrostatic potential surface map in FIGURE 2.31 (RESULTS, Chapter 2.13) shows a negative potential along the z axis of isomer **F**. Furthermore, the former HOMO of **D** is stabilized by the cleavage of the Ru–O bond, since the antibonding interaction between the oxygen and the ruthenium is weakened. FIGURE 3.19 shows the relevant orbital for this consideration which is the HOMO–1 in **F**.

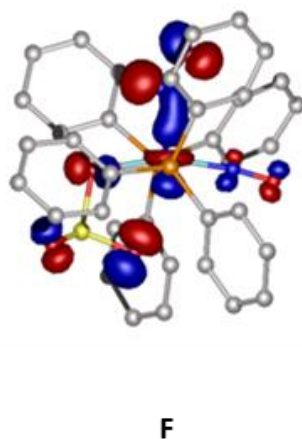


Figure 3.19: HOMO–1 of the penta-coordinated isomer **F** of [Ru(NO)₂(PPh₃)₂SO₄] (**16**). Calculated using the def2-TZVP basis set and the BP86 functional with the COSMO solvation model and dispersion correction.

Theoretical solution studies by application of the COSMO solvation model with the solvent parameters of toluene, ethanol and water resulted in global minima for both structures in toluene. In water and ethanol **F** is the only minimum structure, since the refinement of **D** converges into **F**. In water **F** is 69 kJ mol^{–1} more stable than in toluene. The reason for the increased stability of **F** in polar solvents is the stabilization of the charge separation which occurs upon cleaving the Ru–O bond. But even in toluene the energetic difference between **D** and **F** is very small (5 kJ mol^{–1}).

In summary the octahedral coordination of **16** is exceptional for a $\{\text{RuNO}\}^8$ compound and its stabilization is based on three effects: The π acidity of the second linearly coordinated nitrosyl relieving the excess electron density on the z axis, the chelating effect of the sulfate ligand and the prevention of charge separation in the complex.

3.3 Populations analyses

For a better understanding of the electronic state of the RuNO unit QTAIM and NPA calculations were performed (see RESULTS, Chapter 2.13.2). QTAIM bases its calculations on the calculated electron density and NPA is based on the linear combination of the atomic orbitals and therefore the wave function of the molecule.^[134,135] In contrast to Mulliken population analysis which is based on the wave function as well, NPA differentiates between non-bonding, bonding, antibonding and core orbitals.^[135] In general, NPA gives lower charges than QTAIM, but both approaches estimate trends for the different electronic states of the ruthenium-nitrosyl compounds. Since the binding mode of the nitrosyl ligand correlates with the Ru–N–O angle, the calculated charges of the $\{\text{RuNO}\}^8$ and the charges of the $\{\text{Ru}(\text{NO})_2\}^8$ and $\{\text{Ru}(\text{NO})_2\}^{10}$ species were plotted against the Ru–N–O angle (FIGURE 3.20). Formally the NO^+ ligand is assigned to a linear Ru–N–O angle and the NO^- ligand to more acute angles. FIGURE 3.20 indeed shows lower NO charges for **10b**, **13a** and **11a** with a bent RuNO moiety and higher charges for the compounds with linear RuNO moieties. For the dinitrosyl species with unequal nitrosyl ligands different NO charges are calculated, with the linear NO group having the higher charge as well. The NO charges of the equally bonded nitrosyl ligands in **20** and **17**, are according to sample equal. Even though the NO charges as a function of the Ru–N–O angle differ from each other, it must be stated that the difference is slight. The small charge difference indicates a high covalence of the Ru–NO bond irrespective of the angle. Especially in the case of a linear RuNO moiety, the NO ligand can hardly be assigned as a cation due to the extensive back donation. Thus, the formal NO^+ and NO^- binding modes are the two limiting cases for the coordination of the nitrosyl ligand to the ruthenium center.

Discussion

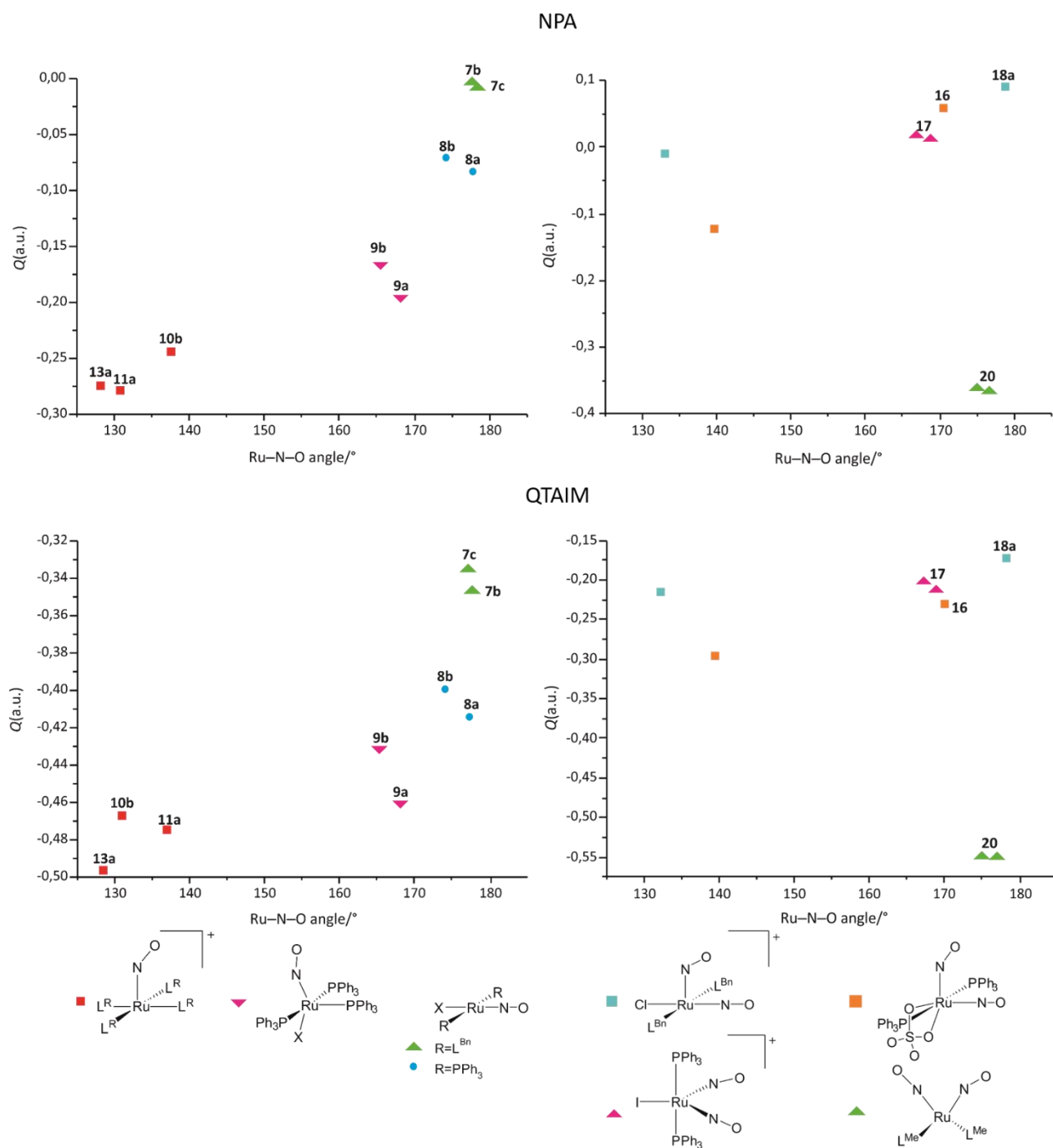


Figure 3.20: NPA (top) and QTAIM (bottom) NO charges of the $\{\text{RuNO}\}^8$ mononitrosyl species (left) and the dinitrosyl species (right) in this work plotted against the Ru-N-O angle. All values are elementary charges. All calculations were performed by using the def2-TZVP basis set and the BP86 functional with the COSMO solvation model and dispersion correction.

4 Summary

Ruthenium–nitrosyl complexes offer a wide variety of compounds that differ in their structure, their electronic states of their RuNO moiety and their reaction behavior. By now there are reports on $\{\text{RuNO}\}^m$ mononitrosyl compounds with $m = 5\text{--}8$ and $\{\text{Ru}(\text{NO})_2\}^m$ dinitrosyl compounds with $m = 8, 10$.^[46,48–60] The focus of this work is on the electronic states of the RuNO moiety and its influence on the coordination mode of the nitrosyl ligands in different $\{\text{Ru}(\text{NO})_n\}^m$ species. A total of twenty-five novel ruthenium-nitrosyl complexes was synthesized of which seventeen are mononitrosyls of the $\{\text{RuNO}\}^6$ or $\{\text{RuNO}\}^8$ type and eight are dinitrosyls of the $\{\text{Ru}(\text{NO})_2\}^8$ or $\{\text{Ru}(\text{NO})_2\}^{10}$ type. All complexes were characterized by elemental analyses, IR spectroscopy and mass spectrometry (where possible). Furthermore, the phosphane derivatives were characterized by $^{31}\text{P}\{^1\text{H}\}$ NMR and, in the case of **9a** and **9b**, by $^{31}\text{P}\{^1\text{H}\}$ NMR solid-state spectroscopy, and the NHC derivatives by $^{13}\text{C}\{^1\text{H}\}$ NMR and ^1H NMR spectroscopy. In the second part of this work the binding modes of the nitrosyl ligands and the resulting electronic states of the RuNO moiety were analyzed by quantum-chemical calculations.

The square-planar $\{\text{RuNO}\}^8$ species **7a–c** and **8a, 8b** of the general formula $[\text{RuX}(\text{NO})\text{L}_2]$ with $\text{X} = \text{Cl}, \text{Br}, \text{I}$ and $\text{L} = \text{PPh}_3, \text{L}^{\text{Bn}}$ were synthesized by a slightly modified procedure adopted from Lappert *et al.* The compounds **7b, 7c, 8a** and **8b** were characterized by single-crystal X-ray diffraction (FIGURE 4.1). The nitrosyl ligand in this species is linearly coordinated and quantum-chemical calculations revealed two strong π back bonds from the metal to the $\pi^*(\text{NO})$ orbitals, thus, the electronic state of the RuNO moiety can formally be regarded as $\text{Ru}^0(\text{NO}^+)$.

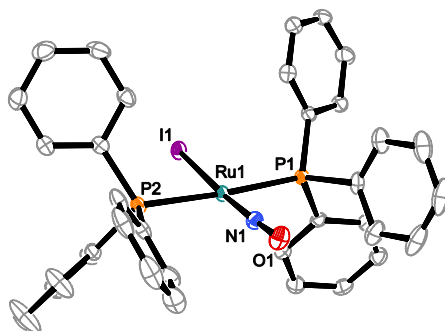


Figure 4.1: ORTEP plot of the complex $[\text{RuI}(\text{NO})(\text{PPh}_3)_2]$ in crystals of **7b**.

The penta-coordinated $\{\text{RuNO}\}^8$ phosphane species **9a** and **9b** of the general formula $[\text{RuX}(\text{NO})(\text{PPh}_3)_3]$ ($\text{X} = \text{Cl}, \text{I}$), were obtained by the addition of excess PPh_3 to **7a** or **7b**. Both compounds were characterized by single-crystal X-ray diffraction and adopt a square-pyramidal structure with a slightly bent RuNO moiety in the plane (FIGURE 4.2, left). This structure motif is not known for $\{\text{RuNO}\}^8$ compounds in literature and was further investigated by quantum-chemical calculations. The relaxed surface scan of the I–Ru–N angle in **9b** revealed that the Ru–N–O angle depends on the I–Ru–N angle and proved the square pyramid with a Ru–N–O angle of 164° to be the energetically most convenient structure for **9a** and **9b** since the π interactions between ruthenium and both the nitrosyl and the

halogenido ligand are suitable, while the antibonding character of the HOMO is minimized. Furthermore, the Ru–N–O angle is large enough to preserve both π back bonds, thus, taking the spectroscopic data into account, the formal electronic state of the RuNO moiety of **9a** and **9b** can best be described as $\text{Ru}^0(\text{NO}^+)$.

The penta-coordinated $\{\text{RuNO}\}^8$ NHC species **10a**, **10b**, **11a–c**, **12a–c**, **13a** and **13b** of the general formula $[\text{Ru}(\text{NO})\text{L}^{\text{R}}_4]\text{X}$ with R = Me, Et, *n*Pr, Bn and X = Cl, Br, I were synthesized by the addition of an excess of the corresponding enetetramine to **7a–c**. **10b**, **11a** and **13a** were characterized by single-crystal X-ray diffraction and adopt a square-pyramidal structure with a strongly bent RuNO moiety in the axial position (FIGURE 4.2, right). This structure motif is characteristic for penta-coordinated $\{\text{RuNO}\}^8$ species especially with strong σ donors. Due to the small Ru–N–O angle, only one π back bond from the metal to the nitrosyl remains and the electronic state of the RuNO moiety can formally be determined as $\text{Ru}^{+II}(\text{NO}^-)$.

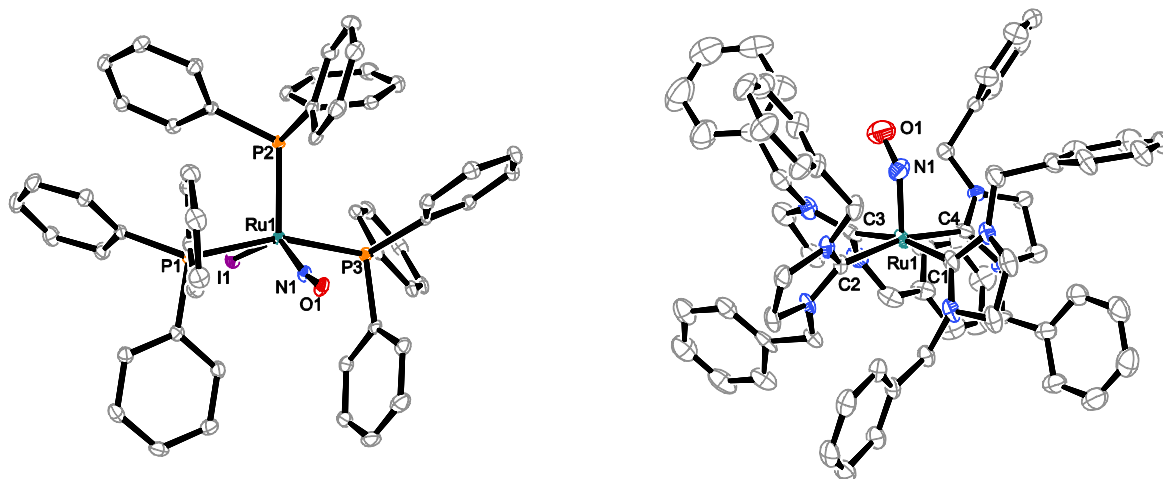


Figure 4.2: Ortep plots of the complex $[\text{Ru}(\text{NO})(\text{PPh}_3)_3]$ in crystals of **9b** and of the cation $[\text{Ru}(\text{NO})(\text{L}^{\text{Bn}})_4]^+$ in crystals of **13a**.

Interestingly, the penta-coordinated $\{\text{RuNO}\}^8$ phosphane species **9a** and **9b** as well as the penta-coordinated $\{\text{RuNO}\}^8$ NHC species **13a** and **13b** equilibrate with their corresponding tetra-coordinated species in solution. In the case of the phosphane compounds, the system equilibrates between a 16 and an 18 electron complex, while the oxidation state of the ruthenium remains 0. In contrast, the equilibrium of the NHC derivatives can be assigned as an intramolecular redox process, in which the number of electrons remains constant, while the electronic state of the RuNO moiety changes ($\text{Ru}^0(\text{NO}^+) \rightleftharpoons \text{Ru}^{+II}(\text{NO}^-)$).

The hexa-coordinated $\{\text{RuNO}\}^6$ NHC species **14a**, **14b** and **15a–c** of the general formula $[\text{RuX}(\text{NO})(\text{L}^{\text{R}})_4](\text{I}_n)_2$ (X = Cl, Br, I; R = Me, Et) were synthesized by the oxidation of the corresponding penta-coordinated $\{\text{RuNO}\}^8$ species with I_2 . All compounds of this species are stable to air and adopt the $\{\text{RuNO}\}^6$ typical octahedral structure with a linearly coordinated nitrosyl (FIGURE 4.3). **14a** and **15a–c** were characterized by single-crystal X-ray diffraction. Due to the linearity of the nitrosyl, two π back

Summary

bonds from the metal to the nitrosyl are possible, and, taking the high nitrosyl-stretching frequency into account the electronic state of the RuNO moiety can be regarded as $\text{Ru}^{\text{II}}(\text{NO}^+)$.

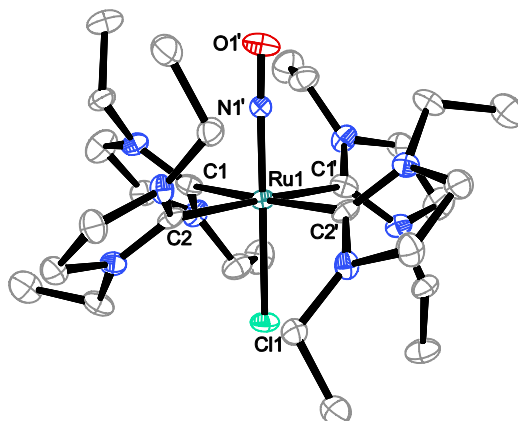


Figure 4.3: ORTEP plot of the cation $[\text{RuCl}(\text{NO})(\text{L}^{\text{Et}})_4]^{2+}$ in crystals of **15a**.

The penta-coordinated $\{\text{Ru}(\text{NO})_2\}^8$ NHC species **18a** and **18b** of the general formula $[\text{RuX}(\text{NO})_2(\text{L}^{\text{Bn}})_2]\text{BF}_4$ with $\text{X} = \text{Cl}, \text{Br}$ and the $\{\text{Ru}(\text{NO})_2\}^8$ phosphane species $[\text{RuI}(\text{NO})_2(\text{PPh}_3)_2]\text{BF}_4$ **17** were synthesized by the addition of an excess of $\text{NO}(\text{BF}_4)$ to the corresponding tetra-coordinated $\{\text{RuNO}\}^8$ compounds. All three compounds were characterized by single-crystal X-ray diffraction. In the case of the NHC derivatives, a square-pyramidal structure with two unequally coordinated nitrosyl ligands (bent and linear) is adopted (FIGURE 4.4, left). The unequal bonding of the nitrosyls is in accordance with the different nitrosyl-stretching frequencies and quantum-chemical calculation revealed that the best description of the formal electronic state is $\text{Ru}^{\text{II}}(\text{NO}^-)(\text{NO}^+)$. In contrast, the phosphane analog adopts a trigonal-bipyramidal structure with two linearly coordinated nitrosyls (FIGURE 4.4, right). The equal coordination of the nitrosyls is, again, confirmed by the nitrosyl-stretching frequencies and the quantum-chemical calculations. Thus, the electronic state of the RuNO moiety can be regarded as $\text{Ru}^0(\text{NO}^+)_2$. These results are in accordance with the investigations of the structural and electronic properties of halogenido-bis(phosphane)-type $\{\text{Ru}(\text{NO})_2\}^8$ compounds by Klüfers *et al.*^[34]

Summary

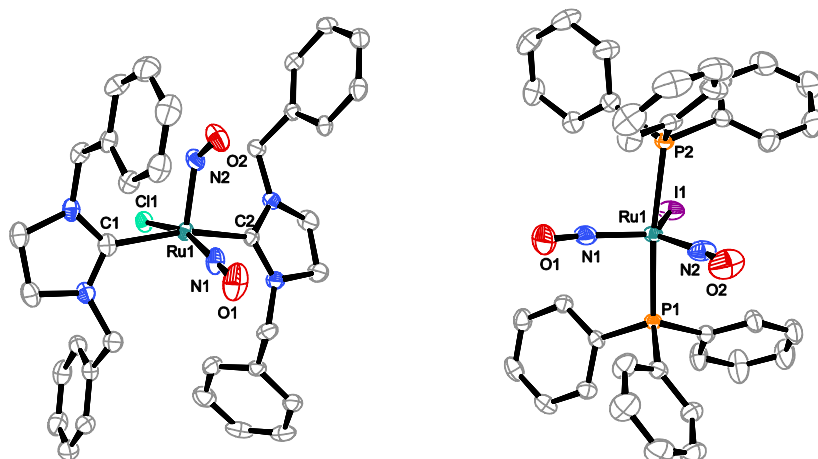


Figure 4.4: Ortep plots of the cation $[\text{RuCl}(\text{NO})_2(\text{L}^{\text{Bn}})_2]^+$ in crystals of **18a** and of the cation $[\text{RuI}(\text{NO})_2(\text{PPh}_3)_2]^+$ in crystals of **17**.

The hexa-coordinated $\{\text{Ru}(\text{NO})_2\}^8$ species $[\text{Ru}(\text{NO})_2(\text{PPh}_3)_2\text{SO}_4]$ (**16**) was synthesized by adding $\text{NO}(\text{HSO}_4)$ to $[\text{RuH}_2(\text{PPh}_3)_4]$. In the crystalline structure, **16** adopts an octahedral structure with two rotational disordered nitrosyl ligands, thus, unequal and equal bonding of the nitrosyl is possible (FIGURE 4.5). Both quantum-chemical calculations and the nitrosyl-stretching frequencies proved the unequal bonding of the nitrosyls and the formal electronic state $\{\text{Ru}^{\text{II}}(\text{NO}^-/\text{NO}^+)\}^8$ as most convenient. In general, $\{\text{RuNO}\}^8$ and $\{\text{Ru}(\text{NO})_2\}^8$ compounds are tetra- or penta-coordinated due to the high electron density on the z axis, thus, the octahedral structure of **16** was unexpected. Theoretical-solution studies reveal a global minimum for the hexa-coordinated isomer only in toluene, while in water and ethanol the refinement converges into the penta-coordinated structure.

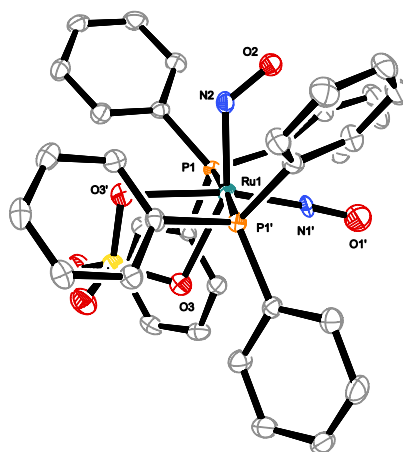


Figure 4.5: ORTEP plot of the molecule $[\text{Ru}(\text{NO})_2(\text{PPh}_3)_2\text{SO}_4]$ in crystals of **16**.

The $\{\text{Ru}(\text{NO})_2\}^{10}$ phosphane compound $[\text{Ru}(\text{NO})_2(\text{PPh}_3)_2]$ (**19**) known in literature was synthesized by a route by Gaughan *et al.*^[123] The analog NHC compounds **20–23** were obtained by ligand substitution upon the addition of the corresponding enetetramine to **19**. The addition of L^{nPr_2} to **19** afforded only the monocarbene complex $[\text{Ru}(\text{NO})_2(\text{L}^{\text{nPr}_2})(\text{PPh}_3)]$ (**23**). All $\{\text{Ru}(\text{NO})_2\}^{10}$ derivatives were characterized by single-crystal X-ray diffraction and adopt a tetrahedral structure with two linearly coordinating

Summary

nitrosyls (FIGURE 4.6). In general, the N–Ru–N angles are wider than the L–Ru–L angles (L = PPh₃, L^R), but in **20–23** both angles are smaller than in **19** which is due to the stronger $d_{z^2}+a_{1g}\pi^*(NO)$ orbital contribution caused by the strong σ -donating NHC ligands. The linearity of both nitrosyl ligands enables two π back bonds from the metal to the nitrosyl and the formal electronic state of the RuNO moiety can be determined as Ru^{-II}(NO⁺)₂.

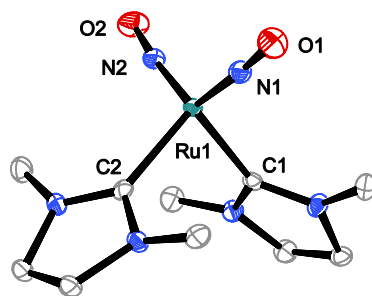


Figure 4.6: ORTEP plot of the molecule [Ru(NO)₂(L^{Me})₂] in crystals of **20**.

5 Experimental Part

5.1 Common working techniques

All reactions, as far as not explicitly described otherwise, were carried out under inert gas atmosphere using standard *Schlenk* techniques.

The syringes and cannulas which were used to transfer reagents and solvents, were purged three times with argon prior to use. Diethyl ether which was used for the purification of the raw products, and ethanol (used as solvent for the nitrosyl tetrafluoroborate or for the preparation of the ruthenium mononitrosyl precursors) were dried by heating to reflux, cooled and stored under argon atmosphere over 4 Å molecular sieves. Water was degassed by a continuously argon flow. The solvents, as well as the electron-rich olefins, were stored under argon atmosphere. The nitrosyl tetrafluoroborate was kept in a *Schlenk* tube at 4°C under argon atmosphere.

For crystallization, various techniques were applied: {RuNO}⁶-species of the type [RuX(NO)(L^R)₄]_n were prepared as powders and recrystallized by covering DMSO-solutions with ethanol. {RuNO}⁸-compounds were crystallized either directly from the reaction solution by means of adjusting different concentrations or by covering the reaction solutions with diethyl ether. Dinitrosyls were prepared as powders and recrystallized in dichloromethane, covered with diethyl ether.

In those cases where no data of elemental analysis is given, high resolution mass spectra were recorded.

The absorption bands of the infrared spectra were reported in wave numbers (cm⁻¹) and the bands of the $\tilde{\nu}(\text{NO})$ are referred to these of the nitrosyl ligands NO⁺ and NO⁻.

NMR spectra were recorded on solutions in:

CD₂Cl₂ (residual dichloromethane: δ 5.32 ppm for ¹H NMR; δ 53.84 ppm for ¹³C{¹H} NMR),

D6-dmso (residual dimethyl sulfoxide: δ 2.54 ppm for ¹H NMR; δ 41.31 ppm for ¹³C{¹H} NMR).

D8-toluene (residual toluene: δ 7.09, 7.01, 6.97, 2.08 ppm for ¹H NMR; δ 137.48, 128.87, 127.96, 125.13, 20.43 ppm for ¹³C{¹H} NMR).

Chemical shifts are reported as δ -values in ppm relative to the solvent peak.

5.2 Analytical methods

Table 5.1: Analytical methods and equipment.

analytic method	equipment
elemental analysis	<i>Elementar vario EL (C, H, N content)</i>
	<i>Metrohm 888 Titrande (Cl, Br, I content)</i>
	<i>Varian Vista RL CCD simultaneous ICP-AES (Ru, K, P content)</i>
infrared spectrometer	<i>Jasco FT/IR-460Plus with ATR Diamond Plate</i>
crystal selection	microscope Leica MZ6 with polarization filter
NMR spectrometer	Bruker 400 TR
	Bruker 400
	Jeol 270
	Jeol 400
X-ray diffraction experiments	Oxford XCalibur 3
	Bruker D8 Venture
scales	<i>Sartorius BP410S</i>
	<i>Sartorius ED124S</i>
mass spectrometer	<i>Jeol JMS 700, Thermo Finnigan MAT 95, FAB</i>

5.3 Reagents and solvents

Table 5.2: Manufacturer and percentage purity of the solvents and reagents.

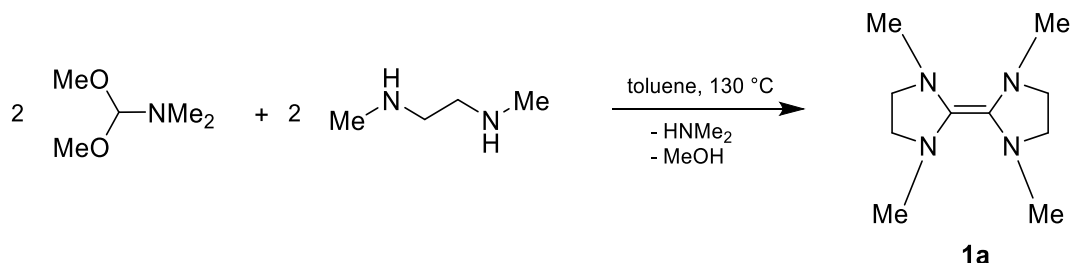
solvents and reagents	percentage purity	manufacturer
sulfamic acid	99.5 %	Fluka
<i>N,N'</i> -dibenzylethylenediamine	97 %	Aldrich
<i>d</i> ₂ -dichloromethane	99.9 % (H ₂ O < 0.01 %)	EURISO-top
dichloromethane	99.9 %	Brenntag
dichloromethane (over molecular sieve)	99.5 %	Aldrich
diethyl ether	99.9 %	VWR
<i>N,N'</i> -diethylethylenediamine	95 %	Aldrich
<i>N,N'</i> -dimethylethylenediamine	99 %	Aldrich
<i>N,N</i> -dimethylformamide dimethyl acetal	97 %	ABCR
<i>N,N'</i> -di- <i>n</i> -propylethylenediamine	97 %	ABCR
<i>N,N'</i> -diphenylethylenediamine	98 %	Aldrich
dimethyl sulfoxide (over molecular sieve)	99.5 %	Aldrich
ethanol	abs.	BfB
<i>n</i> -hexane	puriss.	Grüssing
hydrobromic acid	48 wt %	Acros
hydrochloric acid (1.0 M)	standard solution	AppliChem
hydroiodic acid	57 wt. %	Merck
iodine	99.5 %	Acros
methylcyclohexane (over molecular sieve)	99 %	Aldrich
molecular sieve 4 Å	8–12 mesh	Acros

Experimental Part

nitrosyl tetrafluoroborate	95 %	Aldrich
potassium hydroxide	85 % p.A.	Grüssing
potassium nitrite	≥98 %, puriss. p.a.	Fluka
pyrrolidine	99.5 %	Aldrich
ruthenium(III) chloride hydrate	99 %	Aldrich
tetrakis(dimethylamino)ethylene	-	Aldrich
<i>d</i> ₈ -toluene	99.5 % (H ₂ O < 0.02 %)	EURISO-top
toluene (over molecular sieve)	99.7 %	Aldrich
triphenylphosphane	99 %	Acros
water	de-ionized	house installation
xylene (over molecular sieve)	97 %	Brenntag

5.4 Preparation of the enetetramines

5.4.1 Bis-1,3-dimethyl-imidazoline-2-ylidene (L^{Me_2}) (**1a**)



According to H. Goldwhite et al., *J. Organomet. Chem.* **1986**, *310*, 21–25.

Starting materials: *N,N*-dimethylformamide dimethyl acetal, *N,N'*-dimethylethylenediamine, toluene, hydrochloric acid.

Procedure: *N,N*-dimethylformamide dimethyl acetal (17.86 g, 20.0 mL, 150 mmol, 1.2 eq.) and *N,N'*-diethyl-ethylenediamine (14.52 g, 18.0 mL, 125 mmol) were dissolved in toluene (10 mL) and were heated under refluxing conditions at 130°C for 3 h, until the evolution of dimethylamine was finished. The evolving dimethylamine was passed into a washing bottle (1.0 M HCl) and a cold trap for disposal. After cooling the solution to room temperature the azeotropic methanol/toluene mixture was removed *in vacuo*. The yellow product was obtained by fractional distillation at 130°C under reduced pressure. After cooling to room temperature the product crystallized as a colorless solid (13.33 g) which was dissolved in toluene (26.42 mL) to get a precursor solution (2 mol L⁻¹, 1 mL = 2 mmol) for further reactions.

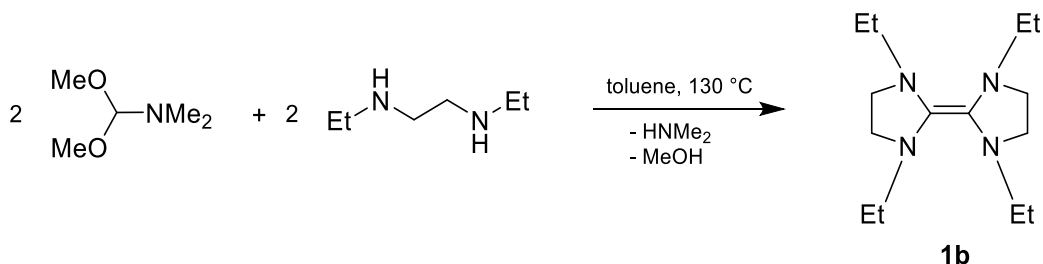
Empirical formula: C₁₀H₂₀N₄ (196.17 g mol⁻¹, **1a**).

Yield: 13.33 g (52.84 mmol), 96 % of th., yellow crystals with a low melting point.

MS (M = C₁₀H₂₀N₄): EI⁺: *m/z* = 196.2 ([M⁺], calcd. 196.17).

¹H NMR spectroscopy (*d*₈-toluene, 400 MHz): δ = 2.49 (s, 8 H, N-CH₂-CH₂-N), 2.31 (s, 12 H, N-CH₃) ppm.

¹³C{¹H} NMR spectroscopy (*d*₈-toluene, 101 MHz): δ = 128.27 (N-C-N), 51.36 (N-CH₂-CH₂-N), 38.82 (N-CH₃) ppm.

5.4.2 Bis-1,3-diethyl-imidazoline-2-ylidene (L^{Et}₂) (**1b**)

Literature: H. Goldwhite et al., *J. Organomet. Chem.* **1986**, *310*, 21–25.

Starting materials: *N,N*-dimethylformamide dimethyl acetal, *N,N'*-diethylethylenediamine, toluene, hydrochloric acid.

Procedure: *N,N*-dimethylformamide dimethyl acetal (17.86 g, 19.90 mL, 150 mmol, 1.2 eq.) and *N,N'*-diethyl-ethylenediamine (11.02 g, 13.50 mL, 125 mmol) were dissolved in toluene (10 mL) and were heated under refluxing conditions at 130°C for 3 h, until the evolution of dimethylamine was finished. The evolving dimethylamine was passed into a washing bottle (1.0 M HCl) and a cold trap for disposal. After cooling the solution to room temperature the azeotropic methanol/toluene mixture was removed *in vacuo*. The yellow product was obtained by fractional distillation at 90°C under reduced pressure. After cooling to room temperature the product crystallized as a colorless solid (11.70 g) which was dissolved in toluene (29.7 mL) to get a precursor solution (2 mol L⁻¹, 1 mL = 2 mmol) for further reactions.

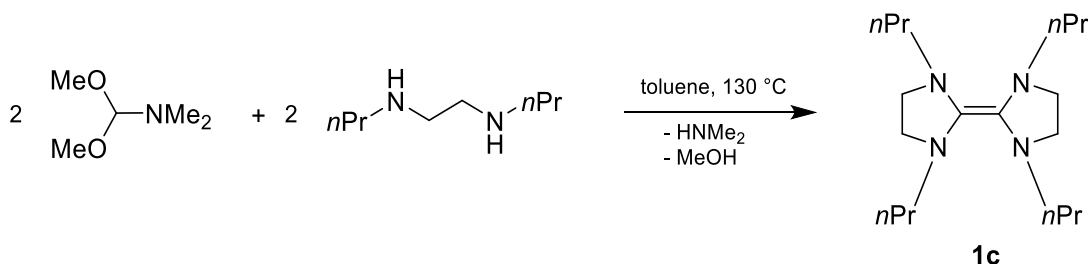
Empirical formula: C₁₄H₂₈N₄ (252.23 g mol⁻¹, **1b**).

Yield: 11.7 g (59.43 mmol), 84 % of th., yellow crystals with a low melting point.

¹H NMR spectroscopy (*d*₈-toluene, 400 MHz): δ = 3.00 (q, 8 H, ³*J* = 7.1 Hz, N-CH₂-CH₃), 2.79 (s, 8 H, N-CH₂-CH₂-N), 1.04 (t, 12 H, ³*J* = 7.1 Hz, N-CH₂-CH₃) ppm.

¹³C{¹H} NMR spectroscopy (*d*₈-toluene, 101 MHz): δ = 125.70 (N-C-N), 49.05 (N-CH₂-CH₃) 45.60 (N-CH₂-CH₂-N), 12.88 (N-CH₂-CH₃) ppm.

MS (M = C₁₄H₂₈N₄): EI⁺: *m/z* = 252.4 ([M⁺], calcd. 252.23).

5.4.3 Bis-1,3-di-*n*-propyl-imidazoline-2-ylidene (L^{*n*Pr}2) (**1c**)

According to H. Goldwhite et al., *J. Organomet. Chem.* **1986**, 310, 21–25.

Starting materials: *N,N*-dimethylformamide dimethyl acetal, *N,N'*-di-*n*-propylethylenediamine, toluene, hydrochloric acid.

Procedure: *N,N*-dimethylformamide dimethyl acetal (24.78 g, 27.63 mL, 208 mmol, 1.2 eq.) and *N,N'*-*n*-propyl-ethylenediamine (25 g, 31.17 mL, 173 mmol) were dissolved in toluene (17.6 mL) and were heated under refluxing conditions at 130°C for 3 h, until the evolution of dimethylamine was finished. The evolving dimethylamine was passed into a washing bottle (1.0 M HCl) and a cold trap for disposal. After cooling the solution to room temperature the azeotropic methanol/toluene mixture was removed *in vacuo*. The yellow product was obtained by fractional distillation at 130°C under reduced pressure. After cooling to room temperature the product crystallized as a colorless solid (22.7 g) which was dissolved in toluene (36.8 mL) to get a precursor solution (2 mol L⁻¹, 1 mL = 2 mmol) for further reactions.

Empirical formula: C₁₈H₃₆N₄ (308.29 g mol⁻¹, **1c**).

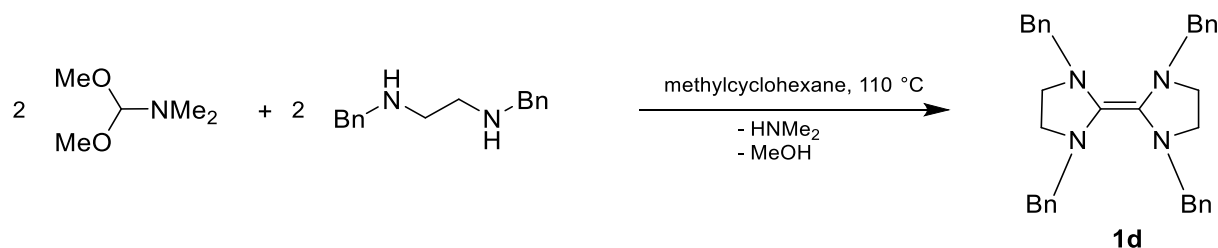
Yield: 22.7 g (73.61 mmol), 85 % of th., yellow crystals with a low melting point.

Elemental analysis: (calcd. For C₁₈H₃₆N₄, 196.17 g mol⁻¹), found (calcd.): C 67.68 % (70.08 %), H 11.71 % (11.76 %), N 17.76 % (18.16 %).

MS (M = C₁₄H₂₈N₄): EI⁺: *m/z* = 308.5 ([M⁺], calcd. 308.29).

¹H NMR spectroscopy (*d*₈-toluene, 400 MHz): δ = 2.85–2.79 (m, 16 H, N-CH₂-CH₂-N; N-CH₂-CH₂-CH₃), 1.52–1.42 (m, 8 H, N-CH₂-CH₂-CH₃), 0.87 (t, 12 H, ³J = 7.5 Hz, N-CH₂-CH₂-CH₃) ppm.

¹³C{¹H} NMR spectroscopy (*d*₈-toluene, 101 MHz): δ = 127.19 (N-C-N), 54.54 (N-CH₂-CH₂-CH₃), 50.00 (N-CH₂-CH₂-N), 22.12 (N-CH₂-CH₂-CH₃), 12.49 (N-CH₂-CH₂-CH₃) ppm.

5.4.4 Bis-1,3-dibenzyl-imidazoline-2-ylidene (L^{Bn_2}) (**1d**)

Literature: M. F. Lappert, P. L. Pye, *J. Chem. Soc., Dalton Trans.* **1978**, 7, 837–844.

Starting materials: *N,N*-dimethylformamide dimethyl acetal, *N,N'*-dibenzylethylenediamine, methylcyclohexane, hydrochloric acid.

Procedure: *N,N*-dimethylformamide dimethyl acetal (7.8 mL, 0.06 mol, 1.2 eq.) was added to a solution of *N,N'*-dibenzylethylenediamine (11.7 mL, 0.05 mol) dissolved in methylcyclohexane (50 mL). The mixture was heated under reflux at 110 °C for 6 h. The evolving azeotropic methanol/dimethylamine mixture was passed into a washing bottle (1.0 M HCl) and a cold trap for disposal. The reaction mixture was cooled to room temperature, whereupon the product crystallized. The mother liquid was pipetted off and the product was washed with methylcyclohexane (15 mL), cold diethyl ether (−30 °C, 3 × 15 mL) and dried *in vacuo*.

Empirical formula: $C_{34}H_{36}N_4$ (500.29 g mol^{−1}, **1d**).

Yield: 9.46 g (0.019 mol), 76 % of th., pale cream crystals.

Elemental analysis: (calcd. for $C_{34}H_{36}N_4$, 500.29 g mol^{−1}), found (calcd.): C 81.29 % (81.56 %), H 7.35 % (7.25 %), N 11.20 % (11.19 %).

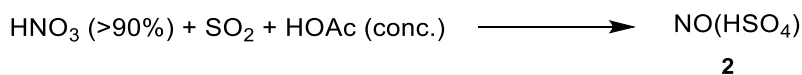
MS ($M = C_{34}H_{36}N_4$): FAB⁺: $m/z = 501.8$ ($[M]^+$, calcd. 500.3).

¹H NMR spectroscopy (CD₂Cl₂, 270 MHz): $\delta = 7.36$ – 7.17 (m, 20H, Ph), 4.26 (s, 8H, N-CH₂-Ph), 2.88 (s, 8H, N-CH₂-CH₂-N) ppm.

¹³C{¹H} NMR spectroscopy (CD₂Cl₂, 68 MHz): $\delta = 140.45$ (*ipso*-C), 129.29 (*meta*-CH), 128.58 (*ortho*-CH), 127.09 (*para*-CH), 56.07 (N-CH₂-CH₂-N), 49.33 (N-CH₂-Ph) ppm.

5.5 Preparation of the precursor compounds

5.5.1 Synthesis of NO(HSO₄) (2)



Literature: H. Biltz, W. Biltz, *Laboratory methods of inorganic chemistry*, John Wiley & Sons, 2nd edition, New York, **1928**, 204–205.

Starting materials: Nitric acid (anhydrous, >90 %), Acetic acid (conc.), SO₂.

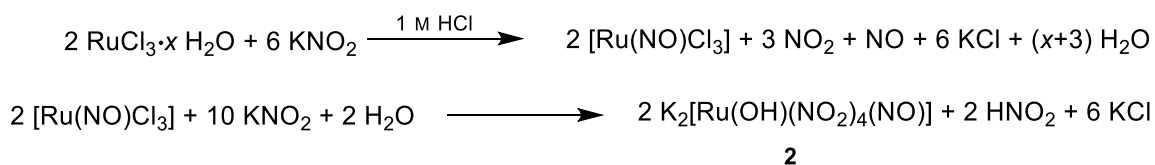
Procedure: Anhydrous nitric acid (30 mL, 762 mmol, 3.8 eq.) and acetic acid (11 mL, 200 mmol) were combined under nitrogen atmosphere and cooled to –5 °C. Then gaseous SO₂ was first passed through MgSO₄ and then slowly passed through the reaction mixture. The temperature of the exothermic reaction was kept between –5 °C and 5 °C for the whole time. Unconsumed SO₂ was passed into a system of washing bottles (2 M KOH/ 2 M KOH) for disposal. After 3 h a thick crystalline paste established. The white crystals were isolated by filtration, washed with acetic acid (conc.) and dichloromethane and dried *in vacuo*.

Empirical formula: HNO₅S (g mol⁻¹, 2).

Yield: 36.48 g (289.56 mmol), 38 % of th., white crystals.

Raman spectroscopy (RT, solid), (intensity): $\tilde{\nu} = 2275$ (s, NO).

X-ray structure analysis: tv281

5.5.2 $\text{K}_2[\text{Ru}(\text{OH})(\text{NO}_2)_4(\text{NO})]$ (**3**)

Literature: J.M. Fletcher, I.L. Jenkins, F.M. Lever, F.S. Martin, A.R. Powell, R. Todd, *J. Inorg. Nucl. Chem.* **1955**, *1*, 378–401.

Starting material: Ruthenium(III) chloride hydrate (40.31 % Ru), hydrochloric acid (1 M), potassium nitrite, sulfamic acid, diethyl ether, water.

Procedure: Ruthenium(III) chloride hydrate (15.6 g, 58.1 mmol) was suspended in 60 mL of hydrochloric acid and the mixture was heated until boiling. Subsequently, solid potassium nitrite (14.9 g, 175 mmol) was added in small portions over a period of one hour. Evolving nitrogen oxides were passed into a system of washing bottles (sulfamic acid acid/ sulfamic acid) for disposal. After cooling the solution to 80 °C small portions of potassium nitrite (24.8 g, 291 mmol) were added over a period of four hours. Hereupon, the red-orange reaction mixture was filtered into a crystallization dish and covered with a watch glass. The product which crystallized as an orange solid overnight, was washed with iced water (5 mL) and diethyl ether (50 mL) and freed from all volatile components *in vacuo*.

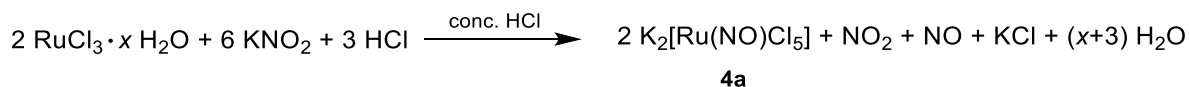
Empirical formula: $\text{HK}_2\text{N}_5\text{O}_{10}\text{Ru}$ (410.30 g mol⁻¹, **2**).

Yield: 10.7 g (26.0 mmol), 45 % of th., orange crystals.

Elemental analysis: (calcd. for $\text{HK}_2\text{N}_5\text{O}_{10}\text{Ru}$, 410.30 g mol⁻¹), found (calcd.): H 0.32 % (0.25 %), K 20.92 % (19.06 %), N 16.56 % (17.07 %), Ru 23.84 % (24.63 %).

MS ($\text{H}_2\text{O}/\text{CH}_3\text{CN}$, $M = \text{HK}_2\text{N}_5\text{O}_{10}\text{Ru}$): ESI+: $m/z = 410.09497$ ($[M]^+$, calcd. 410.8041).

IR spectroscopy (RT, solid), (intensity): $\tilde{\nu} = 3529$ (vw), 1880 (m, NO), 1398 (s), 1330 (vs), 956 (m), 829 (s) cm⁻¹.

5.5.3 $\text{K}_2[\text{RuCl}_5(\text{NO})]$ (**4a**)

Literature: M. J. Cleare, W. P. Griffith, *J. Chem. Soc. (A)* **1967**, 7, 1144–1147.

Starting materials: Ruthenium(III) chloride hydrate (36 %, 40.31 % Ru), water, potassium nitrite, hydrochloric acid, conc. sulfamic acid, diethyl ether.

Procedure: Ruthenium(III) chloride hydrate (8.0 g, 30.6 mmol) was dissolved in water (60 mL) at 80 °C. Then potassium nitrate (7.81 g, 91.8 mmol, 3 eq.) was added in small portions. Subsequently, HCl (60 mL, 38 %) were added dropwise and the mixture was stirred at 80 °C for 1.5 h. The evolving nitrogen oxides were passed into a system of washing bottles (sulfamic acid / sulfamic acid) for disposal. The reaction mixture was concentrated *in vacuo*, whereupon a violet solid crystallized. The product was separated by filtration, washed with iced water and diethyl ether (100 mL) and freed from all volatile components *in vacuo*.

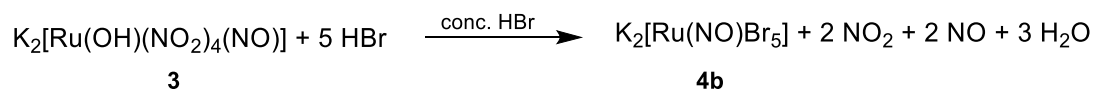
Empirical formula: $\text{Cl}_5\text{K}_2\text{NORu}$ (384.67 g mol⁻¹, **4a**).

Yield: 7.55 g (19.6 mmol), 90 % of th., violet crystals.

Elemental analysis: (calcd. for $\text{Cl}_5\text{K}_2\text{NORu}$, 384.67 g mol⁻¹), found (calcd.): Cl 45.70 % (45.86 %), K 21.29 % (20.23 %), N 3.33 % (3.62 %), Ru 21.62 % (26.15 %).

MS ($M = \text{Cl}_5\text{K}_2\text{NORu}$, 384.67 g mol⁻¹): ESI⁻: $m/z = 153.92$ ($[M-2 \text{K}^{2+}]$, calcd.: 153.4).

IR spectroscopy (RT, solid), (intensity): $\tilde{\nu} = 1898$ (vs, NO) cm⁻¹.

5.5.4 $\text{K}_2[\text{RuBr}_5(\text{NO})]$ (**4b**)

Literature: M. J. Cleare, W. P. Griffith, *J. Chem. Soc. (A)* **1967**, 7, 1144–1147.

Starting materials: Dipotassium hydroxido tetranitrito nitrosyl ruthenate (**2**), hydrobromic acid (conc.), sulfamic acid, water.

Procedure: Dipotassium hydroxido tetranitrito nitrosyl ruthenate (**3**, 6.07 g, 14.8 mmol) was dissolved in water (30 mL) at 50 °C. Then hydrobromic acid (70 mL, 2.86 mol, in excess) was added dropwise and the mixture was stirred at 80 °C for 2 h. The evolving nitrogen oxides were passed into a system of washing bottles (sulfamic acid/ sulfamic acid) for disposal. The reaction mixture was concentrated *in vacuo*, whereupon a solid crystallized. After Filtration the dark violet product was washed with hydrobromic acid and diethyl ether and freed from all volatile components *in vacuo*.

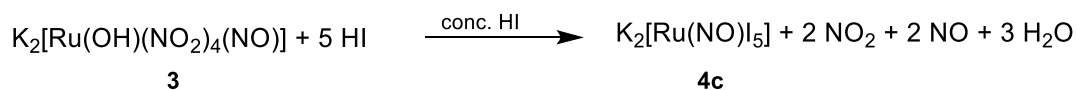
Empirical formula: $\text{Br}_5\text{K}_2\text{NORu}$ (608.79 g mol⁻¹, **4b**).

Yield: 3.94 g, 6.5 mmol, 44 % of th., dark violet crystals.

Elemental analysis: (calcd. for $\text{Br}_5\text{K}_2\text{NORu}$, 608.79 g mol⁻¹), found (calcd.): Br 65.08 % (65.63 %), N 2.33 % (2.30 %), K 13.67 % (12.98 %), Ru 14.61 % (16.60 %).

MS ($M = \text{Br}_5\text{K}_2\text{NORu}$, 608.79 g mol⁻¹): FAB⁻: $m/z = 570.09$ ($[M - K]^-$, calcd. 569.69).

IR spectroscopy (RT, solid), (intensity): $\tilde{\nu} = 1875$ (vs, NO) cm⁻¹.

5.5.5 $\text{K}_2[\text{RuI}_5(\text{NO})]$ (**4c**)

Literature: M. J. Cleare, W. P. Griffith, *J. Chem. Soc. (A)* **1967**, 7, 1144–1147.

Starting materials: Dipotassium hydroxido tetranitrito nitrosyl ruthenate (**2**), hydroiodic acid (conc.), sulfamic acid, water.

Procedure: Dipotassium hydroxido tetranitrito nitrosyl ruthenate (**3**, 4.17 g, 10.2 mmol) was dissolved in water (40 mL) at 50 °C. Then hydroiodic acid (59 mL, 0.785 mol, in excess) was added dropwise and the mixture was stirred at 80 °C for 2 h. The evolving nitrogen oxides were passed into a system of washing bottles (sulfamic acid/ sulfamic acid) for disposal. The reaction mixture was concentrated *in vacuo* to 15 mL, whereupon a solid crystallized which was washed with diethyl ether (3 × 30 mL) and freed from all volatile components *in vacuo*.

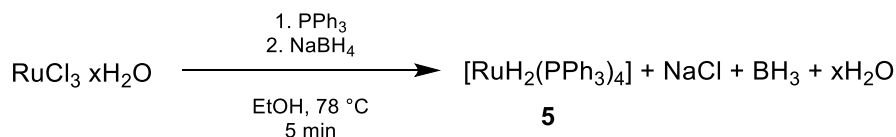
Empirical formula: $\text{I}_5\text{K}_2\text{NORu}$ (844.35 g mol⁻¹, **4c**).

Yield: 7.76 g (9.19 mmol), 90 % of th., crystals of anthracite color.

Elemental analysis: (calcd. for $\text{I}_5\text{K}_2\text{NORu}$, 844.35 g mol⁻¹), found (calcd.): N 1.57 % (1.66 %), I 74.37 % (74.94 %).

MS ($M = \text{I}_5\text{K}_2\text{NORu}$, 844.35 g mol⁻¹): FAB⁻: $m/z = 805.7$ ($[M - K]^-$, calcd. 805.4), 768.9 ($[M - 2K]^-$, calcd. 766.4), 639.9 ($[M - I - 2K]^-$, 639.5).

IR spectroscopy (RT, solid), (intensity): $\tilde{\nu} = 1842$ (vs, NO) cm⁻¹.

5.5.6 [RuH₂(PPh₃)₄] (5)

Literature: J. J. Levison, S. D. Robinson, *J. Chem. Soc.* **1970**, 2947–2954.

Starting Materials: Ruthenium(III) chloride hydrate (39 % Ru), triphenylphosphane, sodium borohydride, ethanol, water.

Processing: Ruthenium(III) chloride hydrate (250 mg, 0.94 mmol) was dissolved in hot ethanol (10 mL) and was rapidly added to a solution of triphenylphosphane (1.57 g, 6.0 mmol) in hot ethanol (60 mL). Then sodium borohydride (190 mg, 5 mmol), dissolved in hot ethanol (10 mL), was added portion wise to the reaction mixture, whereupon a yellow solid precipitated. The solid was then filtered off, washed with ethanol (3 x 10 mL), water (3 x 10 mL), ethanol (2 x 15 mL) and dried *in vacuo*.

Empirical formula: C₇₂H₆₂P₄Ru (1152.25 g mol⁻¹, 5).

Yield: 1.02 g (0.88 mmol), 94 % of th., yellow powder.

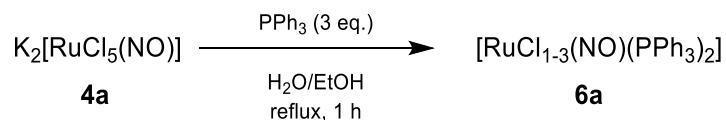
Elemental analysis: (calc. for C₇₂H₆₂P₄Ru 1152.25 g mol⁻¹) found (calcd.): C 71.11 % (75.05 %), H 5.39 % (5.42 %).

MS (*M* = C₇₂H₆₂P₄Ru, 1152.25 g mol⁻¹): FAB⁺: *m/z* = 1152.3 ([*M*]⁺, calcd. 1152.28).

IR spectroscopy (RT, solid), (intensity): $\tilde{\nu}$ = 1477 (w), 1430 (m), 1085(m), 147 (m), 692 (s) cm⁻¹.

5.6 Synthesis of the {RuNO}⁶⁻⁸ phosphane compounds

5.6.1 [RuCl₁₋₃(NO)(PPh₃)₂] (6a)



Literature: J. Chatt, B. L. Shaw, *J. Chem. Soc. (A)* **1966**, 12, 1811–1812.

Starting materials: Dipotassium pentachlorido nitrosyl ruthenate (**4a**), triphenylphosphane, ethanol, water.

Procedure: Triphenylphosphane (4.07 g, 15.52 mmol, 3.0 eq.), dissolved in hot ethanol (15 mL), was added to a solution of dipotassium pentachlorido nitrosyl ruthenate (**4a**, 2.0 g, 5.17 mmol) in a hot water/ethanol mixture (1:1.9, 8 mL/15 mL). The reaction mixture was heated at 70 °C for 1 h. Thus, a chartreuse solid precipitated and the solution was cooled to room temperature. Then the crude product was filtered off, washed with water (3 × 30 mL), ethanol (3 × 30 mL), and diethyl ether (3 × 30 mL) and dried *in vacuo*.

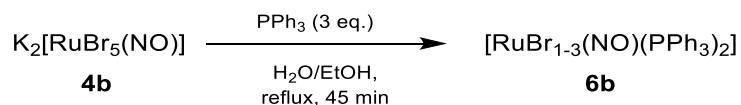
Empirical formula: C₃₆H₃₀Cl₃NOP₂Ru (762.01 g mol⁻¹, **6a**).

Yield: 3.57 g raw product, chartreuse powder.

³¹P{¹H} NMR spectroscopy (toluene, 109 MHz): δ = 25.29 (s) ppm.

MS: Not possible, both FIB/FAB and DEI were unsuccessful.

IR spectroscopy (RT, solid), (intensity): $\tilde{\nu}$ = 1872 (s, NO), 1481 (m), 1435 (s), 1092 (s), 741 (s), 689 (vs) cm⁻¹.

5.6.2 [RuBr₁₋₃(NO)(PPh₃)₂] (**6b**)

Literature: A. K. Gallien, D. Schaniel, T. Woike, P. Klüfers, *Dalton Trans.* **2014**, *43*, 13278–13292.

Starting materials: Dipotassium pentabromido nitrosyl ruthenate (**4b**), triphenylphosphane, ethanol, water.

Procedure: Triphenylphosphane (3.14 g, 12.00 mmol, 3.0 eq.), dissolved in hot ethanol (20 mL), was added to dipotassium pentabromido nitrosyl ruthenate (**4b**, 2.44 g, 4.00 mmol) which was dissolved in a water/ethanol mixture (1:1, 20 mL/20 mL). The reaction mixture was heated under refluxing conditions at 100 °C for 45 min, whereupon a green solid precipitated and then the solution was cooled to room temperature. The crude product was filtered off, washed with ethanol (3 × 20 mL), diethyl ether (3 × 20 mL) and freed from all volatile components *in vacuo*.

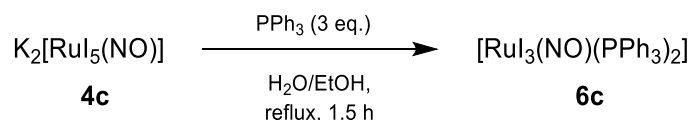
Empirical formula: C₃₆H₃₀Br₃NOP₂Ru (895.37 g mol⁻¹, **6b**).

Yield: 3.37 g raw product, green powder.

³¹P{¹H} NMR spectroscopy (toluene, 109 MHz): δ = 25.56 (s) ppm.

MS: Not possible, both FIB/FAB and DEI were unsuccessful.

IR spectroscopy (RT, solid), (intensity): $\tilde{\nu}$ = 1869 (s, NO), 1788 (s, NO), 1740 (s, NO), 1479 (m), 1435 (s), 1092 (s), 743 (s), 689 (vs) cm⁻¹.

5.6.3 $[\text{RuI}_3(\text{NO})(\text{PPh}_3)_2]$ (**6c**)

Literature: A. K. Gallien, *Synthesis, Characterisation and DFT Analysis of $\{\text{Ru}(\text{NO})_2\}^8$ Compounds*, dissertation, LMU-Munich, **2014**.

Starting materials: Dipotassium pentaiodido nitrosyl ruthenate (**4c**), triphenylphosphane, ethanol, water.

Procedure: A hot ethanolic solution (8 mL) of triphenylphosphane (2.93 g, 10.67 mmol, 3.0 eq.) was added to dipotassium pentaiodido nitrosyl ruthenate (**4c**, 3.00 g, 3.56 mmol), dissolved in a water/ethanol mixture (1:1, 8 mL/8 mL). The reaction mixture was heated under reflux at 100 °C for 1.5 h. Thus, a reddish brown solid was formed. The precipitate was filtered off after cooling to room temperature and was washed with ethanol (3 × 30 mL), diethyl ether (3 × 30 mL) and dried *in vacuo*.

Empirical formula: $\text{C}_{36}\text{H}_{30}\text{I}_3\text{NOP}_2\text{Ru}$ (1036.36 g mol⁻¹, **6c**).

Yield: 3.50 g (3.38 mmol), 95 % of th., reddish brown powder.

Elemental analysis: (calcd. for $\text{C}_{36}\text{H}_{30}\text{I}_3\text{NOP}_2\text{Ru}$, 1036.36 g mol⁻¹), found (calcd.): C 42.16 % (42.58 %), H 2.89 % (2.92 %), N 1.42 % (1.35 %).

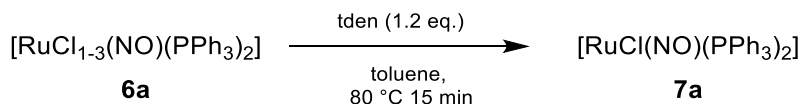
³¹P{¹H} NMR spectroscopy (toluene, 109 MHz): $\delta = 25.58$ (s) ppm.

MS: Not possible, both FIB/FAB and DEI were unsuccessful.

IR spectroscopy (RT, solid), (intensity): $\tilde{\nu} = 1857$ (s, NO), 1479 (m), 1433 (s), 1086 (s), 741 (s), 689 (vs) cm⁻¹.

5.7 Synthesis of the tetra-coordinated {RuNO}⁸ phosphane compounds

5.7.1 [RuCl(NO)(PPh₃)₂] (7a)



According to M. F. Lappert, P. L. Pye, *J. Chem. Soc., Dalton Trans.* **1978**, 7, 837–844.

Starting materials: [RuCl₁₋₃(NO)(PPh₃)₂] (**6a**), tden, toluene, diethylether.

Procedure: Compound **6a** (995 mg, 1.3 mmol) was suspended in toluene (20 mL) and tden (0.3 mL, 1.3 mmol) was added. The reaction mixture was heated under refluxing conditions at 80 °C for 15 min. The initially green suspension turned into a dark green solution and a dark solid precipitated during the reaction. The mixture was filtered under an inert gas atmosphere while hot, in order to remove the carbocation salt. The solvent was removed *in vacuo* until a dark green crystalline solid remained. The product was washed with diethyl ether and dried *in vacuo*.

Empirical formula: C₃₆H₃₀ClN₂O₂P₂Ru (691.05 g mol⁻¹, **7a**).

Yield: 171 mg (0.25 mmol), 19 % of th., dark green crystals.

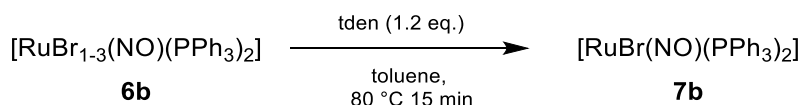
Elemental analysis: (calcd. C₃₆H₃₀ClN₂O₂P₂Ru x 3 H₂O, 745.15 g mol⁻¹), found (calcd.): C 61.5 % (62.57 %), H 4.46 % (4.38 %), N 2.03 % (1.91 %).

³¹P{¹H} NMR spectroscopy (toluene, 109 MHz): δ = 33.54 ppm.

³¹P{¹H} solid-state NMR spectroscopy (10 kHz mas, 202 MHz): δ = 34.22 (d, J = 274 Hz) 31.65 (d, J = 272 Hz) ppm.

MS: (M = C₃₆H₃₀ClN₂O₂P₂Ru, 691.10 g mol⁻¹): FAB⁺: m/z = 691.1 ([M]⁺, calcd. 691.05).

IR spectroscopy (RT, solid), (intensity): ν̃ = 1767 (vw, NO), 1727 (m, NO) cm⁻¹.

5.7.2 [RuBr(NO)(PPh₃)₂] (**7b**)

According to M. F. Lappert, P. L. Pye, *J. Chem. Soc., Dalton Trans.* **1978**, 7, 837–844.

Starting materials: [RuBr₁₋₃(NO)(PPh₃)₂] (**6b**), tden, toluene.

Procedure: Compound **6b** (1.0 g, 1.1 mmol) was suspended in toluene (20 mL) and tden (0.26 mL, 1.1 mmol) was added. The reaction mixture was heated under refluxing conditions at 80 °C for 15 min. The initially green suspension turned into a dark green solution and a dark solid precipitated during the reaction. The mixture was filtered under an inert gas atmosphere while hot, in order to remove the carbocation salt. Upon cooling to room temperature dark green crystals formed, to increase the yield the solvent was reduced *in vacuo*. The mother liquid was pipetted off, the dark green crystalline product was washed with diethyl ether and dried *in vacuo*.

Empirical formula: C₃₆H₃₀BrNOP₂Ru (735.0 g mol⁻¹, **7b**).

Yield: 173 mg (0.24 mmol), 22 % of th., dark green crystals.

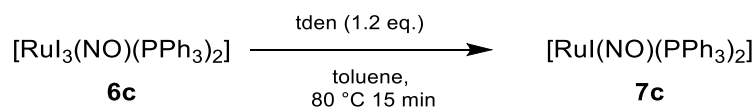
Elemental analysis: (calcd. C₃₆H₃₀BrNOP₂Ru, 735.0 g mol⁻¹), found (calcd.): C 57.19 % (58.78 %), H 4.33 % (4.11 %), N 1.86 (1.90 %).

³¹P{¹H} NMR spectroscopy (toluene, 162 MHz): δ = 35.94 (s, br) , 32.11 (s, br) ppm.

³¹P{¹H} solid-state NMR spectroscopy (10 kHz mas, 202 MHz): δ = 36.15 (d, J = 303 Hz) 32.05 (d, J = 303 Hz) ppm.

MS: (M = C₃₆H₃₀BrNOP₂Ru, 735.0 g mol⁻¹): FAB⁺: m/z = 737.3 ([M]⁺, calcd. 737.0).

IR spectroscopy (RT, solid), (intensity): ν̃ = 1727 (s, NO) cm⁻¹.

5.7.3 [RuI(NO)(PPh₃)₂] (**7c**)

According to M. F. Lappert, P. L. Pye, *J. Chem. Soc., Dalton Trans.* **1978**, 7, 837–844.

Starting materials: [RuI₃(NO)(PPh₃)₂] (**6c**), tden, toluene.

Procedure: Compound **6c** (1.0 g, 0.96 mmol) was suspended in toluene (20 mL) and tden (0.22 mL, 0.96 mmol) was added. The reaction mixture was heated under refluxing conditions at 80 °C for 15 min. The initially green suspension turned into a dark green solution and a dark solid precipitated during the reaction. The mixture was filtered under an inert gas atmosphere while hot, in order to remove the carbocation salt. Upon cooling to room temperature dark green crystals formed. The mother liquid was pipetted of, the dark green crystalline product was washed with diethyl ether and dried *in vacuo*.

Empirical formula: C₃₆H₃₀INOP₂Ru (782.99 g mol⁻¹, **7c**).

Yield: 616 mg (0.79 mmol), 82 % of th., dark green crystals.

Elemental analysis: (calcd. C₃₆H₃₀INOP₂Ru, 782.99 g mol⁻¹), found (calcd.): C 51.79 % (55.25 %), H 3.78 (3.86 %), N 1.57 (1.79 %).

³¹P{¹H} NMR spectroscopy (toluene, 162 MHz): δ = 28.95 (s, br) ppm.

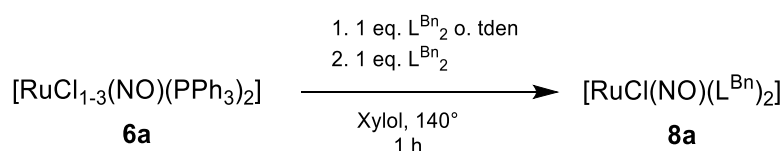
³¹P{¹H} solid-state NMR spectroscopy (10 kHz mas, 202 MHz): δ = 30.07 (d, *J* = 304 Hz) 24.06 (d, *J* = 300 Hz) ppm.

MS: (*M* = C₃₆H₃₀INOP₂Ru, 782.99 g mol⁻¹): FAB⁺: *m/z* = 783.3 ([*M*]⁺, calcd. 782.99).

IR spectroscopy (RT, solid), (intensity): $\tilde{\nu}$ = 1739 (s, NO) cm⁻¹.

5.8 Synthesis of the tetra-coordinated {RuNO}⁸ NHC compounds

5.8.1 [RuCl(NO)(L^{Bn})₂] (8a)



Literature: M. F. Lappert, P. L. Pye, *J. Chem. Soc., Dalton Trans.* **1978**, 7, 837–844.

Starting materials: [RuCl₁₋₃(NO)(PPh₃)₂] (**6a**), L^{Bn}₂ (**1d**), xylene.

Procedure: Compound **6a** (883.90 mg, 1.16 mmol) was added to a solution of L^{Bn}₂ (**1d**, 1.45 g, 2.90 mmol, 2.5 eq.) in xylene (20 mL). The reaction mixture was heated under refluxing conditions at 140 °C for 1.5 h. The initially chartreuse suspension first turned into a dark green solution which turned dark grey during the course of the reaction. The mixture was filtered under an inert gas atmosphere while hot to remove the carbocation salt. After slowly cooling to room temperature in the oil bath, deep blue crystals precipitated. In order to magnify the yield, the mixture was stored at 7 °C for 1 h. The mother liquid was pipetted off and the deep blue product was washed with diethyl ether (15 mL) and dried *in vacuo*.

Empirical formula: C₃₄H₃₆ClN₅ORu (667.2 g mol⁻¹, **8a**).

Yield: 403 mg (0.60 mmol), 52 % of th., deep blue crystals.

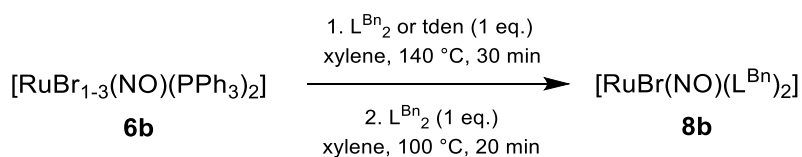
Elemental analysis: (calcd. for C₃₄H₃₆ClN₅ORu · 0.5 C₇H₈, 667.2 g mol⁻¹), found (calcd.): C 63.06 % (63.15 %), H 5.68 % (5.65 %), N 9.90 % (9.82 %).

¹H NMR spectroscopy (CD₂Cl₂, 400 MHz): δ = 7.36–7.23 (m, 20H, Ph), 5.41 (s, 8H, N-CH₂-Ph), 3.70 (s, 8H, N-CH₂-CH₂-N) ppm.

¹³C{¹H} NMR spectroscopy (CD₂Cl₂, 101 MHz): δ = 216.67 (N₂C), 137.92 (*ipso*-C), 129.05 (*meta*-CH), 128.97 (*ortho*-CH), 127.99 (*para*-CH), 56.37 (N-CH₂-CH₂-N), 48.92 (N-CH₂-Ph) ppm.

MS (*M* = C₃₄H₃₆ClN₅ORu, 667.2 g mol⁻¹): FAB⁺: *m/z* = 667.5 ([*M*⁺], calcd. 667.2), 633.5 ([*M*-Cl]⁺, calcd. 632.2), 602.6 ([*M*-Cl-NO]⁺ calcd. 602.2).

IR spectroscopy (RT, solid), (intensity): $\tilde{\nu}$ = 1686 (vs, NO), 1496 (vs, CN₂), cm⁻¹.

5.8.2 [RuBr(NO)(L^{Bn})₂] (**8b**)

According to M. F. Lappert, P. L. Pye, *J. Chem. Soc., Dalton Trans.* **1978**, 7, 837–844.

Starting materials: [RuBr₁₋₃(NO)(PPh₃)₂] (**6b**), L^{Bn}₂ (**1d**), xylene.

Procedure: Compound **6b** (546 mg, 0.61 mmol) was added to a solution of L^{Bn}₂ (**1d**, 305 mg, 0.61 mmol) in xylene (20 mL). The reaction mixture was heated under refluxing conditions at 140 °C for 30 min. The initially green suspension turned into a dark green solution and a dark solid precipitated during the reaction. The mixture was filtered under an inert gas atmosphere while hot to remove the carbocation salt. Further L^{Bn}₂ (**1d**, 305 mg, 0.61 mmol, 1.0 eq.) was added to the dark green solution and the mixture was stirred at 100 °C for another 20 min. The emerald-green solution turned deep purple and the mixture was cooled slowly to room temperature in the oil bath, whereupon blue solid precipitated. The mother liquid was pipetted off, the dark blue product was washed with diethyl ether (15 mL) and dried *in vacuo*.

Empirical formula: C₃₄H₃₆BrN₅ORu (711.11 g mol⁻¹, **8b**).

Yield: 298 mg (0.42 mmol), 69 % of th., blue crystals.

Elemental analysis: (calcd. for C₃₄H₃₆BrN₅ORu, 711.11 g mol⁻¹), found (calcd.): C 57.51 % (57.38 %), H 5.13 % (5.10 %), N 9.67 % (9.84 %), Br 10.41 % (11.23 %).

¹H NMR spectroscopy (CD₂Cl₂, 400 MHz): δ = 7.47–7.23 (m, 20H, *H_{arom.}*), 5.42 (s, 8H, N-CH₂-Ph), 3.72 (s, 8H, N-CH₂-CH₂-N) ppm.

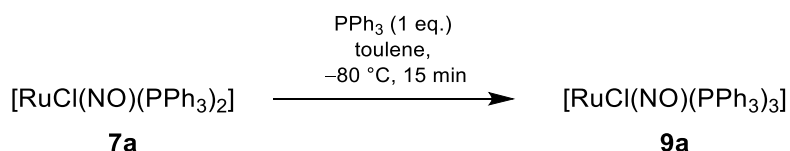
¹³C{¹H} NMR spectroscopy (CD₂Cl₂, 101 MHz): δ = 216.28 (N₂C) 137.86 (*ipso*-C), 129.06 (*meta*-CH), 128.97 (*ortho*-CH), 127.99 (*para*-CH), 56.49 (N-CH₂-CH₂-N), 48.98 (N-CH₂-Ph) ppm.

MS (*M* = C₃₄H₃₆BrN₅ORu, 711.11 g mol⁻¹): FAB⁺: *m/z* = 711.8 ([*M*]⁺, calcd. 711.1), 632.0 ([*M* - Br]⁺, calcd. 632.2), 602.8 ([*M* - NO - Br]⁺, calcd. 602.2).

IR spectroscopy (RT, solid), (intensity): $\tilde{\nu}$ = 1686 (vs, NO), 1497 (vs, CN₂) cm⁻¹.

5.9 Synthesis of the penta-coordinated {RuNO}⁸ phosphane compounds

5.9.1 [RuCl(NO)(PPh₃)₃] (9a)



Starting materials: [RuCl(NO)(PPh₃)₂] (**7a**), triphenylphosphane, toluene.

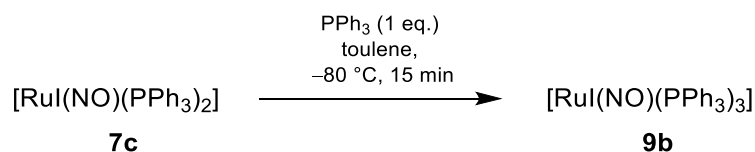
Procedure: Compound **7a** (171 mg, 0.25 mmol) was dissolved in toluene (15 mL) and triphenylphosphane (65 mg, 0.25 mmol) was added. The reaction mixture was heated under refluxing conditions at 100 °C for 5 min to ensure the dissolution of triphenylphosphane. After cooling to -80 °C the initially green solution turned dark brown. For the following steps it was essential to keep the temperature under -50 °C. To precipitate the product, the solution was layered with diethyl ether and the mixture was stored over night at -60 °C. The mother liquid was pipetted off, the dark brown crystalline product was washed with diethyl ether and dried *in vacuo*.

Empirical formula: C₅₄H₄₅ClNOP₃Ru (691.05 g mol⁻¹, **9a**).

Yield: 151 mg (0.16 mmol), 64 % of th., dark brown crystals.

MS: (*M* = C₅₄H₄₅ClNOP₃Ru, 953.40 g mol⁻¹): FAB⁺: *m/z* = 691.7 ([*M*-PPh₃]⁺, calcd. 691.05), 262.4 ([PPh₃]⁺, calcd. 262.09).

IR spectroscopy (RT, solid), (intensity): $\tilde{\nu}$ = 1630 (s, NO) cm⁻¹.

5.9.2 [RuI(NO)(PPh₃)₃] (**9b**)

Starting materials: [RuI(NO)(PPh₃)₂] (**7c**), triphenylphosphane, toluene.

Procedure: Compound **7c** (942 mg, 1.36 mmol) was dissolved in toluene (20 mL) and triphenylphosphane (325 mg, 1.24 mmol) was added. The reaction mixture was heated under refluxing conditions at 100 °C for 5 min to ensure the dissolution of triphenylphosphane. The solution was cooled down to -80 °C. The initially green solution already turned brownish at room temperature and was completely dark brown at about -50 °C. For the following steps it was essential to keep the temperature under -50 °C. To precipitate the product, the solution was layered with diethyl ether and the mixture was stored over night at -60 °C. The mother liquid was pipetted off, the dark red crystalline product was washed with diethyl ether and dried *in vacuo*.

Empirical formula: C₅₄H₄₅INOP₃Ru (1045.08 g mol⁻¹, **9b**).

Yield: 1.13 g (1.08 mmol), 80 % of th., dark red crystals.

Elemental analysis: (calcd. C₃₆H₃₀ClNOP₂Ru·H₂O, 1080.87 g mol⁻¹), found (calcd.): C 60.93 % (61.02 %), H 4.45 (4.46 %), N 1.33 (1.32 %).

³¹P{¹H} NMR spectroscopy (toluene, 162 MHz, -80 °C): δ = 48.71 (s, br) 20.33 (s, br) ppm.

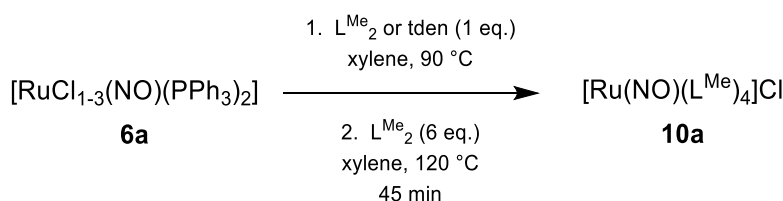
³¹P{¹H} solid-state NMR spectroscopy (10 kHz mas, 202 MHz): δ = 52.0 (s, P_{ax}), 18.3 (d, J = 267 Hz, P_{eq}), 16.05 (d, J = 267 Hz, P_{eq}) ppm.

MS: (M = C₅₄H₄₅INOP₃Ru, 1044.86 g mol⁻¹): FAB⁺: m/z = 919.8 ([M-I]⁺, calcd. 918.18), 782.6 ([M-PPh₃]⁺, calcd. 782.99), 262.4 ([PPh₃]⁺, calcd. 262.09).

IR spectroscopy (RT, solid), (intensity): ν̃ = 1625 (s, NO) cm⁻¹.

5.10 Synthesis of the penta-coordinated {RuNO}⁸ NHC compounds

5.10.1 [Ru(NO)(L^{Me})₄]Cl (**10a**)



Literature: M. F. Lappert, P. L. Pye, *J. Chem. Soc., Dalton Trans.* **1978**, 7, 837–844.

Starting materials: [RuCl₁₋₃(NO)(PPh₃)₂] (**6a**), L^{Me}₂ (**1a**), xylene.

Procedure: To a suspension of compound **6a** (500 mg, 0.66 mmol) in xylene (30 mL) was added tden (0.15 mL, 0.66 mmol) and the mixture was stirred at 90 °C for 15 min. The initially chartreuse suspension turned dark green and a dark solid precipitated during the reaction. The mixture was filtered under an inert gas atmosphere while hot to remove the carbocation salt. L^{Me}₂ (1.98 mL of a 2 M stock solution, 3.96 mmol, 6 eq.) was added and the mixture was stirred at 120 °C for 45 min, whereupon the solution turned red and a micro-crystalline red solid precipitated. After cooling to room temperature, the mother liquid was pipetted off, the product was washed with diethyl ether and dried *in vacuo*.

Empirical formula: C₂₀H₄₀ClN₉ORu (559.21 g mol⁻¹, **10a**).

Yield: 100 mg (0.18 mmol), 27 % of th., red crystals.

Elemental analysis: (calcd. For C₂₀H₄₀ClN₉ORu, 559.21 g mol⁻¹), found (calcd.): C 42.60 % (42.96 %), H 7.08 % (7.21 %), N 20.50 % (22.55 %).

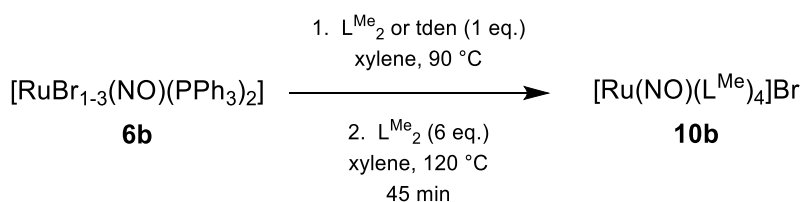
¹H NMR spectroscopy (DMSO-d₆; 400 MHz): δ = 3.51 (s, 16 H, N-CH₂-CH₂-N), 2.70 (s, 24 H, N-CH₃) ppm.

¹³C{¹H} NMR spectroscopy (DMSO-d₆; 101 MHz): δ = 51.22 (N-CH₂-CH₂-N), 37.54 (N-CH₃) ppm.

MS (M⁺ = C₂₀H₄₀N₉ORu⁺, 524.24 g mol⁻¹): FAB⁺: m/z = 540.8 ([M + O]⁺, calcd.: 540.23).

IR spectroscopy (RT, solid), (intensity): ν̃ = 1498 (s, NCN), 1471 (s, NO) cm⁻¹.

5.10.2 [Ru(NO)(L^{Me})₄]Br (**10b**)



According to M. F. Lappert, P. L. Pye, *J. Chem. Soc., Dalton Trans.* **1978**, 7, 837–844.

Starting materials: [RuBr₁₋₃(NO)(PPh₃)₂] (**6b**), L^{Me}₂ (**1a**), xylene.

Procedure: To a suspension of compound **6b** (1.0 g, 1.12 mmol) in xylene (60 mL) was added tden (0.28 mL, 1.12 mmol) and the mixture was stirred at 90 °C for 15 min. The initially chartreuse suspension turned dark green and a dark solid precipitated during the reaction. The mixture was filtered under an inert gas atmosphere while hot to remove the carbocation salt. L^{Me}₂ (**1a**, 3.36 mL of a 2 M stock solution, 6.72 mmol, 6 eq.) was added and the mixture was stirred at 120 °C for 45 min, whereupon the solution turned red and a micro crystalline red solid precipitated. After cooling to room temperature the mother liquid was pipetted off, the product was washed with diethyl ether and dried *in vacuo*.

Empirical formula: C₂₀H₄₀BrN₉ORu (603.16 g mol⁻¹, **10b**).

Yield: 239 mg (0.4 mmol), 35 % of th., red crystals.

Elemental analysis: (calcd. For C₂₀H₄₀BrN₉ORu, 603.16 g mol⁻¹), found (calcd.): C 38.13 % (39.80 %), H 6.63 % (6.68 %), N 19.53 % (20.89 %).

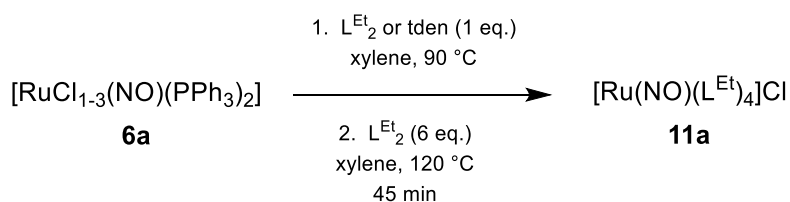
¹H NMR spectroscopy (DMSO-d₆; 400 MHz): δ = 3.48 (s, 16 H, N-CH₂-CH₂-N), 2.67 (s, 24 H, N-CH₃) ppm.

¹³C{¹H} NMR spectroscopy (DMSO-d₆; 101 MHz): δ = 51.22, 51.22 (N-CH₂-CH₂-N), 37.54, 37.54 (N-CH₃) ppm.

MS (M⁺ = C₂₀H₄₀BrN₉ORu, 603.16 g mol⁻¹): FAB⁺: m/z = 603.2 ([M]⁺, calcd.: 603.16).

IR spectroscopy (RT, solid), (intensity): ν̃ = 1491 (s, NCN), 1469 (vs, NO) cm⁻¹.

X-ray structure analysis: tv074

5.10.3 [Ru(NO)(L^{Et})₄]Cl (**11a**)

According to M. F. Lappert, P. L. Pye, *J. Chem. Soc., Dalton Trans.* **1978**, 7, 837–844.

Starting materials: [RuCl₁₋₃(NO)(PPh₃)₂] (**6a**), L^{Et}₂ (**1b**), xylene.

Procedure: To a suspension of compound **6a** (1.50 g, 2.0 mmol) in xylene (60 mL) was added tden (0.45 mL, 2.0 mmol) and the mixture was stirred at 90 °C for 15 min. The initially chartreuse suspension turned dark green and a dark solid precipitated during the reaction. The mixture was filtered under an inert gas atmosphere while hot to remove the carbocation salt. L^{Et}₂ (**1b**, 6.0 mL of a 2 M stock solution, 12.0 mmol, 6 eq.) was added and the mixture was stirred at 120 °C for 45 min, whereupon the solution turned red. After cooling to room temperature the mixture was layered with diethyl ether (20 mL) and stored over night at room temperature. The crystalized red product was isolated by pipetting off the mother liquid, washed with diethyl ether and dried *in vacuo*.

Empirical formula: C₂₈H₅₆ClN₉ORu (671.33 g mol⁻¹, **11a**).

Yield: 255 mg (0.38 mmol), 19 % of th., red crystals.

Elemental analysis: (calcd. For C₂₈H₅₆ClN₉ORu, 671.33 g mol⁻¹), found (calcd.): C 48.95 % (50.10 %), H 8.50 % (8.41 %), N 17.41 % (18.78 %).

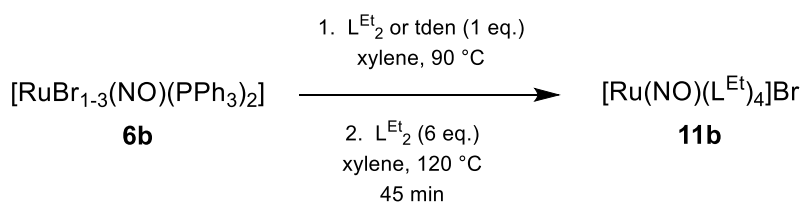
¹H NMR spectroscopy (DMSO-d₆; 400 MHz): δ = 3.58–3.21 (m, 32 H, N-CH₂-CH₃; N-CH₂-CH₂-N), 1.10–0.85 (m, 24 H, N-CH₂-CH₃) ppm.

¹³C{¹H} NMR spectroscopy (DMSO-d₆; 101 MHz): δ = 218.29 (N_CN), 13.08 (N-CH₂-CH₃) ppm.

MS (M⁺ = C₂₈H₅₆N₉ORu⁺, 636.37 g mol⁻¹): FAB⁺: m/z = 636.9 ([M]⁺, calcd.: 636.37).

IR spectroscopy (RT, solid), (intensity): $\tilde{\nu}$ = 1491 (s, NCN), 1469 (vs, NO) cm⁻¹.

X-ray structure analysis: so030

5.10.4 [Ru(NO)(L^{Et})₄]Br (**11b**)

According to M. F. Lappert, P. L. Pye, *J. Chem. Soc., Dalton Trans.* **1978**, 7, 837–844.

Starting materials: [RuBr₁₋₃(NO)(PPh₃)₂] (**6b**), L^{Et}₂ (**1b**), xylene.

Procedure: To a suspension of compound **6b** (1.79 g, 2.0 mmol) in xylene (60 mL) was added tden (0.45 mL, 2.0 mmol) and the mixture was stirred at 90 °C for 15 min. The initially chartreuse suspension turned dark green and a dark solid precipitated during the reaction. The mixture was filtered under an inert gas atmosphere while hot to remove the carbocation salt. L^{Et}₂ (**1b**, 6.0 mL of a 2 M stock solution, 12.0 mmol, 6 eq.) was added and the mixture was stirred at 120 °C for 45 min, whereupon the solution turned red. After cooling to room temperature the mixture was layered with diethyl ether (15 mL) and stored over night at room temperature. The crystalized red product was isolated by pipetting off the mother liquid, washed with diethyl ether and dried *in vacuo*.

Empirical formula: C₂₈H₅₆BrN₉ORu (715.28 g mol⁻¹, **11b**).

Yield: 212 mg (0.30 mmol), 15 % of th., red crystals.

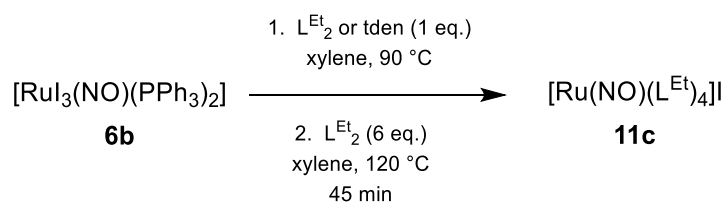
Elemental analysis: (calcd. For C₂₈H₅₆ClN₉ORu, 671.33 g mol⁻¹), found (calcd.): C 46.54 % (46.98 %), H 7.91 % (7.89 %), N 17.26 % (17.61 %).

¹H NMR spectroscopy (DMSO-d₆; 400 MHz): δ = 3.68–3.05 (m, 32 H, N-CH₂-CH₃; N-CH₂-CH₂-N), 1.20–0.88 (m, 24 H, N-CH₂-CH₃) ppm.

¹³C{¹H} NMR spectroscopy (DMSO-d₆; 101 MHz): δ = 218.28 (N-CN), 46.94, 43.57 (br, N-CH₂-CH₂-N; N-CH₂-CH₃) 13.08 (N-CH₂-CH₃) ppm.

MS (M⁺ = C₂₈H₅₆N₉ORu⁺, 636.37 g mol⁻¹): FAB⁺: m/z = 636.8 ([M]⁺, calcd.: 636.37).

IR spectroscopy (RT, solid), (intensity): ν̃ = 1479 (s, NO) cm⁻¹.

5.10.5 [Ru(NO)(L^{Et})₄]I (**11c**)

According to M. F. Lappert, P. L. Pye, *J. Chem. Soc., Dalton Trans.* **1978**, 7, 837–844.

Starting materials: [RuI₁₋₃(NO)(PPh₃)₂] (**6c**), L^{Et}₂ (**1b**), xylene.

Procedure: To a suspension of compound **6c** (1.0 g, 0.96 mmol) in xylene (40 mL) was added tden (0.22 mL, 0.96 mmol) and the mixture was stirred at 90 °C for 15 min. The initially chartreuse suspension turned dark green and a dark solid precipitated during the reaction. The mixture was filtered under an inert gas atmosphere while hot to remove the carbocation salt. L^{Et}₂ (**1b**, 2.88 mL of a 2 M stock solution, 5.76 mmol, 6 eq.) was added and the mixture was stirred at 120 °C for 45 min, whereupon the solution turned red. After cooling to room temperature the mixture was layered with diethyl ether (20 mL) and stored over night at room temperature. The crystalized red product was isolated by pipetting off the mother liquid, washed with diethyl ether and dried *in vacuo*.

Empirical formula: C₂₈H₅₆IN₉ORu (763.27 g mol⁻¹, **11c**).

Yield: 385 mg (0.50 mmol), 52 % of th., red crystals.

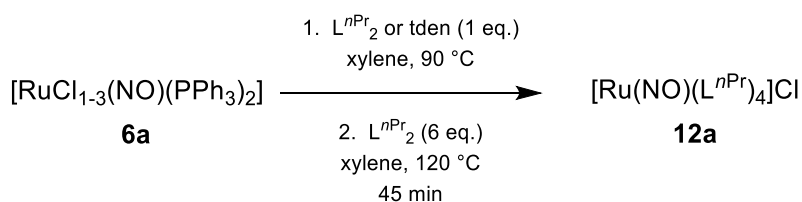
Elemental analysis: (calcd. For C₂₈H₅₆ClN₉ORu, 671.33 g mol⁻¹), found (calcd.): C 45.61 % (44.09 %), H 7.37 % (7.40 %), N 15.07 % (16.53 %).

¹H NMR spectroscopy (DMSO-d₆; 400 MHz): δ = 3.87–2.90 (m, 32 H, N-CH₂-CH₃; N-CH₂-CH₂-N), 1.18–0.93 (m, 24 H, N-CH₂-CH₃) ppm.

¹³C{¹H} NMR spectroscopy (DMSO-d₆; 101 MHz): δ = 218.30 (N_CN), 47.06, 43.50 (br, N-CH₂-CH₂-N; N-CH₂-CH₃) 13.05 (N-CH₂-CH₃) ppm.

MS (M⁺ = C₂₈H₅₆N₉ORu⁺, 636.37 g mol⁻¹): FAB⁺: m/z = 636.92 ([M]⁺, calcd.: 636.37).

IR spectroscopy (RT, solid), (intensity): ν̃ = 1479 (s, NO) cm⁻¹.

5.10.6 [Ru(NO)(L^{nPr})₄]Cl (**12a**)

According to M. F. Lappert, P. L. Pye, *J. Chem. Soc., Dalton Trans.* **1978**, 7, 837–844.

Starting materials: [RuCl₁₋₃(NO)(PPh₃)₂] (**6a**), L^{nPr}₂ (**1c**), xylene.

Procedure: To a suspension of compound **6a** (0.75 g, 1.0 mmol) in xylene (30 mL) was added tden (0.23 mL, 1.0 mmol) and the mixture was stirred at 90 °C for 15 min. The initially chartreuse suspension turned dark green and a dark solid precipitated during the reaction. The mixture was filtered under an inert gas atmosphere while hot to remove the carbocation salt. L^{nPr}₂ (**1c**, 3.0 mL of a 2 M stock solution, 6.0 mmol, 6 eq.) was added and the mixture was stirred at 140 °C for 45 min, whereupon the solution turned red. After cooling to room temperature the mixture was layered with diethyl ether (10 mL) and stored over night at room temperature. The crystalized red product was isolated by pipetting off the mother liquid, washed with diethyl ether and dried *in vacuo*.

Empirical formula: C₃₆H₇₂ClN₉ORu (783.46 g mol⁻¹, **12a**).

Yield: 171 mg (0.22 mmol), 22 % of th., red crystals.

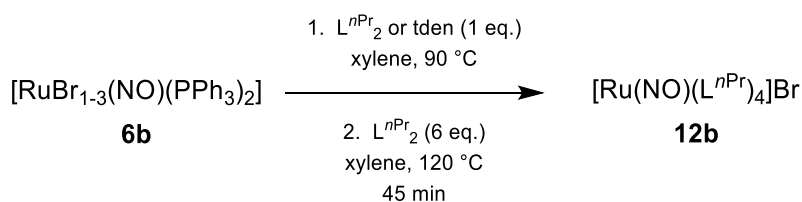
Elemental analysis: (calcd. For C₃₆H₇₂ClN₉ORu, 738.46 g mol⁻¹), found (calcd.): C 54.39 % (55.18 %), H 9.56 % (9.26 %), N 15.92 % (16.09 %).

¹H NMR spectroscopy (DMSO-d₆; 400 MHz): δ = 3.77–2.57 (m, 32 H, N-CH₂-CH₂-N, N-CH₂-CH₂-CH₃), 1.52–1.34 (m, 16 H, N-CH₂-CH₂-CH₃), 0.89–0.73 (m, 24 H, N-CH₂-CH₂-CH₃) ppm.

¹³C{¹H} NMR spectroscopy (DMSO-d₆; 101 MHz, 80 °C): δ = 219.07 (N-CN), 51.61 (N-CH₂-CH₂-N), 47.50 (N-CH₂-CH₂-CH₃), 20.36 (N-CH₂-CH₂-CH₃), 10.74 (N-CH₂-CH₂-CH₃) ppm.

MS (M = C₂₈H₅₆N₉ORu⁺; 748.49 g mol⁻¹): FAB⁺: m/z = 764.8 ([M]⁺, calcd.: 764.49).

IR spectroscopy (RT, solid), (intensity): ν̃ = 1479 (s, NO) cm⁻¹.

5.10.7 [Ru(NO)(L^{nPr})₄]Br (**12b**)

According to M. F. Lappert, P. L. Pye, *J. Chem. Soc., Dalton Trans.* **1978**, 7, 837–844.

Starting materials: [RuBr₁₋₃(NO)(PPh₃)₂] (**6b**), L^{nPr}₂ (**1c**), xylene.

Procedure: To a suspension of compound **6b** (1.39 g, 1.56 mmol) in xylene (40 mL) was added tden (0.36 mL, 1.56 mmol) and the mixture was stirred at 90 °C for 15 min. The initially chartreuse suspension turned dark green and a dark solid precipitated during the reaction. The mixture was filtered under an inert gas atmosphere while hot to remove the carbocation salt. L^{nPr}₂ (**1c**, 4.68 mL of a 2 M stock solution, 9.36 mmol, 6 eq.) was added and the mixture was stirred at 140 °C for 45 min, whereupon the solution turned red. After cooling to room temperature the mixture was layered with diethyl ether (20 mL) and stored over night at room temperature. The crystalized red product was isolated by pipetting off the mother liquid, washed with diethyl ether and dried *in vacuo*.

Empirical formula: C₃₆H₇₂BrN₉ORu (827.41 g mol⁻¹, **12b**).

Yield: 297 mg (0.36 mmol), 23 % of th., red crystals.

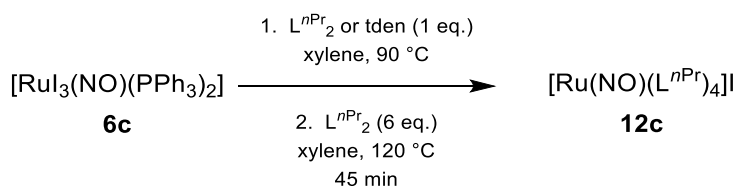
Elemental analysis: (calcd. For C₃₆H₇₂BrN₉ORu, 827.41 g mol⁻¹), found (calcd.): C 50.73 % (52.22 %), H 8.57 % (8.77 %), N 14.64 % (15.22 %).

¹H NMR spectroscopy (DMSO-d₆; 400 MHz): δ = 3.75–2.83 (m, 32 H, N-CH₂-CH₂-N, N-CH₂-CH₂-CH₃), 1.61–1.19 (m, 16 H, N-CH₂-CH₂-CH₃), 0.88–0.80 (m, 24 H, N-CH₂-CH₂-CH₃) ppm.

¹³C{¹H} NMR spectroscopy (DMSO-d₆; 101 MHz, 80 °C): δ = 219.26 (N_CN), 51.61, 47.50 (N-CH₂-CH₂-N, N-CH₂-CH₂-CH₃), 20.37 (N-CH₂-CH₂-CH₃), 10.73 (N-CH₂-CH₂-CH₃) ppm.

MS (M = C₂₈H₅₆N₉ORu⁺; 748.49 g mol⁻¹): FAB⁺: m/z = 747.9 ([M]⁺, calcd.: 748.49).

IR spectroscopy (RT, solid), (intensity): ν̃ = 1479 (s, NO) cm⁻¹.

5.10.8 [Ru(NO)(L^{nPr})₄]I (**12c**)

According to M. F. Lappert, P. L. Pye, *J. Chem. Soc., Dalton Trans.* **1978**, 7, 837–844.

Starting materials: [Ru₃(NO)(PPh₃)₂] (**6c**), L^{nPr}₂ (**1c**), xylene.

Procedure: To a suspension of compound **6c** (1.0 g, 0.96 mmol) in xylene (40 mL) was added tden (0.22 mL, 0.96 mmol) and the mixture was stirred at 90 °C for 15 min. The initially chartreuse suspension turned dark green and a dark solid precipitated during the reaction. The mixture was filtered under an inert gas atmosphere while hot to remove the carbocation salt. L^{nPr}₂ (**1c**, 4.68 mL of a 2 M stock solution, 9.36 mmol, 6 eq.) was added and the mixture was stirred at 140 °C for 45 min, whereupon the solution turned red. After cooling to room temperature the mixture was layered with diethyl ether (20 mL) and stored over night at room temperature. The crystallized red product was isolated by pipetting off the mother liquid, washed with diethyl ether and dried *in vacuo*.

Empirical formula: C₃₆H₇₂BrN₉ORu (827.41 g mol⁻¹, **12c**).

Yield: 297 mg (0.36 mmol), 23 % of th., red crystals.

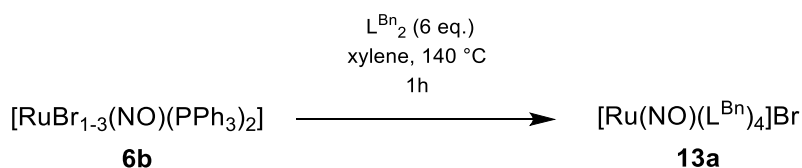
Elemental analysis: (calcd. For C₃₆H₇₂BrN₉ORu, 827.41 g mol⁻¹), found (calcd.): C 50.73 % (52.22 %), H 8.57 % (8.77 %), N 14.64 % (15.22 %).

¹H NMR spectroscopy (DMSO-d₆; 400 MHz): δ = 3.90–2.88 (m, 32 H, N-CH₂-CH₂-N, N-CH₂-CH₂-CH₃), 1.74–1.34 (m, 16 H, N-CH₂-CH₂-CH₃), 0.89–0.80 (m, 24 H, N-CH₂-CH₂-CH₃) ppm.

¹³C{¹H} NMR spectroscopy (DMSO-d₆; 101 MHz, 80 °C): δ = 219.26 (N_CN), 51.61, 47.53 (N-CH₂-CH₂-N, N-CH₂-CH₂-CH₃), 20.38 (N-CH₂-CH₂-CH₃), 10.76 (N-CH₂-CH₂-CH₃) ppm.

MS (*M* = C₂₈H₅₆N₉ORu⁺; 748.49 g mol⁻¹): FAB⁺: *m/z* = 747.9 ([*M*]⁺, calcd.: 748.49).

IR spectroscopy (RT, solid), (intensity): $\tilde{\nu}$ = 1479 (s, NO) cm⁻¹.

5.10.9 [Ru(NO)(L^{Bn})₄]Br (**13a**)

According to M. F. Lappert, P. L. Pye, *J. Chem. Soc., Dalton Trans.* **1978**, 7, 837–844.

Starting materials: [RuBr₁₋₃(NO)(PPh₃)₂] (**6b**), L^{Bn}₂ (**1d**), xylene.

Procedure: To a suspension of compound **6b** (269 g, 0.33 mmol) in xylene (10 mL) was added L^{Bn}₂ (**1d**, 987 mg, 1.97 mmol, 6 eq) and the mixture was stirred at 140 °C for 1 h. The initially chartreuse suspension turned first dark green then deep red and a dark solid precipitated during the reaction. The mixture was filtered under an inert gas atmosphere while hot to remove the carbocation salt. After cooling to room temperature the product precipitated as red crystals which were isolated by pipetting off the mother liquid, washed with diethyl ether and dried *in vacuo*.

Empirical formula: C₆₈H₇₂BrN₉ORu (1211.41 g mol⁻¹, **13a**).

Yield: 182 mg (0.15 mmol), 45 % of th., red crystals.

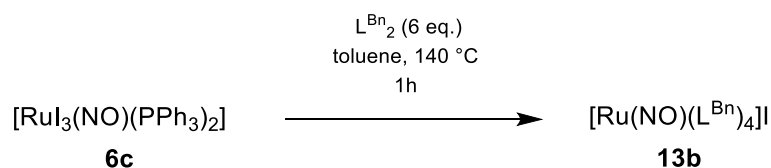
Elemental analysis: (calcd. For C₆₈H₇₂BrN₉ORu, 1211.41 g mol⁻¹), found (calcd.): C 67.38 % (67.37 %), H 6.16 % (5.99 %), N 10.10 % (10.40 %), Br 6.13 % (6.59 %).

¹H NMR spectroscopy (CD₂Cl₂, 400 MHz): δ = 7.44–7.05 (m, 40 H, *H_{arom.}*), 5.28–3.88 (m, 16 H, N-CH₂-Ph), 3.85–2.66 (m, 16 H, N-CH₂-CH₂-N) ppm.

¹³C{¹H} NMR spectroscopy (CD₂Cl₂, 101 MHz): δ = 221.24 (N₂C) 137.02 (*ipso*-C), 129.23–128.65 (m, *meta*-CH), 127.91 (*ortho*-CH), 126.70 (*para*-CH), 57.54, 55.01 (N-CH₂-CH₂-N), 50.39, 47.87 (N-CH₂-Ph) ppm.

MS (*M* = C₆₈H₇₂N₉ORu⁺; 1131.46 g mol⁻¹): FAB⁺: *m/z* = 1131.6 ([*M*]⁺, calcd.: 1131.46).

IR spectroscopy (RT, solid), (intensity): $\tilde{\nu}$ = 1481 (s, NO) cm⁻¹.

5.10.10 [Ru(NO)(L^{Bn})₄]I (**13b**)

According to M. F. Lappert, P. L. Pye, *J. Chem. Soc., Dalton Trans.* **1978**, 7, 837–844.

Starting materials: [Ru₃(NO)(PPh₃)₂] (**6c**), L^{Bn}₂ (**1d**), xylene.

Procedure: To a suspension of compound **6c** (500 mg, 0.48 mmol) in toluene (10 mL) was added L^{Bn}₂ (**1d**, 967 mg, 1.93 mmol, 4 eq) and the mixture was stirred at 130 °C for 30 min. The initially chartreuse suspension turned first dark green then deep red and a dark solid precipitated during the reaction. The mixture was filtered under an inert gas atmosphere while hot to remove the carbocation salt. After cooling to room temperature the product precipitated as red crystals which were isolated by pipetting off the mother liquid, washed with diethyl ether and dried *in vacuo*.

Empirical formula: C₆₈H₇₂IN₉ORu (1259.40 g mol⁻¹, **13b**).

Yield: 430 mg (0.34 mmol), 71 % of th., red crystals.

Elemental analysis: (calcd. For C₆₈H₇₂IN₉ORu · 0.65 C₇H₈, 1420.40 g mol⁻¹), found (calcd.): C 67.66 % (67.85 %), H 6.04 % (6.10 %), N 8.65 % (8.87 %).

¹H NMR spectroscopy (DMSO-*d*₆, 400 MHz): δ = 7.36–7.13 (m, 40H, *H*_{arom.}), 4.68–3.33 (m, 16 H, N-CH₂-CH₂-N), 2.30 (s, 16 H, N-CH₂-Ph) ppm.

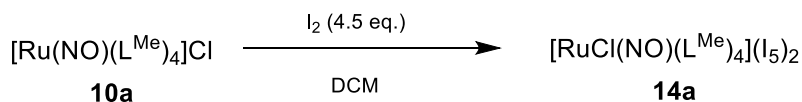
¹³C{¹H} NMR spectroscopy (DMSO-*d*₆, 101 MHz, 80 °C): δ = 221.05 (N₂C) 137.33 (*ipso*-C), 128.89 (*meta*-CH), 128.19 (*ortho*-CH), 125.30 (*para*-CH), 48.98 (N-CH₂-Ph) ppm.

MS (*M* = C₆₈H₇₂N₉ORu⁺; 1131.46 g mol⁻¹): FAB⁺: *m/z* = 1131.6 ([*M*]⁺, calcd.: 1131.46).

IR spectroscopy (RT, solid), (intensity): $\tilde{\nu}$ = 1494 (s, NO) cm⁻¹.

5.11 Synthesis of the {RuNO}⁶ NHC compounds

5.11.1 [RuCl(NO)(L^{Me})₄](I₅)₂ (**14a**)



Starting materials: [Ru(NO)(L^{Me})₄]Cl (**10a**), iodine, dichloromethane.

Procedure: Compound **10a** (271 mg, 0.48 mmol) was dissolved in dichloromethane (15 mL), then I₂ (548 mg, 2.16 mmol, 4.5 eq.) was added. Whereupon the color changed instantly from red to brown and a dark solid precipitated. The mother liquid was pipetted off and the product was washed with diethyl ether (3 × 10 mL) and dried *in vacuo*. Analytically pure black crystals were obtained by covering dimethyl sulfoxide solutions of the raw product with a layer of ethanol.

Empirical formula: C₂₀H₄₀ClI₁₀N₉ORu (1828.25 g mol⁻¹, **14a**).

Yield: 257 mg (0.14 mmol), 29 % of th., black crystals.

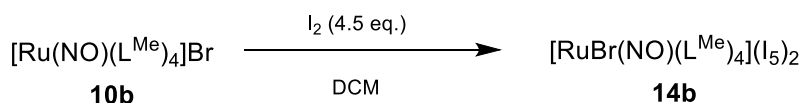
¹H NMR spectroscopy(DMSO-*d*₆; 400 MHz): δ = 3.87–3.68 (m, 16 H, N-CH₂-CH₂-N), 3.08 (s, 12 H, N-CH₃), 2.96 (s, 12 H, N-CH₃) ppm.

¹³C{¹H} NMR spectroscopy (DMSO-*d*₆; 101 MHz): δ = 190.41 (N-CN), 52.17 (N-CH₂-CH₂-N), 51.53 (N-CH₂-CH₂-N), 37.95, 37.22 (N-CH₃) ppm.

MS (M²⁺ = C₂₀H₄₀ClN₉ORu²⁺, 559.21 g mol⁻¹): FAB⁺: *m/z* = 559.4 ([M]⁺, calcd. 559.21).

IR spectroscopy (RT, solid), (intensity): ν̃ = 1840 (s, NO).

X-ray structure analysis: to062

5.11.2 [RuBr(NO)(L^{Me})₄](I₅)₂ (**14b**)

Starting materials: [Ru(NO)(L^{Me})₄]Br (**10b**), iodine, dichloromethane.

Procedure: Compound **10b** (409 mg, 0.68 mmol) was dissolved in dichloromethane (15 mL), then I₂ (774 mg, 3.05 mmol, 4.5 eq.) was added. Whereupon the color changed instantly from red to brown and a dark solid precipitated. The mother liquid was pipetted off and the product was washed with diethyl ether (3 × 10 mL) and dried *in vacuo*. Analytically pure black crystals were obtained by covering dimethyl sulfoxide solutions of the raw product with a layer of ethanol.

Empirical formula: C₂₀H₄₀BrI₁₀N₉ORu (1872.20 g mol⁻¹, **14b**).

Yield: 385 mg (0.28 mmol), 41 % of th., black crystals.

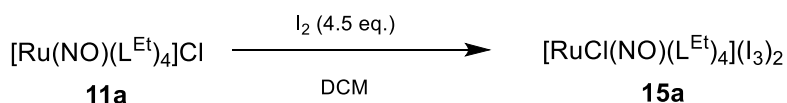
Elemental analysis: (calcd. for C₂₀H₄₀BrI₁₀N₉ORu, 1872.20 g mol⁻¹), found (calcd.): C 13.37 % (12.83 %), H 2.30 % (2.15 %), N 6.78 % (6.73 %).

¹H NMR spectroscopy (DMSO-*d*₆; 400 MHz): δ = 3.90–3.68 (m, 16 H, N-CH₂-CH₂-N), 3.09 (s, 12 H, N-CH₃), 2.96 (s, 12 H, N-CH₃) ppm.

¹³C{¹H} NMR spectroscopy (DMSO-*d*₆; 101 MHz): δ = 188.94 (N-CN), 52.14, 51.38 (N-CH₂-CH₂-N), 37.95, 37.38 (N-CH₃) ppm.

MS (M²⁺ = C₂₀H₄₀BrN₉ORu²⁺, 603.58 g mol⁻¹): FAB⁺: m/z = 603.7 ([M]⁺, calcd. 603.16).

IR spectroscopy (RT, solid), (intensity): ν̃ = 1834 (s, NO).

5.11.3 $[\text{RuCl}(\text{NO})(\text{L}^{\text{Et}})_4](\text{I}_3)_2$ (**15a**)

Starting materials: $[\text{Ru}(\text{NO})(\text{L}^{\text{Et}})_4]\text{Cl}$ (**11a**), iodine, dichloromethane.

Procedure: Compound **11a** (272 mg, 0.40 mmol) was dissolved in dichloromethane (15 mL), then I_2 (462 mg, 1.82 mmol, 4.5 eq.) was added. Whereupon the color changed instantly from red to brown and a dark solid precipitated. The mother liquid was pipetted off and the product was washed with diethyl ether (3×10 mL) and dried *in vacuo*. Analytically pure black crystals were obtained by covering dimethyl sulfoxide solutions of the raw product with a layer of ethanol.

Empirical formula: $\text{C}_{28}\text{H}_{56}\text{ClI}_6\text{N}_9\text{ORu}$ ($1432.76 \text{ g mol}^{-1}$, **x**).

Yield: 261 mg (0.18 mmol), 45 % of th., black crystals.

Elemental analysis: (calcd. For $\text{C}_{28}\text{H}_{56}\text{ClI}_{16}\text{N}_9\text{ORu}$, $1432.76 \text{ g mol}^{-1}$), found (calcd.): C 23.50 % (23.47 %), H 9.99 % (9.94 %), N 8.24 % (8.80 %).

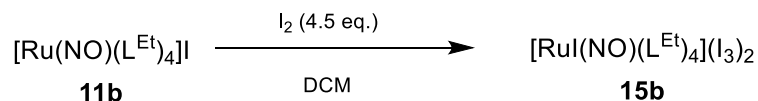
^1H NMR spectroscopy (DMSO- d_6 ; 400 MHz): $\delta = 4.01\text{--}3.82$ (m, 12 H, N- $\text{CH}_2\text{-CH}_3$; N- $\text{CH}_2\text{-CH}_2\text{-N}$), 3.70–3.53 (m, 8 H, N- $\text{CH}_2\text{-CH}_2\text{-N}$), 3.26 (dq, $J = 14.3, 7.2$ Hz, 8 H, N- $\text{CH}_2\text{-CH}_3$), 3.07 (dq, $J = 13.3, 6.52$ Hz, 4 H, N- $\text{CH}_2\text{-CH}_3$) 1.22 (t, $J = 7.0$ Hz, 12 H, N- $\text{CH}_2\text{-CH}_3$), 1.10, 12 H, N- $\text{CH}_2\text{-CH}_3$) ppm.

$^{13}\text{C}\{^1\text{H}\}$ NMR spectroscopy (DMSO- d_6 ; 101 MHz): $\delta = 190.80$ (N $\underline{\text{C}}\text{N}$), 48.22, 47.38 (N- $\text{CH}_2\text{-CH}_2\text{-N}$), 44.93, 44.46 (N- $\text{CH}_2\text{-CH}_3$), 13.42, 13.18 (N- CH_3) ppm.

MS ($M^{2+} = \text{C}_{28}\text{H}_{56}\text{ClI}_6\text{N}_9\text{ORu}^{2+}$, $671.33 \text{ g mol}^{-1}$): FAB $^+$: $m/z = 336.0$ ($[M]^{2+}$, calcd. 335.67).

IR spectroscopy (RT, solid), (intensity): $\tilde{\nu} = 1836$ (s, NO).

X-ray structure analysis: to061

5.11.4 [RuBr(NO)(L^{Et})₄](I₃)₂ (**15b**)

Starting materials: [Ru(NO)(L^{Et})₄]Br (**11b**), iodine, dichloromethane.

Procedure: Compound **11b** (302 mg, 0.42 mmol) was dissolved in dichloromethane (13 mL), then I₂ (481 mg, 1.89 mmol, 4.5 eq.) was added. Whereupon the color changed instantly from red to brown and a dark solid precipitated. The mother liquid was pipetted off and the product was washed with diethyl ether (3 × 10 mL) and dried *in vacuo*. Black crystals were obtained by covering dimethyl sulfoxide solutions of the raw product with a layer of ethanol.

Empirical formula: C₂₈H₅₆BrI₆N₉ORu (1476.71 g mol⁻¹, **15b**).

Yield: 210 mg (0.14 mmol), 33 % of th., black crystals.

Elemental analysis: (calcd. For C₂₈H₅₆BrI₆N₉ORu, 1476.71 g mol⁻¹), found (calcd.): C 21.00 % (22.77 %), H 3.58 % (3.82 %), N 7.61 % (8.53 %).

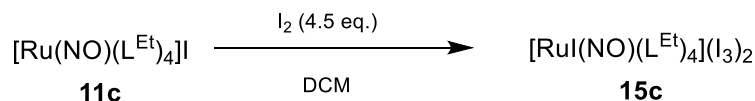
¹H NMR spectroscopy (DMSO-*d*₆; 400 MHz): δ = 4.05–3.84 (m, 12 H, N-CH₂-CH₂-N, N-CH₂-CH₃), 3.67–3.54 (m, 8 H, N-CH₂-CH₂-N), 3.17–3.34 (m, 8 H, N-CH₂-CH₃), 3.05 (dq, *J* = 13.5, 6.7 Hz, 4 H, N-CH₂-CH₃), 1.22 (t, *J* = 7.1 Hz, 12 H, N-CH₂-CH₃), 1.13 (t, *J* = 6.7 Hz, 12 H, N-CH₂-CH₃) ppm.

¹³C{¹H} NMR spectroscopy (DMSO-*d*₆; 101 MHz): δ = 189.46 (N-CN), 48.24, 47.40 (N-CH₂-CH₂-N), 45.94, 44.48 (N-CH₂-CH₃), 13.50, 13.33 (N-CH₃) ppm.

MS (*M*²⁺ = C₂₈H₅₆BrN₉ORu²⁺, 715.28 g mol⁻¹): FAB⁺: *m/z* = 715.8 ([*M*]⁺, calcd.715.98).

IR spectroscopy (RT, solid), (intensity): $\tilde{\nu}$ = 1829 (s, NO).

X-ray structure analysis: to063

5.11.5 [RuI(NO)(L^{Et})₄](I₃)₂ (**15c**)

Starting materials: [Ru(NO)(L^{Et})₄]I (**11c**), iodine, dichloromethane.

Procedure: Compound **11c** (304 mg, 0.39 mmol) was dissolved in dichloromethane (20 mL), then I₂ (454 mg, 1.79 mmol, 4.5 eq.) was added. Whereupon the color changed instantly from red to brown and a dark solid precipitated. The mother liquid was pipetted off and the product was washed with diethyl ether (3 × 10 mL) and dried *in vacuo*. Black crystals were obtained by covering dimethyl sulfoxide solutions of the raw product with a layer of ethanol.

Empirical formula: C₂₈H₅₆I₁₀N₉ORu (1905.41 g mol⁻¹, **15c**).

Yield: 304 mg (0.16 mmol), 41 % of th., black crystals.

Elemental analysis: (calcd. For C₂₈H₅₆I₁₀N₉ORu, 1905.41 g mol⁻¹), found (calcd.): C 17.72 % (17.65 %), H 3.09 % (2.96 %), N 6.64 % (6.62 %).

¹H NMR spectroscopy (DMSO-*d*₆; 400 MHz): δ = 4.16 (dq, *J* = 13.9, 7.0 Hz, 4 H, N-CH₂-CH₃), 4.03–3.79 (m, 8 H, N-CH₂-CH₂-N), 3.74–3.49 (m, 8 H, N-CH₂-CH₂-N), 3.29 (dq, *J* = 15.0, 7.0 Hz, 4 H, N-CH₂-CH₃), 3.19 (dq, *J* = 14.2, 7.1 Hz, 4 H, N-CH₂-CH₃), 3.01 (dq, *J* = 13.4, 6.7 Hz, 4 H, N-CH₂-CH₃), 1.22 (t, *J* = 7.1 Hz, 12 H, N-CH₂-CH₃), 1.13 (t, *J* = 6.7 Hz, 12 H, N-CH₂-CH₃) ppm.

¹³C{¹H} NMR spectroscopy (DMSO-*d*₆; 101 MHz): δ = 187.74 (N-CN), 48.18, 47.80 (N-CH₂-CH₂-N), 47.41, 44.46 (N-CH₂-CH₃), 13.54, 13.33 (N-CH₃) ppm.

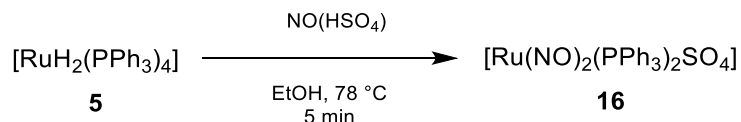
MS (*M*²⁺ = C₂₈H₅₆I₁₀N₉ORu²⁺, 763.27 g mol⁻¹): FAB⁺: *m/z* = 381.8 ([*M*]²⁺, calcd. 381.64).

IR spectroscopy (RT, solid), (intensity): $\tilde{\nu}$ = 1828 (s, NO).

X-ray structure analysis: tq015

5.12 Synthesis of the {Ru(NO)₂}⁸ phosphane compounds

5.12.1 [Ru(NO)₂(PPh₃)₂SO₄] (16)



According to A. P. Gaughan, B. J. Corden, R. Eisenberg et al., *Inorg. Chem.* **1974**, *13*, 789–791.

Starting materials: [RuH₂(PPh₃)₄] (**5**), nitrosyl hydrogensulfate (**2**), ethanol.

Procedure: [RuH₂(PPh₃)₄] (**5**, 200 mg, 0.17 mmol) was dissolved in ethanol (10 mL) and heated to reflux. Then solid NO(HSO₄) (**2**) was added in small quantities until the color changed from yellow to dark brown and a black crystalline solid precipitated. The solution was cooled down, the solvent decanted off and the product was dried *in vacuo*.

Empirical formula: C₃₆H₃₀N₂O₆P₂RuS (781.72 g mol⁻¹, **16**).

Yield: 105 mg (0.13 mmol), 77 % of th.

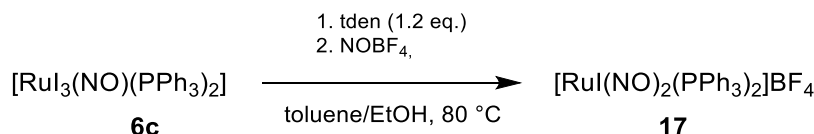
Elemental analysis: (calcd. for C₃₆H₃₀N₂O₆P₂RuS · 2 H₂O, 817.75 g mol⁻¹), found (calcd.): C 51.03 % (52.88 %), H 4.72 % (4.19 %), N 2.81 % (3.43 %), S 4.24 % (3.92 %).

³¹P{¹H} NMR spectroscopy (CH₂Cl₂, 109 MHz): δ = 31.0 (s, br), 30.52 (s), 23.01 (s, br), 19.82 ppm.

MS (*M* = C₃₆H₃₀N₂O₆P₂RuS, 782.02 g mol⁻¹): FAB⁺: *m/z* = 783.0 ([*M*]⁺, calcd. 782.02), 721.2 ([*M* - 2NO]⁺, calcd. 722.04).

IR spectroscopy (RT, solid), (intensity): $\tilde{\nu}$ = 1814 (m, NO), 1614 (s, NO) cm⁻¹.

X-ray structure analysis: uv126.

5.12.2 [RuI(NO)₂(PPh₃)₂]BF₄ (**17**)

Starting materials: [RuI₃(NO)(PPh₃)₂] (**6c**), tden, toluene, nitrosyl tetrafluoroborate, ethanol.

Procedure: Tden (0.14 mL, 0.59 mmol, 1.0 eq.) was added to a solution of compound **6c** (612 mg, 0.59 mmol) in toluene (10 mL) and was stirred at 80 °C for 10 min. The initially brown suspension turned into a green solution and a dark solid precipitated during the reaction. The mixture was filtered under an inert gas atmosphere while hot to remove the carbocation salt. First ethanol (1 mL) and then NO(BF₄) (270 mg, 2.31 mmol, 3.9 eq.) was added to the solution at room temperature. A rapid color change from dark green to dark brown took place and dark brown solid precipitated which was collected by filtration, washed with diethyl ether (3 × 20 mL) and dried *in vacuo*. Brown crystals were obtained by covering dichloromethane solutions with a layer of diethyl ether.

Empirical formula: C₃₆H₃₀BF₄IN₂O₂P₂Ru (899.99 g mol⁻¹, **17**).

Yield: 181 mg (0.20 mmol), 34 % of th., brown crystals.

Elemental analysis: (calcd. for C₃₆H₃₀BF₄IN₂O₂P₂Ru, 899.99 g mol⁻¹), found (calcd.): C 46.60 % (48.08 %), H 3.65 % (3.36 %), N 2.93 % (3.11 %).

³¹P{¹H} NMR spectroscopy (CH₂Cl₂, 109 MHz): δ = 17.13 (s) ppm.

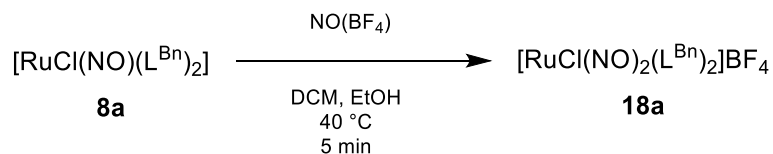
MS (M⁺ = C₃₆H₃₀IN₂O₂P₂Ru⁺, 812.99 g mol⁻¹): FAB⁺: m/z = 813.3 ([M]⁺, calcd. 812.9), 783.2 ([M - NO]⁺, calcd. 782.9).

IR spectroscopy (RT, solid), (intensity): $\tilde{\nu}$ = 1817 (m, NO), 1771 (s, NO) cm⁻¹.

X-ray structure analysis: sv250.

5.13 Synthesis of the {Ru(NO)₂}⁸ NHC compounds

5.13.1 [RuCl(NO)₂(L^{Bn})₂]BF₄ (**18a**)



Starting materials: [RuCl(NO)(L^{Bn})₂] (**8a**), nitrosyl tetrafluoroborate, dichloromethane, ethanol.

Procedure: Compound **8a** (300 mg, 0.45 mmol) was dissolved in dichloromethane (15 mL). First ethanol (0.5 mL), then solid NO(BF₄) was added in small quantities until the color changed from dark blue to orange. The solvent was removed *in vacuo* and the product was washed with diethyl ether (4 × 20 mL) and dried *in vacuo*. Thus, the crude product **18a** was gained in form of red powder. Analytically pure red crystals were obtained by covering dichloromethane solutions of the raw product with a layer of diethyl ether.

Empirical formula: C₃₄H₃₆ClBF₄N₆O₂Ru (784.17 g mol⁻¹, **18a**).

Yield: 212 mg (0.27 mmol), 60 % of th., red powder.

Elemental analysis: (calcd. for C₃₄H₃₆BClF₄N₆O₂Ru · 2 C₄H₁₀O · 0.4 CH₂Cl₂, 918.33 g mol⁻¹), found (calcd.): C 53.51 % (54.11 %), H 5.25 % (6.05 %), N 7.73 % (9.01 %).

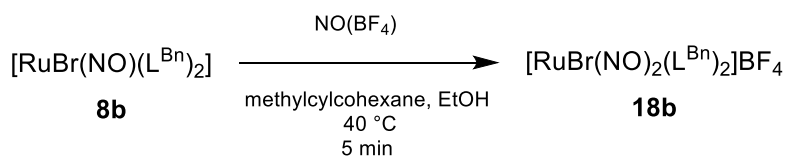
¹H NMR spectroscopy (DMSO-*d*₆, 400 MHz): δ = 7.71–7.13 (m, 20H, *H*_{arom.}), 5.75–3.14 (m, 16H, N-CH₂-Ph, N-CH₂-CH₂-N) ppm.

¹³C{¹H} NMR spectroscopy (DMSO-*d*₆, 101 MHz): δ = 190.34 (N₂C) 135.44 (*ipso*-C), 134.78–126.76 (m, *C*_{arom.}) 53.46 (N-CH₂-CH₂-N) 49.50 (N-CH₂-Ph) ppm.

MS (*M*⁺ = C₃₄H₃₆ClN₆O₂Ru⁺, 697.16 g mol⁻¹): FAB⁺: *m/z* = 697.6 ([*M*]⁺, calcd. 697.16), 667.6, ([*M* - NO]⁺, calcd. 667.1).

IR spectroscopy (RT, solid), (intensity): $\tilde{\nu}$ = 1847 (s, NO), 1672 (s, NO).

X-ray structure analysis: sv070

5.13.2 [RuBr(NO)₂(L^{Bn})₂]BF₄ (**18b**)

Starting materials: [RuBr(NO)(L^{Bn})₂] (**8b**), nitrosyl tetrafluoroborate, methylcyclohexane, ethanol.

Procedure: Compound **8b** (230 mg, 0.32 mmol) was dissolved in dichloromethane (15 mL). First ethanol (0.5 mL), then solid NO(BF₄) was added in small quantities until the color changed from dark blue to orange. The solvent was removed *in vacuo* and the product was washed with diethyl ether (4 × 5 mL) and dried *in vacuo*. Thus, the crude product was gained in form of red powder. Analytically pure red crystals were obtained by covering dichloromethane solutions of the raw product with a layer of diethyl ether.

Empirical formula: C₃₄H₃₆BBBrF₄N₆O₂Ru (828.12 g mol⁻¹, **18b**).

Yield: 150 mg (0.18 mmol), 56 % of th., red powder.

Elemental analysis: (calcd. for C₃₄H₃₆BBBrF₄N₆O₂Ru, 828.12 g mol⁻¹), found (calcd.): C 48.99 % (49.29 %), H 4.94 % (4.38 %), N 8.92 % (10.14 %).

¹H NMR spectroscopy (CD₂Cl₂, 400 MHz): δ = 7.70–7.01 (m, 20H, *H*_{arom.}), 5.36–3.71 (m, 16H, N-CH₂-Ph, N-CH₂-CH₂-N) ppm.

¹³C{¹H} NMR spectroscopy (CD₂Cl₂, 101 MHz): δ = 190.78 (N₂C) 135.44 (*ipso*-C), 128.88–127.05 (m, *C*_{arom.}) 55.46, 52.91 (N-CH₂-CH₂-N) 50.27, 48.49 (N-CH₂-Ph) ppm.

MS (*M*⁺ = C₃₄H₃₆BrN₆O₂Ru⁺, 741.11 g mol⁻¹): FAB⁺: *m/z* = 743.4 ([*M*]⁺, calcd. 741.1), 713.4 ([*M* - NO]⁺, calcd. 711.1).

IR spectroscopy (RT, solid), (intensity): $\tilde{\nu}$ = 1836 (s, NO), 1684 (s, NO).

X-ray structure analysis: sv118

5.14 Synthesis of the {Ru(NO)₂}¹⁰ compounds

5.14.1 [Ru(NO)₂(PPh₃)₂] (19)



Literature: A. P. Gaughan, B. J. Corden, R. Eisenberg, *Inorg. Chem.* **1974**, *13*, 789–791.

Starting materials: [RuH₂(PPh₃)₄] (**5**), diazald, ethanol.

Processing: [RuH₂(PPh₃)₄] (**5**) (950 mg, 0.82 mmol) and diazald (950 mg, 4.4 mmol) were mixed in a *Schlenk* tube and degassed. The mixture was dissolved in ethanol and refluxed for 10 minutes at 80 °C whereupon a red solid precipitated. After cooling to room temperature the product was filtered off and washed with ethanol (2 x 10 mL) and *n*-hexane (2 x 10 mL) and was dried *in vacuo*.

Empirical formula: C₃₆H₃₀N₂O₂P₂Ru (685.67 g mol⁻¹, **19**).

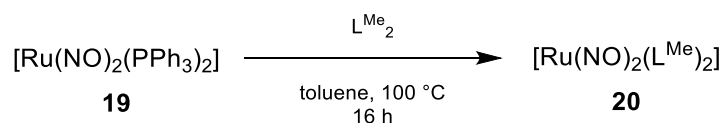
Yield: 260 mg (0.38 mmol), 46 % of th.

Elemental analysis (calc. For C₃₆H₃₀N₂O₂P₂Ru 685.67 g mol⁻¹) found (calcd.): C 62.93 % (63.06 %), N 4.08 % (4.09 %), H 4.48 % (4.41 %).

³¹P{¹H} NMR spectroscopy (CD₂Cl₂; 162 MHz): δ = 55.81 (s) ppm.

IR spectroscopy (RT,solid), (intensity): 1652 (w, NO), 1605 (m, NO) cm⁻¹.

X-ray structure analysis: tv276

5.14.2 [Ru(NO)₂(L^{Me})₂] (**20**)

According to M. F. Lappert, P. L. Pye, *J. Chem. Soc., Dalton Trans.* **1978**, 7, 837–844.

Starting materials: Diethyl ether, [Ru(NO)₂(PPh₃)₂] (**19**), L^{Me}₂ (**1a**), toluene.

Procedure: [Ru(NO)₂(PPh₃)₂] (**19**) (520 mg, 0.76 mmol, 1.0 eq.) was dissolved in toluene (15 mL) and L^{Me}₂ (**1a**, 0.58 mL of a 2M stock solution, 2.27 mmol, 3.0 eq.) was added. The reaction mixture was stirred at 100 °C for 16 h, whereupon the solution turned orange and a purple oily residue occurred. The suspension was cooled down to room temperature, the orange solution was isolated by decantation and the oily residue was discarded. The solvent was removed *in vacuo*, whereby an orange solid precipitated. Red crystals were obtained by covering dichloromethane solutions with a layer of diethyl ether.

Empirical formula: C₁₀H₂₀N₆O₂Ru (357.38 g/mol, **20**).

Yield: 190 mg (0.53 mmol), 70 % of th.

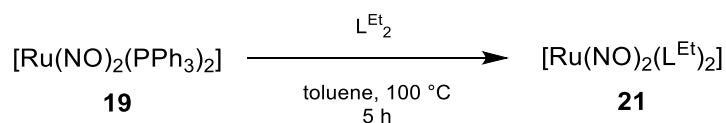
Elemental analysis: (calcd. for C₁₀H₂₀N₆O₂Ru, 357.38 g mol⁻¹), found (calcd.): C 33.61 % (34.20 %), H 5.61 % (5.64 %), N 23.52 % (22.49 %).

¹H NMR spectroscopy (CD₂Cl₂; 400 MHz): δ = 3.60 (s, 8 H, N-CH₂-CH₂-N), 3.07 (s, 12 H, N-CH₃) ppm.

¹³C{¹H} NMR spectroscopy (CD₂Cl₂; 101 MHz): δ = 219.59 (N-CN), 52.32 (N-CH₂-CH₂-N), 38.56, 38.49 (N-CH₃) ppm.

IR spectroscopy (RT, solid), (intensity): 1590 (m, NO), 1539 (m, NO) cm⁻¹.

X-ray structure analysis: uv027

5.14.3 [Ru(NO)₂(L^{Et})₂] (**21**)

According to M. F. Lappert, P. L. Pye, *J. Chem. Soc., Dalton Trans.* **1978**, 7, 837–844.

Starting materials: Diethyl ether, [Ru(NO)₂(PPh₃)₂] (**19**), L^{Et}₂ (**1b**), toluene.

Procedure: [Ru(NO)₂(PPh₃)₂] (**19**) (200 mg, 0.29 mmol.) was dissolved in toluene (15 mL) and L^{Et}₂ (**1b**, 0.15 mL of a 2 M stock solution, 0.29 mmol) was added. The reaction mixture was stirred at 100 °C for 5 h, whereupon a red oily residue occurred. The suspension was cooled down to room temperature, the orange solution was isolated by filtration and the residue was discarded. The solution was stored at –70 °C for 72 hours, whereby orange crystals precipitated.

Empirical formula: C₁₄H₃₀N₆O₂Ru (415.5 g/mol, **21**).

Yield: 190 mg (0.53 mmol), 70 % of th.

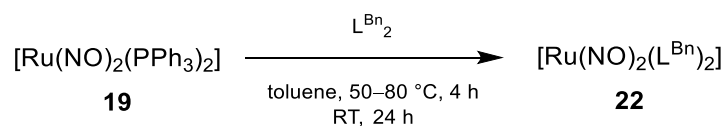
Elemental analysis: (calcd. For C₁₄H₃₀N₆O₂Ru · 0.65 C₇H₈ · 1.35 H₂O, 499.64 g mol⁻¹), found (calcd.): C 43.64 % (44.59 %), H 6.76 % (7.64 %), N 15.94 % (16.82 %).

¹H NMR spectroscopy (CD₂Cl₂; 400 MHz): δ = 3.48 (q, *J* = 7.16 Hz, 8 H, N-CH₂-CH₃), 2.81 (s, 8 H, N-CH₂-CH₂-N), 0.97 (t, *J* = 7.16 Hz, 12 H, N-CH₂-CH₃) ppm.

¹³C{¹H} NMR spectroscopy (CD₂Cl₂; 101 MHz): δ = 220.53 (N-CN), 47.87(N-CH₂-CH₂-N) 45.88 (N-CH₂-CH₃), 13.42 (N-CH₂-CH₃) ppm.

IR spectroscopy (RT, solid), (intensity): 1600 (m, NO), 1550 (m, NO) cm⁻¹.

X-ray structure analysis: uv108

5.14.4 [Ru(NO)₂(L^{Bn})₂] (**22**)

According to M. F. Lappert, P. L. Pye, *J. Chem. Soc., Dalton Trans.* **1978**, 7, 837–844.

Starting materials: Diethyl ether, [Ru(NO)₂(PPh₃)₂] (**19**), L^{Bn}₂ (**1d**), toluene.

Procedure: [Ru(NO)₂(PPh₃)₂] (**19**) (156 mg, 0.32 mmol) was dissolved in toluene (15 mL) and L^{Bn}₂ (**x**) (**1d**, 100 mg, 0.20 mmol) was added. The reaction mixture was stirred at 50 °C for 3 h, 1 h at 80 °C and 24 h at room temperature. The solution was stored at –20 °C for 24 hours, whereby orange crystals precipitated.

Empirical formula: C₃₄H₃₈N₆O₂Ru (607.68 g/mol, **22**).

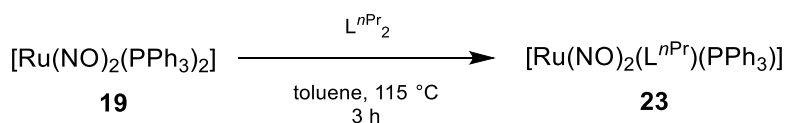
Yield: 181mg (0.153 mmol), 77 % of th., orange crystals.

¹H NMR spectroscopy (CD₂Cl₂; 400 MHz): δ = 7.26–7.16 (m, 24 H, H_{arom}) 4.64 (s, 8 H, N-CH₂-CH₂-N) 3.23 (s, 8 H, N-CH₂-Bn) ppm.

¹³C{¹H} NMR spectroscopy (CD₂Cl₂; 101 MHz): δ = 219.9 (N-C-N), 137.62 (*ipso*-C), 129.11 (*meta*-CH), 128.20 (*ortho*-CH), 128.06 (*para*-CH), 55.66 (N-CH₂-CH₂-N), 49.15 (N-CH₂-Ph) ppm.

IR spectroscopy (RT, solid), (intensity): 1599 (m, NO), 1549 (m, NO) cm⁻¹.

X-ray structure analysis: uv118

5.14.5 $[\text{Ru}(\text{NO})_2(\text{L}^{\text{nPr}})(\text{PPh}_3)]$ (**23**)

According to M. F. Lappert, P. L. Pye, *J. Chem. Soc., Dalton Trans.* **1978**, 7, 837–844.

Starting materials: Diethyl ether, $[\text{Ru}(\text{NO})_2(\text{PPh}_3)_2]$ (**19**), L^{nPr}_2 (**1c**), toluene.

Procedure: $[\text{Ru}(\text{NO})_2(\text{PPh}_3)_2]$ (**19**) (390 mg, 0.57 mmol) was dissolved in toluene (15 mL) and L^{nPr}_2 (**1c**), 0.23 mL of a 2 M stock solution, 0.46 mmol, 0.8 eq) was added. The reaction mixture was stirred at 115 °C for 3 h. The solution was stored at –20 °C for 24 hours, whereby red crystals precipitated.

Empirical formula: $\text{C}_{27}\text{H}_{33}\text{N}_4\text{O}_2\text{PRu}$ (578.14 g/mol, **23**).

Yield: 318 mg (0.55 mmol), 96 % of th., red crystals.

Elemental analysis: (calcd. For $\text{C}_{27}\text{H}_{33}\text{N}_4\text{O}_2\text{PRu} \cdot 0.65 \text{ C}_7\text{H}_8 \cdot 1.35 \text{ H}_2\text{O}$, 662.28 g mol⁻¹) found (calcd.): C 55.64 % (55.50 %), H 5.72 % (5.92 %), N 9.14 % (9.35 %).

¹H NMR spectroscopy (CD_2Cl_2 ; 270 MHz): δ = 7.48–7.33 (m, 15 H, *PPh*₃) 3.43 (s, 4 H, N-CH₂-CH₂-N) 2.81 (t, *J* = 8.1 Hz, 4 H, N-CH₂-CH₂-CH₃), 1.34 (dt, *J* = 7.6, 7.8 Hz, 4 H, N-CH₂-CH₂-CH₃), 0.72 (t, *J* = 7.4 Hz, 6 H, N-CH₂-CH₂-CH₃) ppm.

¹³C{¹H} NMR spectroscopy (CD_2Cl_2 ; 68 MHz): δ = 137.62 (d, *J* = 38.6 Hz, *ipso*-C), 133.66 (d, *J* = 12.61, *meta*-CH), 128.80 (d, *J* = 10.2 Hz, *ortho*-CH), 130.22 (d, 2.2 Hz, *para*-CH), 53.08 (N-CH₂-CH₂-N), 49.55 (N-CH₂-CH₂-CH₃), 21.73 (N-CH₂-CH₂-CH₃), 11.31 (N-CH₂-CH₂-CH₃) ppm.

³¹P{¹H} NMR spectroscopy (CD_2Cl_2 , 109 MHz): δ = 53.8(s) ppm.

IR spectroscopy (RT, solid), (intensity): 1625 (m, NO), 1590 (m, NO) cm⁻¹.

X-ray structure analysis: uv190

5.15 Computational methods

All quantum-chemical calculations at the DFT level were done with the program system ORCA 3.0.3^[147]. Initial geometries were taken from crystal-structure analyses. Wave functions were calculated at the multipole-accelerated RI-DFT level^[148,149] using TZVP^[126] and def2-TZVP basis sets^[127] and the functionals BP86^[124,125] and TPSSH.^[131–133] The COSMO solvation mode^[130] and dispersion correction was applied, using Grimme's DFT-D3^[128] with BJ-damping^[129]. Frequency analyses were done numerically. NPA analyses have been done at the BP86 level with the def2-TZVP basis set, as implemented in ORCA 3.0.3. QTAIM analyses were performed with the program system MULTIWFN.^[134] Continuous shape measures were calculated with the program SHAPE.^[150,151]

6 Appendix

6.1 Packing diagrams of the crystal structures

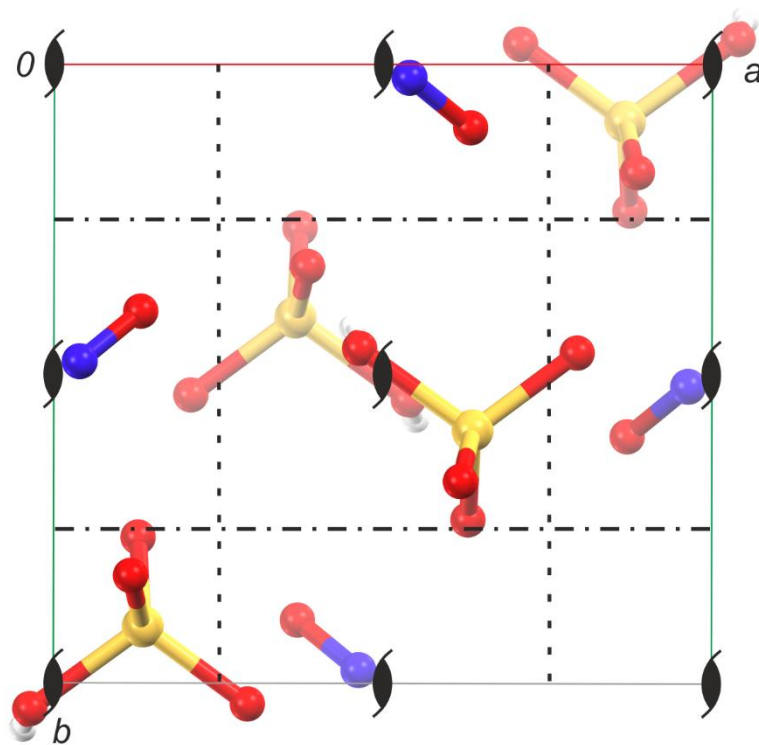


Figure 6.1: (tv281): Packing diagram of **2** in the orthorhombic space group $Pna2_1$ with view along $[001]$. The symmetry elements of the space group $Pna2_1$ are overlaid. Atoms: hydrogen (white), nitrogen (blue), oxygen (red), sulfur (yellow).

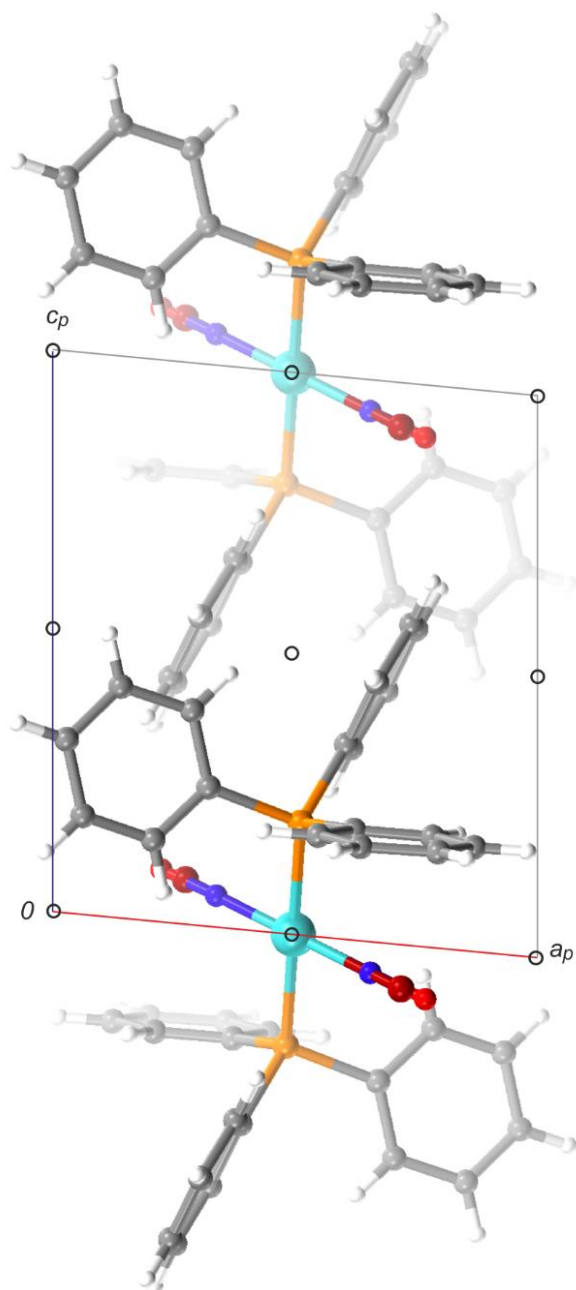


Figure 6.2: (tv429): Packing diagram of **7b** in the triclinic space group $P\bar{1}$ with view along $[010]$. The symmetry elements of the space group $P\bar{1}$ are overlaid. Atoms: carbon (grey), hydrogen (white), bromine (red), nitrogen (blue), oxygen (red), phosphorus (orange), ruthenium (turquoise).

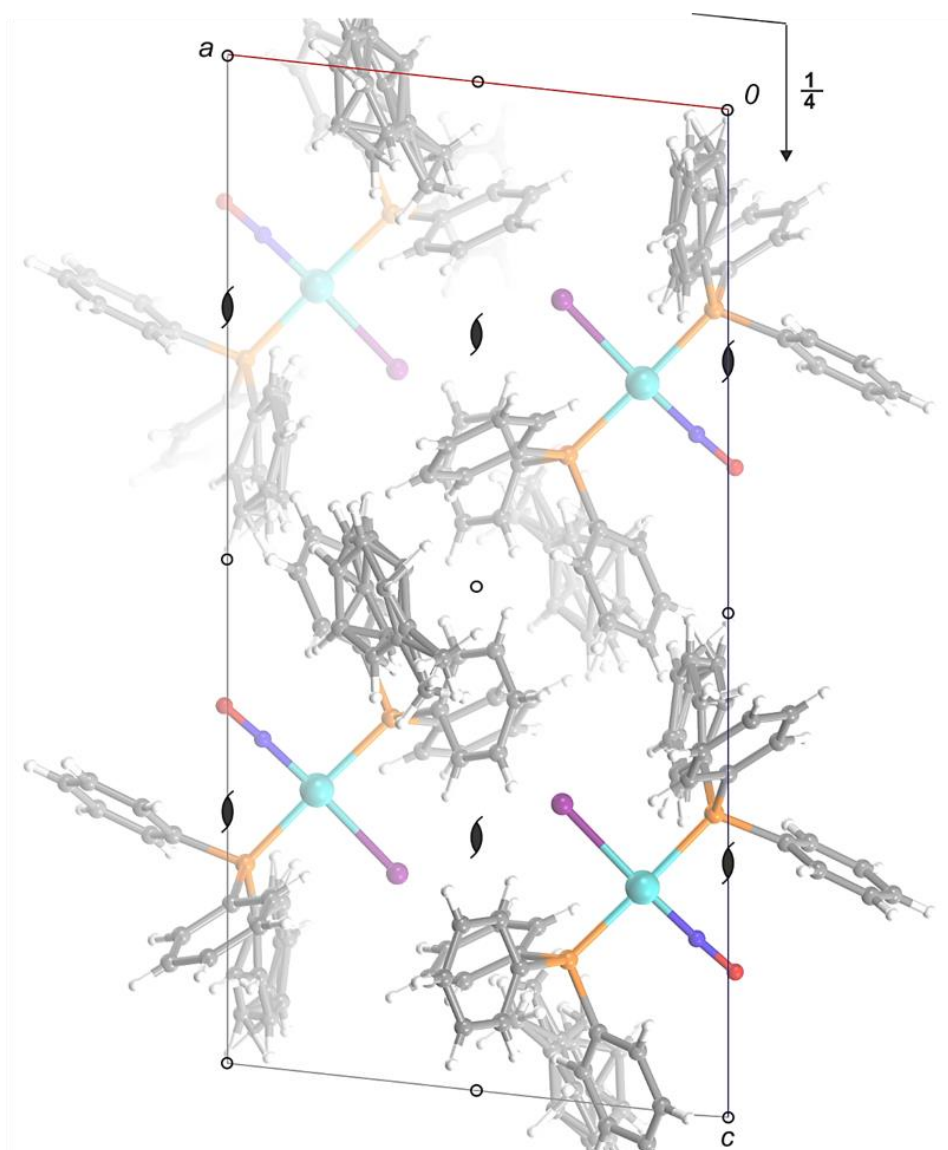


Figure 6.3: (tv132): Packing diagram of **7c** in the monoclinic space group $P2_1/c$ with view along $[010]$. The symmetry elements of the space group $P2_1/c$ are overlaid. Atoms: carbon (grey), hydrogen (white), iodine (purple), nitrogen (blue), oxygen (red), ruthenium (turquoise).

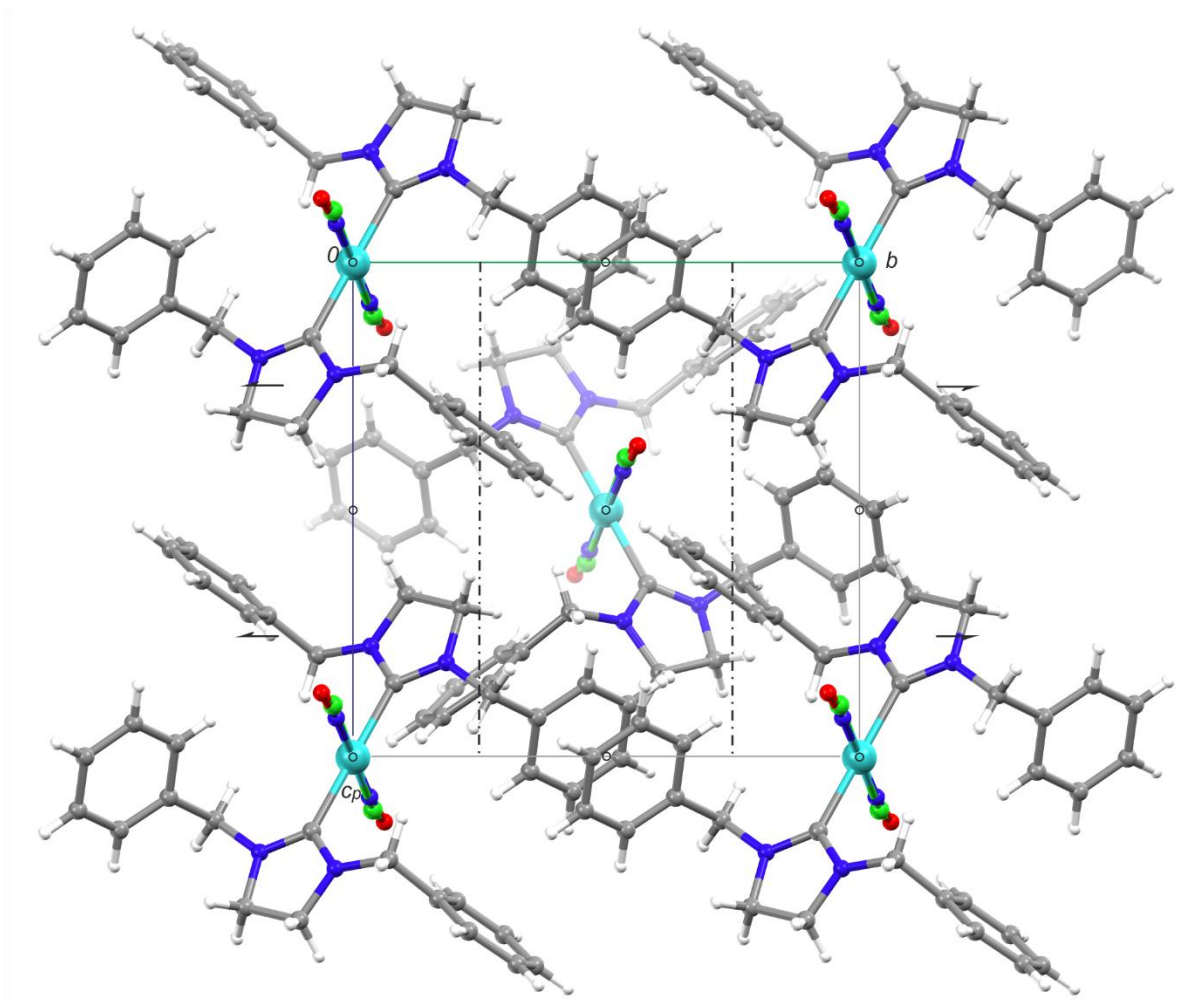


Figure 6.4: (sv026): Packing diagram of **8a** in the monoclinic space group $P2_1/n$ with view along $[100]$. The symmetry elements of the space group $P2_1/n$ are overlaid. Atoms: carbon (grey), hydrogen (white), chlorine (green) nitrogen (blue), oxygen (red), ruthenium (turquoise).

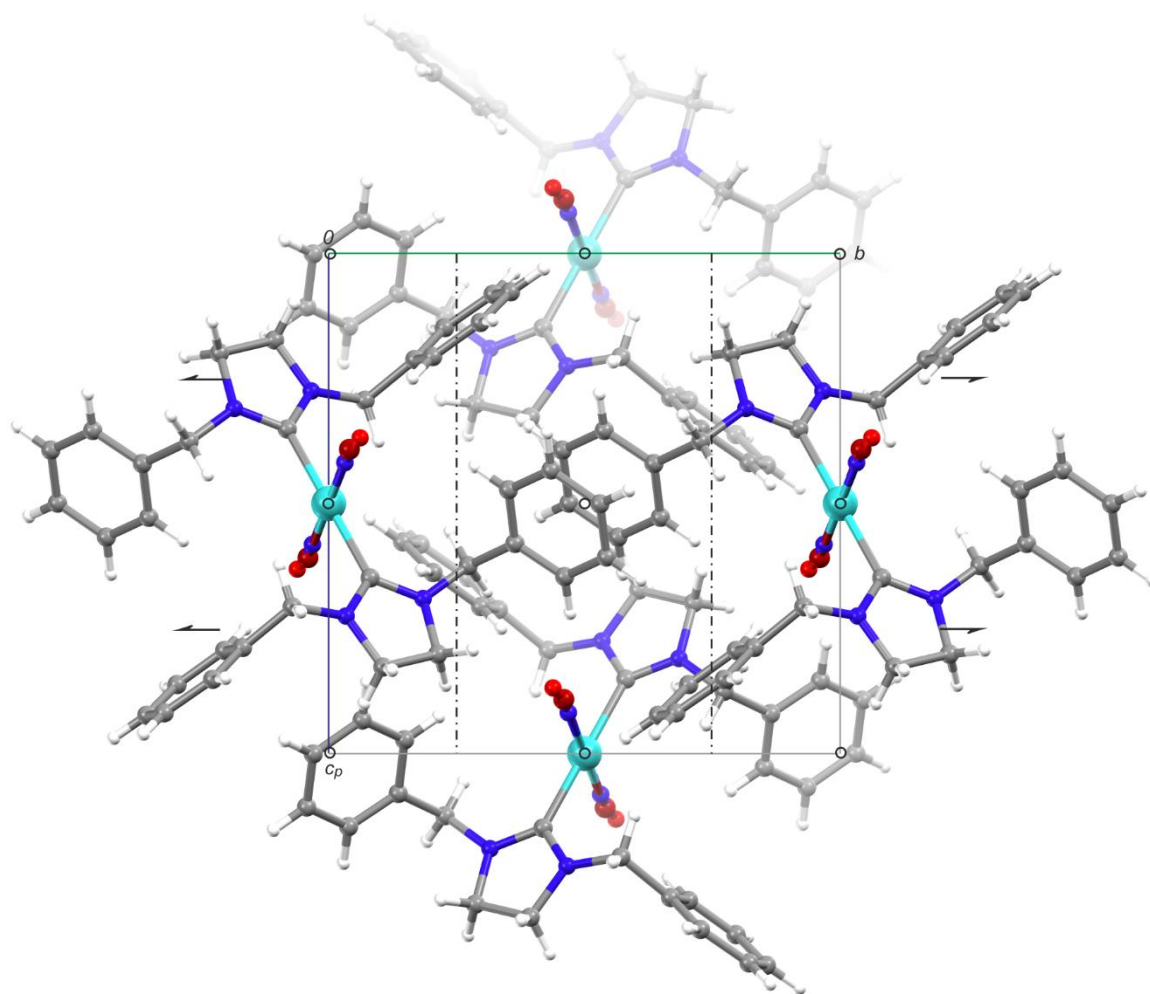


Figure 6.5: (sq028): Packing diagram of **8b** in the monoclinic space group $P2_1/n$ with view along $[100]$. The symmetry elements of the space group $P2_1/n$ are overlaid. Atoms: carbon (grey), hydrogen (white), bromine (dark red), nitrogen (blue), oxygen (red), ruthenium (turquoise).

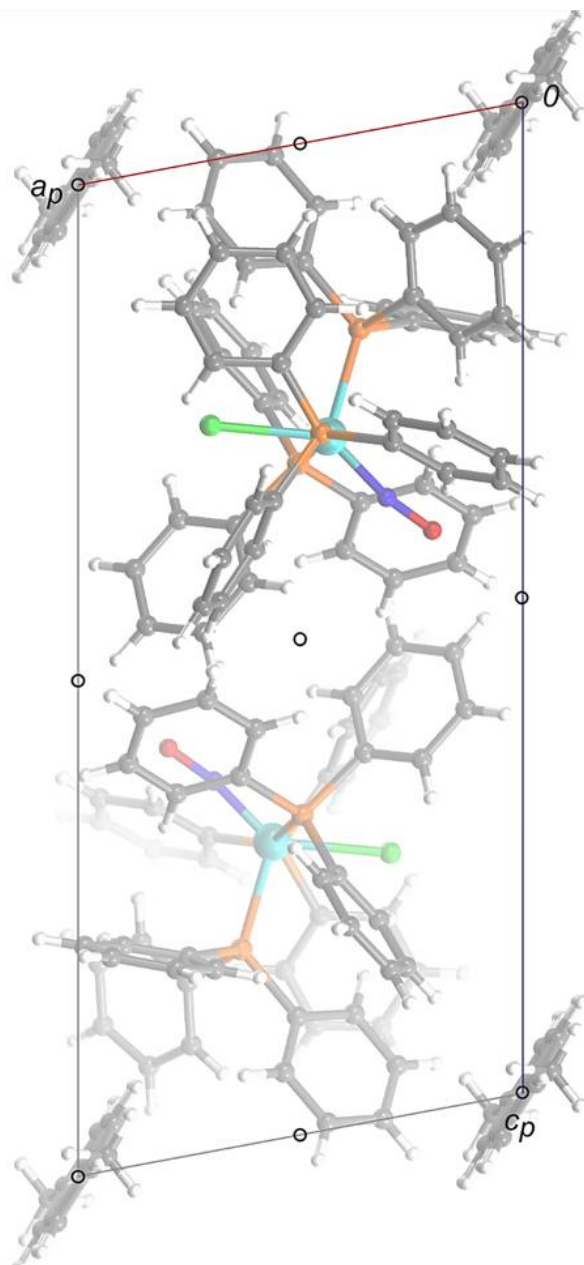


Figure 6.6: (sv255) Packing diagram of **9a** in the triclinic space group $P\bar{1}$ with view along $[010]$. The symmetry elements of the space group $P\bar{1}$ are overlaid. Atoms: carbon (grey), hydrogen (white), chlorine (green), nitrogen (blue), oxygen (red), phosphorus (orange), ruthenium (turquoise).

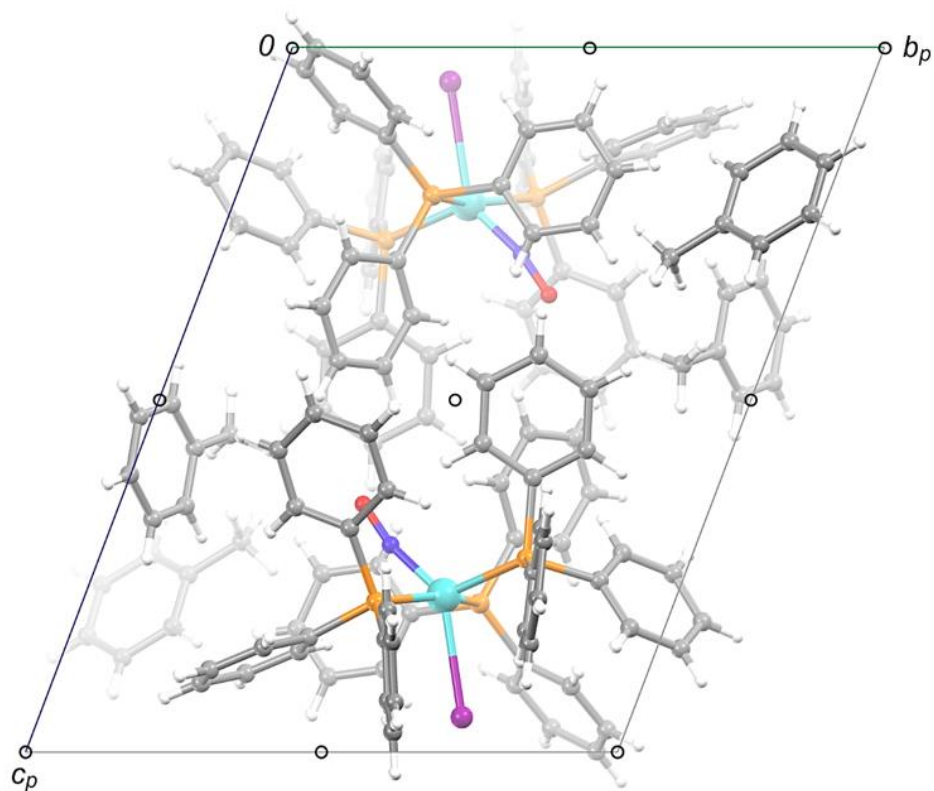


Figure 6.7: (tv134) Packing diagram of **9b** in the triclinic space group $P\bar{1}$ with view along $[100]$. The symmetry elements of the space group $P\bar{1}$ are overlaid. Atoms: carbon (grey), hydrogen (white), iodine (purple), nitrogen (blue), oxygen (red), phosphorus (orange), ruthenium (turquoise).

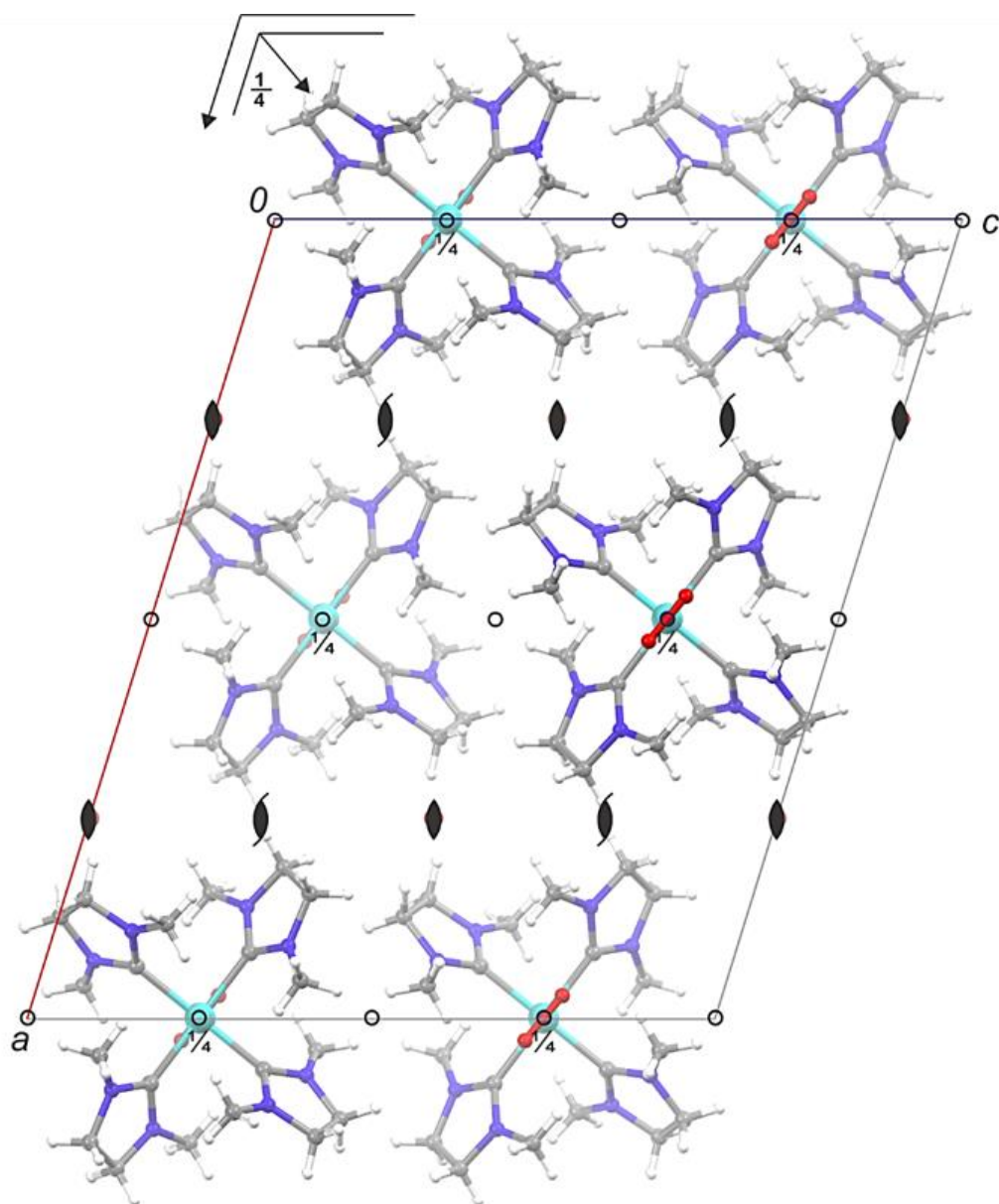


Figure 6.8: (tv074): Packing diagram of **10b** in the monoclinic space group $C_{2/c}$ with view along $[010]$. The symmetry elements of the space group $C_{2/c}$ are overlaid. Atoms: carbon (grey), hydrogen (white), bromine (dark red), nitrogen (blue), oxygen (red), ruthenium (turquoise).

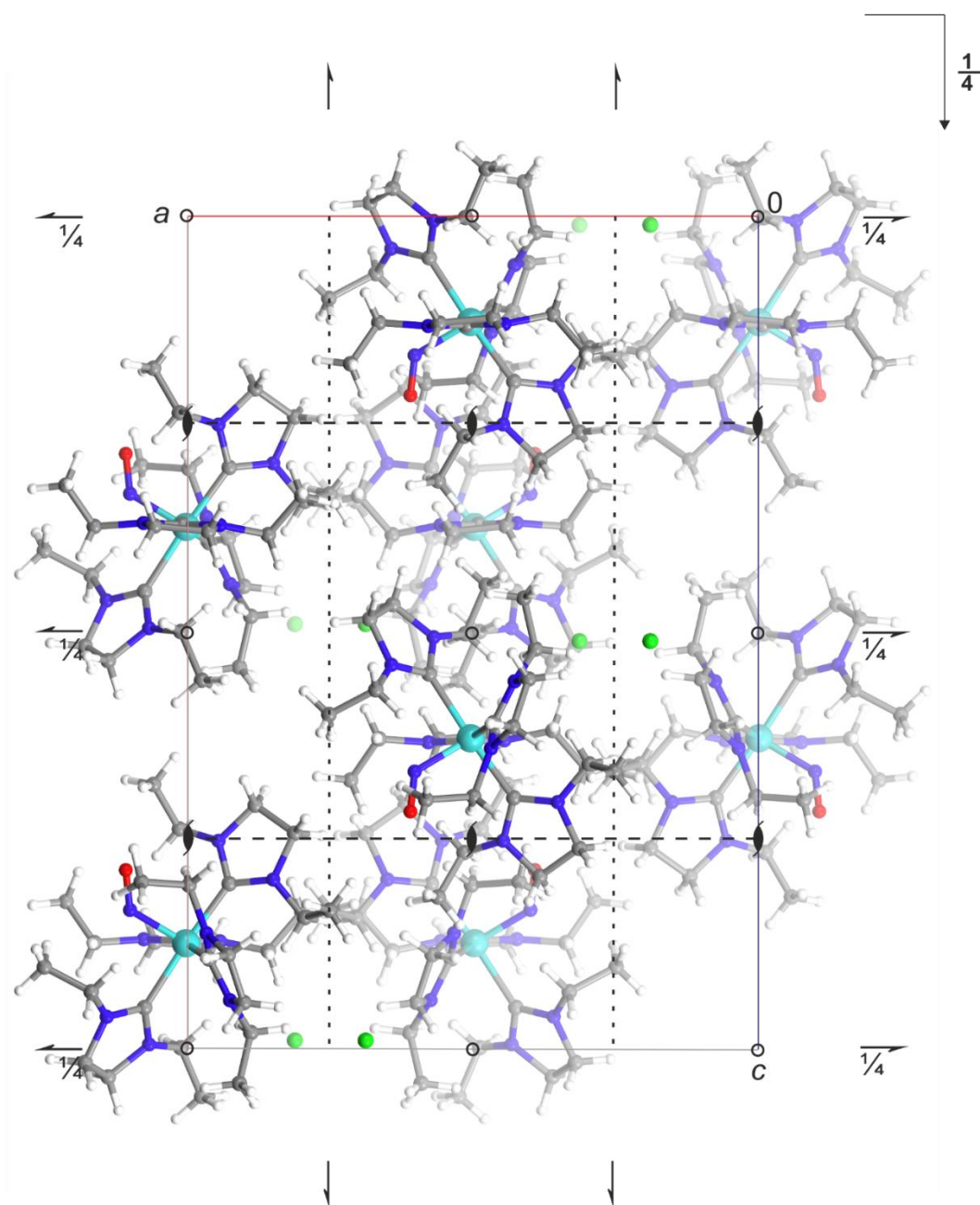


Figure 6.9: (so030): Packing diagram of **11a** in the orthorhombic space group *Pbcm* with view along [010]. The symmetry elements of the space group *Pbcm* are overlaid. Atoms: carbon (grey), hydrogen (white), chlorine (green), nitrogen (blue), oxygen (red), ruthenium (turquoise).

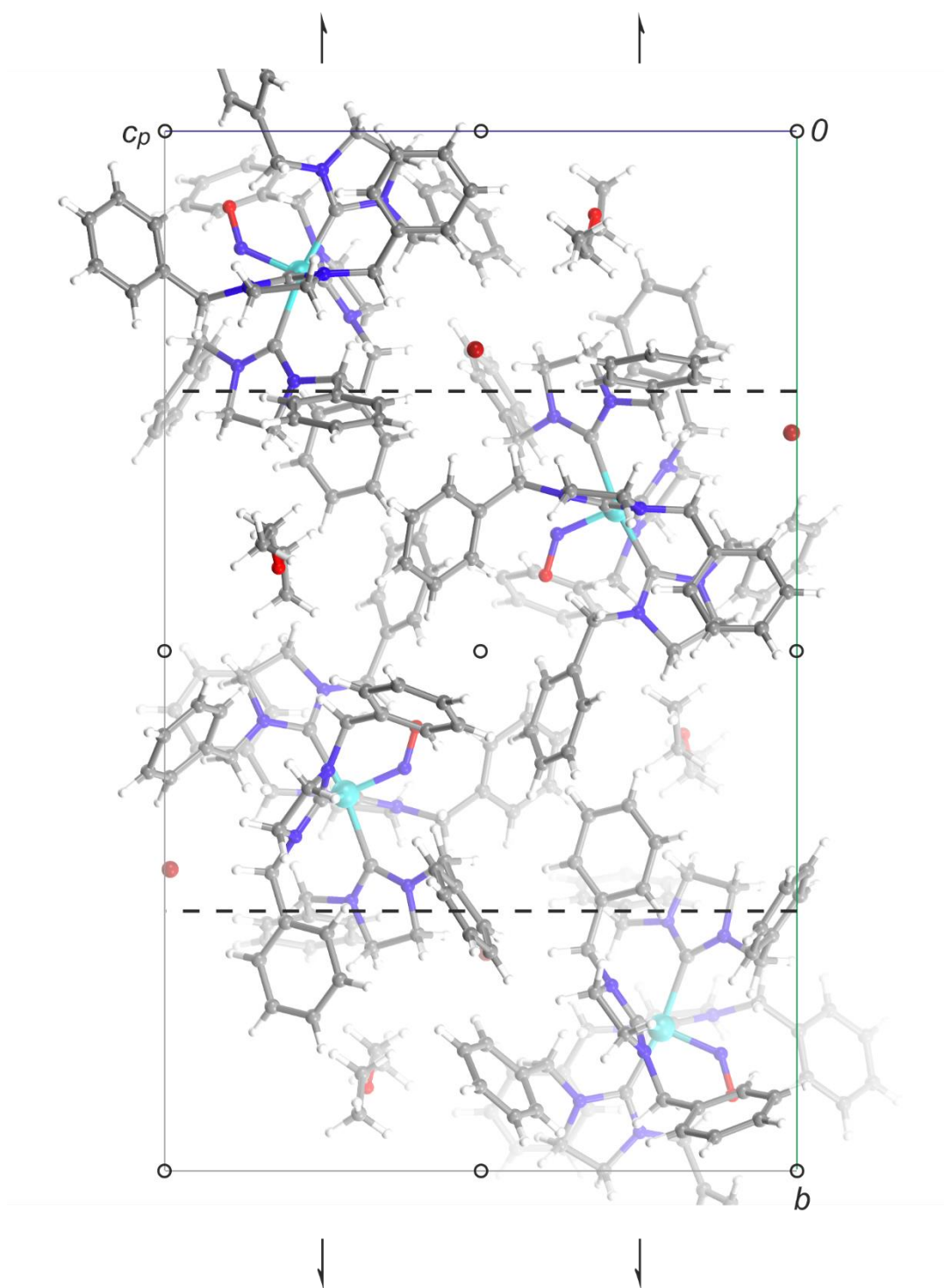


Figure 6.10: (sv283): Packing diagram of **13b** in the monoclinic space group $P2_1/c$ with view along $[100]$. The symmetry elements of the space group $P2_1/c$ are overlaid. Atoms: carbon (grey), hydrogen (white), bromine (dark red), nitrogen (blue), oxygen (red), ruthenium (turquoise).

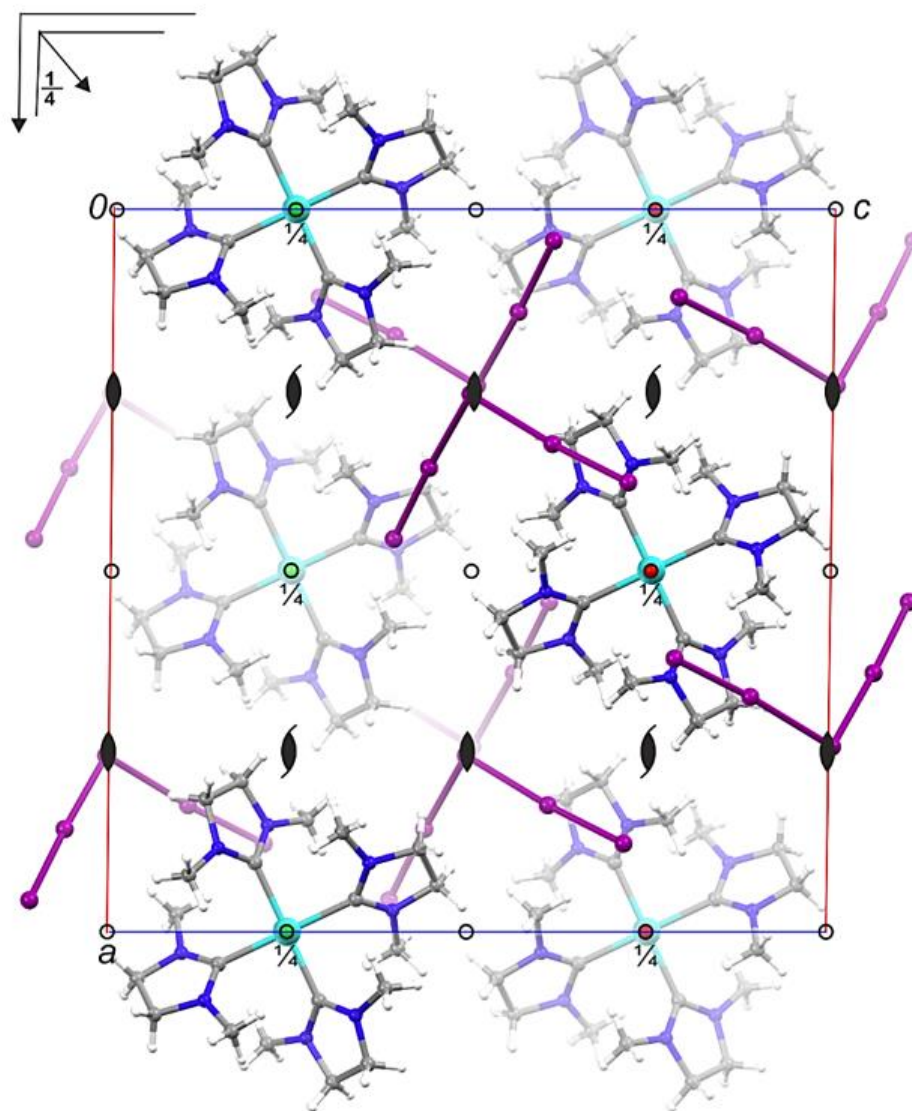


Figure 6.11: (to062): Packing diagram of **14a** in the monoclinic space group $C_{2/c}$ with view along $[010]$. The symmetry elements of the space group $C_{2/c}$ are overlaid. Atoms: carbon (grey), hydrogen (white), chlorine (green), iodine (purple), nitrogen (blue), oxygen (red), ruthenium (turquoise).

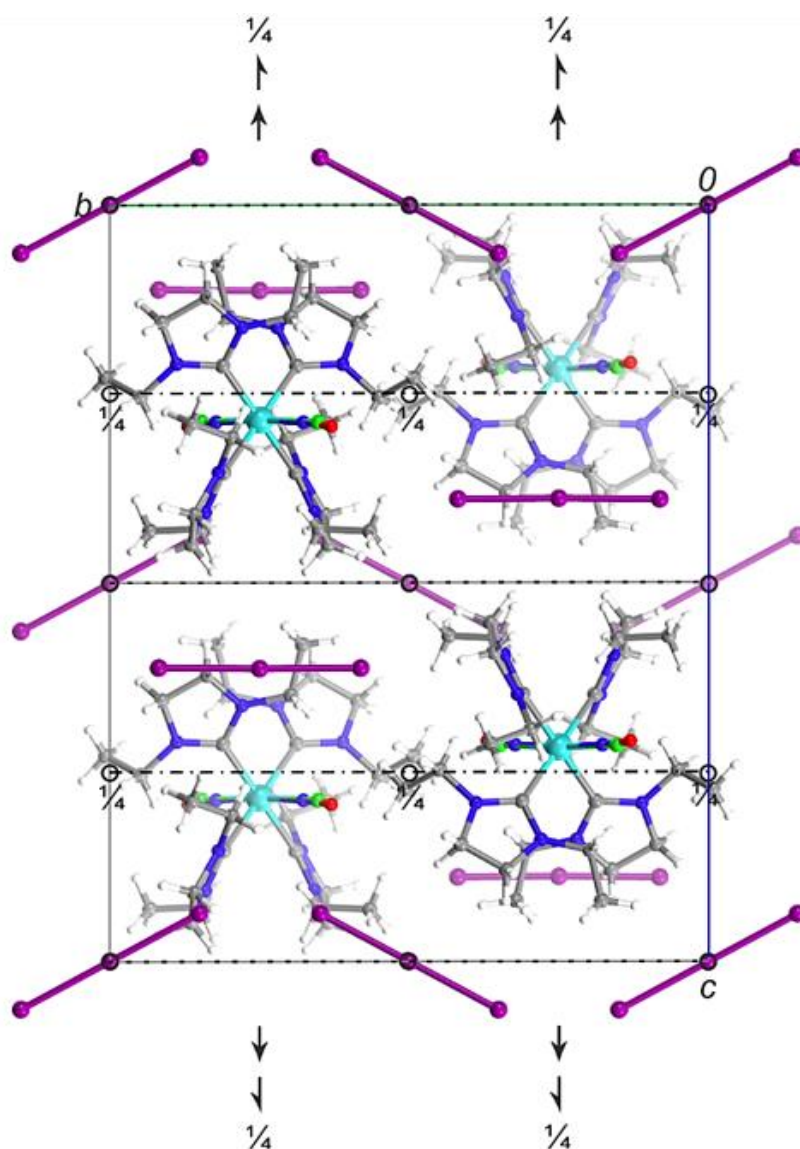


Figure 6.12: (to061): Packing diagram of **15a** in the monoclinic space group $C2/c$ with view along $[010]$. The symmetry elements of the space group $C2/c$ are overlaid. Atoms: carbon (grey), hydrogen (white), chlorine (green), iodine (purple), nitrogen (blue), oxygen (red), ruthenium (turquoise).

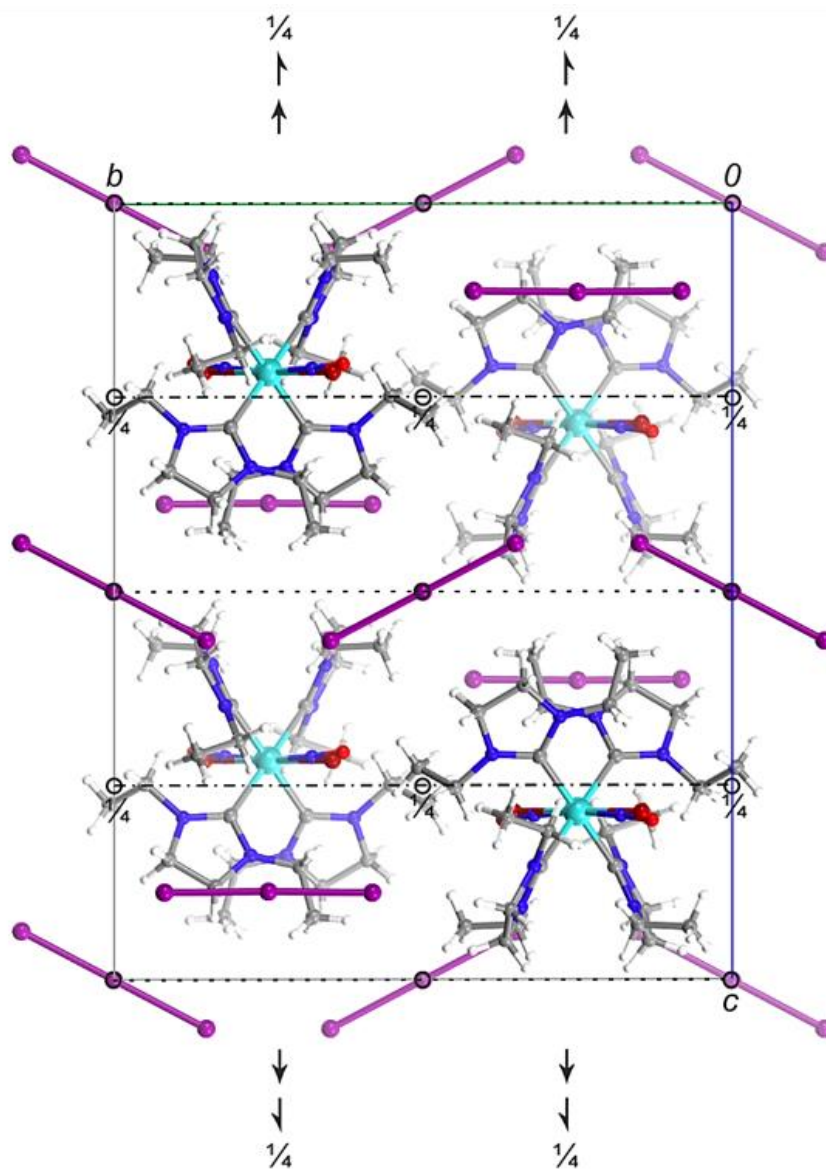


Figure 6.13: (to063): Packing diagram of **15b** in the monoclinic space group $C2/c$ with view along $[010]$. The symmetry elements of the space group $C2/c$ are overlaid. Atoms: carbon (grey), hydrogen (white), bromine (dark red), iodine (purple), nitrogen (blue), oxygen (red), ruthenium (turquoise).

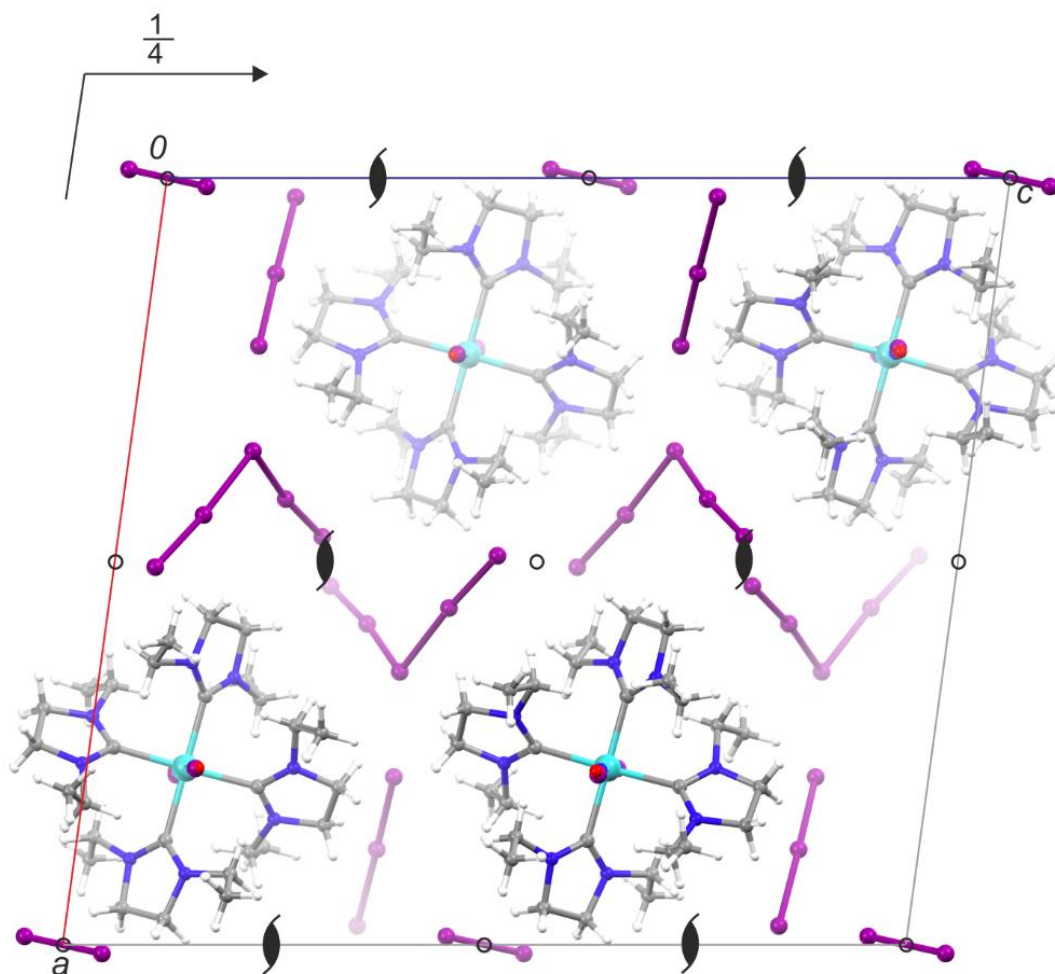


Figure 6.14: (tqo015): Packing diagram of **15c** in the monoclinic space group $P2_1/c$ with view along $[010]$. The symmetry elements of the space group $P2_1/c$ are overlaid. Atoms: carbon (grey), hydrogen (white), iodine (purple), nitrogen (blue), oxygen (red), ruthenium (turquoise).

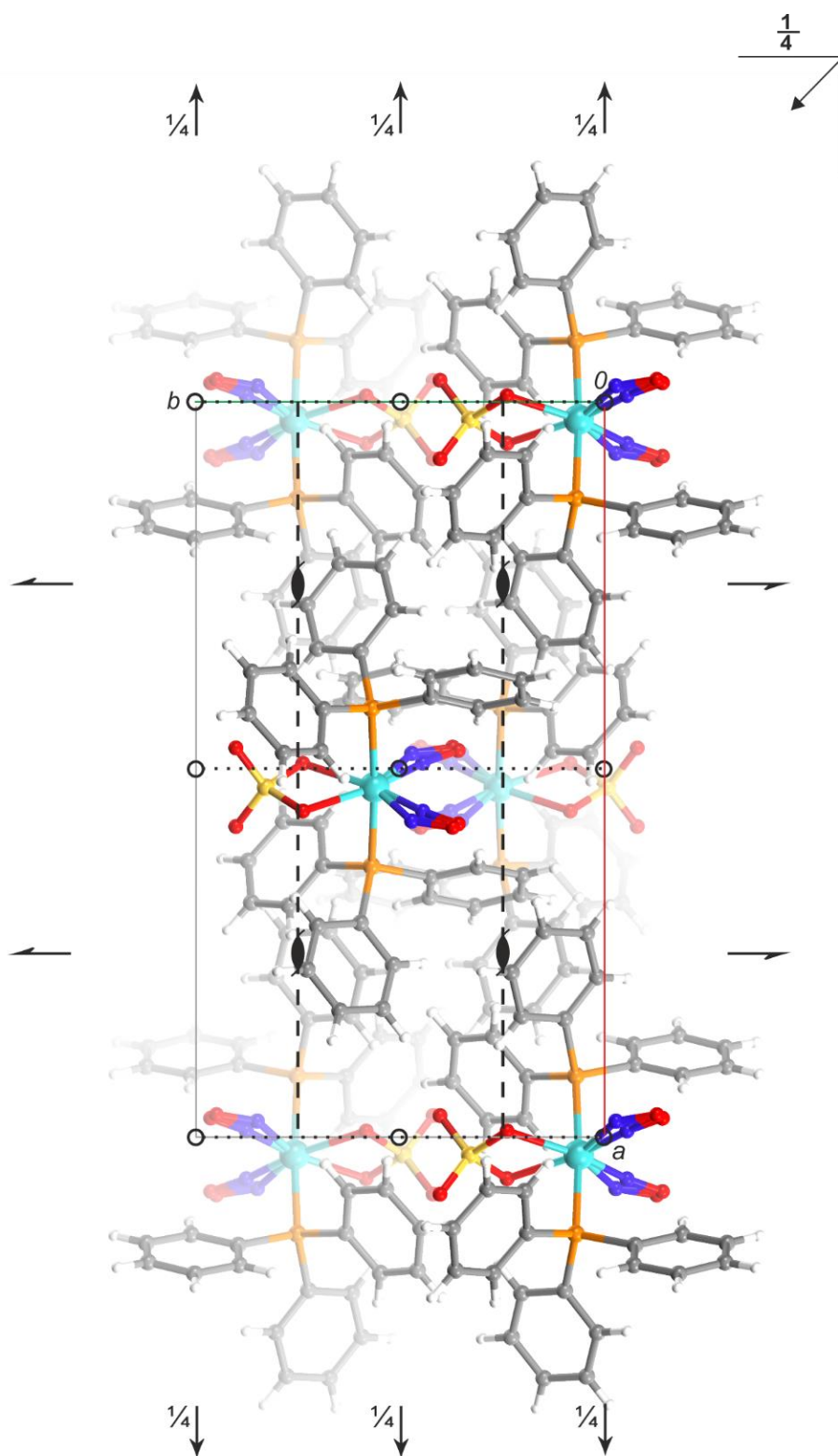


Figure 6.15: (uv126): Packing diagram of **16** in the orthorhombic space group *Pbcn* with view along [001]. The symmetry elements of the space group *Pbcn* are overlaid. Atoms: carbon (grey), hydrogen (white), nitrogen (blue), oxygen (red), phosphorus (orange), ruthenium (turquoise), sulfur (yellow).

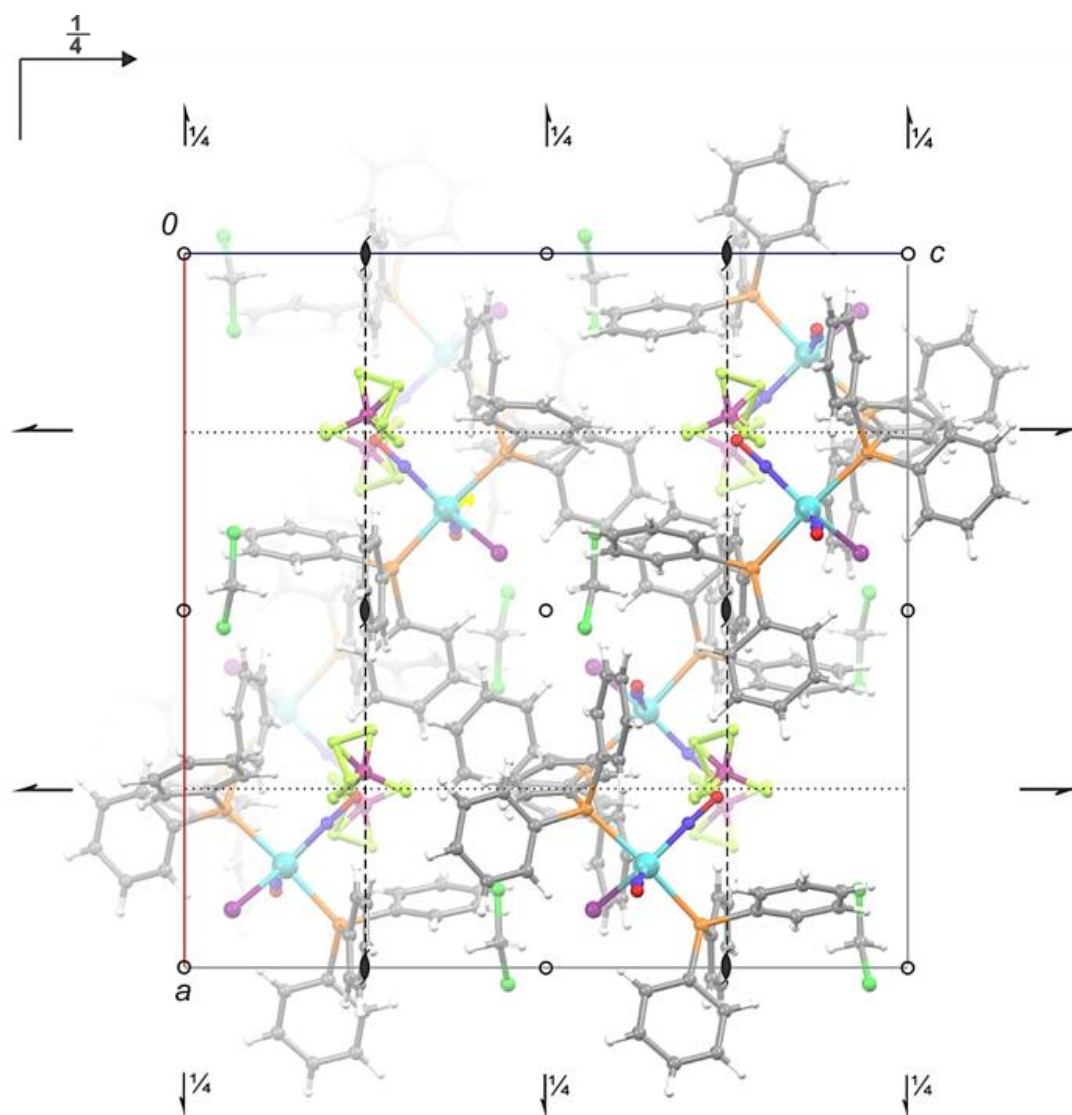


Figure 6.16: (sv250): Packing diagram of **17** in the orthorhombic space group *Pbc_a* with view along [010]. The symmetry elements of the space group *Pbc_a* are overlaid. Atoms: carbon (grey), hydrogen (white), boron (magenta), chlorine (green), fluorine (light green), iodine (purple), nitrogen (blue), oxygen (red), phosphorus (orange), ruthenium (turquoise).

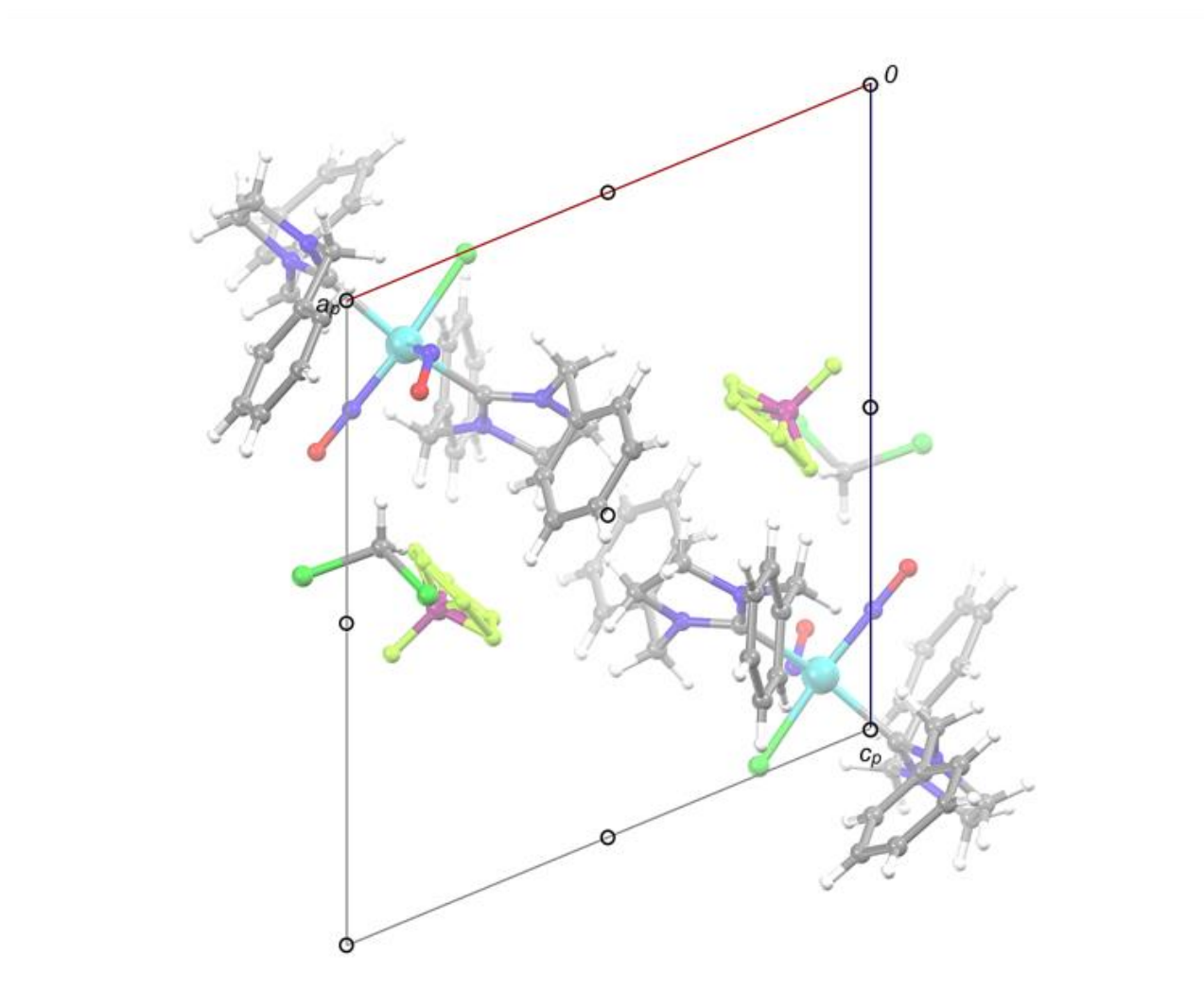


Figure 6.17: (sv070) Packing diagram of **18a** in the triclinic space group $P\bar{1}$ with view along [010]. The symmetry elements of the space group $P\bar{1}$ are overlaid. Atoms: carbon (grey), hydrogen (white), boron (magenta), chlorine (green), fluorine (light green), nitrogen (blue), oxygen (red), phosphorus (orange), ruthenium (turquoise).

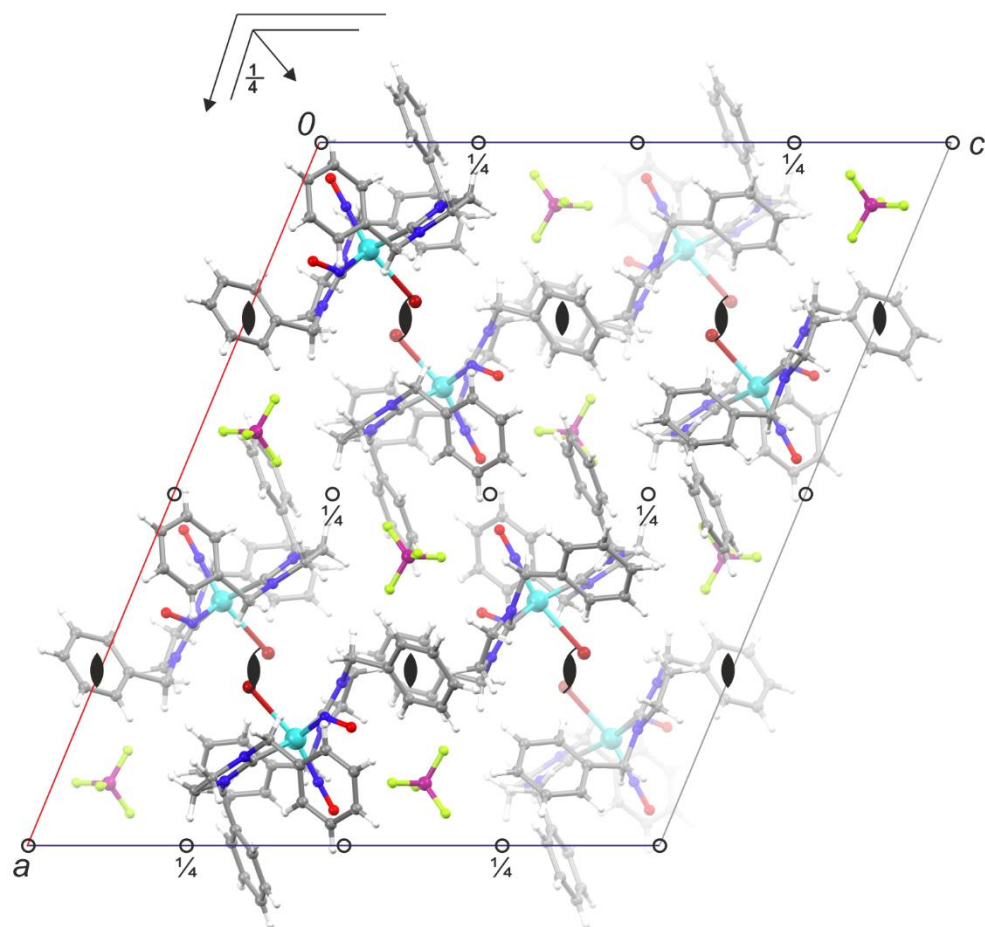


Figure 6.18: (sv118): Packing diagram of **18b** in the monoclinic space group $C2/c$ with view along $[010]$. The symmetry elements of the space group $C2/c$ are overlaid. Atoms: carbon (grey), hydrogen (white), boron (magenta), bromine (red), fluorine (light green), nitrogen (blue), oxygen (red), ruthenium (turquoise).

Appendix

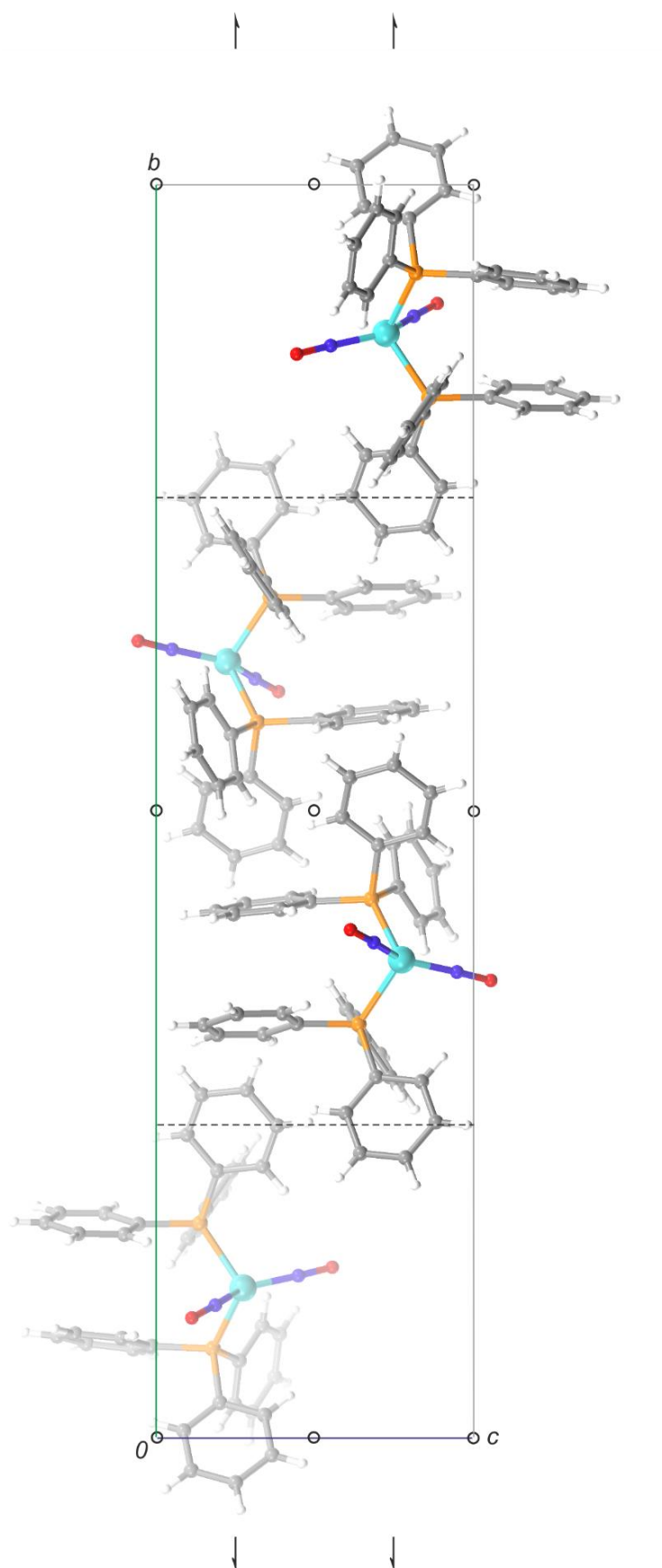


Figure 6.19: (tv276): Packing diagram of **19** in the monoclinic space group $P2_1/n$ with view along $[100]$. The symmetry elements of the space group $P2_1/n$ are overlaid. Atoms: carbon (grey), hydrogen (white), nitrogen (blue), oxygen (red), phosphorus (orange), ruthenium (turquoise).

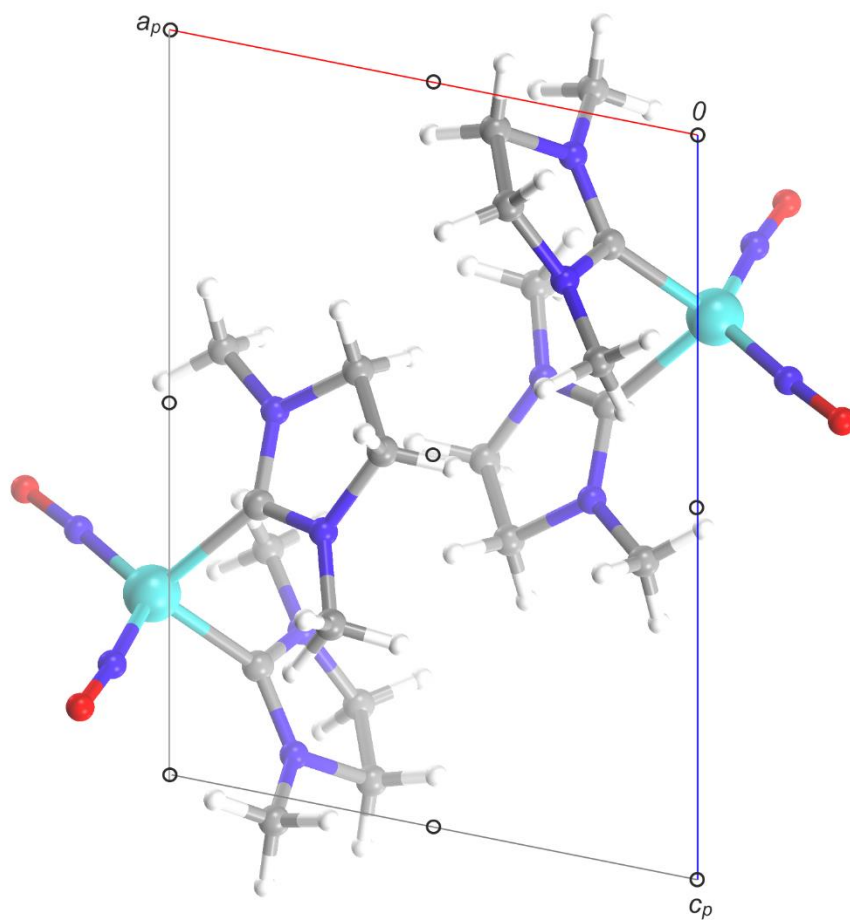


Figure 6.20: (uv027) Packing diagram of **20** in the triclinic space group $P\bar{1}$ with view along $[010]$. The symmetry elements of the space group $P\bar{1}$ are overlaid. Atoms: carbon (grey), hydrogen (white), nitrogen (blue), oxygen (red), ruthenium (turquoise).

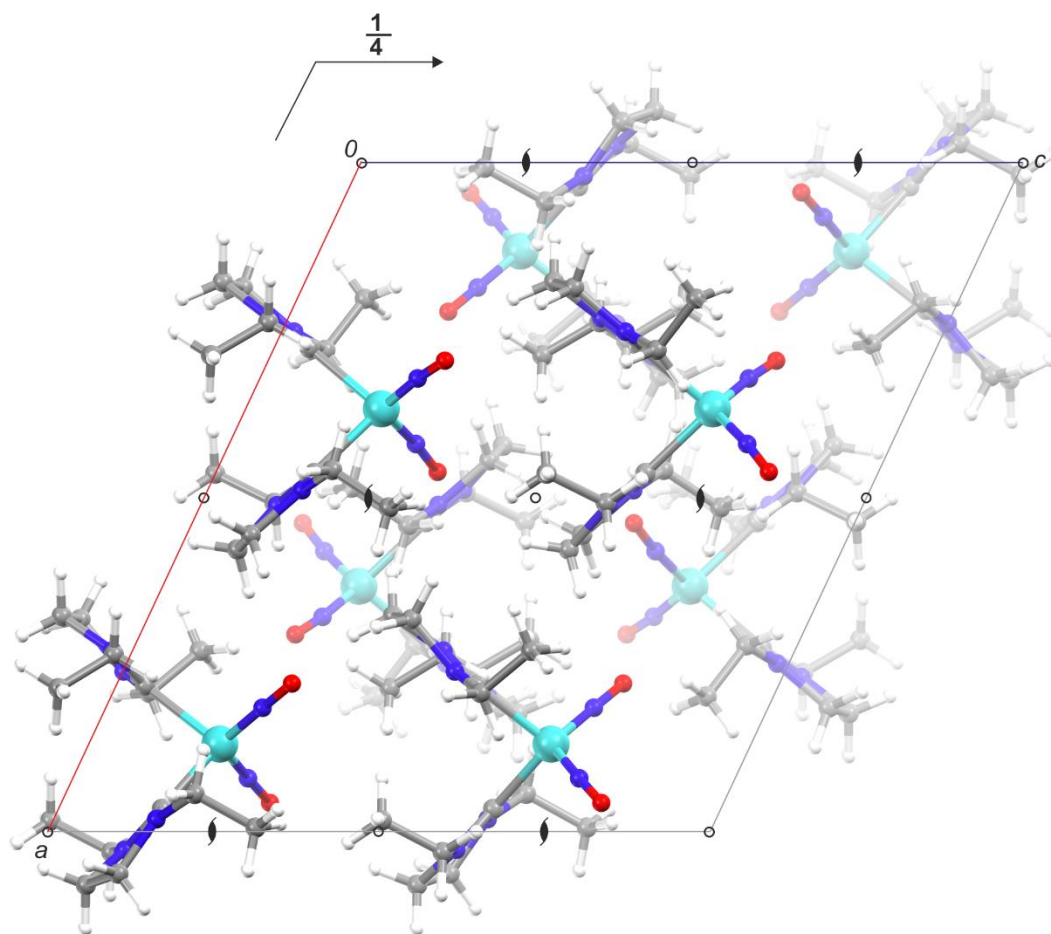


Figure 6.21: (uv108): Packing diagram of **21** in the monoclinic space group $P2_1/c$ with view along $[010]$. The symmetry elements of the space group $P2_1/c$ are overlaid. Atoms: carbon (grey), hydrogen (white), nitrogen (blue), oxygen (red), ruthenium (turquoise).

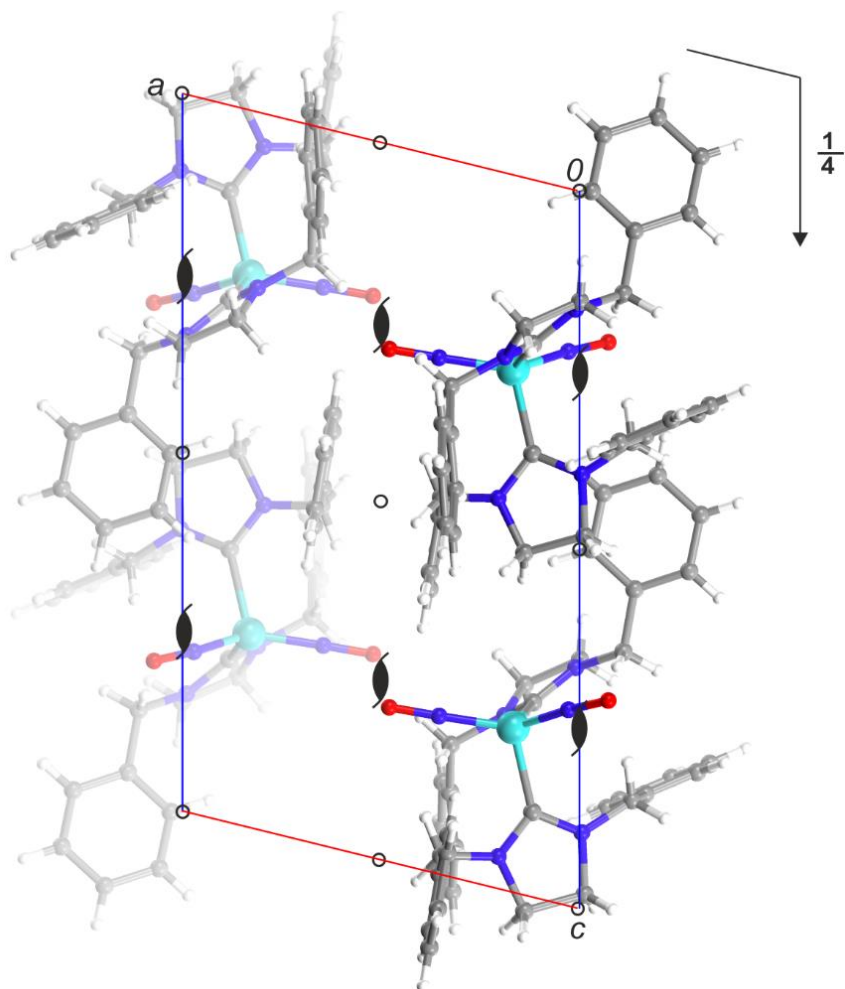


Figure 6.22: (uv118): Packing diagram of **22** in the monoclinic space group $P2_1/c$ with view along $[010]$. The symmetry elements of the space group $P2_1/c$ are overlaid. Atoms: carbon (grey), hydrogen (white), nitrogen (blue), oxygen (red), ruthenium (turquoise).

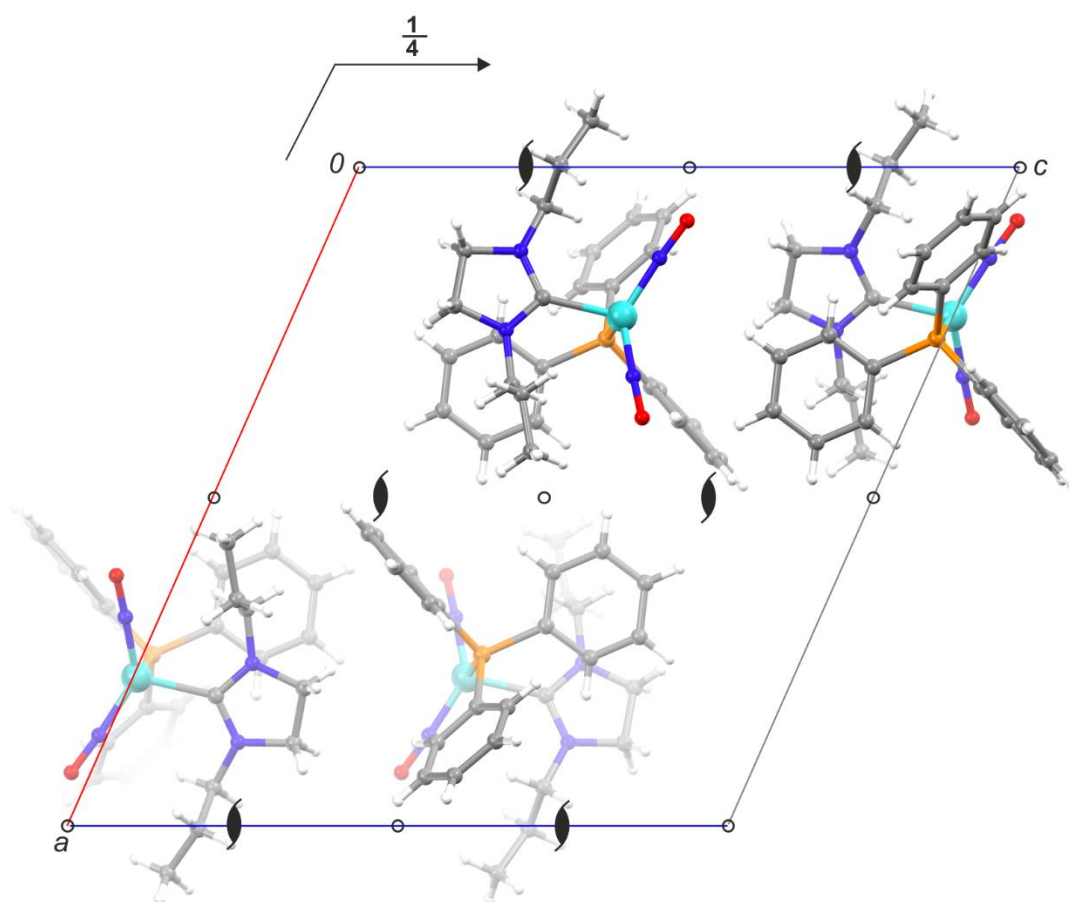


Figure 6.23: (uv190): Packing diagram of **23** in the monoclinic space group $P2_1/c$ with view along $[010]$. The symmetry elements of the space group $P2_1/c$ are overlaid. Atoms: carbon (grey), hydrogen (white), nitrogen (blue), oxygen (red), phosphorus (orange), ruthenium (turquoise).

6.2 Crystallographic tables

Table 6.1: Crystallographic data of NO(HSO₄) (**2**), [RuBr(NO)(PPh₃)₂] (**7b**) and [RuI(NO)(PPh₃)₂] · C₇H₈ (**7c** · C₇H₈).

	2	7b	7c · C ₇ H ₈
netto formula	HNO ₅ S	C ₁₄ H ₂₈ N ₆ O ₂ Ru	C ₄₃ H ₃₈ INOP ₂ Ru
<i>M_r</i> /g mol ⁻¹	127.08	413.49	874.65
crystal system	orthorhombic	monoclinic	monoclinic
space group	<i>Pna</i> 2 ₁	<i>P</i> 2 ₁ / <i>n</i>	<i>P</i> 2 ₁ / <i>c</i>
<i>a</i> /Å	7.3558(4)	7.9790(3)	11.6166(4)
<i>b</i> /Å	6.8924(3)	17.4789(8)	13.8512(5)
<i>c</i> /Å	7.7017(3)	13.0895(7)	23.2588(7)
<i>α</i> /°	90	90	90
<i>β</i> /°	90	98.3941(15)	96.2040(10)
<i>γ</i> /°	90	90	90
<i>V</i> /Å ³	390.47(3)	1805.96(14)	3720.5(2)
<i>Z</i>	4	4	4
<i>ρ</i> /g cm ⁻³	2.162	1.521	1.561
<i>μ</i> /mm ⁻¹	0.732	0.886	1.372
crystal size/mm	0.100 × 0.080 × 0.020	0.070 × 0.050 × 0.020	0.080 × 0.060 × 0.030
temperature/K	100(2)	100(2)	100(2)
diffractometer	Bruker D8Venture	Bruker D8Venture	Bruker D8Venture
radiation	MoK _α	MoK _α	MoK _α
anode	rotating anode	rotating anode	rotating anode
rate input/kW	2.5	2.5	2.5
<i>θ</i> range /°	3.967–27.15	2.831–27.19	2.295–27.30
reflexes for metric	6120	9942	9827
absorption correction	multi-scan	multi-scan	multi-scan
transmission factors	0.6905–0.9582	0.687600–0.743700	0.7014–0.7455
reflexes measured	4760	72057	64814
independent reflexes	473	4007	8199
<i>R</i> _{int}	0.0203	0.0751	0.0319
mean <i>σ</i> (<i>I</i>)/ <i>I</i>	0.0300	0.0514	0.0203
reflexes with <i>I</i> ≥ 2 <i>σ</i> (<i>I</i>)	457	3378	7048
<i>x</i> , <i>y</i> (weighting scheme)	0.0434, 0.0895	0.0158, 1.8706	0.0197, 3.3560
hydrogen refinement	^a	^a	^a
Flack parameter	-0.09(9)	–	–
parameters	71	287	554
<i>restraints</i>	2	0	0
<i>R</i> (<i>F</i> _{obs})	0.0207	0.0317	0.0230
<i>R</i> _w (<i>F</i> ²)	0.0601	0.0611	0.0523
<i>S</i>	1.057	1.043	1.067
<i>shift/error</i> _{max}	0.001	0.001	0.002
max. electron density/e Å ⁻³	0.267	0.453	0.989
min. electron density/e Å ⁻³	-0.260	-0.423	-0.401

^a All H atoms were calculated in idealized positions, riding on their parent atoms.

Appendix

Table 6.2: Crystallographic data of [RuBr(NO)L^{Bn}₂] (**8a**), [RuBr(NO)L^{Bn}₂] (**8b**) and [RuCl(NO)(PPh₃)₃] · 0.5 C₇H₈ (**29a** · C₇H₈).

	8a	8b	29a · C ₇ H ₈
netto formula	C ₃₄ H ₃₆ ClN ₅ ORu	C ₃₄ H ₃₆ BrN ₅ ORu	C ₁₁₅ H ₉₈ Cl ₂ N ₂ O ₂ P ₆ Ru ₂
<i>M_r</i> /g mol ⁻¹	667.20	711.66	1998.81
crystal system	monoclinic	monoclinic	triclinic
space group	<i>P</i> 2 ₁ / <i>n</i>	<i>P</i> 2 ₁ / <i>n</i>	<i>P</i> $\bar{1}$
<i>a</i> /Å	11.2346(7)	11.3332(6)	9.9993(5)
<i>b</i> /Å	11.6448(7)	11.6788(6)	12.5249(6)
<i>c</i> /Å	11.9460(7)	12.0007(6)	20.8398(11)
α /°	90	90	82.355(2)
β /°	107.9121(19)	107.6068(17)	77.287(2)
γ /°	90	90	70.495(2)
<i>V</i> /Å ³	1487.08(16)	1513.98(14)	2394.8(2)
<i>Z</i>	2	2	1
ρ /g cm ⁻³	1.490	1.561	1.386
μ /mm ⁻¹	0.654	1.874	0.525
crystal size/mm	0.140 × 0.052 × 0.037	0.145 × 0.144 × 0.046	0.160 × 0.100 × 0.030
temperature/K	101(2)	130(2)	173(2)
diffractometer	Bruker D8Venture	Bruker D8 Quest	Bruker D8Venture
radiation	MoK α	MoK α	MoK α
anode	rotating anode	Bruker I/mS	rotating anode
rate input/kW	2.5	0.05	2.5
ϑ range /°	2.990–30.60	2.492–26.414	2.712–26.42
reflexes for metric	9862	123	9915
absorption correction	multi-scan	multi-scan	multi-scan
transmission factors	0.7270–0.7461	0.6750–0.7454	0.6834–0.7454
reflexes measured	61341	26222	58466
independent reflexes	4556	3110	9854
<i>R</i> _{int}	0.0501	0.0605	0.0617
mean $\sigma(I)/I$	0.0250	0.0316	0.0341
reflexes with $I \geq 2\sigma(I)$	3716	2621	7948
<i>x</i> , <i>y</i> (weighting scheme)	0.0378, 0.9962	0.0295, 1.9701	0.0169, 7.3632
hydrogen refinement	^a , ^b	^a , ^b	^a
Flack parameter	–	–	–
parameters	205	195	566
<i>restraints</i>	2	0	16
<i>R</i> (<i>F</i> _{obs})	0.0302	0.0366	0.0473
<i>R</i> _w (<i>F</i> ²)	0.0764	0.0839	0.1063
<i>S</i>	1.061	1.164	1.129
<i>shift/error</i> _{max}	0.001	0.001	0.001
max. electron density/e Å ⁻³	0.531	0.379	1.642
min. electron density/e Å ⁻³	-0.319	-0.539	-0.698

^a All H atoms were calculated in idealized positions, riding on their parent atoms. ^b The NO group and the halogenido ligand are disordered in such a way as to be superimposed onto each other.

Appendix

Table 6.3: Crystallographic data of [Ru(NO)(PPh₃)₃] · 2 C₇H₈ (**9b** · 2C₇H₈), [Ru(NO)(L^{Me})₄]Br (**10b**) and [Ru(NO)(L^{Et})₄]Cl (**11a**).

	9b · 2C ₇ H ₈	10b	11a
netto formula	C ₆₈ H ₆₁ INOP ₃ Ru	C ₂₀ H ₄₀ BrN ₉ ORu	C ₂₈ H ₅₆ ClN ₉ ORu
<i>M_r</i> /g mol ⁻¹	1229.05	603.59	671.33
crystal system	triclinic	monoclinic	orthorhombic
space group	<i>P</i> $\bar{1}$	<i>C</i> 2/ <i>c</i>	<i>Pbca</i>
<i>a</i> /Å	12.9051(5)	21.379(2)	16.1071(10)
<i>b</i> /Å	13.7774(6)	7.3415(8)	17.6202(13)
<i>c</i> /Å	17.2510(7)	17.5819(18)	23.5548(15)
α /°	109.2310(10)	90	90
β /°	95.3630(10)	107.192(2)	90
γ /°	101.4120(10)	90	90
<i>V</i> /Å ³	2796.8(2)	2636.2(5)	6685.1(8)
<i>Z</i>	2	4	8
ρ /g cm ⁻³	1.459	1.521	1.334
μ /mm ⁻¹	0.963	2.140	0.584
crystal size/mm	0.090 × 0.060 × 0.020	0.080 × 0.040 × 0.010	0.320 × 0.113 × 0.092
temperature/K	173(2)	298(2)	173(2)
diffractometer	Bruker D8Venture	Bruker D8Venture	Oxford XCalibur
radiation	MoK α	MoK α	MoK α
anode	rotating anode	rotating anode	fine-focus sealed tube
rate input/kW	2.5	2.5	2.0
ϑ range /°	2.943–27.13	3.074–24.10	4.163–28.800
reflexes for metric	9942	4225	2156
absorption correction	multi-scan	multi-scan	multi-scan
transmission factors	0.7084–0.7455	0.6713–0.7450	0.96536–1.00000
reflexes measured	65660	20974	16195
independent reflexes	12378	2088	7614
<i>R</i> _{int}	0.0397	0.0811	0.0584
mean $\sigma(I)/I$	0.0341	0.0346	0.1010
reflexes with $I \geq 2\sigma(I)$	10043	1784	4229
<i>x</i> , <i>y</i> (weighting scheme)	0.0257, 2.6320	0.0314, 0.9028	0.0216,
hydrogen refinement	^a	^{a, b}	^a
Flack parameter	–	–	–
parameters	682	156	369
<i>restraints</i>	2	2	0
<i>R</i> (<i>F</i> _{obs})	0.0274	0.0297	0.0538
<i>R</i> _w (<i>F</i> ²)	0.0624	0.0592	0.1052
<i>S</i>	1.027	1.011	1.002
<i>shift/error</i> _{max}	0.002	0.001	0.001
max. electron density/e Å ⁻³	0.988	0.500	0.727
min. electron density/e Å ⁻³	-0.464	-0.222	-0.864

^a All H atoms were calculated in idealized positions, riding on their parent atoms. ^b O1 is disordered over a crystallographic twofold rotation axis passing through Ru1 and N1.

Appendix

Table 6.4: Crystallographic data of [Ru(NO)(L^{Bn})₄]Br (**13a**), [RuCl(NO)(L^{Me})₄](I₅)₂ (**14a**) and [RuCl(NO)(L^{Et})₄](I₃)₂ (**15a**).

	13a	14b	15a
netto formula	C ₇₂ H ₈₂ BrN ₉ O ₂ Ru	C ₂₀ H ₄₀ ClI ₁₀ N ₉ ORu	C ₂₈ H ₅₆ ClI ₆ N ₉ ORu
<i>M_r</i> /g mol ⁻¹	1286.44	1828.13	1432.73
crystal system	monoclinic	monoclinic	monoclinic
space group	<i>P</i> 2 ₁ / <i>c</i>	<i>C</i> 2/ <i>c</i>	<i>C</i> 2/ <i>c</i>
<i>a</i> /Å	12.1665(3)	20.2640(10)	11.9301(4)
<i>b</i> /Å	29.3257(8)	10.6211(3)	21.7200(5)
<i>c</i> /Å	18.3643(5)	20.1846(8)	17.5800(5)
<i>α</i> /°	90	90	90
<i>β</i> /°	103.9180(10)	90.748(4)	101.903(3)
<i>γ</i> /°	90	90	90
<i>V</i> /Å ³	6359.9(3)	4343.9(3)	4457.4(2)
<i>Z</i>	4	4	4
<i>ρ</i> /g cm ⁻³	1.344	2.795	2.135
<i>μ</i> /mm ⁻¹	0.928	7.558	4.600
crystal size/mm	0.130 × 0.070 × 0.050	0.126 × 0.110 × 0.016	0.238 × 0.148 × 0.055
temperature/K	100(2)	121(2)	121(2)
diffractometer	Bruker D8Venture	Oxford XCalibur	Oxford XCalibur
radiation	MoK _α	MoK _α	MoK _α
anode	rotating anode	fine-focus sealed tube	fine-focus sealed tu
rate input/kW	2.5	2.0	2.0
<i>θ</i> range /°	2.869–25.06	4.126–26.371	4.277–27.485
reflexes for metric	9766	1984	4024
absorption correction	multi-scan	multi-scan	multi-scan
transmission factors	0.6876–0.7452	0.78549–1.00000	0.92088–1.00000
reflexes measured	112761	13120	14991
independent reflexes	11244	4440	5088
<i>R</i> _{int}	0.0715	0.0679	0.0423
mean <i>σ</i> (<i>I</i>)/ <i>I</i>	0.0354	0.0816	0.0487
reflexes with <i>I</i> ≥ 2 <i>σ</i> (<i>I</i>)	9553	2969	3984
<i>x</i> , <i>y</i> (weighting scheme)	0.0432, 24.0468	0.0315, 0	0.0212, 0
hydrogen refinement	^a , ^b	^a	^a , ^c
Flack parameter	–	–	–
parameters	743	190	223
<i>restraints</i>	2	0	0
<i>R</i> (<i>F</i> _{obs})	0.0508	0.0475	0.0323
<i>R</i> _w (<i>F</i> ²)	0.1274	0.1056	0.0660
<i>S</i>	1.046	1.019	1.035
<i>shift/error</i> _{max}	0.001	0.001	0.001
max. electron density/e Å ⁻³	1.797	1.412	0.923
min. electron density/e Å ⁻³	-1.149	-1.748	-0.855

^a All H atoms were calculated in idealized positions, riding on their parent atoms. ^b The diethylether molecule is isotropic due to an unresolved disorder. ^c The nitrosyl group and the Cl ligand are disordered in such a way as to be superimposed onto each other.

Appendix

Table 6.5: Crystallographic data of [RuBr(NO)(L^{Et})₄](I₃)₂ (**15b**), [RuI(NO)(L^{Et})₄](I₃)(I₃) (**15c**) and [Ru(NO)₂(PPh₃)₂SO₄] (**16**).

	15b	15c	16
netto formula	C ₂₈ H ₅₆ BrI ₆ N ₉ ORu	C ₂₈ H ₅₆ I ₁₀ N ₉ ORu	C ₃₆ H ₃₀ N ₂ O ₆ P ₂ RuS
<i>M_r</i> /g mol ⁻¹	1477.19	1904.88	781.69
crystal system	monoclinic	monoclinic	orthorhombic
space group	<i>C2₁/c</i>	<i>P2₁/c</i>	<i>Pbcn</i>
<i>a</i> /Å	12.0347(5)	22.4193(10)	19.3292(10)
<i>b</i> /Å	21.6534(8)	9.6104(4)	10.7254(5)
<i>c</i> /Å	17.5978(7)	24.4005(11)	15.5415(9)
α /°	90	90	90
β /°	101.483(4)	97.7502(14)	90
γ /°	90	90	90
<i>V</i> /Å ³	4494.1(3)	5209.3(4)	3222.0(3)
<i>Z</i>	4	4	4
ρ /g cm ⁻³	2.183	2.429	1.611
μ /mm ⁻¹	5.393	6.259	0.703
crystal size/mm	0.450 × 0.248 × 0.028	0.100 × 0.090 × 0.050	0.110 × 0.080 × 0.060
temperature/K	293(2)	173(2)	173(2)
diffractometer	Oxford XCalibur	Bruker D8 Quest	'Bruker D8Venture'
radiation	MoK α	MoK α	MoK α
anode	fine-focus sealed tube	Bruker I/mS	rotating anode
rate input/kW	2.0	0.50	2.5
ϑ range /°	4.221–26.369	2.280–25.37	3.125–26.38
reflexes for metric	2793	9694	9940
absorption correction	multi-scan	multi-scan	multi-scan
transmission factors	0.43349–1.00000	0.6098–0.7452	0.6998–0.7454
reflexes measured	12440	83328	124894
independent reflexes	4569	9568	3295
<i>R</i> _{int}	0.0494	0.0380	0.0628
mean $\sigma(I)/I$	0.0610	0.0226	0.0208
reflexes with $I \geq 2\sigma(I)$	3333	8115	2857
<i>x</i> , <i>y</i> (weighting scheme)	0.0360, 0	0.0119, 15.4479	0.0262, 4.4323
hydrogen refinement	a, b	a, b	a, c
Flack parameter	–	–	–
parameters	228	473	226
restraints	2	0	2
<i>R</i> (<i>F</i> _{obs})	0.0393	0.0275	0.0277
<i>R</i> _w (<i>F</i> ²)	0.0953	0.0507	0.0694
<i>S</i>	1.030	1.104	1.089
shift/error _{max}	0.001	0.002	0.001
max. electron density/e Å ⁻³	1.417	1.262	0.772
min. electron density/e Å ⁻³	-1.216	-1.241	-0.565

^a All H atoms were calculated in idealized positions, riding on their parent atoms. ^b The nitrosyl group and the halogenido ligand are disordered in such a way as to be superimposed onto each other. ^c The two nitrosyl groups are disordered over a crystallographic twofold rotation axis passing through Ru1 and S1.

Appendix

Table 6.6: Crystallographic data of $[\text{Ru}(\text{NO})_2(\text{PPh}_3)_2]\text{BF}_4 \cdot \text{CH}_2\text{Cl}_2$ (**17** · CH_2Cl_2), $[\text{RuCl}(\text{NO})_2(\text{L}^{\text{Bn}})_2]\text{BF}_4$ (**18a**) and $[\text{RuBr}(\text{NO})_2(\text{L}^{\text{Bn}})_2]\text{BF}_4$ (**18b**).

	17 · CH_2Cl_2	18a	18b
netto formula	$\text{C}_{37}\text{H}_{32}\text{BCl}_2\text{F}_4\text{IN}_2\text{O}_2\text{P}_2\text{Ru}$	$\text{C}_{35}\text{H}_{38}\text{BCl}_3\text{F}_4\text{N}_6\text{O}_2\text{Ru}$	$\text{C}_{34}\text{H}_{36}\text{BBrF}_4\text{N}_6\text{O}_2\text{Ru}$
$M_r/\text{g mol}^{-1}$	983.94	868.94	828.12
crystal system	orthorhombic	triclinic	monoclinic
space group	<i>Pbca</i>	$P\bar{1}$	<i>C2/c</i>
$a/\text{Å}$	20.9816(6)	12.4364(7)	27.2786(8)
$b/\text{Å}$	18.1485(5)	12.7754(7)	12.1840(4)
$c/\text{Å}$	21.2324(6)	13.4875(8)	22.6066(8)
$\alpha/^\circ$	90	85.9328(15)	90
$\beta/^\circ$	90	67.4352(14)	112.6770(10)
$\gamma/^\circ$	90	71.6602(16)	90
$V/\text{Å}^3$	8085.0(4)	1875.30(19)	6932.7(4)
<i>Z</i>	8	2	8
$\rho/\text{g cm}^{-3}$	1.602	1.539	1.588
μ/mm^{-1}	1.413	0.693	1.667
crystal size/mm	0.190 × 0.170 × 0.150	0.110 × 0.080 × 0.060	0.200 × 0.200 × 0.200
temperature/K	173(2)	100(2)	173(2)
diffractometer	Bruker D8Venture	Bruker D8Venture	Bruker D8Venture
radiation	$\text{MoK}\alpha$	$\text{MoK}\alpha$	$\text{MoK}\alpha$
anode	rotating anode	rotating anode	rotating anode
rate input/kW	2.5	2.5	2.5
ϑ range /°	2.795–27.17	2.883–27.53	2.795–27.17
reflexes for metric	9983	9938	9718
absorption correction	multi-scan	multi-scan	multi-scan
transmission factors	0.7228–0.7455	0.7228–0.7456	0.8028–0.8620
reflexes measured	267350	55160	139820
independent reflexes	8962	8658	7670
R_{int}	0.0563	0.0629	0.0723
mean $\sigma(I)/I$	0.0147	0.0495	0.0248
reflexes with $I \geq 2\sigma(I)$	7446	6761	6252
x, y (weighting scheme)	0.0186, 0.5383	0.0486, 3.0483	0.0186, 0.5383
hydrogen refinement	^{a, b}	^{a, b}	^a
Flack parameter	–	–	–
parameters	490	497	442
restraints	0	0	0
$R(F_{\text{obs}})$	0.0430	0.0438	0.0285
$R_w(F^2)$	0.1423	0.1109	0.0658
<i>S</i>	0.983	1.050	1.053
shift/error _{max}	0.001	0.001	0.001
max. electron density/ $e \text{ Å}^{-3}$	1.963	1.229	0.585
min. electron density/ $e \text{ Å}^{-3}$	–1.140	–0.921	–0.430

^a All H atoms were calculated in idealized positions, riding on their parent atoms. ^b The counterion is disordered.

Appendix

Table 6.7: Crystallographic data of [Ru(NO)₂(PPh₃)₂] (**19**), [Ru(NO)₂(L^{Me})₂] (**20**) and [Ru(NO)₂(L^{Et})₂] (**21**).

	19	20	21
netto formula	C ₃₆ H ₃₀ N ₂ O ₂ P ₂ Ru	C ₁₀ H ₂₀ N ₆ O ₂ Ru	C ₁₄ H ₃₀ N ₆ O ₂ Ru
<i>M_r</i> /g mol ⁻¹	685.63	357.39	415.5
crystal system	monoclinic	triclinic	monoclinic
space group	<i>P</i> 2 ₁ / <i>n</i>	<i>P</i> $\bar{1}$	<i>P</i> 2 ₁ / <i>n</i>
<i>a</i> /Å	9.2345(2)	8.0399(5)	14.2992(5)
<i>b</i> /Å	36.4830(9)	9.3001(6)	17.4895(6)
<i>c</i> /Å	9.9196(2)	10.5119(6)	15.9621(6)
α /°	90	101.516(2)	90
β /°	111.2380(7)	95.791(2)	115.1561(11)
γ /°	90	112.208(2)	90
<i>V</i> /Å ³	3114.96(12)	699.43(8)	3613.3(2)
<i>Z</i>	4	2	6
ρ /g cm ⁻³	1.462	1.697	1.520
μ /mm ⁻¹	0.642	1.130	0.886
crystal size/mm	0.100 × 0.080 × 0.050	0.500 × 0.020 × 0.010	0.080 × 0.040 × 0.010
temperature/K	173(2)	100(2)	100(2)
diffractometer	Bruker D8Venture	Bruker D8Venture	Bruker D8Venture
radiation	MoK α	MoK α	MoK α
anode	rotating anode	rotating anode	rotating anode
rate input/kW	2.5	2.5	2.5
ϑ range /°	3.080–26.40	2.448–27.11	1.409–26.38
reflexes for metric	9969	9912	9724
absorption correction	multi-scan	multi-scan	multi-scan
transmission factors	0.6966–0.7454	0.64000–0.74550	0.71680–0.74540
reflexes measured	39194	17814	140268
independent reflexes	6385	3092	7376
<i>R</i> _{int}	0.0458	0.0294	0.0365
mean $\sigma(I)/I$	0.0300	0.0338	0.0178
reflexes with $I \geq 2\sigma(I)$	5449	2852	6339
<i>x</i> , <i>y</i> (weighting scheme)	0.0270, 2.8110	0.0107, 0.7505	0.0247, 2.9981
hydrogen refinement	^a	^a	^a
Flack parameter	–	–	–
parameters	388	176	424
restraints	1	1	0
<i>R</i> (<i>F</i> _{obs})	0.0283	0.0230	0.0231
<i>R</i> _w (<i>F</i> ²)	0.0649	0.0517	0.0643
<i>S</i>	1.041	1.062	1.124
shift/error _{max}	0.001	0.001	0.001
max. electron density/e Å ⁻³	1.278	0.456	0.511
min. electron density/e Å ⁻³	–0.392	–0.569	–0.463

^a All H atoms were calculated in idealized positions, riding on their parent atoms.

Appendix

Table 6.8: Crystallographic data of [Ru(NO)₂(L^{Bn})₂] (**22**) and [Ru(NO)₂(L^{NPr})(PPh₃)] (**23**).

	22	23
netto formula	C ₃₄ H ₃₆ N ₆ O ₂ Ru	C ₂₇ H ₃₃ N ₄ O ₂ PRu
<i>M_r</i> /g mol ⁻¹	661.76	577.61
crystal system	monoclinic	monoclinic
space group	<i>P2</i> ₁ / <i>c</i>	<i>P2</i> ₁ / <i>c</i>
<i>a</i> /Å	9.6962(7)	18.5178(8)
<i>b</i> /Å	18.8077(12)	9.2708(4)
<i>c</i> /Å	17.0178(10)	16.9538(7)
α /°	90	90
β /°	103.694(2)	113.8440(10)
γ /°	90	90
<i>V</i> /Å ³	3015.2(3)	2662.1(2)
<i>Z</i>	4	4
ρ /g cm ⁻³	1.458	1.441
μ /mm ⁻¹	0.562	0.680
crystal size/mm	0.100 × 0.050 × 0.020	0.080 × 0.040 × 0.020
temperature/K	100(2)	100(2)
diffractometer	Bruker D8Venture	Bruker D8Venture
radiation	MoK α	MoK α
anode	rotating anode	rotating anode
rate input/kW	2.5	2.5
ϑ range /°	2.937–27.16	3.046–27.12
reflexes for metric	9538	9487
absorption correction	multi-scan	multi-scan
transmission factors	0.61200–0.74550	0.65360–0.74550
reflexes measured	114056	68420
independent reflexes	6665	5864
<i>R</i> _{int}	0.0937	0.0535
mean $\sigma(I)/I$	0.0517	0.0405
reflexes with $I \geq 2\sigma(I)$	4991	5115
<i>x</i> , <i>y</i> (weighting scheme)	0.0336, 6.2872	0.0193, 3.6004
hydrogen refinement	^a	^a
Flack parameter	–	–
parameters	388	318
<i>restraints</i>	0	0
<i>R</i> (<i>F</i> _{obs})	0.0419	0.0315
<i>R</i> _w (<i>F</i> ²)	0.1016	0.0740
<i>S</i>	1.016	1.074
<i>shift/error</i> _{max}	0.001	0.001
max. electron density/e Å ⁻³	0.832	0.561
min. electron density/e Å ⁻³	–0.963	–0.598

^a All H atoms were calculated in idealized positions, riding on their parent atoms.

7 Bibliography

- [1] C. J. Lowenstein, S. H. Snyder, *Cell* **1992**, *70*, 705–707.
- [2] E. Culotta, D. E. Koshland, *Science* **1992**, *258*, 1862–1865.
- [3] R. F. Furchgott, *Physiology or Medicine* **1998**, 152–169.
- [4] L. J. Ignarro, *Angew. Chemie* **1999**, *111*, 2002–2013; L. J. Ignarro, *Angew. Chem. Int. Ed.* **1999**, *38*, 1882–1892.
- [5] F. Murad, *Angew. Chemie* **1999**, *111*, 1976–1989; F. Murad, *Angew. Chem. Int. Ed.* **1999**, *38*, 1856–1868.
- [6] J. C. Toledo, O. Augusto, *Chem. Res. Toxicol.* **2012**, *25*, 975–989.
- [7] M. A. Marletta, *J. Biol. Chem.* **1993**, *268*, 12231–12234.
- [8] X. Liu, M. J. S. Miller, M. S. Joshi, H. Sadowska-Krowicka, D. A. Clark, J. R. J. Lancaster, *Biochim. Biophys. Acta.* **2015**, *1840*, 1–32.
- [9] X. Liu, M. J. S. Miller, M. S. Joshi, H. Sadowska-Krowicka, D. A. Clark, J. R. Lancaster, *J. Biol. Chem.* **1998**, *273*, 18709–18713.
- [10] O. Augusto, R. M. Gatti, R. Radi, *Arch. Biochem. Biophys.* **1994**, *310*, 118–125.
- [11] M. G. Bonini, R. Radi, G. Ferrer-Sueta, A. M. Ferreira, O. Augusto, *J. Biol. Chem.* **1999**, *274*, 10802–10806.
- [12] G. Ferrer-Sueta, R. Radi, *ACS Chem. Biol.* **2009**, *4*, 161–177.
- [13] V. Pogrebnyaya, A. Usov, A. Baranov, A. Nesterenko, P. Bezyazychnyi, *Russ. J. Appl. Chem.* **1975**, *48*, 1004–1007.
- [14] P. C Ford, D. Wink, D. M. Stanbury, *FEBS Lett.* **1993**, *326*, 1–3.
- [15] M. N. Möller, Q. Li, J. R. Lancaster, A. Denicola, *IUBMB Life* **2007**, *59*, 243–8.
- [16] B. Chen, M. Keshive, W. M. Deen, *Biophys. J.* **1998**, *75*, 745–754.
- [17] T. Shimizu, D. Huang, F. Yan, M. Stranova, M. Bartosova, V. Fojtíková, M. Martínková, *Chem. Rev.* **2015**, *115*, 6491–533.
- [18] Y. Henry, A. Guissani, B. Ducastel, *EPR Characterization of Nitric Oxide Binding to Hemoglobin*,

Bibliography

- in Basic EPR Methodology in Nitric Oxide Research from Chemistry to Biology* **1997**, Springer, Austin, TX.
- [19] P. R. Gardner, A. M. Gardner, L. A. Martin, A. L. Salzman, *Proc. Natl. Acad. Sci. U.S.A.* **1998**, *95*, 10378–10383.
- [20] J. S. Olson, E. W. Foley, C. Rogge, A. L. Tsai, M. P. Doyle, D. D. Lemon, *Free Radical Biol. Med.* **2004**, *36*, 685–697.
- [21] R. F. Furchgott, J. V. Zawadzki, *Nature* **1980**, *288*, 373–376.
- [22] M. Russwurm, D. Koesling, *EMBO J.* **2004**, *23*, 4443–4450.
- [23] T. L. Poulos, *Curr. Opin. Struct. Biol.* **2006**, *16*, 736–743.
- [24] S. Cary, J. Winger, M. A. Marletta, *Proc. Natl. Acad. Sci. U.S.A.* **2005**, *102*, 13604–13609.
- [25] B. Roy, J. Garthwaite, *Proc. Natl. Acad. Sci. U.S.A.* **2006**, *103*, 12185–12190.
- [26] P. C. Ford, I. M. Lorkovic, *Chem. Rev.* **2002**, *102*, 993–1017.
- [27] J. A. McCleverty, *Chem. Rev.* **2004**, *104*, 403–418.
- [28] D. Teillet-Billy, F. Fiquet-Fayard, *J. Phys. B: At., Mol. Opt. Phys.* **1977**, *10*, 111–117.
- [29] A. Calver, J. Collier, P. Vallance, *Exp. Physiol.* **1993**, *78*, 303–326.
- [30] U. Hauser, V. Oestreich, H. D. Rohrweck, *Z. Phys. A* **1977**, *280*, 17–25.
- [31] P. Coppens, I. Novozhilova, A. Kovalevsky, *Chem. Rev.* **2002**, *102*, 861–883.
- [32] G. Stochel, A. Wanat, E. Kuliś, Z. Stasicka, *Coord. Chem. Rev.* **1998**, *171*, 203–220.
- [33] C. Jorgenson Klíxbüll, *Coord. Chem. Rev.* **1966**, *1*, 164–178.
- [34] A. K. E. Gallien, D. Schaniel, T. Woike, P. Klüfers, *Dalton Trans.* **2014**, *43*, 13278–13292.
- [35] J. H. Enemark, R. D. Feltham, *Coord. Chem. Rev.* **1974**, *13*, 339–406.
- [36] T. W. Hayton, P. Legzdins, W. B. Sharp, *Chem. Rev.* **2002**, *102*, 935–991.
- [37] D. M. P. Mingos, *J. Organomet. Chem.* **2014**, *751*, 153–173.
- [38] A. K. Patra, P. K. Mascharak, *Inorg. Chem.* **2003**, *42*, 7363–7365.
- [39] M. J. Rose, N. L. Fry, R. Marlow, L. Hinck, P. K. Mascharak, *J. Am. Chem. Soc.* **2008**, *130*, 8834–

Bibliography

- 8846.
- [40] M. J. Rose, M. M. Olmstead, P. K. Mascharak, *J. Am. Chem. Soc.* **2007**, *129*, 5342–5343.
- [41] G. M. Halpenny, M. M. Olmstead, P. K. Mascharak, *Inorg. Chem.* **2007**, *46*, 6601–6606.
- [42] M. Iwamoto, H. Hamada, *Catal. Today* **1991**, *10*, 57–71.
- [43] S. Kuwata, S. Kura, T. Ikariya, *Polyhedron* **2007**, *26*, 4659–4663.
- [44] W. Lange, *Ber. der dtsh. Chem. Ges.* **1927**, *60*, 962–970.
- [45] M. H. Grootaert, J. A. Van Bokhoven, A. Andrea, B. M. Weckhuysen, R. A. Schoonheydt, *INSITU* **2003**, 7629–7640.
- [46] A. Zangl, P. Klüfers, D. Schaniel, T. Woike, *Inorg. Chem. Commun.* **2009**, *12*, 1064–1066.
- [47] B. J. Nablo, M. H. Schoenfisch, *Biomaterials* **2005**, *26*, 4405–4415.
- [48] K. Ghosh, R. Kumar, S. Kumar, J. S. Meena, *Dalton Trans.* **2013**, *42*, 13444–13452.
- [49] M. Sieger, B. Sarkar, S. Zálíš, J. Fiedler, N. Escola, F. Doctorovich, A. Olabe, W. Kaim, *Dalton Trans.* **2004**, *5*, 1797–1800.
- [50] B. R. Cameron, M. C. Darkes, H. Yee, M. Olsen, S. P. Fricker, T. Renato, G. J. Bridger, N. A. Davies, M. T. Wilson, D. J. Rose, *Inorg. Chem.* **2003**, *36*, 1868–1876.
- [51] N. Chanda, D. Paul, S. Kar, S. M. Mobin, A. Datta, V. G. Puranik, K. K. Rao, G. K. Lahiri, *Inorg. Chem.* **2005**, *44*, 3499–3511.
- [52] N. L. Fry, P. K. Mascharak, *Acc. Chem. Res.* **2011**, *44*, 289–298.
- [53] K. Ghosh, S. Kumar, R. Kumar, U. P. Singh, *Eur. J. Inorg. Chem.* **2012**, 929–938.
- [54] S. Maji, B. Sarkar, M. Patra, A. K. Das, S. M. Mobin, W. Kaim, G. K. Lahiri, *Inorg. Chem.* **2008**, *47*, 3218–3227.
- [55] M. G. Sauaia, R. G. de Lima, A. C. Tedesco, R. S. da Silva, *Inorg. Chem.* **2005**, *44*, 9946–9951.
- [56] M. J. Rose, P. K. Mascharak, *Coord. Chem. Rev.* **2008**, *252*, 2093–2114.
- [57] G. K. Lahiri, W. Kaim, *Dalton Trans.* **2010**, *39*, 4471–4478.
- [58] M. H. B. Stiddard, R. E. Townsend, *J. Chem. Soc. D* **1969**, 1372.

Bibliography

- [59] C. G. Pierpont, R. Eisenberg, *Structure* **1971**, *2*, 2826–2829.
- [60] D. Morales-Morales, R. Redon, R. E. Cramer, *Inorg. Chim. Acta* **2001**, *321*, 181–184.
- [61] A. P. Gaughan, B. J. Corden, R. Eisenberg, *Inorg. Chem.* **1974**, *13*, 789–791.
- [62] N. Arulsamy, D. S. Bohle, J. A. Imonigie, R. C. Moore, *Polyhedron* **2007**, *26*, 4737–4745.
- [63] C. S. D. (version 5.34, july 2016).
- [64] G. B. Richter-Addo, R. A. Wheeler, C. A. Hixson, L. Chen, M. A. Khan, M. K. Ellison, C. E. Schulz, W. R. Scheidt, *J. Am. Chem. Soc.* **2001**, *4*, 6314–6326.
- [65] J. T. Veal, D. J. Hodgson, *Acta Crystallogr. Sect. B* **1972**, *28*, 3525–3529.
- [66] J. R. Durig, W. A. McAllister, J. N. Willis, E. E. Mercer, *Spectrochim. Acta* **1966**, *22*, 1091–1100.
- [67] B. L. Haymore, J. A. Ibers, *Inorg. Chem.* **1975**, *14*, 3060–3070.
- [68] F. Bottomley, *J. Chem. Soc., Dalton Trans.* **1974**, 1600–1605.
- [69] B. Serli, E. Zangrando, E. Iengo, G. Mestroni, L. Yellowlees, E. Alessio, *Inorg. Chem.* **2002**, *41*, 4033–4043.
- [70] F. Bottomley, *Coord. Chem. Rev.* **1978**, *26*, 7–32.
- [71] J. H. Enemark, R. D. Feltham, *Proc. Natl. Acad. Sci. U.S.A.* **1972**, *69*, 3534–3536.
- [72] R. Hoffmann, M. M. L. Chen, M. Elia, A. Rossi, D. M. P. Mingos, *Inorg. Chem.* **1974**, *13*, 2666–2675.
- [73] D. M. P. Mingos, *Inorg. Chem.* **1973**, *12*, 1209–12211.
- [74] A. W. Addison, T. N. Rao, *J. Chem. Soc., Dalton Trans.* **1984**, 1349–1356.
- [75] M. Ogasawara, F. Maseras, N. Gallego-Planas, K. Kawamura, K. Ito, K. Toyota, W. E. Streib, S. Komiya, O. Eisenstein, K. G. Caulton, *Organometallics* **1997**, *16*, 1979–1993.
- [76] C. G. Pierpont, R. Eisenberg, *Inorg. Chem.* **1973**, *12*, 199–205.
- [77] E. Fogler, M. A. Iron, J. Zhang, Y. Ben-David, Y. Diskin-Posner, G. Leitus, L. J. W. Shimon, D. Milstein, *Inorg. Chem.* **2013**, *52*, 11469–11479.
- [78] M. Yamaguchi, Y. Arikawa, Y. Nishimura, K. Umakoshi, M. Onishi, *Chem. Commun.* **2009**, 2911–2913.

Bibliography

- [79] R. Prakash, A. U. Czaja, F. W. Heinemann, D. Sellmann, *J. Am. Chem. Soc.* **2005**, *127*, 13758–13759.
- [80] A. K. E. Gallien, *Dissertation*, LMU München **2014**.
- [81] C. G. Pierpont, R. Eisenberg, *Inorg. Chem.* **1972**, *11*, 1088–1094.
- [82] D. M. P. Mingos, D. J. Sherman, I. D. Williams, *Transit. Met. Chem.* **1987**, *12*, 493–496.
- [83] M. R. Crimmin, R. G. Bergman, F. D. Toste, *Angew. Chemie* **2011**, *123*, 4576–4579; M. R. Crimmin, R. G. Bergman, F. D. Toste, *Angew. Chem. Int. Ed.* **2011**, *50*, 4484–4487.
- [84] L. A. Watson, M. Pink, K. G. Caulton, *J. Mol. Catal. A: Chem.* **2004**, *224*, 51–59.
- [85] W. A. Herrmann, C. Köcher, *Angew. Chemie* **1997**, *109*, 2256–2282; W. A. Herrman, C. Köcher, *Angew. Chem. Int. Ed.* **1997**, *36*, 2162–2187.
- [86] R. H. Crabtree, *J. Organomet. Chem.* **2005**, *690*, 5451–5457.
- [87] D. J. Nelson, S. P. Nolan, *Chem. Soc. Rev.* **2013**, *42*, 6723–6753.
- [88] A. J. Arduengo III, R. L. Harlow, M. A. Kline, *J. Am Chem. Soc.* **1991**, 363–365.
- [89] H. Jacobsen, A. Correa, A. Poater, C. Costabile, L. Cavallo, *Coord. Chem. Rev.* **2009**, *253*, 687–703.
- [90] D. Bourissou, O. Guerret, F. P. Gabbaï, G. Bertrand, *Chem. Rev.* **2000**, *100*, 39–92.
- [91] R. W. Alder, M. E. Blake, L. Chaker, J. N. Harvey, F. Paolini, J. Schütz, *Angew. Chemie* **2004**, *116*, 6020–6036; R. W. Alder, M. E. Blake, L. Chaker, J. N. Harvey, F. Paolini, J. Schütz, *Angew. Chem. Int. Ed.* **2004**, *43*, 5896–5911.
- [92] H. W. Wanzlick, R. Schikora, *Angew. Chem.* **1960**, *72*, 494; H. W. Wanzlick, R. Schikora, *Angew. Chem. Int. Ed.* **1962**, *1*, 75.
- [93] H. W. Wanzlick, *Angew. Chem.* **1962**, *74*, 129–134; H. W. Wanzlick, *Angew. Chem. Int. Ed.* **1962**, *1*, 75–80.
- [94] H. W. Wanzlick, H. J. Kleiner, *Angew. Chem.* **1961**, *73*, 493.
- [95] H. W. Wanzlick, F. Esser, H. J. Kleiner, *Ber. der dtsh. Chem. Ges.* **1963**, *96*, 1208–1212.
- [96] D. M. Lemal, R. A. Loveald, I. K. Kawano, *J. Am. Chem. Soc.* **1964**, *86*, 2518–2519.

Bibliography

- [97] M. F. Lappert, P. B. Hitchcock, P. L. Pye, *J. Chem. Soc., Dalton Trans.* **1977**, 2160–2172.
- [98] M. F. Lappert, *J. Organomet. Chem.* **2005**, *690*, 5467–5473.
- [99] M. F. Lappert, *J. Organomet. Chem.* **1988**, *358*, 185–214.
- [100] J. A. Love, M. S. Sanford, M. W. Day, R. H. Grubbs, *J. Am. Chem. Soc.* **2003**, *125*, 10103–10109.
- [101] M. Scholl, S. Ding, C. W. Lee, R. H. Grubbs, *Org. Lett.* **1999**, *1*, 953–956.
- [102] T. Weskamp, W. C. Schattenmann, M. Spiegler, W. A. Herrmann, *Angew. Chemie* **1998**, *110*, 2631–2633; T. Weskamp, W. C. Schattenmann, M. Spiegler, W. A. Herrmann, *Angew. Chem. Int. Ed.* **1998**, *37*, 2490–2493.
- [103] J. Huang, E. D. Stevens, S. P. Nolan, J. L. Petersen, *J. Am. Chem. Soc.* **1999**, *121*, 2674–2678.
- [104] T. M. Trnka, J. P. Morgan, M. S. Sanford, T. E. Wilhelm, M. Scholl, T. L. Choi, S. Ding, M. W. Day, R. H. Grubbs, *J. Am. Chem. Soc.* **2003**, *125*, 2546–2558.
- [105] E. O. Fischer, *Adv. Organomet. Chem.* **1976**, *14*, 1–32.
- [106] E. O. Fischer, A. Maasböl, *Angew. Chemie* **1964**, *76*, 645–645; E. O. Fischer, A. Maasböl, *Angew. Chem. Int.* **1964**, *3*, 580–581.
- [107] R. R. Schrock, *Acc. Chem. Res.* **1979**, *12*, 98–104.
- [108] R. R. Schrock, *J. Am. Chem. Soc.* **1975**, *97*, 6577–6578.
- [109] D. J. Cardin, B. Cetinkaya, M. F. Lappert, *Chem. Rev.* **1972**, *72*, 545–574.
- [110] T. E. Taylor, M. B. Hall, *J. Am. Chem. Soc.* **1984**, *106*, 1576–1584.
- [111] S. F. Vyboishchikov, G. Frenking, *Chem. Eur. J.* **1998**, *4*, 1428–1438.
- [112] P. de Frémont, N. Marion, S. P. Nolan, *Coord. Chem. Rev.* **2009**, *253*, 862–892.
- [113] M. F. Lappert, H. Goldwhite, J. Kaminski, G. Millhauser, J. Ortiz, M. Vargas, L. Vertal, S. J. Smith, *J. Organomet. Chem.* **1986**, *310*, 21–25.
- [114] H. Biltz, W. Biltz, in *Laboratory Methods of Inorganic Chemistry*, John Wiley & Sons, New York, pp. 204–205, **1928**.
- [115] Z. Mazej, M. Ponikvar-Svet, J. F. Liebman, J. Passmore, H. D. B. Jenkins, *J. Fluorine Chem.* **2009**, *130*, 788–791.

Bibliography

- [116] J. M. Fletcher, I. L. Jenkins, F. M. Lever, F. S. Martin, A. R. Powell, R. Todd, *J. Inorg. Nucl. Chem.* **1955**, *1*, 378–401.
- [117] B. M. J. Cleare, W. P. Griffith, *J. Chem. Soc. (A)* **1967**, 1144–1147.
- [118] J. J. Levison, S. D. Robinson, *J. Chem. Soc. (A)* **1970**, 2947–2954.
- [119] J. Chatt, B. L. Shaw, *J. Chem. Soc. (A)* **1966**, 1811–1812.
- [120] M. F. Lappert, P. L. Pye, *J. Chem. Soc., Dalton Trans.* **1978**, 837–844.
- [121] C. Burkholder, J. William, R. Dolbier, *J. Org. Chem.* **1998**, *63*, 5385–5394.
- [122] K. R. Dixon, *Multinuclear NMR* (Ed.: J. Mason), Plenum Press, New York, pp. 369, **1987**.
- [123] A. P. Gaughan, B. J. Corden, R. Eisenberg, J. A. Ibers, *Inorg. Chem.* **1974**, *13*, 786–791.
- [124] J. P. Perdew, *Phys. Rev. B: Condens. Matter Mater. Phys.* **1986**, *33*, 8822.
- [125] A. D. Becke, *Phys. Rev. A: At., Mol., Opt. Phys.* **1999**, *38*, 3098.
- [126] A. Schaefer, H. Horn, R. Ahlrich, *J. Chem. Phys.* **1992**, *97*, 2571–2577.
- [127] F. Weigend, R. Ahlrich, *Phys. Chem.* **2005**, *7*, 3297–3305.
- [128] S. Grimme, J. Antony, S. Ehrlich, H. Krieg, *J. Chem. Phys.* **2010**, *132*, 154104.
- [129] S. Grimme, S. Ehrlich, L. Goerigk, *J. Comput. Chem.* **2011**, *32*, 1456–1465.
- [130] A. Klamt, G. Schüürmann, *J. Chem. Soc., Perkin Trans. 2* **1993**, 799–805.
- [131] J. P. Perdew, Y. Wang, *Phys. Rev. B: Condens. Matter Mater. Phys.* **1992**, *45*, 13244–13249.
- [132] V. N. Staroverov, G. E. Scuseria, J. Tao, J. P. Perdew, *J. Chem. Phys.* **2003**, *119*, 12129–12137.
- [133] J. Tao, J. P. Perdew, V. N. Staroverov, G. E. Scuseria, *Phys. Rev. Lett.* **2003**, *91*, 1464011–1464014.
- [134] T. Lu, F. Chen, *J. Comput. Chem.* **2012**, *33*, 580–592.
- [135] A. E. Reed, F. Weinstock, J. Weinhold, *J. Chem. Phys.* **1985**, *83*, 735–746.
- [136] C. Elschenbroich, A. Salzer, *Organometallics: A Concise Introduction*, Wiley-VCH: Weinheim, **1992**.
- [137] C. A. Tolman, *Chem. Rev.* **1977**, *77*, 313–348.

Bibliography

- [138] C. A. Streuli, *Anal. Chem.* **1960**, *32*, 985–987.
- [139] L. Perrin, E. Clot, O. Eisenstein, J. Loch, R. H. Crabtree, *Inorg. Chem.* **2001**, *40*, 5806–5811.
- [140] A. T. Termaten, M. Schakel, A. W. Ehler, M. Lutz, A. L. Spek, *Chem. Eur. J.* **2003**, *9*, 3577–3582.
- [141] X. L. Hu, I. Castro-Rodriguez, K. Meyer, *J. Am. Chem. Soc.* **2004**, *126*, 13464–13473.
- [142] M. T. Lee, C. H. Hu, *Organometallics* **2003**, *22*, 612–614.
- [143] M. K. Denk, A. Thadani, K. Hatano, A. J. Lough, *Angew. Chemie* **1997**, *109*, 2719–2721; M. K. Denk, A. Thadani, K. Hatano, A. J. Lough, *Angew. Chem. Int. Ed.* **1997**, *36*, 2607–2609.
- [144] R. Flügel, B. Windmüller, O. Gevert, H. Werner, *Chem. Ber.* **1996**, *129*, 1007–1013.
- [145] R. Hoffmann, M. M. L. Chen, D. L. Thorn, *Inorg. Chem.* **1977**, *16*, 503–511.
- [146] R. H. Summerville, R. Hoffmann, *J. Am. Chem. Soc.* **1976**, *98*, 7240–7254.
- [147] F. Neese, *Wiley Interdiscip. Rev.: Comput. Mol. Sci.* **2012**, *2*, 73–78.
- [148] M. Sierka, A. Hogekamp, R. Ahlrichs, *J. Chem. Phys.* **2003**, *118*, 9136–9148.
- [149] O. Treutler, R. Ahlrichs, *J. Chem. Phys.* **1995**, *102*, 346–354.
- [150] J. Cirera, E. Ruiz, S. Alvarez, *Chem. Eur. J.* **2006**, *12*, 3162–3167.
- [151] S. Alvarez, D. Alemany, J. Casanova, J. Cirera, M. Llunell, D. Avnir, *Coord. Chem. Rev.* **2005**, *249*, 1693–1708.

Danksagung

Danksagung

Herrn Prof. Dr. Peter Klüfers danke ich für freundliche Aufnahme in seinem Arbeitskreis, die sehr interessante Themenstellung, den großen wissenschaftlichen Freiraum und die ausgezeichneten Arbeitsbedingungen.

Herrn Prof. Dr. Hans-Christian Böttcher danke ich für die Erstellung des Zweitgutachtens für die vorliegende Arbeit, sowie für die wertvollen Tipps für die Chemie der Metalnitrosyle.

Für Ihre Mitwirkung in der Promotionskommission danke ich Prof. Dr. Lena Daumann, Prof. Dr. Konstantin Karaghiosoff, Prof. Dr. Achim Hartschuh und Prof. Dr. Wolfgang Beck.

Lida Holowaty-den Toom danke ich für die Hilfe bei allen organisatorischen Dingen, das Korrekturlesen der vorliegenden Arbeit und ihre stets lustige und hilfsbereite Art.

Christine Neumann danke ich für den steten Nachschub an Laborgeräten, sowie vieler nützlicher Tipps zu Arbeitstechniken aller Art und die Messung von unzähliger NMR-Proben.

Sandra Albrecht und Dr. Peter Mayer danke ich für die geduldige und gründliche Einarbeitung in die Praxis des Kristallaufsetzens.

Markus Wolf, Xaver Wurzenberger und Anna Gallien für die geduldige Einführung ins Lösen von Kristallstrukturen und in die anfänglich verwirrende Welt der DFT-Rechnungen.

Vielen Dank an alle, die meine Arbeit so aufmerksam Korrektur gelesen haben: der Klugologe, Töbi Riggermann, Frau Galliene, Banca und Daniel Becky Sonnenschein.

Herzlichen Dank auch an alle meine F-Praktikanten und Bacheloranden – Edward Uhl, Ralf Walczak, Maximilian Sirtl, Kerstin Schmalzgruber, Laura Löbber und Moritz Kofen – für ihre gewissenhafte und fleißige Mitarbeit.

Meinen drei treuen Mitstreitern aus Würzburg Christine Schies, Annike Weißenstein und Jonathan Maier für die unvergessliche Zeit während des Studiums.

Sämtlichen Mitgliedern des Arbeitskreises Klüfers, die mich während meiner Doktorarbeit begleitet haben, danke ich für die hilfsbereite, freundschaftliche Atmosphäre und die lustige und schöne Zeit auch außerhalb des Labors, dabei geht besonderer Dank an meine Laborkollegen Anna Gallien, Daniel Beck und Oliver Richter.

Den letzten Satz widme ich Tobias und meiner Familie: Ohne Euch wäre es nicht gegangen, vielen Dank für alles!